Akademiya Nauk SSSR

NASA
TT
F-629
pt.2
c.1

PROCEEDINGS OF THE SIXTH WINTER SCHOOL ON SPACE PHYSICS

(Apatity, 18 March - 1 April 1969)

Part II

Edited by S.N. Vernov and G.E. Kocharov

TRANSLATED FROM RUSSIAN

Published for the National Aeronautics and Space Administration
and the National Science Foundation, Washington, D.C.
by the Israel Program for Scientific Translations

AKADEMIYA NAUK SSSR · NAUCHNYI SOVET PO KOMPLE
"KOSMICHESKIE LUCHI"·KOL'SKII FILIAL IM. S. M.
POLYARNYI GEOFIZICHESKII INSTITUT

Academy of Sciences of the USSR·Scientific Council on Cosmic Rays
Kola Branch im. S. M. Kirov·Polar Geophysical Institute

PROCEEDINGS OF THE SIXTH WINTER SCHOOL ON SPACE PHYSICS

(Trudy Shestoi Vsesoyuznoi ezhegodnoi zimnei shkoly po kosmofizike)

(Apatity, 18 March — 1 April 1969)

Part II

Edited by S.N. Vernov and G.E. Kocharov

Translated from Russian

Israel Program for Scientific Translations
Jerusalem 1971

TT 70-50080
NASA TT F-630

Published Pursuant to an Agreement with
THE NATIONAL AERONAUTICS AND SPACE ADMINISTRATION
and
THE NATIONAL SCIENCE FOUNDATION, WASHINGTON, D.C.

Copyright © 1971
Israel Program for Scientific Translations Ltd.
IPST Cat. No. 5772

Translated by Y. Oren and A. Moscona
Edited by B. Benny

Printed in Jerusalem by Keter Press
Binding: Wiener Bindery Ltd., Jerusalem

Available from the
U.S. DEPARTMENT OF COMMERCE
National Technical Information Service
Springfield, Va. 22151

XII/16/3

Table of Contents

Section IV. COMETS, METEORITES AND THE MOON

A. Z. Dolginov. The comets in space 3

E. A. Kaimakov and V. I. Sharkov. Laboratory simulation of cometary phenomena 15

K. I. Churyumov. Absolute photometry of cometary nuclei by focal star images 23

K. I. Churyumov and T. Maizlina. Investigation of Comet Honda 1968c from two points of view 24

A. A. Demenko and K. I. Churyumov. A study of the brightness of Comet Ikeya-Seki 1967n during three solar revolutions 25

Z. M. Ioffe. Dynamic processes in comets and their analogy with the dynamics of the Earth's magnetosphere 27

S. V. Viktorov. Morphology of the moon and the analysis of the chemical composition of the lunar surface 28

A. V. Zolotov. Geophysical effects of the Tunguska blast of 1908 29

Section V. GENERATION, ENERGY SPECTRUM, VARIATIONS AND PROPAGATION OF COSMIC RAYS

L. I. Miroshnichenko. Current concepts on the acceleration and propagation of solar cosmic rays 33

A. N. Charakhch'yan and T. N. Charakhch'yan. The energy spectrum of cosmic rays in interstellar space 38

A. N. Charakhch'yan and T. N. Charakhch'yan. The diffusion coefficients of cosmic rays 44

V. A. Dogel' and S. I. Syrovatskii. The diffusion of relativistic electrons in the galaxy and their energy spectrum 53

G. B. Khristiansen. Ultrahigh-energy cosmic rays 56

L. Kh. Shatashvili. 27-day cosmic-radiation variation from ground and stratospheric data (1966—1967) 65

K. K. Fedchenko. Measurement of the cosmic-ray anisotropy during a solar cycle 72

Yu. I. Stozhkov. The 11-year intensity modulation of the galactic cosmic rays and the heliographic distribution of sunspots 77

A. G. Zusmanovich, E. V. Kolomeets, and Yu. A. Shakhova. The modulation of galactic cosmic rays 82

V. P. Okhlopkov. The 27-day variations of cosmic rays and solar activity during 1966—1967 87

V. I. Shishov. Galactic cosmic-ray fluctuations of interplanetary origin 88

M. V. Alaniya and O. G. Rogava. The barometric coefficient of the neutron cosmic-ray component with allowance for proton and muon absorption 89

L. I. Dorman and A. V. Sergeev. Estimate of the partial barometric coefficient of integral multiplicity for the neutron component of secondary cosmic rays 90

V. A. El'tekov and V. F. Nikitin. Comparative analysis of different geomagnetic-field models 92

S. A. Bel'skii. The meteoric variation of cosmic rays near the new solar-activity peak in 1967—1968 93

Section VI. METHODOLOGICAL PROBLEMS

Yu. I. Serebrennikov. Statistical analysis of hypotheses 97

O. B. Vasil'ev. Analysis of hidden periodicities and the possibility of statistical prediction 121

K. A. Kandaurova. A fast Fourier transform 129

Ya. L. Blokh and I. N. Kapustin. A performance criterion for a neutron supermonitor 131

I. N. Kapustin. Mathematical correction of data from multiplicity recorders 134

I. N. Kapustin and V. A. Radkevich. On the coincidence effect in the recording of the neutron component of cosmic rays 141

V. S. Smirnov and V. G. Ustinovich. Computer processing of SCR data 144

I. A. Kuz'min. Instrumentation for the measurement of X-ray bremsstrahlung in the stratosphere in the zone of polar aurorae 146

L. A. Shapovalova and V. I. Tergoev. Device for obtaining cosmic-ray intensities at five-minute intervals 148

M. A. Kovalenko and L. A. Shapovalova. Performance data of the Irkutsk SCR station 149

A. S. Inchin, A. Manshalina, Yu. I. Okulov and I. A. Pimenov. One possibility of approximating the latitude dependence curve 151

E. A. Damaskinskii. Spark chambers 155

L. V. Bakonov, K. N. Ermakov, V. D. Lebedev, A. V. Monakhov, V. I. Rozum and M. V. Stabnakov. Heavy-liquid bubble chamber for investigations in cosmic-ray physics 166

V. S. Chukin. Materials for the optical systems of Cherenkov and scintillation counters 173

G. M. Gorodinskii and E. M. Kruglov. On the possibility of determining the direction and polarization of a photon by two consecutive Compton scatterings in the detector material 175

V. V. Petrov. Five-channel analyzer for low-level signals 177

V. S. Eletskii. A method for determining the parameters of tunnel-diode pulse-height discriminations 182

V. V. Yur'ev, A. M. Romanov and E. V. Myakinin. A "phoswich" fast-neutron scintillation detector 184

S. V. Golenetskii, V. N. Il'inskii, R. L. Aptekar', Yu. A. Gar'yan, E. P. Mazets, V. N. Panov and T. V. Kharitonova. Multichannel gamma spectrometer for cosmic-ray investigations 185

R. S. Zavel'skii. Absolute age determination by the radioactive carbon method 186

Section IV

COMETS, METEORITES AND THE MOON

Edited by V. A. Dergachev and G. E. Kocharov

A. Z. Dolginov

THE COMETS IN SPACE

The physics of comets has long been neglected in the development of astrophysics. It is only lately that these phenomena have roused interest, mainly because of the possibility of using comet observations in the study of interplanetary space. Let us recall that the existence of a solar wind and of interplanetary magnetic fields was predicted from observations of comets, and even the wind velocity was estimated. However, due to the lack of a quantitative theory of cometary atmospheres and some obscure problems in the physics of comets, it has not been possible to describe quantitatively the relationship between cometary activity and the state of interplanetary space. The first step towards such a description must be the construction of a theory of comets in the normal state under the average conditions of interplanetary space.

PRINCIPAL CHARACTERISTICS OF COMETS

Comets may be defined as small bodies of the solar system, whose atmosphere is continuously renewed. Since the beginning of astronomy, more than 2000 comets have been observed for 500 of which the orbits have been determined. Cometary orbits have been found to fall into 2 distinct groups — parabolic and elliptic. A number of hyperbolic orbits have been observed, but there is some evidence that these were originally parabolic and changed under the effect of planetary perturbations. For this reason comets are considered members of the solar system. About 4 new comets are discovered every year. Comets with an elliptic orbit complete, on the average, several hundred revolutions about the sun before losing a considerable amount of volatile substances; then they disintegrate into a stream of meteors scattered over the orbit, which may fall to the Earth if the latter intersects this orbit.

In the observation of comets the following structural formations are clearly distinguished: 1) a roughly spherical luminous coma around a bright center, forming the cometary head; 2) a long straight tail composed of filaments — tail of type I; 3) a curved, wider tail, of type II; 4) a strongly curved tail of type III is sometimes observed. The parts of a comet vary in size within fairly broad limits, but the most typical dimensions are: head diameter $\sim 10^5$ km, tail width also $\sim 10^5$ km and length $10^7 - 10^8$ km. The comet becomes visible as a shining spot, sometimes with the rudiments of a tail, when it approaches to a distance of 5 — 6 AU from the sun. It then

displays a continuous spectrum. At a distance of $r \sim 3$ AU it starts emitting in individual molecular lines, usually the CN lines. At $r \sim 2$ AU the C_2 and NH_2 lines appear, then the C_2 and CO_2 lines, and an extended tail develops. At $r \sim 1.5$ AU the lines of the radicals OH, NH, CH, and of the ions CO^+, CO_2^+, CH^+, and OH^+ appear. At $r \sim 0.7$ AU the Na line shows up, and in the immediate vicinity of the sun, at $r \sim 10^{-2}$ AU, the lines of Mg, Fe, and Ni. It is worth noting that all these molecules are secondary and can be produced only by the dissociation of certain primary particles. The radical molecules, ions, or molecules of such high-melting substances as carbon cannot directly evaporate from the surface of the solid cometary nucleus from which the atmosphere is produced. The blackbody temperature at a distance ~1 AU from the sun is close to room temperature, at which evaporation of carbon or ion formation do not occur. As shown in /1/, the temperature of ice under such conditions is about −70. It is possible that some chemical reactions take place near the nucleus. The coma occupies an enormous volume, but it has a low mean density. Near the nucleus the density is about $10^{12} - 10^{13}$ cm^{-3} and it decreases away from the nucleus first inversely to the square of the distance and then exponentially. The nucleus itself has never been observed directly, since it is surrounded by a bright envelope and is very small, just a few tens of km in radius. The size of the head varies when observed in different spectral lines. This indicates that the various kinds of molecules have different distributions. Some of them dissociate rapidly or are driven into the tail, others are relatively long-lived and drift into the tail more slowly. The tails of type I have an ionic spectrum while those of types II and III have a continuous one. In tails of type I there are apparently no neutral molecules. The lines of these molecules have not been detected in tails of types II and III either, possibly because there are few of them, or else because the molecular lines are not visible against the more intense continuous spectrum. Since the continuous spectrum of tails reproduces the solar spectrum, including the absorption lines of the solar atmosphere, it is normally assumed that these tails consist mainly of dust particles reflecting sunlight. The curved shape of the tails also tends to indicate that they are made up of dust. The trajectories of dust particles moving under the effect of light pressure lie exactly within the region occupied by tails of types II and III, if allowance is made for the motion of the dust source, i.e., the comet. The deflection of the trajectory from the direction to the sun should vary according to the size and density of the dust particles. The width of the tail is determined by the size and density distribution of the particles. The acceleration of dust particles under the effect of light pressure exceeds by a factor of $2 - 3$ the acceleration due to the sun's gravitational attraction. The shape of the tails corresponds to trajectories of dust particles with a density of ~1 g per cm^3 and sizes of $\sim 10^{-4} - 10^{-5}$ cm. The acceleration of ions in tails of type I is $10 - 100$ times higher than that due to the sun's gravity. This acceleration results apparently not from light pressure but from the magnetic field pressure of the solar wind.

THE NEUTRAL GASEOUS COMPONENT OF THE COMETARY HEAD

The distribution function of neutral gaseous molecules may be found from the kinetic equation

$$\frac{\partial N}{\partial t} + \bar{v}\frac{\partial N}{\partial \bar{r}} + \bar{g}\frac{\partial N}{\partial \bar{v}} = -S - \frac{N}{\tau}, \qquad (1)$$

where t is the lifetime of the molecules transforming into other particles by dissociation or ionization; g is the acceleration of the molecules under the effect of light pressure and the sun's gravitational attraction; S is the number of particles emitted by the source per unit time.

Since the region about the nucleus where particle collisions are significant ($\sim$100 km) is much smaller than the head, we will consider it as a point source of molecules. We assume that there exists some hydrodynamic velocity $\bar{u}$ of gas emission from the immediate neighborhood of the nucleus, where collisions are of fundamental importance, that this velocity is directed along the radius vector from the cometary nucleus, i.e., $\bar{u} = u\bar{r}$, and that the emitted particles have a Maxwellian velocity distribution in the coordinate system moving with the velocity u. We accordingly assume a source in the form

$$S(\bar{r}, \bar{v}, t) = (\alpha/\pi)^{3/2} G(t) \delta(\bar{r}) \exp[-\alpha(\bar{v} - u\bar{n})^2], \qquad (2)$$

where $\alpha = v_T^{-2} = (m/2kT)$ is the thermal velocity of the molecules in the neighborhood of the nucleus, and T is the gas temperature in this region. $G(t)$ is the total number of particles emitted with any velocity per unit time interval at time t. Substituting (2) into (1) and solving equation (1), we find the molecular distribution. The solution is derived in /2/. We will consider here only the basic results. The distribution function significantly depends on the Mach number $M = u/v_T$. In the near-nuclear regions (at $\alpha g r \ll 1$, but outside the region of molecular collisions), we get for $M \gg 1$:

$$N(\bar{r}, t) = \frac{\sqrt{\pi} M}{\alpha r^2} G(t) \left[1 + \frac{e^{-M^2}}{M\sqrt{\pi}} \alpha \bar{g} \bar{r}\right], \qquad (3)$$

and for $M \ll 1$:

$$N(\bar{r}, t) = \frac{1 + \sqrt{\pi} M}{2\alpha r^2} G(t) \left[1 + (1 - \sqrt{\pi} M) \alpha \bar{g} \bar{r}\right]. \qquad (4)$$

Thus, at small distances from the nucleus, the hydrodynamic emission velocity tends to reduce the anisotropy in the density distribution and when $M \gg 1$, the distribution is practically isotropic. At large distances from the nucleus, at which $2\alpha g r \gg |2 + M(1 - \cos\vartheta\sqrt{2\alpha g r} + (2r/gt^2)^{1/2}|$ we get

$$N(\bar{r}, t) = \frac{G(t) \exp(-M^2)}{2r} \sqrt{\frac{\alpha g}{2\alpha r}} \exp\left\{-\alpha g r (1 - \cos\vartheta) - \left(\frac{2r}{gt^2}\right)^{1/2} + M\sqrt{2\alpha g r}(1 - \cos\vartheta)\right\}, \qquad (5)$$

where ϑ is the angle of the radius vector of a molecule in the cometocentric coordinate system. The value $\vartheta = 0$ corresponds to the direction away from the sun, in the cometary orbit plane. It is seen from (5) that when $M \ll 1$, the density of particles in the front periphery of the head decreases exponentially. This density distribution is due to the action of the radiation pressure which drives the neutral molecules into the tail. In the case $M \gtrsim 1$ the density in the front of the head first increases, and beyond a distance of $r \sim 2M^2/\alpha g$ it starts decreasing. In fact, if the hydrodynamic thrust is strong, the particles accumulate in the front of the head and cannot escape into the tail. In the back of the head the hydrodynamic velocity and light pressure interact. It is therefore possible that the density in the front of the head is higher than in the back. This has in fact been observed in the case of Encke's and Ikeya — Seki's comets. However, the distribution is usually drawn out backwards, which suggests that M has a low value.

The luminous flux in the frequency interval $\Delta\nu$ which reaches a terrestrial observer from the coma surface visible under a solid angle $\Delta\Omega$ at the time t, and incident upon a unit area of a detector at right angles to the line of sight, is given by

$$I(t) = B_\nu(t) \int_0^{\bar{\tau}} d\tau_B \int_{\Delta\Omega} d\Omega N(\bar{\tau}_B - \bar{\tau}_A, t), \quad (6)$$

$$B_\nu(t) = c \int_{\Delta\nu} d\nu h\nu n_\nu \sigma_\nu(\vartheta, \varphi), \quad (7)$$

where n_ν is the number of solar quanta of frequency ν per unit frequency interval and unit volume of the part under observation; $\sigma_\nu(\vartheta, \varphi)$ is the cross section of a molecule for reemission of a quantum of frequency ν per unit solid angle at the angles ϑ, φ to the incident radiation; c is the speed of light; h is Planck's constant; $\bar{\tau}_A$ is the radius vector between the terrestrial observer and the cometary nucleus; $\bar{\tau}_B$ is the radius vector to the observed point of the coma; $\bar{\tau} = \bar{\tau}_B - \bar{\tau}_A$.

The explicit form of I(t), which is easily obtained by substituting (3)– (5) into (6) and integrating, is given in /2/. Comparison of the isophots observed for the comets listed in the table with those theoretically calculated from (3)–(6) shows a fairly good agreement. The table gives the parameters characterizing the near nuclear region and corresponding to the theoretical isophots.

Values of the parameters characterizing the near-nuclear region and corresponding to the theoretical isophots

Comet	v, cm/sec	T, deg. K	B, cm/sec^2	τ, sec^{-1}
1955 g 0.93 AU C_2	10^5	$1.7 \cdot 10^3$	0.395	$1.35 \cdot 10$
1956 h 0.64 AU C_2	$9.6 \cdot 10^4$	$1.6 \cdot 10^3$	0.844	$\tau_\infty = 3 \cdot 10^6$ $\tau_1 = 3.4 \cdot 10^5$
1959 k 1.055 AU C_2	$8.1 \cdot 10^4$	$1.1 \cdot 10^3$	0.308	$1.48 \cdot 10^5$
1951 l 1.2 AU CN	$1.2 \cdot 10^5$	$2.5 \cdot 10^3$	0.365	$2 \cdot 10^5$
1956 h 0.64 AU CN	$1.36 \cdot 10^5$	$3.15 \cdot 10^3$	1.28	$\tau_\infty = 1.8 \cdot 10^{-5}$ $= 1.26 \cdot 10^5$

It is worth noting that the lifetime of the molecules as calculated from the observed isophots is different for the front and back of the head. This can be explained by the fact that the ultraviolet solar radiation, which is responsible for dissociation and ionization, is strongly absorbed by the molecules and dust particles in the coma. Analysis of the isophots of the Arend-Roland comet (1956h) shows that the molecular lifetime in this comet varies with the angle between the radius vector of the molecule in the cometocentric system and the direction to the sun. In order to evaluate the

optical thickness of the coma, let us compare the lifetime of the C_2 molecule in the comet 1956h with the lifetime of C_2 in the comet 1959k. If both comets were optically thin, the ratio between the lifetimes would be equal to the ratio between the squares of the distances to the sun, i.e., 0.36 in the present case. In actual fact the ratio is equal to 20 (see table). The intensity of the solar ultraviolet radiation is exponentially attenuated by absorption in the coma, therefore when we take the logarithms of the lifetime ratios, we get $x_1 - x_2 = 3$ and $x_1 - x_3 = 1.6$, where x_1, x_2, and x_3 are the optical thicknesses of the comets 1956h, 1959k, and 1951l, respectively. The lifetime ratio for the C_2 molecules in the comets 1955g and 1959k is proportional to the ratio between the squares of their distances from the sun. These comets apparently have optically thin comas, and therefore $x_2 \ll 1$; then $x_1 = 3$ and $x_3 = 1.84$ for the total optical thickness over the head diameter along the direction to the sun. Let us note that the optical thickness in the ultraviolet spectrum does not necessarily have to be the same as the optical thickness in the visible range. This is obvious for molecules, in which the number of levels and the width vary in the different spectral ranges. Such may also be the case for dust particles. If the size distribution of dust particles cuts off sharply at the long-wave ultraviolet and short-wave visible radiation, the ultraviolet will be mainly absorbed and the visible light will be defracted and scattered. Also, if their temperature is very low, cometary dust particles are apt not to absorb visible light quanta while still being able to absorb ultraviolet quanta. Given the optical thickness, it is possible to evaluate the number of molecules leaving the source per unit time. For the Arend-Roland comet we obtain $10^{29} - 10^{30}$ mol/sec.

We mentioned before that apparently the molecules observed cannot be primary, i.e., cannot evaporate directly from the nucleus. Nevertheless, the observed distribution of these molecules indicates that they must be formed near the nucleus, in the region where the number of collisions is high. It is possible that they are produced by chemical reactions.

THE DUST COMPONENT OF THE COMETARY ATMOSPHERE

The most widespread hypothesis on the origin of the dust component of the coma is that of Whipple /3/. The assumption is that the cometary nucleus consists of a conglomerate of volatile ices of substances such as methane, ammonia, etc., including more or less uniformly embedded grains of higher-melting substances, for example, carbon, iron, etc. When the ices evaporate, the gas stream entrains and accelerates the grains, after which they are driven by light pressure into tails of types II and III. This hypothesis makes it difficult to explain the hazy dust envelopes around the nucleus, which expand at a rate of ~ 1 km per sec. The shining haze may enhance for a short time the brightness of the comet by a factor of 1000. The energy required to eject the envelope is very high (of the order of 10^{21} ergs). This cannot be easily attributed to an increased evaporation rate.

We postulated /4/ another origin for the dust component — the appearance and growth of grains on the surface and in the neighborhood of the nucleus. The point is that some cometary gases, including such abundant ones as C_2,

are highly supersaturated and may coalesce into grains if there are enough condensation centers and a sufficient number of collisions to enable the centers to grow to grain size. When the volatile gases evaporate, the high-melting substances contained in the nucleus (as solid solutions or in some other form) do not evaporate at the same rate but settle in the form of a porous crust /1/. This crust may be disrupted by the gas and its particles may act as condensation centers. The condensation involves, of course, not the primary evaporated gases, but the secondary ones formed near the nucleus, such as C_2. Another source of condensation centers are ions. A relatively insignificant number of centers is sufficient to produce the observed amount of dust, since the number of molecules is $10^8 - 10^{11}$ times greater than that of grains. Such a number of centers is easily formed in the vicinity of the nucleus. If the bulk of primary particles goes into the formation of secondary particles (e.g., C_2), with which we are concerned, and if the source of primary particles is the nucleus surface, the concentration of secondary particles is given by

$$n(r) = \frac{Q}{v r^2}\left[1 - e^{\frac{R-r}{v\tau}}\right], \tag{8}$$

where Q is the number of primary particles produced per unit time; v is the velocity of the particles; τ is the lifetime of the particles; R is the radius of the nucleus; r is the distance between the nucleus center and the given point.

The growth of the grains is described by the equation

$$\frac{dG}{dt} = \beta n v S\left[1 - e^{-\frac{q\theta}{kT}}\right], \; G = \left(4\pi\rho^3/3\delta\right), \; S = 4\pi\rho^2, \tag{9}$$

where δ is the number of atoms per unit volume of grain material; G is the total number of atoms in a grain; ρ is the grain radius; q is the heat of sublimation; $\theta = (T - T_s)\,T_s^{-1}$ is the degree of vapor supersaturation; T is the vapor temperature; T_s is the vapor saturation temperature; β is the probability of vapor molecules adhering to a grain and which is taken close to 1.

For carbon in the vicinity of the nucleus $T < 1000°K$, $T_s \sim 2500°K$ $(q/k) \sim 8 \cdot 10^4$. The exponent $(-\frac{q\theta}{kT})$ defining the rate of evaporation of a grain is very small at the given values of Q, q and T and may be omitted. Taking into account that $dr = v\,dt$, we obtain from (9) the following equation for the growth of the grain radius with distance from the nucleus:

$$\frac{d\rho}{dr} = \frac{\beta Q}{v r^2}\left[1 - e^{\frac{R-r}{v\tau}}\right], \tag{10}$$

which has the solution

$$\begin{aligned} \rho &= \beta \frac{Q\delta}{vR}\left[\frac{R}{v\tau}\ln\frac{v\tau}{R} - 0.577\frac{R}{v\tau} + \cdots\right] \quad \text{for} \quad R \ll v\tau, \\ \rho &= \beta \frac{Q\delta}{vR}\left[1 - \frac{v\tau}{R} + \cdots\right], \quad \text{при} \quad R \gg v\tau. \end{aligned} \tag{11}$$

For a further determination we must know the lifetime of the primary particles and the grain density. Putting $\delta \approx 1.2 \cdot 10^{-23}\,cm^{-3}$ (graphite), $\beta \geq 0.5$, $Q \cong 10^{30}$ particles/sec, $v \cong 10^5$ cm/sec and $\tau \sim 10 - 100$ sec, we get $\rho \sim 10^{-4} - 10^{-5}$ cm, which agrees with the observed grain size.

The amount of dust in the cometary atmosphere may increase as a result of: a) a layer of the nucleus becoming exposed and evaporating a large number of condensible parent molecules, or b) an intensification of the hard electromagnetic or corpuscular emission of the sun, which raises the efficiency of the chemical reactions yielding condensible products. The hard radiations may have a controlling effect on the reaction rate, even though they make up a small part of the total solar radiation.

An increase in the dust content raises the brightness of the comet. Accordingly, a correlation may be expected between the brightness of a comet and solar activity. Such a correlation is in fact observed /5/. For instance, the brightness of the head of Halley's comet and the appearance of a halo in it has been closely correlated with solar activity. The strong and abrupt glares associated with the formation of dust halos can be attributed to an enhanced condensation caused by the above-mentioned factors. As any other condensation, the formation of a halo does not require the supply of energy, on the contrary, it releases energy. The change in chemical composition coupled with the increase of condensible matter manifests itself as a change in brightness, even if the amount of matter evaporating per unit time from a unit surface of the nucleus remains constant.

As has been noted, the shape of tails of types II and III is characteristic of the path followed by dust grains under the effect of light pressure. The tails sometimes show luminous condensations which look like clusters of grains simultaneously emitted from the nucleus (synchrones). This suggests that grains are ejected from the vicinity of the nucleus in surges. Sometimes several synchrones occur in a series at roughly regular intervals. This might result from rotation of the nucleus and nonuniformities in its surface composition. When the side with a higher concentration of dust-producing material faces the sun, the ejection may become stronger. This may recur several times, after each period of rotation of the nucleus, until the surface layer involved is depleted.

We have no direct data on the dust composition. Some information may be obtained from measurements of the polarization of light. However, existing analyses of the polarization /6/ are based on the assumption that the grains are randomly oriented, which is apparently incorrect. It has been shown /7/ that the cometary dust grains are brought into rotation by the solar wind, with their rotational axis perpendicular to the wind direction. This alignment results from fluctuations in the number of proton impacts on either side of the center of gravity of each grain. The root-mean-square number of excess protons falling on one side of the center of gravity varies proportionally to the square root of the time. The mean angular momentum acquired by a grain in time t is, therefore,

$$\bar{M} = m\,[\bar{\rho}\,\bar{v}_p]\,(W_p\,t)^{1/2}, \qquad (12)$$

where m is the proton mass; $\bar{v}_p$ is the proton velocity; $\bar{\rho}$ is the mean impact parameter; W_p is the mean number of protons hitting the grain per unit time.

Consider a homogeneous grain of dimensions $B = C$ along two axes and $A = \gamma B$ along the third axis. The motion of such a grain consists of a rotation about the axis $\bar{A}$ and a precession about the direction $\bar{M}$. If the grain is elongated ($\gamma > 1$), the component of angular momentum about the short axis is the largest, since it is associated with the largest mean

impact parameter $\rho_A = \gamma B/4$. The angle between the axis $\vec{A}$ and the direction of the momentum is given by the usual equations of motion of a symmetric top:

$$\cos\theta = M_A/M = (1+\gamma^2)^{-\frac{1}{2}}. \tag{13}$$

The rotational velocity about the axis $\vec{A}$ and the precessional velocity about $\vec{M}$ are given by

$$\omega_A = \omega_{pr}\sqrt{1+\gamma^2}\,\gamma^{-1} = 3\,mv(Wt)^{1/2}(2\gamma B^4\delta)^{-1}. \tag{14}$$

For $B \cong 10^{-4}$ cm, $\rho \approx 5\cdot 10^{-5}$ cm, $\gamma = 1$, $\delta = 1\,\mathrm{g\cdot cm^{-3}}$, given a mean proton flux $J_p \sim 2\cdot 10^8\,\mathrm{cm^2 sec^{-1}}$ and $W \simeq J_p S \approx 2$, we get $\omega_A = \omega_{pr} \approx \sqrt{t}$ radian $\cdot\,\mathrm{sec^{-1}}$. Thus, a dust grain at a solar distance of 1 AU should acquire in the course of a day an angular velocity $\sim 200-300$ radian $\cdot\,\mathrm{sec^{-1}}$, its momentum being perpendicular to the sun's direction.

The dust grains collide not only with solar-wind protons but also with gas molecules of the cometary atmosphere. The molecules in the tail move essentially in the same direction as the solar wind, but they may have at the same time a transverse momentum of the order of $\ell_\perp/\ell_\parallel$ of the longitudinal component, where $\ell_\perp$ and $\ell_\parallel$ are respectively the transverse and longitudinal dimensions of the tail. According to rocket observations, at a distance $\sim$1 AU the solar protons also have a transverse velocity component of about 0.1 their longitudinal velocity. The transverse impulses have a disordering effect on the alignment of angular momenta, though both the molecules and protons basically impart to the grains an oriented momentum. The resultant angular momentum distribution function of the grains is given by

$$F(t,\vec{M}) = \frac{e^{-M_\perp^2/4\mathcal{D}_\perp t}}{4\pi\mathcal{D}_\perp t}\,\frac{e^{-M_\parallel^2/4\mathcal{D}_\parallel t}}{\sqrt{4\pi\mathcal{D}_\parallel t}},$$

where $M_\perp^2 = M_x^2 + M_y^2$, and $M_\parallel^2 = M_z^2$, if the z axis is directed to the sun. The quantities $\mathcal{D}_\parallel$ and $\mathcal{D}_\perp$ play the part of diffusion coefficients in angular momentum space and are respectively parallel and perpendicular to z. They are easily determined by taking into account that the mean values $\langle M_x^2\rangle = 2\mathcal{D}_\perp t$, $\langle M_y^2\rangle = 0$, $\langle M_z^2\rangle = \ell^2\mathcal{D}_\parallel t$, and by using expression (12) for both proton and molecular collisions.

We do not consider here any other momentum-disordering effects, since they are unimportant. A significant fact is that the direction of the radius vector to the sun changes in the cometocentric system during the orbital motion of the comet. This restricts the time t in equation (15) over which an oriented angular momentum can be acquired. Since according to (13) the direction of the momentum is related to the direction of the grain axes, the orientation of the momentum imposes a restriction upon the possible orientations of the grains. For instance, the allowable planes of rotation for very thin grains are the meridian planes of a sphere with its axis along z. Any of the rotating particles can at some time be aligned with this axis, while other orientations are permissible only for some of the particles. The optical thickness is therefore highest along z. The optical anisotropy of the dust medium produces a polarization and angular distribution of the scattered light, and this has to be taken into account in the analysis of the observation results.

THE COMETARY PLASMA

Besides the spectrum of neutral gas and dust, the cometary head also exhibits an ionic spectrum. The ionic spectrum of the head is usually observable only near the nucleus, but in Comet Morehouse it was visible throughout the head. This may be due to the fact that the strong emission observed in the CO^+ lines was not obstructed by the emission of CN and C_2 molecules and dust because of their low content. In Comet Morehouse the development of CO^+ emission could be clearly seen. It appeared on the sunward side, spread out and formed a shell which then contracted towards the nucleus and started collapsing. Its end on the far side of the nucleus extended into thin streamers (500 — 1000 km thick at the base) which converged towards the type-I tail axis like the ribs of an umbrella. The streamers were not quite straight, but slightly wavy. Sometimes they were twisted around the tail axis. The axes of type-I tails are usually perfectly straight. In some cases they may be deflected, without curving, by as much as 10° from the sun's direction. The deflection is most commonly in a retrograde direction, but occasionally is towards the direction of orbital motion. The axis of type-I tails sometimes oscillates slightly about the sun's direction. The structure of the tails, and particularly the ion acceleration, which exceeds by a factor of 100 — 1000 the acceleration due to the sun's gravitational attraction at a distance of 1 AU (0.5 cm sec^{-2}), cannot be attributed to light pressure. This can apparently be explained only by the interaction of the cometary ions with the solar wind and its magnetic field. Specifically, the fact that a type-I tail has been observed in Comet Humason at a distance ~ 5 AU indicates that the solar wind penetrates to such distances. We may note that the tail in Honda's comet displayed a most unusual behavior: it developed an Ω-shaped kink in its middle, covering about one-third of the tail, which later disappeared. This phenomenon can hardly be explained without taking into consideration the interaction of cometary plasma with the interplanetary magnetic field.

The behavior of type-I tails has been studied by many authors. Some of them assume the formation of a shock wave on the plasma boundary and deduce that the appearance of the head in the ionic lines is determined by the shape of the wave. Others consider the development of instability in the interpenetration of two plasma beams (the cometary ions and the solar protons). Some others draw an analogy between the tail of the Earth's magnetosphere and the cometary tail, etc. We will not discuss all these in detail, but only give our view on the coupling mechanism between the cometary plasma and the solar wind.

Let us note first that the interplanetary magnetic field cannot penetrate into the comet. The highly conducting plasma is diamagnetic. Its surface becomes polarized by the electrical fields arising from the moving magnetic fields of the solar wind, and it should separate the interplanetary field lines, which can couple with it only to the extent that its conductivity is not ideal. It therefore seems incorrect to assert, as has been done many times, that the interplanetary field extends over a type-I tail throughout its length. On its own the existence of a radial magnetic field in the ionic tail is not inconsistent with observations (though it does not follow from them), since such a field does not affect the ion motion along the tail. However, this field cannot pass over smoothly into the interplanetary field. In

an interplanetary field of $H \sim 5 \cdot 10^{-5}$ oersted the ions have a Larmor radius of ~100 km at a velocity of ~1 km/sec. This means that they are practically incapable of moving across the field, and after forming in the field they must be immediately trapped and driven into the tail with the velocity of the solar wind. The fact that the ions do not acquire this velocity from the start, but only gradually approach it during their motion in the tail, proves directly that the interplanetary field does not penetrate into the comet. Moreover, solar protons with an energy of ~1 keV are not prevented from penetrating into the comet, since their Larmor radius is ~40,000 km outside the comet, and apparently even larger inside. The solar wind is usually not uniform, but may be described as "gusty." The faster jets overtake the slower ones and interact magnetically with them. As a result various oscillation modes build up. Interaction with the cometary plasma only further reinforces the oscillations. This generates in the comet a random magnetic field traveling with the velocity of the solar wind. This field apparently causes the acceleration of the ions.

In order to describe the behavior of the cometary plasma we need the simultaneous solution of the kinetic equation defining the distribution function of the ions in a self-consistent magnetic field (produced both by the cometary ions and the solar wind) and of Maxwell's equation defining the field. The boundary conditions are defined by the characteristics of the interplanetary medium. Unfortunately, this problem is mathematically too involved. A simpler one may be solved, however. What assumptions have to be made concerning the random magnetic field in the comet in order to explain the observed behavior of type-I tails? In order to answer this question, it is sufficient to solve the kinetic equation for ions in such a field. An equation for the distribution function of charged particles in a random magnetic field traveling with a velocity $\bar{u}$ was derived by the author and I. N. Toptygin /8/. In the case when the Larmor radius of the particles is much larger than the inhomogeneity scale, the equation has the form

$$\bar{v}\frac{\partial F}{\partial t} - \frac{\sqrt{\pi}e^2\langle H^2\rangle L_c}{12\,uc^2}\left[\bar{v}-\bar{u},\frac{\partial}{\partial \bar{p}}\right]^2 F = Q\,, \qquad (16)$$

where $F \equiv F(\bar{r},\bar{p},t)$ is the distribution function of the ions with momentum $\bar{p}$ at the point $\bar{r}$ at the instant t; $\langle H^2\rangle$ is the mean-square random field in the comet; L_c is the characteristic scale of field inhomogeneities; $\bar{u}$ is the velocity of motion of the inhomogeneity, approximately equal to the wind velocity.

Equation (16) is based on a Gaussian size distribution of inhomogeneities. The spectral function defining the field density per unit frequency interval, is taken in the form $(\sqrt{\pi}\langle H^2\rangle L_c/6u)\exp[-\omega^2 L_c/2u^2]$. The ions originate in the near-nuclear region, which is far smaller than the tail. We can therefore take $Q = G(v)\delta(\bar{r})$, where $G(v)$ defines the velocity distribution of the ions at the instant of formation. Since the ion velocity is appreciably smaller than the wind velocity u virtually through out the tail, we can expand the right-hand side of (16) in powers of v/u and discard the small terms. Further, let us resolve the ion velocity $v_\alpha = S_\alpha + w n_\alpha$ into a component $w = v_\alpha n_\alpha$ parallel to the solar-wind velocity $u_\alpha = u n_\alpha$, and S_α perpendicular to it, i.e., $S_\alpha n_\alpha = 0$. After some simple transpositions, equation (16) then assumes

the form

$$\sigma \frac{\partial^2 F}{\partial \sigma^2} + \frac{\partial F}{\partial \sigma} - 2\sigma^2 \frac{\partial F}{\partial R_\perp} - 2\sigma\gamma \frac{\partial F}{\partial R_\parallel} = \frac{2G\sigma}{u} \delta(\vec{R}),$$
$$R_\alpha = (R_\perp)_\alpha + R_\parallel n_\alpha = \frac{e^2 \langle H^2 \rangle}{m^2 c^2} \frac{\sqrt{\pi}}{6} \frac{L_c}{u^2} x_\alpha , \qquad (17)$$

where x_α are the components of the radius vector $\vec{r}$ from the cometary nucleus; $\sigma^2 = s^2/u^2$ and $\gamma = N/u$. From an analysis of (17) we found /9/ that the observed ion acceleration can be attributed to the disorderly magnetic fields carried by the solar wind. However, some values have to be assumed for L_c and $\langle H^2 \rangle$. It is known that particles are most strongly scattered by magnetic inhomogeneities comparable to their Larmor radius or slightly smaller, even if there are inhomogeneities of other sizes. Thus, if we set $L_c \sim 100$ km for a field of $\sim 10^{-5}$ oersted, we select the most effective inhomogeneities. It then follows from (17) that at a distance of 10^{12} cm the ions may reach a longitudinal velocity of ~ 100 km/sec.

CONCLUSION

According to the foregoing, the theory of cometary phenomena is far from complete, even for the case of a quiescent interplanetary medium. A number of advances have nevertheless been made. Besides purely theoretical investigations, further developments require observational data, which are difficult or even impossible to derive from the existing material. What is required is: 1) the study of the molecular and atomic emission spectra of all appearing comets, in order to find the spatial distribution of the various kinds of particles and determine the level populations; 2) analysis of the spectral lines in order to obtain the particle velocity distribution as well as information on collisons, magnetic fields, etc.; 3) study of the polarization in the different lines and in the continuous spectrum in order to ascertain the internal magnetic field and to establish the nature of the dust grains; 4) simulation of cometary phenomena both under laboratory and space conditions.

Bibliography

1. Kaimakov, E.A. and V.I. Sharkov.— Present collection, p. 15.
2. Dolginov, A.Z., Ya.N. Gnedin, and G.G. Novikov.— Planet. and Space Sci. (in print); Dolginov, A.Z. and Yu.N. Gnedin.— Icarus, 5, 64. 1966.
3. Whipple, F.L.— Astrophys. J., 113, 464. 1951.
4. Dolginov, A.Z.— Astronomicheskii Zhurnal, 44, 434. 1967.
5. Dobrovolskii, O.V. Komety (Comets).— Moskva, Izdatel'stvo Nauka. 1966.
6. Liller, W.— Astrophys. J., 132, 867. 1960.

7. Dolginov, A.Z.— Doklady AN SSSR, 179, 1070. 1968.
8. Dolginov, A.Z. and I.N. Toptygin.— ZhETF, 51, 1771. 1966; Geomagnetizm i aeronomiya, 7, 967. 1967; Trudy V Vsesoyuznoi ezhegodnoi zimnei shkoly po kosmofizike, Izdatel'stvo Kol'skogo filiala AN SSSR, Apatity, p.167. 1968; Dolginov, A.Z. and I.N. Toptygin.— Icarus, 8, 54. 1968.
9. Dolginov, A.Z.— In: Sbornik "Fizika komet i meteorov," Kiev, "Naukova Dumka." 1969 (in print).

E. A. Kaimakov and V. I. Sharkov

LABORATORY SIMULATION OF COMETARY PHENOMENA

There are several hypotheses concerning the structure and composition of cometary nuclei /1, 2, 3/ which explain to varying extents the observed processes in comets. Currently many cometologists subscribe to Whipple's hypothesis, which has become classical. According to this hypothesis, cometary nuclei are conglomerates of rocky particles and ices of various kinds. Solar radiation causes sublimation of the ices. The stream of sublimation products drags along solid particles, which leave the nucleus and form the dust component of the cometary atmosphere.

The solar wind and electromagnetic radiation interact with the gaseous cometary atmosphere, producing ionization and photodissociation of parent molecules. The spectra of comets show that the cometary nuclei might consist of H_2O, CO_2, CH_4, NH_3, C_2H_2, etc., in the solid phase. However, the recent laboratory investigations of Potter and Del Duca /4/ reduce the range of possible parent substances yielding cometary radicals. An evaluation of the lifetime of elements forming CN, CH, and C_2, showed that most of them have a lifetime of more than 10 hours at a solar distance of 1 AU, whereas in order to account for the observation data it should be one order of magnitude smaller. Accordingly, pure ices and their mixtures (mechanical) are probably not parent substances for the CN, C_2, and CH groups, and other less stable substances have to be found.

An interesting experiment bearing on the origin of cometary ices was performed by Berger (at General Dynamics, 1967). Berger bombarded with cyclotron protons a frozen mixture of H_2O, CH_4, and H_2 at $-230°C$. A chemical analysis of the reaction products revealed traces of urea ($CO(NH_2)_2$), acetic acid (CH_3COOH), and acetone (CH_3COCH_3). These experiments show that some fairly complex compounds may form in cometary nuclei during their evolution.

Another experiment on the laboratory simulation of cometary phenomena is that of Danielson and Kacai /5/. They studied the ionization and acceleration mechanisms of molecules in cometary atmospheres by means of the interaction of CO_2 ice with hydrogen plasma. It was found that the particles in the coma and tail of the "comet" consist primarily of heavy molecular CO_2^+ ions and that they are accelerated by the plasma stream up to velocities of $\sim 10^5$ cm/sec, which is 10% of the plasma flow velocity. Such laboratory experiments on the simulation of cometary phenomena are of scientific interest, since the direct study of real comets presents considerable difficulties.

The A. F. Ioffe Leningrad Physico-Technical Institute of the USSR Academy of Sciences has been conducting for some years systematic studies on the behavior of low-temperature ices of H_2O and aqueous electrolyte solutions under vacuum. The first investigations were made with pure water ice, of which many properties have been well studied /6/.

A sample of ice prepared from distilled water was placed in a special tray inside a vacuum chamber (pressure $10^{-5}-10^{-6}$ mm Hg) whose walls were cooled by liquid nitrogen. Within the ice were inserted a miniature heating element (electrical) supplying energy to the ice and several copper-constantan thermocouples for recording the temperature at different points of the ice. The ice tray was suspended in the chamber on a spring balance for measuring the change in the weight of the ice sample during sublimation under vacuum.

From the sublimation experiments we determined the following:

1. The variation of the equilibrium temperature T of the ice with the specific power input $W_{sp}(W/cm^2)$ to its surface (Figure 1). The equilibrium temperature is the ice surface temperature at which the energy input goes only to the sublimation of molecules. If we take for the albedo of water ice A = 0.7, we can find from curve 1 the temperature that a cometary nucleus of H_2O would have at various distances from the sun, assuming that the nucleus is not screened by the cometary atmosphere. Thus, for example, at r = 1 AU the nucleus temperature would be −75°.

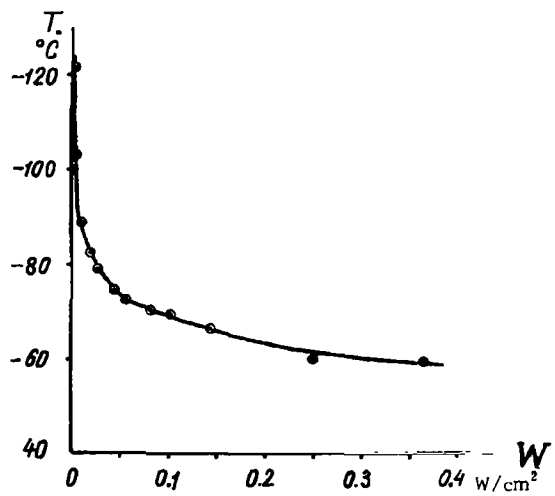

FIGURE 1. Temperature of H_2O ice as a function of the specific power input.

2. The ice consumption I at different temperatures (Figure 2). The dashed curve in the figure is plotted from the kinetic-theory equation

$$J = \alpha p \cdot \sqrt{\frac{M}{2\pi RT}}, \qquad (1)$$

where P is the saturated vapor pressure at temperature T; M is the molecular weight of the substance; R is the gas constant; α is Langmuir's constant of condensation.

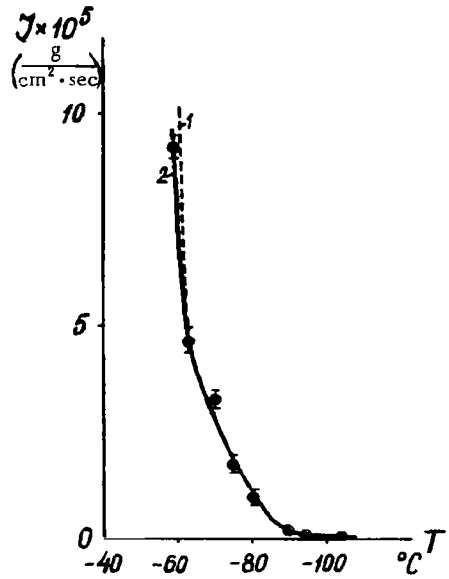

FIGURE 2. Ice consumption at different temperatures:

1 — theoretical curve; 2 — experimental curve.

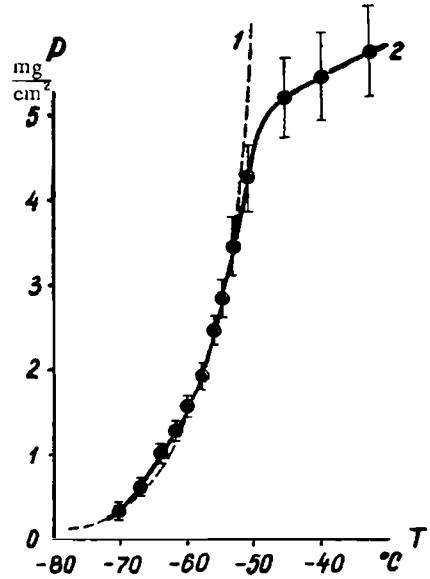

FIGURE 3. Pressure of the products of sublimation of H_2O ice as a function of the temperature:

1 — theoretical curve; 2 — experimental curve.

The agreement of the experimental and calculated curves at low temperatures indicates that in the experiments the sublimation products are efficiently removed from the ice surface ($\alpha = 1$).

3. The heat of sublimation, i.e., the separation energy of a molecule on the ice surface plus its kinetic energy. In the temperature range from −60 to −90° the sublimation energy equals 670 ± 20 cal/g.

We studied the sublimation of H_2O ice in a vacuum under the effect of a light beam. We used as light source a superhigh-pressure mercury-vapor lamp, whose spectral composition in the wavelength range between 2300 and 10,000 Å is close to that of sunlight. A light beam of known power was shined on the ice surface, and the consumption of ice was measured in the temperature range from −55 to −60°. The absorbed light power was calculated by taking the ice albedo equal to 0.7. The results of experiments performed with light agreed within the measurement error with those obtained by heating.

We measured the pressure of the sublimation products of water ice in the temperature range from −75 to −33°. For this purpose a torsion balance with a sensitivity of 4.4 grad/mg was used. The values found for the thrust of H_2O molecules are plotted in Figure 3. The dashed curve was obtained by calculation.

The pressure of the sublimation products may be calculated from

$$P = J v_x , \qquad (2)$$

where I is the rate of discharge, given by equation (1); v_x is the mean velocity of molecules escaping in the given direction,

$$v_x = \sqrt{\frac{kT}{2\pi m}} , \qquad (3)$$

where m is the molecule mass; k is Boltzmann's constant; and T is the ice temperature (in the calculations α was taken equal to 1).

The agreement of the curves in the temperature range from −75 to −50° indicates that the angular distribution of molecules satisfies the cosine emission law, since equation (3) was derived on that assumption. The divergence of the curves above −50° is due to a "greenhouse effect" — an atmosphere of H_2O forms over the ice surface, in which the molecules undergo mutual collisions. Some of the molecules return to the ice surface, and this reduces the net increase of the thrust with the ice temperature. It should be noted that all the experiments were made on ice samples whose size did not exceed the molecular mean free path.

Besides tests with pure water ice, we are carrying out a series of experiments with frozen aqueous solutions of electrolytes. The study of the behavior of such systems under high vacuum at low temperatures is of interest both in solid-state physics and the physics of comets. Swing and Delsemme /7/, for instance, believe that the "parent" molecules must exist in cometary nuclei not in the form of pure ices, but as frozen hydrates of the form $B \cdot n \cdot H_2O$, where B is the considered parent molecule and $n \cdot H_2O$ is the number of water molecules bonded to it.

According to their outward behavior in a vacuum, frozen solutions may be divided into two types:

1. Solutions whose ices form by sublimation a porous salt matrix (e.g., KCl or $CO(NH_2)_2$ solutions);

2. Solutions which do not form a matrix. Among these are NH_4OH, $(NH_4)_2CO_3$, etc. The first type is more commonly encountered.

A special position is occupied by solutions of the LiCl type, which have hydrated ions. Initial results on the ice consumption, pressure of sublimation products, and temperature as functions of the specific power input have been obtained for solutions of NH_4OH, $(NH_4)_2CO_3$, LiCl, and KCl. Figure 4 shows the time variation of pressure of the sublimation products of a KCl solution (C = 1.5 g-equiv. /l), for two values of the specific power. The pressure rise at the beginning is due to the warmup of the ice. Subsequently a salt matrix forms on the sample surface, and as its thickness increases the thrust drops. Independent tests on the determination of the consumption of ice made of a KCl solution showed that the discharge of H_2O from the frozen solution corresponds to the discharge from water ice at the same power input. The decrease of the thrust with time is therefore due to a reduction in the velocity of the sublimating molecules when they pass through the pores of the matrix.

Experimentation with frozen solutions helps to eliminate many of the difficulties involved in working with ices of other chemical nature, for example, CO_2, C_2H_2, CH_4, etc. The range of substances is quite varied,

and thus appropriate combinations can be chosen which would yield by sublimation under solar radiation spectra similar to those observed in real comets.

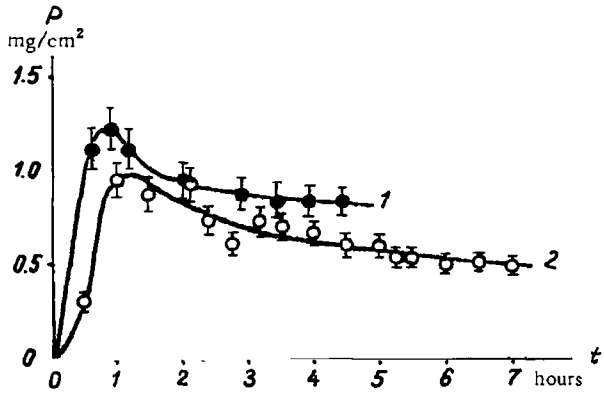

FIGURE 4. Pressure of the sublimation products of a frozen KCl solution:

1 — $W_1 = 0.064$ W/cm²; 2 — $W_2 = 0.058$ W/cm².

It is known that sunlight is scattered by dust particles in the atmospheres and tails of comets. Many cometologists are concerned with the mechanism of formation and acceleration of the cometary dust particles, as well as other relevant characteristics of the dust component. We therefore made it a point to study the behavior of "contaminated" ices in a vacuum, i.e., ices containing some specified dust component /8/.

The experiments were performed in a glass vacuum chamber with walls cooled by liquid nitrogen. The sample of ice with dust inclusions was prepared as follows: a batch of dust and a measured volume of distilled water were placed in a separate container. After being thoroughly stirred and cooled to +1—+2° the mixture was quickly transferred to a nickel tray cooled by liquid nitrogen. The tray with the ice was then suspended in the vacuum chamber over a special glass plate. Measurements were started when the pressure in the chamber dropped to 10^{-5}—10^{-6} mm Hg. Either heat or light energy was supplied to the ice, and it reached some steady-state temperature T_{st} depending on the power input /8/. At that temperature sublimation took place with either the emission of particles and their conglomerates or the formation of a dust matrix. The dust particles and conglomerates produced a track on the glass plate, from which we could determine the velocities of the escaping particles and their angular distribution, and find the difference in size between the original particles and the particles forming the track on the substrate. The angular distribution of the particles and their emission velocities were determined by photometry of the obtained track. The results showed that the angles of departure of the particles are nearly normal to the ice surface (the deviation from the normal was less than 15°), the angles being little affected by the nature, concentration, and size of the particles. The number

of particles appreciably deviating from normal emission increases with the ice temperature. Figure 5 shows the velocity curves of different particles as functions of the temperature. The indexes M on the curves denote the points corresponding to the conditions of formation of disintegrating dust matrixes. The conditions for the formation of dust matrixes are as follows:

1. The smaller the density and size of the particles and the higher their concentration, the easier it is for the matrix to form;

2. The probability of matrix formation decreases with increasing ice temperature, since at a higher temperature the dust particles receive a larger resultant momentum from the sublimation products;

3. The higher the albedo of the ice with dust inclusions the larger the probability of matrix formation. This has been found in tests using a light beam ($\lambda = 3000 - 7000$ Å) on the surface of dust-containing ice.

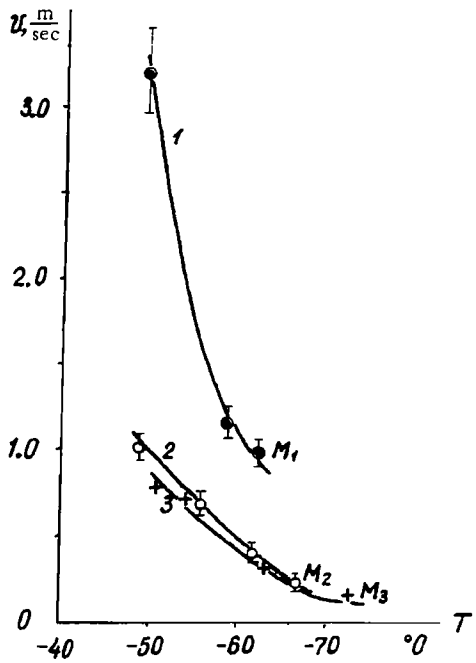

FIGURE 5. Velocity of dust particles as a function of the surface temperature of H_2O ice:

1 – Al_2O_3, particle size 2μ, C = 0.35%; 2 – Al_2O_3, particle size 2μ, C = 1.05%; 3 – SiO_2, particle size 20μ, C = 5%.

FIGURE 6. Section of dust-particle track. The conglomerates formed of original particles are clearly seen.

If the dust-particle track on the substrate is examined under a microscope, the following is observed. At small distances from the ice surface the bulk of original particles comprises conglomerates (Figure 6). With increasing distance the number of particles in conglomerates decreases and more individual particles are visible in the field. The size of the conglomerates

increases the higher the particle concentration, the smaller the particles, and the lower the ice temperature. For example, 2-μ particles of Ni at a volume concentration C = 0.35% form conglomerates averaging 5 — 7 mm in length and 2 — 3 mm in width. Our findings give rise to the following assumptions and conclusions concerning the physical processes occurring in comets.

1. At large heliocentric distances the temperature of the dust-containing cometary nucleus is very low, and this favors the formation of a dust matrix.

2. As it approaches the sun the matrix-sheathed nucleus warms up which may cause disintegration and ejection of the matrix. The process may be explosive, resulting in an abrupt increase of dust content in the cometary head; this is observed as a flare-up in brightness.

3. After ejection of the matrix the discharge of volatile component from the exposed ice surface increases; this cools down the nucleus and again creates conditions for the formation of a matrix. Thus, a matrix may be formed and ejected periodically as the comet approaches the sun. The formation cycles occur at an increasing frequency.

4. The bulk of micron-sized dust is emitted from the cometary nucleus not in the form of individual particles but as conglomerates of varying size, shape, and structure.

5. Individual submicron particles can escape from the ice surface only at small heliocentric distances. The production of submicronic dust far from the sun is apparently due to some other mechanism, for example, that proposed by A. Z. Dolginov /9/.

6. If a conglomerate emitted from the nucleus contains a volatile component, then when the latter sublimates, it may break up the conglomerate and accelerate it by the force of the reaction.

7. Periodic meteor streams are cometary fragments. According to our concepts, these meteors should consist of conglomerates of particles. When the conglomerates enter the upper atmosphere they tend to shine brightly, because of the large size associated with their loose-grained structure, their reduced density being correspondingly low.

Note. At the end of the report a film was viewed, showing:

1. The emission of dust particles and their conglomerates in the sublimation of H_2O ice under vacuum;

2. The effect of the pressure of sublimation products on the ice surface;

3. The explosive disintegration of a matrix of 20-μ particles of SiO_2 under the effect of a luminous flux.

Bibliography

1. Levin, B. Yu. — Astronomicheskii Zhurnal, 20, 27. 1943.
2. Whipple, F. L. — Astrophys. J., 111. 375. 1950.
3. Konstantinov, B. P., M. M. Bredov, A. I. Belyaevskii, and A. I. Sokolov. — Kosmicheskie Issledovaniya, 4, 66. 1966.
4. Potter, A. F. and B. Del Duca. — Icarus, 3, 103. 1964.
5. Danielson, L. R. and G. H. Kacai. — J. Geophys. Res., 73. 1968.

6. Dorsey, N.E. Properties of Ordinary Water-Substance. 1940.
7. Swing, P. and A.A. Delsemme.— Ann. Astrophys., 15, 1. 1952.
8. Kaimakov, E.A. and V.I. Sharkov.— Komety i Meteory, 15(16), 21. 1967.
9. Dolginov, A.Z.— Astronomicheskii Zhurnal, 44, 434. 1967.

K.I. Churyumov

ABSOLUTE PHOTOMETRY OF COMETARY NUCLEI BY FOCAL STAR IMAGES

A method is proposed for the absolute photometry of cometary nuclei by the focal images of stars lying in the normal blackening range of short-focus cameras of the type "Astropetzval" (f = 60 cm) and "Telemar" (f = 100 cm). The method is based on using the star streaks obtained on the film during tracking of the comet as calibration steps for plotting the characteristic curve. The effective (mean) densities of the star images are measured on a microphotometer or a densitometer. The photographic density is averaged over the area of the star image, consisting of the circle of confusion (the Airy and aberration circles) and the turbulence circle, by means of an individual slit for each star. The reading D_0 obtained on the logarithmic microphotometer scale by scanning a star is compared with the reading D obtained with the same slit from a sample of constant density (this is normally a clear film of the same thickness as the one being measured). The reading D_0 is also compared against the background reading D_b, which is used to check the zero setting of the density scale.

The characteristic curve plotted from the known stellar magnitudes m and the measured blackening densities D can be used to determine the stellar magnitude of the cometary nucleus. During comet tracking the magnitude of each star is attenuated by a factor $n = \frac{l}{d}$ (l is the length of the star streak and d is its width), and thus each star magnitude has to be corrected by an amount

$$\Delta m = 2.5\, p \log n,$$

where p is Schwarzschild's coefficient.

In order to determine the absolute magnitude of the cometary nuclei from the magnitudes obtained by the plotted characteristic curves, it is necessary to introduce the correction Δm_{abs} derived from several extra-focal sightings for the whole series of films.

The confidence intervals, plotted for the characteristic curves of different films from a sampling of 20 — 25 stars, lie within 0.1 and 0.2 stellar magnitude.

The given method does not require preliminary laboratory calibration and standardization, and makes it possible to examine the brightness variations in the photometric nuclei of comets while studying their structural characteristics on focal photographs. The photometric measurement accuracy is 0.1 — 0.2 stellar magnitude.

K.I. Churyumov and T. Maizlina

INVESTIGATION OF COMET HONDA 1968c FROM TWO POINTS OF VIEW

Comets may be visualized as indicators of conditions in interplanetary space and can be used as inexpensive probes in order to study the parameters of the interplanetary plasma, especially at high heliographic latitudes and large heliocentric distances as yet inaccessible to space vehicles. The reaction of the comet to situational changes in the interplanetary medium may show up as strong fluctuations in the nuclear brightness, a change in the orientation of the plasma tails relative to the radius vector, radiation activity of the cometary plasma, halo formation, etc.

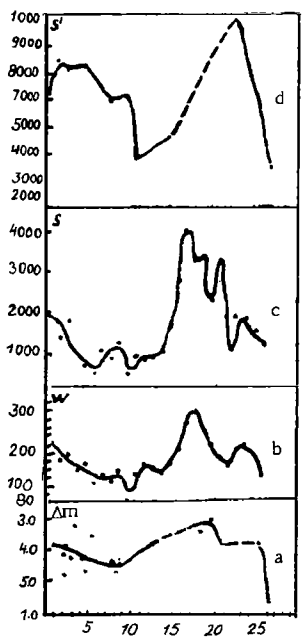

Correlation between the brightness fluctuations of the comet's photometric nucleus and solar activity.

Comet Honda 1968c was observed in Kiev by S.K. Vsekhsvyatskii and K.I. Churyumov on "Astropetzval" (f=60 cm) and "Telemar" (f = 100 cm) cameras and a long-focus astrograph (f = 430 cm), from 31 July to 3 September 1968. The smoothed light curves of the photometric cometary nucleus in the photographic and visual regions over the observational period were compared with the smoothed curves of the relative sunspot number, the total sunspot area, and the total flocculus area, plotted with allowance for the difference in the heliographic longitudes of the earth and the comet. Comparison of the curves of a) the nuclear brightness of Comet Honda, b) the Wolf number, c) the sunspot area, and d) the flocculus area (see figure) shows a distinct correlation between the brightness fluctuations of the photometric cometary nucleus and solar activity. Thus, an increase in the solar activity indexes between 10 and 20 August led to a concurrent rise in the brightness of the cometary nucleus, accompanied by noticeable structural changes in the comet.

A. A. Demenko and K. I. Churyumov

A STUDY OF THE BRIGHTNESS OF COMET IKEYA-SEKI 1967n DURING THREE SOLAR REVOLUTIONS

The investigation of irregular fluctuations in the brightness of comets is important for determining conditions in interplanetary space. Comets have tenuous, often ionized, extended atmospheres, and they constitute natural probes which sensitively react to changes in the parameters of the interplanetary plasma. The rapid fluctuations that strongly distort the regular light curve result from the interaction of the corpuscular streams of the solar corona with the cometary atmosphere, or from variable influences on the cometary ices.

A set of 210 films, taken in Kiev by S. K. Vsekhsvyatskii and K. I. Churyumov in the photographic and visual ranges, was used to plot the light curves of the photometric nucleus of Comet 1967n (in reduced stellar magnitudes allowing for the variation of the comet's heliocentric distance) for the period from 10 March to 3 June 1968, covering three solar revolutions. The smoother light curve of the cometary nucleus was compared with the smoother curves of sunspot and solar flare activity. The nuclear light curve showed two sharp minima—one on 28 March and the other on 24 April. The time interval between the minima is 27 days, roughly equal to the sun's period of rotation. The brightness of the nucleus decreases again one solar revolution later, on about 20 May. The heliographic coordinates of the comet changed insignificantly during that time (on 28 March, $b = 47°$ and $l = 281°$; on 24 April, $b = 41°$ and $l = 272°$). The drop in the nuclear brightness of Comet 1967n at these times may be attributed to the comet entering the same interplume region poor in coronal plasma (in accordance with the conception of a rigid system of streams rotating with the sun). The smoothed solar-activity curves, reduced to the comet, also show an amplitude decrease at the given times. After 28 March the activity of the cometary nucleus lags somewhat behind the fairly strong rise in the sunspot and solar flare activity, which reaches a peak between the noted minima in the nuclear brightness of the comet. This is apparently due to the formation of a matrix crust on the surface of the nucleus at the minimum of 28 March, with an associated reduction in the rate of gas emission. The formation of a matrix crust on the nuclear ice after weak flares, which occurs during the decrease of the solar activity indexes, may have been responsible for the resonance pattern of variation in the nuclear brightness of Comet Ikeya-Seki on 28 March and 24 April.

In the course of several nights the nuclear brightness of the comet underwent considerable fluctuations accompanied by changes in the structure of

the near-nuclear region, in the head and the tail. Some films show a spherical shell (halo) in the head of the comet. The rate of expansion of the shell, determined from two consecutive photographs, was: on 30 March, 1.7 km/sec; on 31 March, 2.8 km/sec; on 1 April, 4.4 km/sec.

The strong fluctuations in the brightness of the photometric nucleus and the rapid structural changes of Comet Ikeya-Seki 1967n characterize its high activity during the whole period of observation.

Z. M. Ioffe

DYNAMIC PROCESSES IN COMETS AND THEIR ANALOGY WITH THE DYNAMICS OF THE EARTH'S MAGNETOSPHERE

The interaction of the solar wind with the ionic component of the cometary atmosphere produces a flow around the comet, which is in many respects similar to the flow pattern of the solar wind around the earth's magnetosphere /1/. Some of the basic similarities are:

a. Upstream from the cometary head a collisionless shock wave should occur, similar to the wave in front of the magnetosphere /2/;

b. The "magnetic tail" of the earth closely resembles cometary tails of type I. The tails follow the geocentric (cometocentric) direction of the solar wind. Deviations from this direction are due to the effect of an oblique magnetic field.

c. According to Ness and Donn /3/, the cometary rays are neutral magnetic field lines, similar to the neutral line in the earth's magnetic field. In comets these lines must be associated with the magnetic field structure behind the collisionless shock wave;

d. Both the earth's magnetic tail and type I cometary tails exhibit a plasma stream of density $2 \cdot 10^2 \, cm^{-1}$.

e. In ionized cometary tails Alfvén waves may be produced by instability of the tangential discontinuity at the boundary between the cometary plasma and the solar wind. Their mechanism of generation is similar to that of geomagnetic micropulsations /4/.

Besides the given common features in the solar-wind flow around the earth and comets, there are also significant differences caused by the earth's proper magnetic field /5/.

Bibliography

1. Biermann, L. On the Interplanetary Plasma.— Sem. d'Etuck Puob. dy ray cosmig. p.477. 1963.
2. Axford, W.— 9. Planet. Space Sci., 12, 7. 1964.
3. Ness, N.F. and B.D. Donn.— Astronom. J., 70, 5. 1965.
4. Ioffe, Z.M.— Astronomicheskii Zhurnal. 1969 (in print).
5. Ioffe, Z.M.— Astronomicheskii Zhurnal, 44, 835. 1967.

S. V. Viktorov

MORPHOLOGY OF THE MOON AND THE ANALYSIS OF THE CHEMICAL COMPOSITION OF THE LUNAR SURFACE

There are a number of problems concerning the structure of the moon and the origin of its surface features, for whose solution the chemical analysis of the lunar surface can yield valuable information. Some of these problems are difficult to solve either by assaying small individual surface areas (such as the tests performed by the Surveyor-5, 6 and 7 spacecraft in the Mare Tranquillitatis, Sinus Medium, and Tycho crater), or by analyzing in the laboratory the limited number of samples collected from a small area and brought back to earth.

It has been recently found that the ring formations on the moon show wide variations in diameter, probably due to their different origin /1/. Presumably these formations should also show differences in their element content. This assumption can be effectively tested by analyzing the chemical composition of the surface (subsurface) layer of the lunar soil over regions which may be relatively small but which include ring structures of varying sizes. Such investigations must be made in several regions, specifically in order to study the diameter-to-depth ratio of the ring structures which somewhat varies in different areas of the moon /2/. The investigations might also help elucidate some infrared anomalies which do not fit the visible formations on the moon. The examination of the degree of uniformity of the chemical composition within separate regions of the lunar surface can also be considered as one aspect of the physical mapping of the moon.

Bibliography

1. Florenskii, P. V., E. I. Zabelin, S. V. Mochalov, and Yu. G. Pimenov. Tezisy dokladov, predstarlenykh na Simpozium po fizike Luny i planet, 15—22 oktyabrya 1968 g. (Report papers read at the Symposium on the Physics of the Moon and Planets, 15—22 October 1968).—Kiev, "Naukova Dumka." 1968.
2. Bouška, J.—Ibid.

A. V. Zolotov

GEOPHYSICAL EFFECTS OF THE TUNGUSKA BLAST OF 1908

The flight and explosion of the Tunguska meteorite gave rise to a series of geophysical phenomena: air and seismic waves, geomagnetic disturbance, anomalous upper-atmosphere glow, etc. The blast also caused heavy damages in the taiga, felling the forest radially as far as 25 — 30 km from the epicenter and flash-burning trees within a range of 18 — 20 km. In the Tunguska blast the geophysical effects produced by the fall of a space object were detected and instrumentally recorded for the first time in the history of science. This factual material (microbarograms, seismograms, magnetograms, map of felled forest, etc.) serves as basis for the study of the Tunguska problem.

The size of the devastation area defines the total energy of the blast — about 4.10^{23} ergs, equivalent to about 10 megatons TNT. The size of the flash-burn area defines the radiant energy of the blast — about $(1-2)\cdot 10^{23}$ ergs, i.e., some tenths of the total energy. The presence of standing trees inside the radially felled forest (in the epicenter region) indicates that the meteorite exploded in mid-air. The size of the intact forest area gives the height of the explosion — 5 — 7 km. A basic question in the Tunguska problem is what energy (kinetic or internal energy of explosive conversion) was responsible for the meteorite blast. Two views are held on the subject.

1. The hypothesis proposed by the Committee on Meteorites of the USSR Academy of Sciences is based on the assumption that the explosion and the resultant destruction were due to the kinetic energy of the meteorite.

2. Our hypothesis is based on the assumption that the explosion was due to the internal energy, either chemical or nuclear, of the falling body.

Since the kinetic-energy explosion does not account for all the potentialities and causes of the blast, and the internal-energy explosion has a finite probability, the two hypotheses are equally valid. The Tunguska problem must therefore be studied in the light of both, which appreciably extends the methodological possibilities. The investigation of the geophysical effects produced by the blast can help elucidate the basic question involved.

From a statistical analysis of the map of the radially felled forest, and the analysis of the interaction of the blast and ballistic waves, it may be deduced that the explosion of the Tunguska meteorite was not due to its kinetic energy, as was earlier supposed, but rather to internal explosive conversion energy, either chemical or nuclear.

A study of the air waves detected in 1908 by many stations throughout the world showed that the Tunguska blast corresponded to a point explosion, with a high energy concentration in a small volume which cannot be achieved by conventional chemical explosives.

From an analysis of magnetograms of the Tunguska blast and of recent large-scale test explosions it can be deduced that the geomagnetic disturbance associated with the blast most likely resulted not from a shock wave, as supposed earlier, but from a stream of magnetically trapped charged particles.

Radioactivity measurements taken on samples of Tunguska trees showed that the wood rings immediately following 1908 display a distinctly anomalous radioactivity, though its source has not yet been properly traced.

It may thus be concluded that the geophysical effects of the Tunguska blast are similar to those of nuclear explosions. Their features coincide in all respects. This similarity does not, however, constitute proof (or sufficient evidence) that the Tunguska blast was of nuclear nature, so that the subject requires further study.

Section V

GENERATION, ENERGY SPECTRUM, VARIATIONS AND PROPAGATION OF COSMIC RAYS

Edited by S. N. Vernov, V. A. Dergachev and G. E. Kocharov

L. I. Miroshnichenko

CURRENT CONCEPTS ON THE ACCELERATION AND PROPAGATION OF SOLAR COSMIC RAYS

Some definite advances have been made in the study of solar cosmic rays /1/: determination of the overall charge composition, energy spectrum, and mode of propagation of solar particles in interplanetary space; correlation of the emission of fast particles with the radio and X-ray emission of the sun; and investigation of the specific influence of solar cosmic rays on some geophysical phenomena (particularly on the absorption of short radio waves in the polar regions). In the last 10 — 15 years intensive studies have also been carried out into the possible mechanisms of acceleration of particles in the sun's atmosphere. However, many details of these processes are still unclear. This is due to the dynamic nature of the object of study, the insufficient measurement accuracy, methodological difficulties, and the strong space and time variability of electromagnetic conditions on the sun, in the interplanetary medium, and in the close neighborhood of the Earth.

The present situation in solar cosmic-ray research may be represented in the form of a diagram. Arrows show the "feedback" connections existing between the different domains of investigation. The interrelation between the various investigations becomes particularly apparent if the main emphasis is laid upon the measurement and interpretation of solar-particle spectra. We will briefly examine in this context some aspects in the research of solar cosmic-ray spectra.

Any physical results obtained from solar cosmic-ray studies are based on the reliability of the method of investigation and on the measurement accuracy. These aspects have been given increasing attention in recent years. Direct measurements of solar protons have been extended into the low-energy range down to $\varepsilon_k \sim 1$ MeV and even to $\varepsilon_k \sim 0.5$ MeV. The study of particles with such energies furnishes information on the fine ("filamentary") structure of the interplanetary magnetic field near the Earth's orbit /2/ and on the possible variation of this structure with increasing distance up to about the orbit of Mars /3/. The fact that 1-MeV protons can be detected in interplanetary space during several solar revolutions poses the problem of finding satisfactory mechanisms for the continuous generation or prolonged emission from the sun's atmosphere. In the case of protons of $\varepsilon_k \sim 1$ MeV the duration and time dependence of the emission also significantly determines their space-time distribution in the solar system.

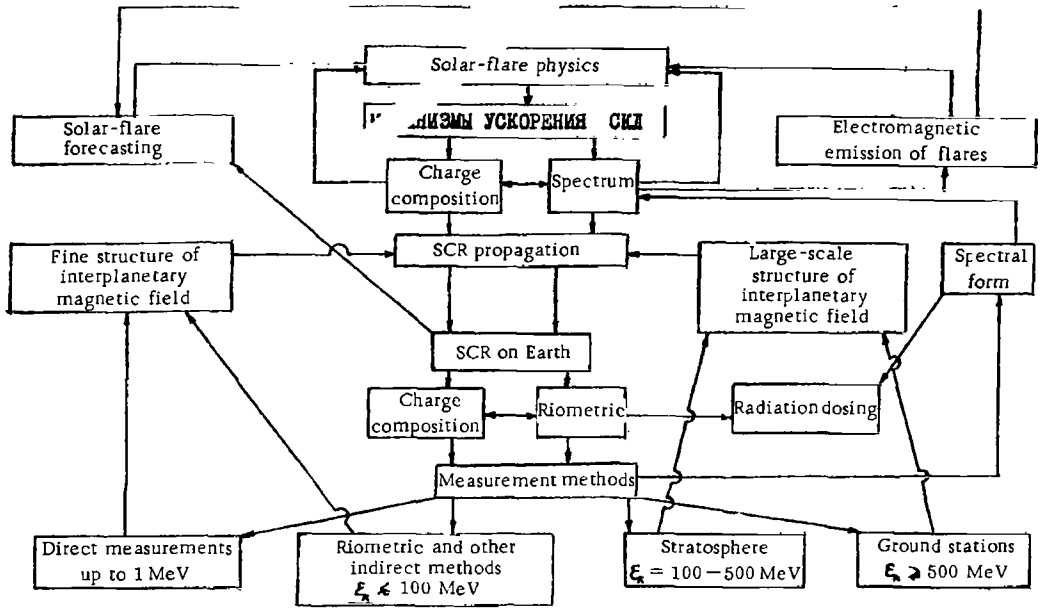

Schematic representation of solar cosmic-ray research.

Direct measurements in interplanetary space yield unique information on one of the most important characteristics of solar cosmic rays, namely, their absolute flux above a given energy level or within a given energy interval. However, direct measurements have so far been only sporadically performed and not always at the time of solar flares, so that indirect methods of measurement of the spectrum and absolute flux of solar cosmic rays still remain the basic ones used.

During some solar cosmic-ray flares, measurements were taken simultaneously on satellites in a polar orbit and at ground riometric stations. By comparing the results of the two types of observations it is possible to correlate the absolute flux of solar particles at the boundary of the terrestrial atmosphere with the absorption amplitude of cosmic radio noise. For example, for particles of $\mathcal{E}_k = 1.3-7$ MeV during the flare of November 21, 1963, the relationship $J = 2 \cdot 10^7 A^2$ was obtained, where J is the proton intensity ($cm^{-2}\,sec^{-1}\,sterad^{-1}$) and A is the absorption amplitude (decibels) of the cosmic radio emission of 30 Mc /4/. From stratospheric measurements on balloons it is also possible to extrapolate the absolute flux of solar particles at the boundary of the terrestrial atmosphere, mainly in the energy range of 100 – 500 MeV /5/.

For the correct interpretation of the solar cosmic-ray spectrum as a whole, it is important to know the absolute fluxes of solar particles in the energy region $\mathcal{E}_K \geq 500$ MeV (rigidity $R \geq 1$ GV). It is precisely in this energy region that the accuracy in the measurement of the spectrum gradient is low because of its steepness and the low particle intensity, as well as the great methodological difficulties involved in the measurement of the absolute flux. In order to determine the absolute flux of solar particles of rigidity R at the boundary of the atmosphere, for example, from the data of neutron supermonitors, it is necessary to know the integral neutron-production multiplicity m, and in order to find the spectrum gradient it is

also required to know the behavior of m with varying rigidity. The values of m are usually calculated by means of the latitude-effect curve of galactic cosmic rays. What is actually calculated by the analysis of continuous ground monitoring data is not the m_i of the i-th component but rather the production multiplicity for the instrument monitoring the i-th component. In order to determine the absolute flux of solar particles at the boundary of the atmosphere, it makes no practical difference what the absolute neutron intensity and production multiplicity really are at the observation level, and it is sufficient to know the relationship between the intensity variations at the observation level and the corresponding variations in the absolute flux of particles at the boundary of the Earth's atmosphere.

An attempt to determine the absolute (non-normalized) values of m for the neutron component was first made by L. I. Dorman and L. I. Miroshnichenko /6/. They found that $m \sim R^{2,5}$ within the range 1 — 10 GV. The dependence of m on R has also been studied in /7/. It was shown that $m_v \sim R^{2.27 \pm 0.03}$ and $m_g \sim R^{2.69 \pm 0.03}$ for the vertical and global multiplicities, respectively, in the range of 1.5 — 3.5 GV. The values of m calculated in /5/ are indeterminate to within a factor of $\gtrsim 2$, so that the problem still remains of improving the accuracy in the determination of the absolute flux of solar particles at $R > 1$ GV.

The investigation of the propagation of solar cosmic rays in interplanetary space involves several problems. One of these is to ascertain the distorting effect of propagation on the spectrum of solar particles. It is important to be able to reconstruct from terrestrial observation data the true spectrum of particles at the time of emission at the source. However, the theoretical and experimental possibilities of such a procedure are as yet limited. Information on the emission spectra may be obtained at present only from a diffusion model and only for particles subject to diffusion /1/. The propagation mechanism of other particles (particularly for particles of energy $\varepsilon_k < 100$ MeV) is by no means understood, and their emission spectra are not known. Moreover, it should be taken into account that their energy may appreciably change during propagation (e.g., due to anti-Fermi deceleration in a divergent flux of magnetic inhomogeneities).

A point of methodological and physical interest concerns the form of the solar cosmic-ray spectrum. In the current literature the following three spectral forms are basically used:

$$\mathcal{D}(\varepsilon_k) \sim \varepsilon_k^{-\gamma}\ ;\ \mathcal{D}(R) \sim R^{-\gamma} \text{ and } \mathcal{D}(R) \sim \exp(-R/R_0)\ .$$

At the currently attainable measurement accuracy it is impossible to choose a single form out of the three, even if one relatively narrow energy (hardness) range is considered. If one compares the spectra obtained for different intervals of ε_k or R, the situation is complicated even further. The point is that the three given forms of spectra may correspond to three types of acceleration mechanisms: 1) the spectrum $\sim \varepsilon_k^{-\gamma}$ corresponds to a statistical acceleration process (Fermi mechanism); 2) betatron acceleration leads to the spectrum $\sim R^{-\gamma}$; 3) acceleration of particles by an electrostatic field yields the spectrum $\exp(-R/R_0)$.

The exponential form was proposed in /8/ in view of the great similarity among the hardness spectra of solar protons, α-particles, and heavier nuclei, recorded on Earth. There are a number of experimental data and theoretical arguments in support of the exponential spectrum. Specifically,

according to /9/, the continuous electromagnetic spectrum of the sun (from radio waves to visible light) during flares may be attributed to the synchrotron radiation of electrons having a spectrum of the type $\exp(-R/R_*)$ with a value of R_* close to that obtained for protons. The electric fields required for the formation of the exponential spectrum may possibly arise during the dynamic dissipation of the sunspot magnetic fields /10/.

A hypothesis has been advanced in /8/, according to which the hardness spectra may be associated with the distribution of particles in the plasma ejected by solar flares, i.e., the complete spectrum of solar protons may include plasma in its low-energy portion. As shown in /11/, however, the mechanism of propagation, which depends on R, imposes some restrictions on this hypothesis. Clearly, in order to deduce conclusively the nature of the processes shaping the spectrum of solar particles, information is required on whether the spectrum is exponential before undergoing modulation in interplanetary space. The results in /12/ obtained from the diffusion theory show that the spectrum of solar protons at the source most likely have the form $\sim R^{-\gamma}$, where γ tends to increase at large values of R. In the low-energy region ($\varepsilon_к = 10-500$ MeV), on the other hand, the source spectrum can be well described by the power function $\sim \varepsilon_к^{-\gamma}$ /1, 12 — 14/, though according to /14/ the representations $\sim R^{-\gamma}$ or $\sim \exp(-R/R_*)$ also fit to within the relevant error limits. The results of /2 — 14/ may be indicative of a difference in the acceleration mechanisms of high-and low-energy particles.

The interpretation of the spectra of low-energy solar protons ($\varepsilon_к < 100$ MeV) measured near the Earth's orbit is complicated by the possibility of their being accelerated in interplanetary space /15 — 20/. Of particular interest are the rises in the low-energy proton fluxes (as on September 30, 1961 /13/) which usually coincide with the onset of a geomagnetic storm (i.e., when a disturbed plasma jet from a solar flare reaches the Earth). The theoretical investigation of the acceleration mechanisms due to plasma oscillations in interplanetary space offers promising possibilities not only for interpreting the spectrum of protons of energy $\varepsilon_к < 100$ MeV (and particularly of $\varepsilon_к = 1-10$ MeV) but also for ascertaining the fine dynamic structure of the interplanetary medium.

Let us note in conclusion that, despite the current theoretical difficulties and experimental shortcomings, there are already means at hand not only for the qualitative description of the acceleration mechanisms of solar particles but also for the quantitative analysis of the physical processes occurring on the sun, in interplanetary space, and in the immediate vicinity of the Earth. The propagation of solar particles must certainly play an important part in the modification of their spectrum. This effect will be clarified only when a satisfactory model of the interplanetary medium has been constructed.

Bibliography

1. Dorman, L.I. and L.I. Miroshnichenko. Solnechnye kosmicheskie luchi (Solar Cosmic Rays).— Moskva, Izdatel'stvo Nauka. 1968.
2. Bartley, W.C., R.P. Bukata, K.G. McCracken, and U.R. Rao.— J. Geophys. Res., 71, 3297. 1966.

3. Vernov, S.N., A.E. Chudakov, P.V. Vakulov, Yu.I. Logachev, G.P. Lyubimov, A.G. Nikolaev, and N.V. Pereslegina.— Doklady AN SSSR, 171, 847. 1966.
4. Chivers, H.A. and J.R. Burrows.— Planet. Space Sci., 14, 131. 1966.
5. Charakhch'yan, A.N.— UFN, 33, 35. 1964.
6. Dorman, L.I. and L.I. Miroshnichenko.— Geomagnetizm i aeronomiya, 6, 215. 1966.
7. Keith, J.E., R.W. Peterson, R.L. Tjoman, and J.R. Wang.— J. Geophys. Res., 73, 353. 1968.
8. Freier, P.S. and W.R. Webber.— J. Geophys. Res., 68, 1605. 1963.
9. Stein, W.A. and E.P. Ney.— J. Geophys. Res., 68, 65. 1963.
10. Syrovatskii, S.I.— Astronomicheskii Zhurnal, 43, 340. 1966.
11. Roederer, J.R.— Space Sci. Rev., 3, 451. 1964.
12. Miroshnichenko, L.I.— Bull. Astron. Inst., 18, 29. Czechoslovakia, 1969.
13. Bryant, D.A., T.L. Cline, U.D. Desai, and F.B. McDonald.— Astrophys. J., 141, 478. 1965.
14. Krimigis, S.M.— J. Geophys. Res., 70, 2943. 1965.
15. Tverskoi, B.A.— ZhETF, 53, 1417. 1967.
16. Yukhimuk, A.K. and M.E. Kats.— Geomagnetizm i aeronomiya, 8, 1100. 1968.
17. Kats, M.E. and A.K. Yukhimuk.— Present collection, Part 1.
18. Tsytovich, V.N.— UFN, 89, 89. 1966.
19. Galeev, A.A.— Doklady AN SSSR, 161, 802. 1965.
20. Rao, U.R., K.G. McCracken, and R.P. Bukata.— Canad. J. Phys., 46, 844. 1968.

A. N. Charakhch'yan and T. N. Charakhch'yan

THE ENERGY SPECTRUM OF COSMIC RAYS IN INTERSTELLAR SPACE

Measurements on which particular emphasis has been placed in the last 10 years consistently exhibit the presence of a peak in the differential energy spectrum of galactic cosmic rays on Earth. Due to the 11-year solar cycle the number of particles at the peak varies by a considerable factor and its position shifts up or down the energy scale, but the peak persists in the spectrum throughout the solar cycle. It is thus pertinent to inquire whether this is the result of the form of the energy spectrum of primary particles coming from interstellar space or whether the peak is produced in interplanetary space by the sun's action on the cosmic rays.

A number of authors assume that the differential energy spectrum of cosmic rays reaching the solar system is a continuously decreasing function of their energy or momentum P, such as $A/P^{2.5}$. Because of the sun's influence, a large number of the cosmic-ray particles cannot penetrate into interplanetary space and approach the Earth, where the observations are made. Since the inhibiting effect of the sun becomes more appreciable as the particle energy decreases, this may, in principle, lead to a cutoff in the spectrum, i.e., produce a peak in it.

According to our data, the solar influence on the cosmic-ray intensity is fairly small during periods of minimum activity, and thus the peaked form of the energy spectrum usually observed during these periods of measurement is also typical of the primary spectrum of particles coming from interstellar space. This result is based on a detailed analysis of the 11-year solar modulation of cosmic rays and borne out by the stratospheric measurement data of 1957—1964.

It is theoretically evident, that, among the various manifestations of the 11-year solar cycle, a dominant part in the modulation of cosmic rays should be played by those effects which are directly or indirectly associated with the solar magnetic fields. Logically enough, therefore, the 11-year modulation of cosmic-ray intensity shows the best correlation primarily with the sunspots, which are known to be the carriers of the strongest magnetic fields on the sun. There are possibly also other solar-activity manifestations which affect the cosmic-ray intensity, such as geoactive M-regions carrying weak magnetic fields, but on the whole the effect of sunspots predominates. Considering that the number of spots during minimum solar activity is several orders smaller than during maximum activity, it may be assumed that the combined field of the sunspots is reduced in roughly the same proportion during periods of minimum activity. If, in the limit, the sunspots completely disappear, the main source of solar

TABLE 1. Intensity of primary cosmic particles, $m^{-2} sec^{-1} sterad^{-1}$

Observation period	Magnetic-rigidity ranges P, GV							Wolf number, W	Number of sunspot groups η
	0.5–2.3	0.5–5.5	0.5–6.6	≥0.5	≥2.3	≥5.5	≥6.6		
July 1957–Apr 1958	230 ± 70							243 ± 13	362 ± 16
May–Dec 1958	420 ± 60	1270 ± 60	–	1690 ± 60	1270 ± 80	420	–	244 ± 11	377 ± 86
Jan–Dec 1959	420 ± 60	1400 ± 60	–	1810 ± 60	1390 ± 80	410	–	217 ± 14	330 ± 13
Jan–Dec 1960	420 ± 40	1550 ± 30	–	1960 ± 30	1540 ± 60	410	–	156 ± 8	254 ± 11
Jan–June 1961	590 ± 70	1850 ± 40	–	2270 ± 40	1680 ± 80	420	–	87 ± 7	145 ± 9
July–Nov 1961	720 ± 120	2050 ± 60	–	2480 ± 60	1760 ± 120	430	–	63 ± 9	114 ± 12
Jan–June 1962	1080 ± 60	–	2570 ± 40	2880 ± 40	1800 ± 70	–	310	53 ± 3	87 ± 4
July–Dec 1962	1020 ± 120	–	2550 ± 50	2870 ± 50	1870 ± 130	–	320	46 ± 7	70 ± 9
Jan–June 1963	1170 ± 70	–	2760 ± 60	3080 ± 60	1950 ± 80	–	320	36 ± 5	64 ± 6
July–Dec 1963	1280 ± 50	–	2700 ± 60	3020 ± 60	1740 ± 80	–	320	32 ± 5	58 ± 6
Jan–June 1964	1350 ± 30	–	2970 ± 50	3300 ± 50	1950 ± 60	–	330	16 ± 2	31 ± 4
July–Dec 1964	1520 ± 30	–	3200 ± 40	3530 ± 40	1990 ± 50	–	330	9 ± 2	20 ± 5
Jan–June 1965	1620 ± 30	–	3450 ± 50	3780 ± 50	2160 ± 60	–	330	20 ± 4	38 ± 5
Apr–May 1965	1740 ± 40		3580 ± 50	3910 ± 50	2170 ± 60	–	330	22	34

modulation obviously disappears as well. Let us examine to what extent the available experimental data make it possible to determine the unmodulated cosmic-ray intensity, i.e., that which corresponds to zero solar activity.

During 1957—1964 more than 11,000 stratospheric radiosonde measurements were taken of cosmic rays at the latitudes of Murmansk, Antarctica, Moscow, Alma-Ata, and Simferopol. The processing of this extensive experimental data yielded practically continuous data on the cosmic-ray intensity in the Earth's atmosphere and beyond it (primary component). The method by which the high-altitude measurements were converted into the values of the primary-component intensity in outer space is given in /1/.

Table 1 lists the mean values of the absolute number of particles in the primary cosmic-ray component for some rigidity ranges (according to the geomagnetic critical rigidity data of /2/), the sunspot number W, and the number of sunspot groups η (totalled per month) versus time. The values we obtained for the total primary-ray intensity are in good agreement with the data of Soviet and American measurements on artificial satellites and space rockets. It must be noted, however, that our data are practically continuous and cover concurrently a few primary-particle energy ranges.

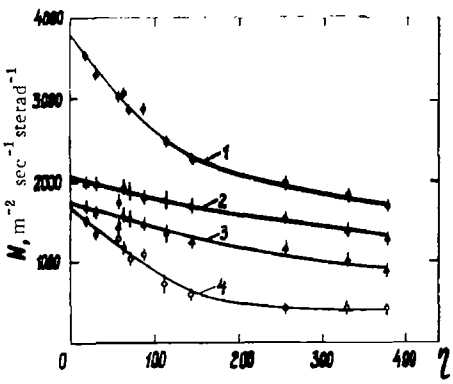

FIGURE 1. Intensity of the primary cosmic-ray component N as a function of the number of sunspot groups η:

1 — P ≥ 0.5 GV; 2 — P > 2.3 GV; 3 — P = = 2.3—6.6 GV; 4 — P = 0.5—2.3 GV.

Figure 1 shows the primary-component intensity values N. There is a practically continuous empirical relation between N and η with an almost twenty-fold variation of N, from 20 to 370, and a fourfold variation of η (for $0.5 \leq P \leq 2.3$ GV).

It should be pointed out that the cosmic-ray intensity variation corresponding to variations of η between 20 and 150 (1960—1964) occurred when there were no changes in the other solar-activity characteristics affecting the amplitude of the 11-year modulation. The propagation velocity of the magnetic inhomogeneities varied during 1960—1964 by a factor of not more than 1.5—2 /3/; the energy spectrum of the 11-year variations remained constant during the whole observation period of 1959—1964 /4/; and, lastly, the heliographic latitude of the sunspots, which, as shown in /5/, has a substantial effect on the amplitude of the 11-year modulation, did not change during that time either and remained at $\varphi \simeq 10°$. The variation of N was therefore in this case mainly due to the variation of η. We note that the sections of the curves with the experimental points for $\eta < 100$ are nearly straight. The intercept of these straight lines with the ordinate axis ($\eta = 0$) has a well-defined physical meaning. The values N ($\eta = 0$) denote the intensity of the primary cosmic-ray component at zero solar activity. Since the slope of the lines is fairly small, the values of N ($\eta = 0$)

are close to N (η = 20). The results obtained for N (η = 0) remain virtually unchanged if allowance is made for the time lag between the variations of N and η which is approximately two months /3/. The extrapolated values of N (η = 0) are given in Table 2. The table also gives the maximum intensity values measured in April—May 1965, which are virtually the same as N (η = 0).

TABLE 2. Extrapolated cosmic-ray intensity values for 4 magnetic-rigidity ranges

Rigidity plane P, GV	Number of particles, $m^{-2} sec^{-1} sterad^{-1}$		
	η = 20	extrapolation η = 0	maximum intensity measured in April—May 1965
≥0.5	3530 ± 40	3850	3910 ± 50
≥2.3	1990 ± 50	2100	2170 ± 60
2.3—6.6	1680 ± 50	1800	1840 ± 60
0.5—2.3	1520 ± 30	1700	1740 ± 40

Using our experimental data and those of other authors, it is possible to construct the galactic cosmic-ray energy spectrum, which must be similar to the modulation-free spectrum.

The results obtained for the primary-component intensity refer to the total number of primary particles, i.e., protons, α-particles and particles with a charge exceeding 3. The contribution of the latter to the total number of particles is insignificant. The α-particles make a significant contribution, however. We assume that the proportion of protons is 85% and that of α-particles 15%. These values fit current experimental findings on the charge distribution in the primary component at various geomagnetic latitudes. Accordingly, our data yield for the number of primary protons $N_p(>E)$ $m^{-2} sec^{-1} sterad^{-1}$: $N_p = 3260 \pm 50$, when the proton kinetic energy E is 0.1 GeV; $N_p = 2530 \pm 70$, when E = 0.7 GeV; $N_p = 1790 \pm 70$, when E = 1.5 GeV; $N_p = 210 \pm 20$, when E = 7.1 GeV; $N_p = 67.5$, when E = 15.7 GeV. The values of N_p for E = 7.1 and 15.7 GeV were already found previously /6/. These results were confirmed more than once by recent measurements in Soviet research expeditions sailing from Leningrad to Antarctica and back. Systematic measurements carried out in Alma-Ata, where the critical geomagnetic cutoff energy $E_c = 5.7$ GeV, indicate that the primary protons do not vary appreciably with time. The variation in any case is less than 10%.

The data in question are plotted in Figure 2. The results of MacDonald and Webber /7, 8/ for high latitudes are probably more accurate, because albedo particles are more reliably corrected for. The discrepancy with our data is 10—15%. The discrepancy at equatorial latitudes seems to be due to the significant contribution of showers in MacDonald's measurements which lead to excessive values for the number of primary particles /9/. As a result, the solid curve in Figure 2 may be considered close to the real

integral energy spectrum of primary protons. This curve can be approximated by the empirical equation

$$N_p(E) = 2 \cdot 10^4 \left[\frac{2}{(2+E)^2} - \frac{15}{(2+E)^5} \right] (m^{-2} sec^{-1} sterad^{-1}),$$

where E is the proton kinetic energy, GeV, $0.1 < E \leq 30$ GeV.

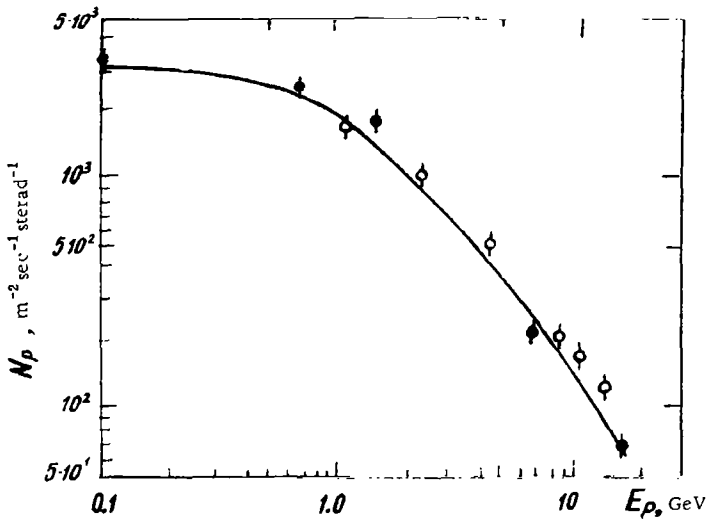

FIGURE 2. Integral energy spectrum of galactic cosmic-ray protons:
● — Authors' data; o — after MacDonald and Webber /7, 8/.

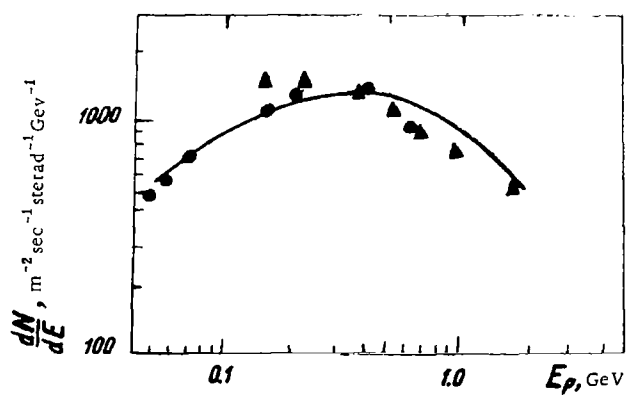

FIGURE 3. Differential energy spectrum of galactic cosmic-ray protons:

▲ — after Webber /8/; ● — after MacDonald et al. /10/. The curve represents the proton differential energy spectrum dN/dE, plotted from the empirical equation given in the above paper.

Figure 3 shows the differential energy spectrum of protons plotted from N(E):

$$\frac{dN_p}{dE} = 2 \cdot 10^4 \left[\frac{2}{(2+E)^3} - \frac{15}{(2+E)^6}\right], (m^{-2}\,sec^{-1}\,sterad^{-1}).$$

The spectrum has a peak at an energy of 0.45 GeV. Also given in the figure are the experimental data of MacDonald and Webber /8, 10/ obtained in 1965.

A detailed analysis of the 11-year modulation of cosmic-ray intensity and its correlation with the 11-year solar cycle thus shows that the energy spectrum of galactic cosmic rays on Earth during a minimum in the 11-year solar cycle is practically the same as the extrapolated spectrum at zero solar activity. The cutoff of the galactic cosmic-ray spectrum on the low-energy side is difficult to attribute to solar modulation. It is associated with the spectrum of the particles coming from interstellar space.

Bibliography

1. Charakhch'yan, A.N.— UFN, 3, No. 5. 1964.
2. Quenby, J.J. and G.I. Wenk.— Philos. Mag., 81, 1475. 1961.
3. Charakhch'yan, A.N. and T.N. Charakhch'yan.— Geomagnetizm i aeronomiya, 8, 822. 1968.
4. Stozhkov, Yu.I. and T.N. Charakhch'yan.— Geomagnetizm i aeronomiya, 8, 624. 1968.
5. Stozhkov, Yu.I. and T.N. Charakhch'yan.— Geomagnetizm i aeronomiya. 1969 (in print).
6. Charakhch'yan, A.N. and T.N. Charakhch'yan.— ZhETF, 35, 1088. 1958.
7. MacDonald, F.B.— Nuovo cimento Suppl., 8, 500. 1958.
8. Webber, W.R. and J.F. Ormes.— Proc. Internat. Conf. on Cosmic Rays, London. September. 1965.
9. Charakhch'yan, A.N. and T.N. Charakhch'yan.— Geomagnetizm i aeronomiya, 7, 974. 1967.
10. Balasubrahmanyan, V.K., D.E. Hagge, G.H. Ludwig, and F.B. MacDonald.— J. Geophys. Res., 71, 1771. 1966.

A. N. Charakhch'yan and T. N. Charakhch'yan

THE DIFFUSION COEFFICIENTS OF COSMIC RAYS

It is now recognized that the propagation of cosmic-ray particles in interplanetary space, and generally in interstellar space, is of a diffusional nature. This phenomenon is related to the scattering of the charged cosmic-ray particles by large-scale magnetic inhomogeneities in outer space.

The extensive experimental data now available make it possible to obtain interesting findings on the diffusive propagation of cosmic-ray particles. This refers primarily to the diffusion coefficients of solar and galactic cosmic rays and their dependence on the processes occurring on the sun and in interplanetary space.

If we consider the simplest case of diffusive propagation of solar cosmic rays in interplanetary space, the diffusion coefficient in the equation is the only parameter characterizing the diffusive property of the medium:

$$\frac{\partial n}{\partial t} = \frac{1}{\xi^2} \frac{\partial}{\partial \xi} \left(\xi^2 \mathfrak{D} \frac{\partial n}{\partial \xi} \right), \qquad (1)$$

where n is the particle concentration, ξ is the distance to the sun, and $\mathfrak{D}$ is the diffusion coefficient.

The diffusion coefficient $\mathfrak{D}$ is inversely proportional to the density of the scattering centers in the medium in which diffusion takes place, in our case the density q of large-scale magnetic inhomogeneities (clouds). The density may be defined by various parameters of the magnetic clouds. The choice of parameters is determined by the experimental conditions in which any specified characteristic of the clouds is studied. Where the scattering of cosmic-ray particles is concerned, the most suitable parameter characterizing the density of the magnetic clouds is the quantity $\varkappa = HL$, where H and L are the mean strength of the turbulent magnetic field and its mean spatial extent, respectively.

By means of the existing experimental data it is possible to obtain the spectral distribution of the density q in terms of $\varkappa$. In addition, q also depends on the space coordinate ξ. We thus put

$$q(\varkappa, \xi) = q_1(\varkappa) q_2(\xi), \qquad (2)$$

i.e., we assume that the variables $\varkappa$ and ξ are separable. It is convenient to refer to q_2 as the space distribution function of the magnetic-inhomogeneity densities.

For the diffusion coefficient we have the relationship

$$\mathcal{D}(x, \xi, \eta, v) = \frac{A(\eta, v)}{q_1(>x)\, q_2(\xi)}, \qquad (3)$$

where A depends on time, or, alternatively, on the solar activity η (the number of sunspot groups), and on the particle velocity v. The function q_1 is the integral magnetic-cloud density, defined by

$$q_1(>x) = \int_x^\infty q_1(x)\, dx, \qquad (4)$$

where $q_1(x)$ is the differential magnetic-cloud spectrum. The coefficient $\mathcal{D}$ is therefore a composite quantity depending on many variables. Still, by an appropriate choice of experimental data it is possible to find empirical relations between $\mathcal{D}$ and these parameters.

So far we have not considered the constant magnetic-field component. In this case isotropy does not hold for the diffusion coefficient and it will have to be expressed in a different form. Qualitatively, however, the net result of a constant magnetic field is to increase the diffusion coefficient, given the same values of parameters in (3). It is probably due to this effect that the diffusion coefficient $\mathcal{D}^s$ of solar cosmic rays is $2-3$ times larger than the coefficient $\mathcal{D}^g$ for galactic cosmic rays. The diffusion coefficient $\mathcal{D}^s$ defines the conditions of propagation of particles at close solar distances (about $1-3$ AU), where the radial magnetic field is still appreciable. The modulation of galactic cosmic rays, on the other hand, involves diffusion phenomena largely occuring far from the sun, where the radial field component is rather small.

THE DIFFUSION COEFFICIENT $\mathcal{D}^s$ OF SOLAR COSMIC RAYS

The dependence of $\mathcal{D}^s$ on η. Analysis of the experimental data on solar cosmic-ray bursts by means of (1) made it possible to determine the absolute values of $\mathcal{D}^s$ referring to different observation periods /1/. The values are given in Table 1, where t_{max} is the time of maximum proton intensity on Earth, $\mathcal{D}_0$ is the diffusion coefficient on Earth, P is the proton momentum, l is the transport mean free path, and β is the power index of the space density distribution function of magnetic inhomogeneities. It was noted that with decreasing solar activity, the value of $\mathcal{D}_0$ increases. By reducing the data it was possible to approximate an empirical relation between $\mathcal{D}_0$ and solar activity, i.e., between A and η in (3):

$$A(\eta) \simeq A_0 \eta^{-\alpha}, \qquad (5)$$

where A_0 is a constant and $\alpha \simeq 0.6$.

It thus follows that the density of large-scale magnetic inhomogeneities varies between maximum and minimum by a factor of about 5. It is worth noting that, according to /2/, variations of the same order are observed in the flux density of solar corpuscles.

TABLE 1. Values of the diffusion coefficients of protons on Earth

Date of burst	Heliocoordinates ℓ	Heliocoordinates φ	t_{max}, hr	$\mathcal{D}_0 \cdot 10^{21}$, $cm^2 sec^{-1}$	P, GeV/c	$\ell_0 \cdot 10^{11}$, cm	β	Number of sunspot groups η
Feb. 23, 1956	+74	+23	0.6	23	2.1	25	0.5	230
			0.5	28	2.8	29	0.5	
			0.34	41	3.5	43	0.5	
			0.46	30	4.1	31	0.5	
			0.26	53	5.9	53	0.5	
			0.20	69	6.0	69	0.5	
			0.30	46	9.0	46	0.5	
			0.15	92	12.0	92	0.5	
			0.14	99	14.0	99	0.5	
Aug. 22, 1958	+18	+0.8	1.8	7.7	0.6	14	0.5	400
Apr 1, 1960	+11	+13	5.4	3.9	0.6	7.1	1.0	220
May 4, 1960	+90	+11	2.5	5.5	0.6	10.0	0.5	230
Sep. 3, 1960	-90	+17	12.5	1.7	0.55	3.4	1	280
			9.2	2.3	0.60	4.2	1	
			5.8	3.6	2.1	4.0	1	
Nov. 15, 1960	+32	+20	5.4	3.9	0.6	7.1	1	200
			3.0	6.9	2.1	7.6	1	
Nov. 20, 1960	+110	+20	2.8	5.0	1.5	5.9	0.5	200
Jul. 18, 1961	+59	-0.8	5.4	3.9	0.6	7.1	1	150
			2.7	7.7	2.1	8.5	1	
Jul. 20, 1961	+90	-0.5	1.9	7.3	0.6	13	0.5	150
Sep. 28, 1961	-29	+13	3.6	5.8	0.4	14.5	1	120
			3.1	6.7	0.5	13.7	1	
			2.7	7.7	0.7	12.8	1	
			2.2	9.5	1.0	13.0	1	
Nov. 10, 1961	+90	+19	6.0	2.3	0.2	13.5	0.5	90
			2.0	6.9	0.4	17.2	0.5	
			1.0	14	0.6	25	0.5	
			0.8	17	0.8	27	0.5	
Oct. 23, 1962	+70	+0.3	2.5	8.3	0.4	22	1	80
			2.1	9.9	0.5	21	1	
			1.9	11	0.7	18	1	
Feb. 5, 1965	+24	+8	5.7	2.4	0.15	16	0.5	40
			4.8	2.9	0.2	14	0.5	
			3.6	3.9	0.3	13	0.5	
Jul. 7, 1966	+45	+34	2.8	7.4	0.6	13.4	1	120
Jan. 28, 1967			4.0	5.1	0.6	9.2	1	230
			3.1	6.7	2.0	7.4	1	
May 28, 1967	+30	+28	7.1	2.9	0.2	14	1	220
			7.1	2.9	0.3	9	1	
			5.7	3.6	0.5	8	1	
			7.0	3.0	0.6	6	1	

The dependence of $\mathcal{D}^s$ on the space coordinate. The time variation of a number of bursts provided the means of determining the relationship between $\mathcal{D}^s$ and the space coordinate ξ, i.e., q_z in (2). In the approximation $q_z \approx \xi^{-\beta}$ it was found that $\beta = 0.5$ for 7 cases out of 16 and $\beta = 1.0$ for the others. We may note that the index β turned out the same

for different proton energy ranges, and thus points to the possibility of separating the variables $\varkappa$ and ξ in (2). In the first approximation, therefore, we may write q_2 for solar cosmic rays as

$$q_2 \simeq q_{2R}\left(\frac{\xi}{R}\right)^{-\beta}, \tag{6}$$

where R is the distance to the Earth's orbit, and q_{2R} is the value of q_2 at $\xi = R$.

The integral density spectrum of magnetic inhomogeneities, $q_1(\geq \varkappa)$. In 5 cases out of 7 the transport mean free path l_0 was constant to within the experimental accuracy for proton momenta P ranging approximately between 0.5 and 2 GV; two cases show an explicit dependence of l_0 on the proton momentum in the form P^{α}, where $\alpha \simeq 0.5$ and $P > 0.5$ GV (Table 1). Accordingly, the integral density spectrum of magnetic inhomogeneities $q_1(\geq \varkappa)$ according to the parameter $\varkappa \sim P$, as obtained from solar cosmic rays, may in the first approximation be divided into two classes:

$$1.\ q_1(\geq \varkappa) = const,$$
$$2.\ q_1(\geq \varkappa) \simeq \frac{const}{\sqrt{\varkappa}}.$$

Consequently, there are large fluctuations in the magnetic-inhomogeneity spectrum, specifically in terms of the differential density spectrum $q_1(\varkappa)$ in (4). In fact, in the first case, the differential spectrum will be practically cut off on the side of small $\varkappa$, while in the second, $q_1(\varkappa)$ is a continuously increasing function of the form $q_1 \sim \varkappa^{-1.5}$. Let us note that classes 1 and 2 are also associated with different space distribution functions q_2, for which $\beta = 1.5$ and 0.5, respectively.

It is worth noting that the variation of the density spectrum in these two classes is mainly due to variations in the number of large magnetic inhomogeneities. This may be seen from the mean values of the diffusion coefficients $\mathcal{D}_0 \cdot (10^{21}\,\mathrm{cm^2 \cdot sec^{-1}})$ given below:

For bursts with $\beta = 0.5$ and a proton magnetic rigidity P = 0.6 GV, $\mathcal{D}_0 = 12 \pm 2$, and for P = 2 GV, $\mathcal{D}_0 = 40$;

For bursts with $\beta = 1.0$ and P = 0.6 GV, $\mathcal{D}_0 = 7 \pm 0.6$, and for P = 2 GV, $\mathcal{D}_0 = 10 \pm 1$.

In the calculation of $\mathcal{D}_0$ the results were reduced to the solar-activity level $\eta = 90$, by means of (5).

It is seen that the relative difference in $\mathcal{D}_0$ for the different β is larger at high rigidities. The change in the functions q_1 and q_2 according to the type of burst thus indicate that complex processes are involved in the propagation of solar cosmic-ray particles in space.

We can consequently describe the diffusion coefficient of solar cosmic rays by two empirical relations, corresponding to different conditions of solar-proton propagation in space:

$$\mathcal{D}^s \simeq 1.3 \cdot 10^{13} \frac{v\sqrt{\rho}}{\eta^{1/3}} \left(\frac{\xi}{R}\right)^{0.5}\ (\mathrm{cm^2\,sec^{-1}})$$

$$\text{and } \mathcal{D}^s \simeq 0.6 \cdot 10^{13} \frac{v}{\eta^{1/3}} \frac{\xi}{R}\ (\mathrm{cm^2\,sec^{-1}}).$$

The first of these applies to the data in Table 1 for which $\beta = 0.5$, and the second to the data for which $\beta = 1.0$.

THE DIFFUSION COEFFICIENT OF GALACTIC COSMIC RAYS

The 11-year solar modulation of the cosmic-ray intensity is well explained by Parker's theory, according to which cosmic-ray particles are expelled from interplanetary space by moving magnetic inhomogeneities. The theory gives the following equations relating the diffusion parameters of cosmic-ray propagation in interplanetary space with experimental data:

$$\psi = \int_{r}^{\tau} \frac{u}{\mathfrak{D}^{g}} d\xi , \tag{7}$$

$$t_{st} = \frac{\psi \mathfrak{D}^{g}}{u^{2}} , \tag{8}$$

$$\frac{1}{N}\frac{\Delta N}{\Delta R} = \frac{u}{\mathfrak{D}^{g}} . \tag{9}$$

On the left-hand side appear the measured quantities: ψ is the cosmic-ray modulation factor /4/, t_{st} is the stabilization time of the cosmic-ray intensity in interplanetary space /5/, $\frac{1}{N}\frac{\Delta N}{\Delta R}$ is the radial cosmic-ray intensity gradient measured in space experiments /6—11/, and N is the integral number of particles.

Using equations (7), (8), (9) and the appropriate experimental data, it is thus possible to calculate each of the diffusion parameters, i.e., the diffusion coefficient $\mathfrak{D}$, the propagation velocity u of large-scale magnetic clouds, and the range τ of solar modulation.

For the actual solution of the problem, the dependence of $\mathfrak{D}$ and u on the space coordinate have to be specified. We calculated the integral (7) by assuming a power dependence $\mathfrak{D}^{g} = \mathfrak{D}_{\bullet}^{g}(\frac{\xi}{R})^{\beta}$ and a constant u. The resultant values of ψ for β = 0, 0.5, 1.0, and 2.0, $u = 4 \cdot 10^{7}$ cm^{2}/sec and τ = 15 AU are given in Table 2.

TABLE 2. Calculated values of the modulation factor ψ_{exp} (0.5 < P < 2.3 GV) for different values of the diffusion coefficient $\mathfrak{D}^{g}$(cm^{2}sec^{-1}10^{22}) and of the power index β, with $u_{o} = 4 \cdot 10^{7}$ cm/sec and τ = 15 AU

ψ_{exp}	Diffusion coefficient $\mathfrak{D}^{g}$												Solar activity η	Diffusion coefficient $\mathfrak{D}_{\bullet}$ (10^{22} cm^{2} sec^{-1})
	β = 0			β = 0.5			β = 1.0			β = 2.0				
	$\mathfrak{D}_{\bullet}$	$\frac{\mathfrak{D}_{\bullet}}{3}$	$\frac{\mathfrak{D}_{\bullet}}{6}$	$\mathfrak{D}_{\bullet}$	$\frac{\mathfrak{D}_{\bullet}}{3}$	$\frac{\mathfrak{D}_{\bullet}}{6}$	$\mathfrak{D}_{\bullet}$	$\frac{\mathfrak{D}_{\bullet}}{3}$	$\frac{\mathfrak{D}_{\bullet}}{6}$	$\mathfrak{D}_{\bullet}$	$\frac{\mathfrak{D}_{\bullet}}{3}$	$\frac{\mathfrak{D}_{\bullet}}{6}$		
0.4	0.35	0.8	1.7	0.1	0.35	0.65	0.06	0.17	0.34	0.06	0.12	0.24	50	3.0
0.6	0.5	1.2	2.4	0.17	0.5	1.0	0.08	0.25	0.48	0.09	0.18	0.36	100	2.0
1.2	0.75	1.9	3.2	0.26	0.8	1.6	0.12	0.35	0.75	0.17	0.3	0.6	200	1.3
1.4	1.0	2.5	5.0	0.34	1.0	2.0	0.16	0.5	0.95	0.18	0.36	0.7	300	1.0

The variation of ψ with η for several particle-energy ranges is plotted in the figure. The data on ψ tabulated in the first column are for the

differential number of particles in the range $0.5 \leq P \leq 2.3$ GV. In the remaining columns appear the values of ψ, calculated for different values of β, and of the galactic cosmic-ray diffusion coefficient $\mathcal{D}_0^g$, expressed in terms of $\mathcal{D}_0$ for solar cosmic rays. It can be seen from the table that for each value of β it is possible to select a value of $\mathcal{D}_0^g$ which gives a good agreement between the calculated and experimental values of ψ. For example, for $\beta = 0$, $\mathcal{D}_0^g = \mathcal{D}_0$; for $\beta = 0.5$, $\mathcal{D}_0^g = \frac{\mathcal{D}_0}{3}$; for $\beta = 1.0$, $\mathcal{D}_0^g = \frac{\mathcal{D}_0}{6}$. In order to draw any definite conclusions in this respect, we need measurement data on the cosmic-ray gradient $\frac{1}{N}\frac{\Delta N}{\Delta R}$.

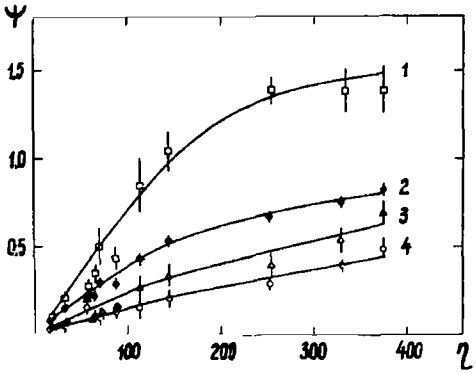

Variation of the modulation factor ψ with the number of sunspot groups η for primary particles of rigidity P, GV:

1 — $0.5 < P < 2.3$; 2 — $P > 0.5$; 3 — $2.3 < P < 5.5$; 4 — $P > 2.3$.

Experiments on modern spacecraft provide qualitatively new findings on the radial cosmic-ray intensity gradient. By performing measurements at different points in interplanetary space and determining the corresponding values of the gradient $\frac{1}{N}\frac{\Delta N}{\Delta R}$, it is possible to calculate $\frac{u}{\mathcal{D}}$ and its variation with the coordinate. This is quite difficult in practice, however; first, because measurements have to be made far from the Earth, and also because the measured intensity variations are often difficult to separate into space and time variations. At a distance of 0.2 — 0.5 AU from the Earth, the expected variation is a few percent. However, variations of the same order of magnitude occur in the Forbush effect and short-period fluctuations, and also in the case of nonuniform spatial distribution of the cosmic rays. In order to obtain reliable gradient data, free of time variations and comparable with theoretical results, long-term observations seem therefore required. The data reported on the subject are nevertheless of high interest. Table 3 gives data on $\frac{u}{\mathcal{D}_0}$ derived from measurements of the gradient $\frac{1}{N}\frac{\Delta N}{\Delta R}$ /6 — 11/. The large spread in $\frac{u}{\mathcal{D}_0}$ can probably be attributed to time variations in the cosmic-ray intensity, which cannot always be accurately computed. According to the data of "Mars-1" and "Pioneer-5" no spatial dependence was found for $\frac{\Delta N}{N}$ within 2 — 3% irregular variations up to a range of 1.24 AU. We may point out the good agreement in the $\frac{u}{\mathcal{D}_0}$ data obtained by "Zond-2," "Zond-3," "Venera-3," and "Venera-4." The measurements of "Mariner-4" apparently yield an incorrect result due to an inaccurate correction for time variations. Given in the table is also our interpretation of the Mariner-4 data. As can be seen, the result obtained by Mariner-4 is appreciably different from the others.

TABLE 3. Values of $\frac{u_0}{\mathcal{D}_0}$ from space-probe measurements of the cosmic-ray intensity gradient and from data on the diffusion coefficient of solar cosmic rays, for $u_0 = 4 \cdot 10^7$ cm/sec.

Solar activity η	Spacecraft and observation time	$u_0/\mathcal{D}_0$, 10^{-15} cm^{-1}	
		from cosmic-ray gradient data	from solar cosmic-ray diffusion coefficients
70	"Mars 1", Nov. 20, 1962 — Jan. 25, 1963 /6/	≤6.0	1.0
250	"Pioneer 5," Apr. 1960 /7/	≤6.0	2.2
70	"Mariner 2," Sep. — Nov. 1962 /8/	10 ± 3	1.0
40	"Zond 2," "Zond 3" "Venera 2," "Venera 3" /9/	~2.0	0.7
40	"Mariner 4," Dec. 1964 — Sep. 1965 /10/	~6.0 <1.0*	0.7
220	"Venera 4," June — Oct. 1967 /11/	3.0	2.0

* Authors' derivation.

The last column of the table gives the values of $\frac{u_0}{\mathcal{D}_0}$ obtained from data on the diffusion coefficient of solar cosmic rays for different solar-activity levels η and a constant velocity $u = 4 \cdot 10^7$ cm/sec. There is a qualitative agreement between the values of $\frac{u_0}{\mathcal{D}_0}$ obtained from solar cosmic-ray data and the radial gradient values. They differ on the average by a factor of about 3. This discrepancy is most likely due to a difference of $\mathcal{D}^g \simeq \frac{1}{3}\mathcal{D}^s$ in the diffusion coefficients. According to Table 2, such a difference in the diffusion coefficients of galactic and solar cosmic rays corresponds to $\beta = 0.5$. It thus turns out that the flux density of large-scale magnetic inhomogeneities in space varies approximately as $\frac{1}{\sqrt{\xi}}$, which is in agreement with the earlier result for one group of bursts.

The energy spectrum of 11-year variations and the density spectrum of magnetic inhomogeneities. The results of systematic cosmic-ray measurements at varying stratospheric altitudes and different observation times furnish interesting data on the variation of the primary-component energy spectrum with the 11-year solar cycle. There is as yet no theory connecting the 11-year modulation with any particular manifestation of solar activity, but the experimental data are nevertheless significant. They can presumably be associated with the spectral density distribution $q_1(\varkappa)$ of large-scale magnetic clouds, as in the case of

solar cosmic rays. Accordingly, it can be deduced from the observational findings that unlike the spectrum $q_1(\varkappa)$ for solar cosmic rays, the form of $q_1(\varkappa)$ obtained from galactic cosmic rays is remarkably constant. Within the experimental accuracy, it showed virtually no changes from 1959 to 1964.

Experimental investigations usually give the ratio of the number of particles undergoing modulation, ΔN, to the overall number of particles N. Referring back to Parker's theory, we have

$$\frac{\Delta N}{N} = 1 - \exp\left[-\int_R^2 \frac{u}{\mathcal{D}^g} d\xi\right]. \qquad (10)$$

Among the parameters appearing in the equation, only the diffusion coefficient depends on the momentum or energy of the cosmic-ray particles. According to our findings from stratospheric measurements, $\mathcal{D}^g$ varies with the magnetic rigidity of the particles as follows:

$$\mathcal{D}^g \sim v\,(2 + P). \qquad (11)$$

This relationship between $\mathcal{D}^g$ and P was consistently observed throughout 1959 — 1964. Accordingly, using the set of experimental data on the 11-year solar modulation of the galactic cosmic-ray intensity in interplanetary space, we get the approximate dependence of the diffusion coefficient $\mathcal{D}^g$ on η, P, and ξ:

$$\mathcal{D}^g \simeq 0.15 \cdot 10^{13} \frac{(2+P)\,v}{\eta^{5/3}} \sqrt{\frac{\xi}{R}} \ (\mathrm{cm}^2 \cdot \mathrm{sec}^{-1}). \qquad (12)$$

According to (3), the corresponding form of the magnetic-inhomogeneity spectrum in terms of $\varkappa$ is given by

$$q_g(\varkappa) \sim \frac{1}{(\varkappa_0 + \varkappa)^2}. \qquad (13)$$

The constant $\varkappa_0$ is determined from the proportionality $\varkappa_0 \approx P = 2$ GeV.

For $\varkappa \ll \varkappa_0$, $q_g(\varkappa)$ - const; for $\varkappa \gg \varkappa_0$, $q_1(\varkappa) \approx \frac{1}{\varkappa^2}$.

Bibliography

1. Charakhch'yan, A.N. and T.N. Charakhch'yan. — Izvestiya AN SSSR, ser. fiz., 32, 1776. 1968.
2. Gringauz, K.I. and E.K. Solomatina. — Kosmicheskie Issledovaniya, 6, 586. 1968.
3. Parker, E.N. — Phys. Rev., 103, 1518. 1956.
4. Charakhch'yan, A.N. and T.N. Charakhch'yan. — Geomagnetizm i aeronomiya, 6, 486. 1966.
5. Charakhch'yan, A.N. and T.N. Charakhch'yan. — Geomagnetizm i aeronomiya, 8, 822. 1968.

6. Vakulov, P.V., S.N. Vernov, E.V. Gorchakov, J.I. Logachov, A.N. Charakhch'yan, T.N. Charakhch'yan and A.E. Chudakov.—COSPAR. North-Holland, Amsterdam. 1964.
7. Fan, C.J., P. Meyer, and J.A. Simpson.— Phys. Rev. Lett., 5, 272. 1960.
8. Neyer, H.V. and H.R. Anderson.— J. Geophys. Res., 69:1911. 1964.
9. Vernov, S.N., A.E. Chudakov, P.V. Vakulov, Yu.I. Logachev, G.P. Lyubimov, and N.V. Pereslegina.— Izvestiya AN SSSR, ser. fiz., 31, 1259. 1967.
10. O'Gollgagher, J.J. and J.A. Simpson.— Astrophys. J., 147, 819. 1967.
11. Vernov, S.N., A.E. Chudakov, P.V. Vakulov, Yu.I. Logachev, G.P. Lyubimov, and N.V. Pereslegina.— Izvestiya AN SSSR, ser. fiz., 1969 (in print).

V. A. Dogel' and S. I. Syrovatskii

THE DIFFUSION OF RELATIVISTIC ELECTRONS IN THE GALAXY AND THEIR ENERGY SPECTRUM

According to modern concepts, cosmic rays originate primarily in supernova outbursts /1/. The electron component is assumed to be primary, i.e., it is accelerated in the source similarly to protons and heavier nuclei /2/. The propagation of relativistic particles in the Galaxy is diffusional in the first approximation, and the problem thus becomes one of correlating the electron intensity observed on Earth /3/ with the strength and distribution of the sources.

In /4/ this problem is considered under the assumption that the sources occupy an ellipsoidal volume, conforming to the observed distribution of supernovae in the Galaxy, and that diffusion takes place in unbounded space, with a constant diffusion coefficient $\mathcal{D}$. Under actual conditions in the Galaxy, however, $\mathcal{D}$ is obviously a function of the coordinates and in particular it increases sharply in the weak intergalactic magnetic field beyond the galactic halo. We accordingly consider the diffusion of electrons in a spherical region assumed to have an absorbing boundary. This corresponds to the free escape of electrons across the boundary of the galactic halo. As in /4/, the source distribution is ellipsoidal.

Under these assumptions, taking into account synchrotron, Compton, and "catastrophic" losses with characteristic time T, the electron spectral density $f(\bar{r},E,t)$ is described by the equation /4/

$$\frac{\partial f}{\partial t} - \mathcal{D}\Delta f + \frac{\partial}{\partial E}\left(B(E)f\right) + \frac{f}{T} = Q(\bar{r},E,t), \qquad f(\bar{r},E,t) = 0 \quad \text{for} \quad |\bar{r}| = R_0, \tag{1}$$

where $B(E) \equiv \frac{dE}{dt} = -\beta E^2$ are the electron energy losses due to Compton and synchrotron radiation.

In the case of axial symmetry the Green's function for equation (1) with the given boundary conditions has the form:

$$G(r,\vartheta,E,t\,|\,r_0,\vartheta_0,E_0,t_0) = \frac{2\pi e^{-\frac{\tau}{T}}}{|B(E)|}\,\delta(t-t_0-\tau)\sum_{n=0}^{\infty}\frac{P_n(\cos\vartheta)\cdot P_n(\cos\vartheta_0)}{\|P_n\|^2}\times$$
$$\times\sum_{m=1}^{\infty}\frac{J_{n+\frac{1}{2}}(\lambda_m^n r)\,J_{n+\frac{1}{2}}(\lambda_m^n r_0)}{\sqrt{r\cdot r_0}\,\|J_{n+\frac{1}{2}}\|^2}\,e^{-\mathcal{D}\left(\lambda_m^n\right)^2\tau}, \tag{2}$$

where $\tau = \int_{E_0}^{E} \frac{dE}{B(E)}$ and λ_m^n is determined from the condition $J_{n+\frac{1}{2}}(\lambda_m^n R_0) = 0$. The distribution function of the sources $Q(r_0, \vartheta_0, E_0)$ was taken as /4/

$$Q(r_0, \vartheta_0, E_0) = \frac{Q E_0^{-\gamma_0}}{\pi^{3/2} a^2 b} \exp\left\{-\left(\frac{z_0}{a}\right)^2 \sin^2\vartheta_0 - \left(\frac{r_0}{b}\right)^2 \cos^2\vartheta_0\right\}. \quad (3)$$

The problem is assumed to be a steady-state one. The electron space and energy distributions are then given by

$$f(r, \vartheta, E) = \int G \cdot Q \cdot dz_0 d\vartheta_0 dt_0 dE_0 = \frac{Q E^{-(\gamma_0+1)}}{\beta} \cdot \frac{2B(1,\mu)}{\pi^{\frac{1}{2}} a^2 R_0^2 b} \cdot \frac{1}{\sqrt{r}} \sum_{l=0}^{\infty} (4l+1) P_{2l}(\cos\vartheta) \times$$
$$\times \int_0^{\pi} P_{2l}(\cos\vartheta_0) \sin\vartheta_0 d\vartheta_0 \sum_{m=1}^{\infty} \frac{J_{2l+\frac{1}{2}}(\lambda_m^{2l} r)}{[J_{2l+\frac{1}{2}}(\lambda_m^{2l} R_0)]^2} F_1\left(1, \mu+1, \frac{\mathcal{D}(\lambda_m^{2l})^2}{\beta E}\right) e^{-\frac{\mathcal{D}(\lambda_m^{2l})^2}{\beta E}} \times \quad (4)$$
$$\times \int_0^{R_0} J_{2l+\frac{1}{2}}(\lambda_m^{2l} r_0)\, e^{-\left(\frac{r}{a}\right)^2 \sin^2\vartheta_0 - \left(\frac{r_0}{b}\right)^2 \cos^2\vartheta_0} r_0^{3/2} dr_0,$$

where $\mu = \gamma_0 - 1$.

Analysis shows that if $r \ll R_0$ and $\vartheta = \pi/2$, the function $f(r, \vartheta, E)$ can be approximated by a power function with two discontinuities; thus, in the energy range $E \ll \mathcal{D}\pi^2/R_0^2\beta$, $\frac{\partial \ln f}{\partial \ln E} = -\gamma$; when $E \gg \mathcal{D}\pi^2/R_0^2\beta$, $\frac{\partial \ln f}{\partial \ln E} = -(\gamma_0+1)$ and, finally, when $\mathcal{D}\pi^2/R_0^2\beta \ll E \ll \mathcal{D}\pi^2/b^2\beta$, $\frac{\partial \ln f}{\partial \ln E} = -(\gamma_0 + \frac{1}{2})$. This result is similar to the one obtained in /5/ for an unbounded space. In the geometry considered, therefore, the spectrum index changes as a result of synchrotron and Compton losses, not by unity, as normally assumed, but twice by one half.

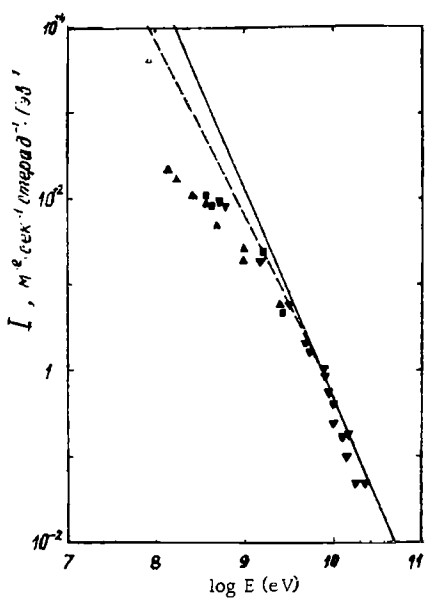

Intensity of galactic electrons near the Earth:

--- spherically bounded case; —— $R_0 = \infty$.

In the general case a simple analytic expression cannot be derived for the spectrum, and we performed numerical calculations with the parameters $a/b = 1.5 \cdot 10^2$, $a/R_0 = 1$, and $r_\odot/R_0 = 2/3$. Given R_0 and β from the position of the discontinuity in the cosmic-electron intensity, it is possible to determine the diffusion coefficient $\mathcal{D}$.

If the condition $r \ll R_0$ does not hold, the position of the first discontinuity is approximately defined by $E \sim \pi^2\mathcal{D}/R'^2\beta$, where $R' = R_0 - r_\odot$; in this case, if $R' \gg b$, the position of the second discontinuity does not change ($\vartheta = \pi/2$).

The observed discontinuity lies approximately at $E_0 \simeq 3$ BeV /3/ and is most probably the first one. In fact, if we identify this discontinuity with the first one in the distribution function, we obtain $\mathcal{D} \sim 10^{28}$ cm^2/sec and if we take it to be the second discontinuity, we obtain $\mathcal{D} \sim 10^{25}$ cm^2/sec. The

latter is rather unlikely as it requires a value of ℓ in $\mathcal{D} \simeq \ell v/3$, which is 3 or 4 orders of magnitude smaller than normally used /1/, and a harder spectrum of injected electrons with $\gamma \simeq 1.6$. We accordingly have the result $\mathcal{D} \sim 10^{28}\,\mathrm{cm}^2/\mathrm{sec}$, and $\gamma \simeq 2$; in order to bring the electron intensity measured on Earth into agreement with the calculated value, it is necessary to take the electron source strength $Q \sim 2.7 \cdot 10^{38}\,\mathrm{erg/sec}$.

The calculation results are plotted in the figure. Shown for comparison is the result calculated with the same parameters and $R_0 = \infty$ /4/. The points in the diagram represent the electron spectrum observed on Earth. As may be seen, the bounded case yields a smaller intensity in the low-energy range. At high energies, beginning from $E > \frac{\pi^2 \mathcal{D}}{\tau^2 \beta}$, where τ is the shortest distance between the given point and the boundary, the values of the function for the spherically bounded case and for $R_0 = \infty$ should coincide.

Bibliography

1. Ginzburg, V.L. and S.I. Syrovatskii. Proiskhozhdenie kosmicheskikh luchei (Origin of Cosmic Rays). — Moskva, Izdatel'stvo AN SSSR. 1963.
2. Ginzburg, V.L. and S.I. Syrovatskii. — Astronomicheskii Zhurnal, 41, 430. 1964.
3. Anand, K.C., R.R. Daniel, and S.A. Stephens. — Phys. Rev. Lett., 20, 764. 1968.
4. Syrovatskii, S.I. — Astronomicheskii Zhurnal, 36, 17. 1959.
5. Jokipii, J.R. and P. Meyer. — Phys. Rev. Lett., 20, 752. 1968.

G. B. Khristiansen

ULTRAHIGH-ENERGY COSMIC RAYS

The only effective method of detecting primary cosmic radiation of ultrahigh energy larger than 10^{15} eV is to record the fluxes of charged particles and electromagnetic radiation that accompany the penetration of ultrahigh-energy particles through the atmosphere. The method most feasible at present is based on the detection of the fluxes of charged particles produced in the atmosphere. We will examine the findings on the energy spectrum, nature, and anisotropy of cosmic rays of energy $E_0 \sim 10^{14} - 10^{19}$ eV obtained by this method, and consider a model which fits the experimental data.

The energy spectrum of ultrahigh-energy primary radiation was studied from the particle spectrum of showers at various altitudes. The number of particles N_e and other parameters of the shower are determined nowadays by means of powerful installations covering an area from some tenths to 10 km^2 according to the relevant N_e. The accuracy in the determination of N_e is within $\sim 15\%$ at $N_e \sim 10^5 - 10^7$ and worsens with increasing N_e, approaching to within $\sim 100\%$ at $N_e \sim 10^{10}$. The determination accuracy in the orientation of the shower axis (ϑ and φ) is, for ordinary installations, $\Delta\vartheta = 2 - 3°$ and $\Delta\varphi = 6 - 8°$. In the most simple case the N_e spectrum represents the primary energy spectrum near the maximum cascade development, since at the maximum $N_e \sim E_0$ up to a factor which is practically independent of E_0. The first precise measurements at $N_e = 10^5 - 10^7$ were made at sea level /1/, however, and revealed that the index γ of the shower particle spectrum changes abruptly by $\Delta\gamma = 0.5 - 0.6$ when N_e varies from $3 \cdot 10^5$ to 10^6. A few years later, this result was confirmed by precision measurements at mountain level (in Chakaltai) /2/ (Figure 1). The value of N_e at which γ effectively changes at mountain level turned out to be 4 — 5 times larger than at sea level, which could be expected if the change of γ is associated with the variation in the form of the primary energy spectrum. Figure 1 gives the results of shower-particle measurements at the Tien Shan extended-shower research complex /3/. These data are inconsistent with the results obtained earlier by the same group, according to which the abrupt variation in γ should occur at the same value of N_e both at sea level and at mountain level.

The presence of an abrupt variation in the form of the primary energy spectrum at $E_0 \sim (2-4) \cdot 10^{15}$ eV * has now been definitely established. In recent years, experimental data have been obtained on the decrease of the

* The value of N_e at mountain level (630 g/cm^2) is reduced to E_0 by means of the conversion factor $1.7 \cdot 10^9$ eV/particle.

index of the shower particle spectrum at $N_e > 10^7$ down to $\alpha = 1.6 - 1.7$. Figure 2 gives the results obtained at Moscow State University /4/, at Cornell University (USA) /5/, at MIT (USA) /6/ and at "Haveral Park" in England /7/. The given data have been converted from the directly measured quantity E, i.e., the energy flux released by the shower in 120-cm water Čerenkov counters, to the number of particles N_e. According to /8/, $E \sim N_e^{as}$. Thus the E spectrum having the form $F(>E) \sim E^{-2.0}$ is transformed into the N_e spectrum $F(>N_e) \sim N_e^{-1.6}$. As Lindsay /6/ points out, the most probable value of α in the range $N_e = 5 \cdot 10^7 - 5 \cdot 10^9$ is 1.7. We may note that the first points in the particle spectrum at $N_e < 3 \cdot 10^8$, from which Lindsay formally derived the higher value $\alpha = 2$, were obtained on the El Alto installation, while the points for $N_e > 3 \cdot 10^8$ were obtained on the Volcano Ranch installation. Figure 2 gives only the measurement results of Volcano Ranch.

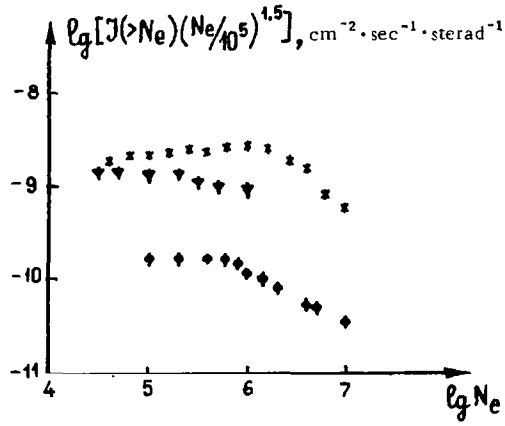

FIGURE 1. Shower particle spectrum at sea level and at mountain level.

Circles — /1/; crosses — /2/; triangles — /3/.

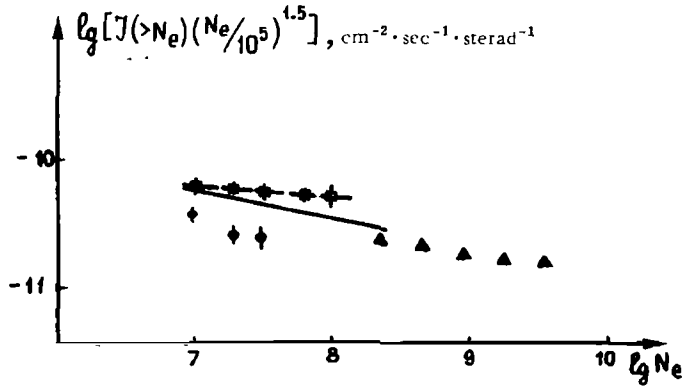

FIGURE 2. Shower particle spectrum at and near sea level for $N_e > 10^7$ from the data of /4/ (circles), /5/ (solid line), /6/ (triangles), and /7/ (squares).

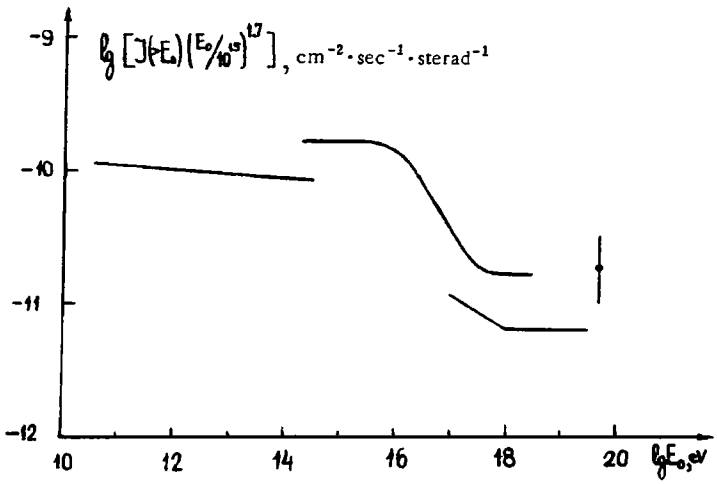

FIGURE 3. Energy spectrum of primary cosmic radiation from extended-shower findings and "Proton" satellite data /9/. The point at $E_0 = 5 \cdot 10^{19}$ eV is obtained from the data of /6/.

Plotted in Figure 3 are the data derived from /1, 2, 5, 6/ on the energy spectrum of the primary particles generating extended air showers. The figure also gives data on the primary spectrum of the particles producing showers in an ionization calorimeter. These data were obtained on a "Proton" artificial satellite. The plotted spectra show good agreement at $E_0 < 10^{15}$ eV, both in form and in absolute value (allowing for the different measurement errors). The primary energy spectrum in the ultrahigh-energy region of $10^{14} - 10^{19}$ eV is therefore characterized by a two-fold shift in its shape. Until recently this was normally interpreted in terms of the diffusional propagation of cosmic rays in our Galaxy, and the superposition of galactic and metagalactic cosmic rays. According to this interpretation, at low E_0 the spectrum index of the galactic component corresponds to the spectrum index of the galactic cosmic-ray sources. Starting at some E_0 the cosmic-ray diffusion coefficient rapidly increases with E_0 which accounts for the first change in the index of the primary energy spectrum. With a further increase in E_0 the metagalactic component starts to predominate over the galactic component and the primary-spectrum index drops again, since in the simplest case the energy-spectrum index of the metagalactic component is the same as that of the galactic sources /10/.

Many attempts have been made to detect anisotropy in the primary ultra-high-energy radiation ever since systematic studies of extended air showers were begun. Until now, however, no significant anisotropy δ has been found, even in the low-energy range, where the measurement statistics is highest. Figure 4 gives the upper limits for the possible variation amplitude on the basis of right ascension for different E_0, according to measurements made in the northern hemisphere; the values are plotted from the most accurate data of /11, 12, 13, 6/. It should be noted that for $E_0 \leq 10^{17}$ eV /11, 12, 13/ the upper limits of the variation amplitude are determined only by order of magnitude, since the measurement errors involved are of the order of the measured quantities themselves. Furthermore, since for these energies /11, 12, 13/ the observations are performed

at high latitudes, the variation amplitude is not equal to the anisotropy but only a fraction thereof /14/. This applies to a lesser extent to the data of /6/, which are obtained at low altitudes. The earlier mentioned superposition model of the galactic and metagalactic cosmic-ray components clearly does not conflict with the experimental anisotropy data /10/ given in Figure 4. In fact, according to /14/, at low energies, where the galactic component diffusion coefficient is independent of the energy, the quantity $\delta \sim 0.1 - 0.01\%$. At energies $\gtrsim (2-3)\cdot 10^{15}$ eV, where the diffusion coefficient $\mathcal{D} \sim E^{\alpha}$ (for $\alpha \simeq 1$), the anisotropy ratio increases up to a value of a few percent at $E_0 \sim 10^{17}$ eV, which was in agreement with the experimental data. At high energies, where the metagalactic component predominates, the anisotropy ratio may even become negative /14/.

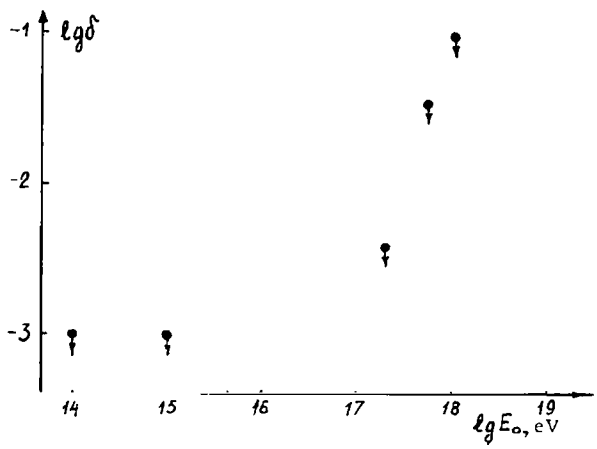

FIGURE 4. Upper limits for the variation amplitude of the primary-radiation intensity as functions of right ascension.

For $E_0 = 10^{14} - 10^{15}$ eV, according to /11/; for $E_0 = 10^{16}$ eV – /12/; for $E_0 = 2\cdot 10^{17}$ and $5\cdot 10^{17}$ eV – /13/; for $E_0 = 10^{18}$ eV – /6/.

Attempts to analyze the nature of ultrahigh-energy primary radiation have been made by a number of authors.* The most definite results have been obtained by studying the relative fluctuations of the number of electrons N_e and muons N_μ in a standard air shower. As is known, for a fixed number of muons N_μ, the mean value of N_e and its relative fluctuations decrease with increasing atomic number A of the shower-producing primary particle.

Figure 5 gives the experimental data of /15/ on the relative fluctuations σ_{N_e} in the number of electrons in showers with a different number of muons, and the calculation results of /16/ for primary radiation consisting only of protons (A = 1) or of heavy nuclei (A = 30). It may be seen that the results

* We will be concerned with nuclear primary radiation. According to experimental data, the contribution of electromagnetic primary radiation is not more than 10^{-4}. After relict radiation was discovered, it was found to cause appreciable absorption of the diffuse component of electromagnetic cosmic radiation.

of /15/ are inconsistent with A = 30 but agree with A = 1. The figure also shows the values of σ_{N_e} calculated for the superposition model of the galactic and metagalactic components /17/ under the assumption that the chemical composition of the primary radiation in the region where the diffusion coefficient is independent of the energy (i.e., at $E_0 \leq 10^{15}$ eV) is similar to that at low energies /14/. The calculation results were found to be in agreement with the experimental data.

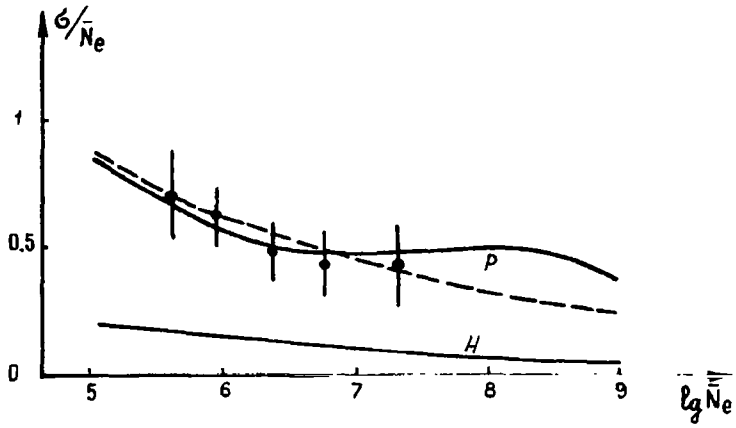

FIGURE 5. Comparison of experimental data on the distortion in the number of particles N_e at various values of N_e (or N_μ) with theoretical calculations. The experimental data were taken from /15/. Curves P and H — calculations for protons and heavy nuclei according to /16/; dashed curve — calculations according to /17/; solid curve — calculation for the chemical composition according to the model of ultrahigh-energy cosmic-ray generation proposed in the present paper.

It has been recognized in recent years that relict radiation with a temperature of 3°K is of fundamental importance in the absorption of ultrahigh-energy cosmic rays. This is associated with the fact that the photons of relict radiation may interact with protons and nuclei of sufficiently high energy. The interaction gives rise to photoproduction of pions or electron-positron pairs, or to photonuclear disintegration. As a result of these processes, the energy of the cosmic-ray particles is reduced. The importance of this effect was pointed out in /18, 19/. According to /19/, at the relict photon density corresponding to our epoch (~ 5000/ cm^3), the lifetime of protons of energy $\geq 10^{19}$ eV is of the order of 10^8 years. Given a lifetime $\geq 10^9$ years estimated for metagalactic cosmic rays from the diffusion theory, the cutoff in the energy spectrum is quite pronounced, starting at $E \sim 3 \cdot 10^{19}$ eV.*

It should be noted that according to /20/ there may exist in the universe also infrared radiation with a temperature of ~ 8°K and a photon density as high as that of relict radiation. In this case, the energy at which the spectrum

* In /20/ an exact calculation was attempted with allowance for: a) different laws of variation of the cosmic-ray source strength with time; b) different laws of variation of Hubble's constant with time; and c) different time origins t (for which a specific law of variation of the cosmic-ray intensity is assumed).

is effectively cut off would clearly be $\sim 10^{19}$ eV, while in the experiment performed in /6/ dozens of events can be observed at this energy. Although both the experiment of /6/ and the data of /20/ need further refinement, it is pertinent to consider other possible models for the origin of ultrahigh-energy cosmic rays which fit the given experimental data and are also consistent with a short propagation time for cosmic rays of critically high energies between the source and the observer.

We will retain our earlier division of cosmic rays into a galactic and a nongalactic component, but assume that the latter originates in the neighboring galaxies. It is most logical to consider those of the Local Group (Supergalaxy), which consists of 16 galaxies and has a radius of $\sim 2 \cdot 10^6$ light years. We will assume as before that at $E_0 < 3 \cdot 10^{15}$ eV the main cosmic-ray source is the Galaxy. At $E_0 > 3 \cdot 10^{15}$ eV the coefficient of diffusion out of the Galaxy increases and at $E_0 \cong 10^{17}$ eV the concentration of the galactic and supergalactic cosmic-ray components becomes approximately the same. At $E_0 > 10^{17}$ eV and up to $5 \cdot 10^{19}$ eV the supergalactic component predominates. The following difficulties are encountered in this model. The volume of the Local Group is $\left(\frac{10^6 \text{ light years}}{10^4 \text{ light years}}\right)^3$ times larger than that of the Galaxy. Assuming that the 16 galaxies of the Local Group behave relative to the generation of cosmic rays in the same way as our Galaxy, the concentration of cosmic rays in the Local Group ought to be almost 10^5 times lower than in our Galaxy, if the buildup factor is the same. In order to account for the second shift in the shape of the primary spectrum it must be assumed that the cosmic-ray concentration in the Local Group is only a few tens of times lower than in the Galaxy. Hence for the required intensity to be obtained, the buildup factor in the Local Group should be thousands of times larger than in the Galaxy. Obviously, given the size of the Local Group, the supergalactic cosmic rays of $E > 10^{19}$ eV cover distances over which the interaction with relict radiation has a decisive effect.

Let us consider a strictly galactic cosmic-ray model, in which besides the steadily generated energy spectrum with integral index $\gamma = 1.7$ there is an unsteady cosmic-ray component produced by the explosion of the galactic center and having the same integral spectrum index. Assuming the diffusion coefficient $\mathcal{D}(E) = \mathcal{D}_0 \left(\frac{E}{E_{cr} \cdot Z}\right)^{\alpha}$ at $E > E_{cr} \cdot Z$ and $\mathcal{D} = \mathcal{D}_0$ at $E < E_{cr} \cdot Z$,* we have for the concentration of the steady component

$$N_{G\,st} = \frac{Q_{st}(E)}{4\pi \mathcal{D}(E) \cdot r} \sim E^{-(\gamma+\alpha)}$$

and for the unsteady component

$$N_{nonst} = \frac{Q_{nonst}(E) \cdot r}{[4\pi \mathcal{D}(E) \cdot t]^{\frac{3}{2}}} e^{-\frac{r^2}{4\mathcal{D}(E)t}},$$

where $Q_{st}(E)\left[\frac{1}{sec}\right]$ is the strength of the steady-state source; r is the distance between the center of the Galaxy and the observer ($r = 3 \cdot 10^{22}$ cm);

* E_{cr} is the proton energy at which the diffusion coefficient starts to vary with E.

$Q_{\text{nonst}}(E)$ is the strength of the nonsteady-state source; τ is the time of action of the nonsteady-state source; t is the time elasped since the explosion ($t \gg \tau$).

Let us note that the above is a simplified expression for N_G which does not take into account fragmentation and interaction with interstellar matter or the spatial distribution of steady-state sources.

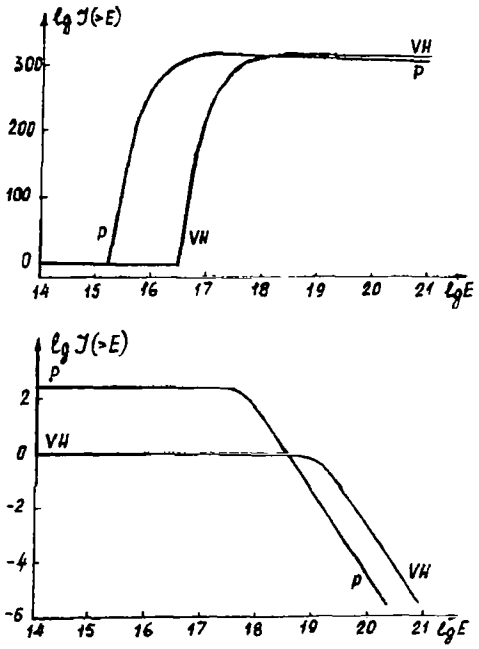

FIGURE 6. Differential and integral spectra of nonsteady-state cosmic rays:

P — for protons; VH — for very heavy nuclei ($\bar{z} = 25$).

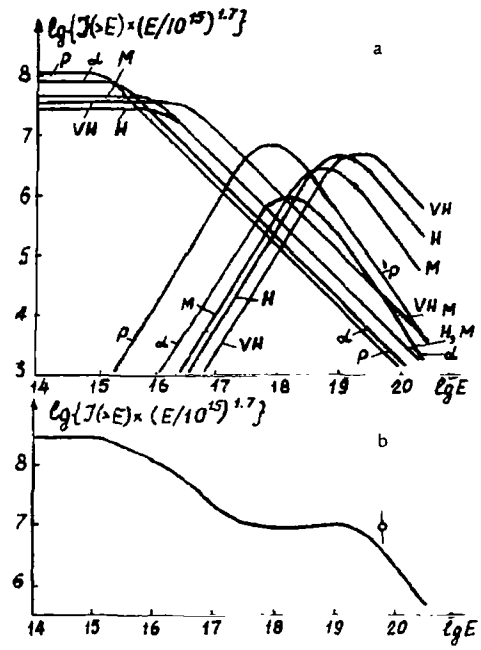

FIGURE 7. Partial integral energy spectra of steady-state and nonsteady-state origin (a), and combined integral energy spectrum of ultrahigh-energy primary cosmic radiation according to the model proposed in the present paper (b).

Excluding the fact of relict radiation, we should have that t in the expression for $N_{G\,\text{nonst}}$ should be less than 10^7 years. Setting $t = 10^6$ years $= 3 \cdot 10^{13}$ sec, $\alpha = 1$, $\tau = 3 \cdot 10^{22}$ cm, and $\mathcal{D}_0 = 10^{28}$ cm/sec, we find that the exponent $\frac{\tau^2}{4\mathcal{D}t}$ has an absolute value much larger than unity at $E \leq E_{cr}$ and decreases with increasing E. As a result the integral energy spectrum $N_{G\,\text{nonst}}$ may have in some energy range an even smaller index than $\gamma = 1.7$ (Figure 6). At sufficiently large E, for which $\frac{\tau^2}{4\mathcal{D}(E)t} \ll 1$, $N_{G\,\text{nonst}} \sim$ $\sim E^{-(\gamma + \frac{3}{2}\alpha)}$.

For nuclei with charge z, $E_{cr(z)} = E_{cr} \cdot z$. Therefore, the fraction of nuclei should appreciably decrease at $E \sim E_{cr}$ and remain small within the range of values of E in which $\frac{\tau^2}{4\mathcal{D}(E)t}$ for protons is larger than unity.

If $\frac{\tau^2}{4\mathcal{D}(E)t} < 1$ for protons, then for large E, on the other hand, the role of nuclei may significantly increase, since the condition $\frac{\tau^2}{4\mathcal{D}(E)t} \geq 1$ may still hold for nuclei. Figure 7 gives the calculation results on the partial spectra $N_{G\,nonst}$ for different Z, as well as the spectra $N_{G\,st}$ for different Z, and the combined primary-radiation energy spectrum $N_{G\,st}+N_{G\,nonst}$. The calculations were made on the basis of the following values of the relevant parameters: $\tau = 3\cdot10^{22}$ cm, $t = 3\cdot10^{13}$ sec, $\mathcal{D}_0 = 10^{28}$ cm^2/sec, $\alpha = 1$, and $\gamma = 1.7$. The distribution of Z for the steady-state component near the observer is taken from the values given in /14/ for the low-energy region. The distribution of Z at the source adopted for the nonsteady-state component, conforms to the one given in /14/ for the steady-state component.* We also note that at $\mathcal{D}_0 = 10^{28}$ cm^2/sec and $\alpha = 1$ the diffusion condition in magnetic fields $H \frac{3\mathcal{D}(E)}{c} \geq \rho$, where $\rho = \frac{E}{300H}$, is fulfilled for $H \sim (3-5)\cdot10^{-6}$ oersted at any E for which the fundamental diffusion approximation condition $\tau \gg \frac{3\mathcal{D}(E)}{c}$ still holds. This condition may be assumed to be valid at $E > 10^{19}$ eV only for heavy nuclei. But it is precisely the latter that make the main contribution to $N_{G\,nonst}$ at $E \geq 10^{19}$ eV. The above model thus accounts for the twofold shift in the shape of the primary energy spectrum and for the possible existence of cosmic rays of energy $\geq 3\cdot10^{19}$ eV.

In the model with a nonsteady-state galactic component, the anisotropy ratio δ at $E > 10^{17}$ eV is independent of the diffusion coefficient and equals $\delta = \frac{3}{2}\tau/ct = 5\cdot10^{-2}$. This value is consistent with the experimental data on the anisotropy of cosmic rays of energy $E > 10^{17}$ eV (see Figure 4). As regards the value of δ at $E < 10^{17}$ eV, it also fits the experimental data, despite the increase in δ with E ($\delta \sim E$ for $\alpha = 1$), if we take $\mathcal{D}_0 = 10^{28}$ cm^2/sec.

Calculations of σ_{N_e} (see Figure 5) were made for the chemical composition in accordance with the spectra in Figure 7. The obtained fluctuations display agreement with the distribution of Z considered in our model

Bibliography

1. Kulikov, G.V. and G.B. Khristiansen.— Nuovo cimento, Supplement to Vol. VIII, Ser. X, 2, 742. 1968.
2. Bradt, H., M.La Pointe, and S. Rappaport.— Proc. Int. Conf. Cosmic Rays, London, 2, 651. 1966.
3. Glavach, T., N.M. Nesterova, S.I. Nikol'skii, and V.A. Romakhin.— Trudy Vsesoyuznoi konferentsii po fizike kosmicheskikh luchei, Tashkent. 1968 (in print).
4. Solov'eva, V.I. Thesis. MGU. 1965.
5. Delvaille, J., P. Kendziorski, and K. Greisen.— J. Phys. Soc. Japan, Suppl. AIII, 17, 76. 1962.
6. Linsley, J.— International Conf. on C.R., Jaipur, 4, 77. 1963.

* Since our value of $t = 10^6$ years is two orders of magnitude smaller than the mean lifetime of the steady-state cosmic-ray component, we can assume that at $E < E_{cr}$ the distribution of Z for the nonsteady-state component near the observer and near the source is the same.

7. Watson, A.A.— First European Symposium on Cosmic Rays, Lodz. 3, 1968.
8. Suri, A.N. Thesis. University of Leeds. 1966.
9. Grigorov, N.L., V.E. Nesterov, I.D. Rapoport, I.A. Savenko, and G.A. Skuridin.— Proceedings of the Tenth International Conf. on Cosmic Rays, Part A, p.512. 1968.
10. Khristiansen, G.B.— Izvestiya AN SSSR, 29(10),1872. 1965.
11. Efimov, N.N., D.D. Krasil'nikov, S.I. Nikolskii, and F.K. Shamsutdinova.— Canadian Jour. of Physics, 46, 884. 1968.
12. Delvaille, J., F. Kendziorski, and K. Greisen.— Proceedings of the International Conference on Cosmic Rays. Moscow. 1959, Moskva, Izdatel'stvo AN SSSR, p.159. 1960.
13. Blake, P.R., J.D. Hollows, H.W. Hunter, R.J.O. Reid, R.M. Teanent, A.A. Watson, and J.G. Wilson.— Canadian J. of Phys., 46, 578. 1968.
14. Ginzburg, V.L. and S.I. Syrovatskii. Proiskhozhdenie kosmicheskikh luchei (Origin of Cosmic Rays).— Moskva, Izdatel'stvo AN SSSR. 1963.
15. Khristiansen, G.B., A.T. Abrosimov, I.F. Belyaeva, G.V. Kulikov, V.I. Solov'eva, and B.A. Khrenov.— Trudy Vsesoyuznoi konferentsii po kosmicheskim lucham. Tashkent. 1968 (in print).
16. Kalmykov, N.N. Thesis, MGU. 1965.
17. Adcock, C., J.F. de Beer, H. Oda, J. Wdowczyk, and A.W. Wolfendale.— J. Phys. (Proc. Phys. Soc.), Ser.2, 1, 82. 1968.
18. Greisen, K.— Phys. Rev. Lett., 16, 748. 1966.
19. Zatsepin, G.T. and V.A. Kuz'min.— Pis'ma v ZhETF, 4, 114. 1966.
20. Hillas, A.M.— Canadian J. of Phys., 46, S623. 1968.

L. Kh. Shatashvili

27-DAY COSMIC-RADIATION VARIATION FROM GROUND AND STRATOSPHERIC DATA (1966—1967)

The azimuthal asymmetry in the distribution of active formations can cause an asymmetric solar wind of magnetic inhomogeneities causing the 27-day modulation of the cosmic rays /1, 2/. The most interesting is the asymmetry caused by long-lived formations upon the sun (with a lifetime longer than several solar revolutions). In such cases it is relatively easy to study the structural properties of the solar wind. The analysis of the data on type-1 comet tails shows /3/ that, in principle, the solar wind can be asymmetric not only in azimuth, but also in the solar meridian. We shall investigate only the simpler case of an azimuthally asymmetric solar wind.

One of the main problems in contemporary interplanetary physics is the determination of the effective volume of the solar wind. The 27-day variation of the cosmic-ray intensity presents the possibility of studying the asymmetric part of the solar wind (it is possible that the solar wind is asymmetric in general).

During the period of the IGY there was probably a long period of asymmetry of the solar wind. It is this fact that can explain the presence of a long-lived 27-day wave ($\tau \sim 9-10$ solar revolutions) in the variation of the cosmic-ray intensity. Generally, the volume of the asymmetric solar wind of magnetic inhomogeneities is determined by the propagation time of the solar activity effects in the interplanetary medium. The main parameters are the solar wind velocity and the lag in the maximum in the 27-day oscillations of the cosmic-ray intensity relative to the 27-day variations of the solar activity m. The magnitude of the asymmetric solar wind depends mainly upon the precision with which m is determined. In /4, 5/ the harmonic coefficients of the mean daily neutron-component intensities N and the number of sunspots W were determined by a 27-day Fourier analysis. From the lags in the effects of W in the harmonic coefficients of the 27-day Fourier analysis of the parameter N the effective volumes of the solar wind were determined for different periods of the solar activity. During the period of maximum solar activity $m \sim 7$ solar revolutions and decreases appreciably with decreasing solar activity /4, 5/. If first the Chree diagrams (Figure 1) are constructed and m is determined from the lag in the 27-day cosmic-ray variation with respect to the corresponding parameters of the solar activity, the value of m for periods of maximum solar activity turns out slightly lower /6/.

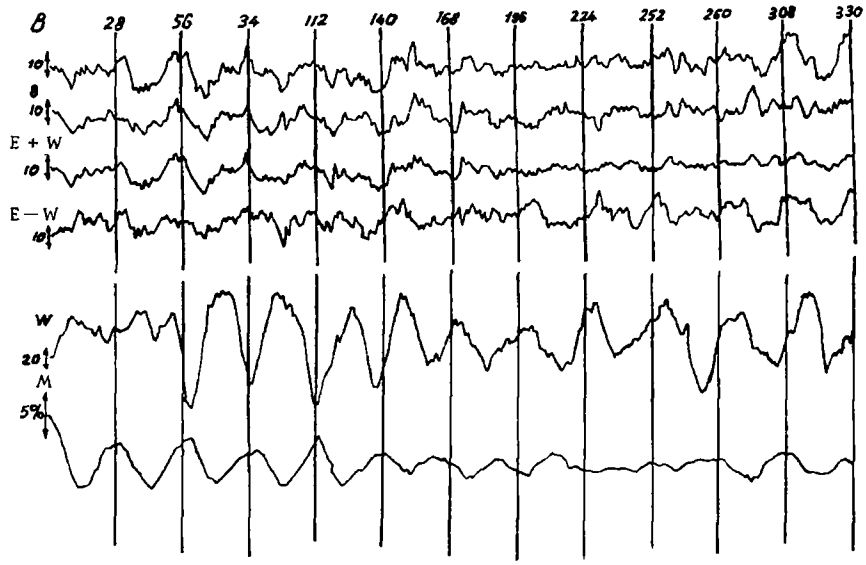

FIGURE 1. The 27-day diagrams of the neutron cosmic-radiation component N (according to data obtained at Climax station), the number of sunspots W and the intensity of the green line $\lambda = 5303$ Å in the solar corona, constructed as differences of curves, one of which was obtained by the method of combining Chree periods according to "0" days (first four months of the IGY) of the maxima N_p^{max}, while the second was obtained by combining the Chree periods according to the "0" days (first four months of the IGY) of the minima N_p^{min} of the planetary intensity of the neutron cosmic-radiation component for the periods of the IGY with the most pronounced effect of the solar rotation upon the cosmic radiation.

In Figure 1 are shown the 27-day variation (according to IGY data) of the number of sunspots W, the neutron cosmic-ray component N and the intensity of the green line ($\lambda = 5303$ Å) in the solar corona for the east (E) and west (W) sides of the solar disk. Also the sum (E+W) and difference (E−W) of the 27-day Chree diagrams are given (for the same period); these were derived from the corresponding curves for the east and west sides. All the curves for E, W, E+W, E−W are obtained by combining the Chree periods solely according to the "0" days of the planetary neutron cosmic-ray component intensity /1, 7/. From Figure 1 it can be seen that if m is determined from the time of vanishing (or the minimum in the amplitude) of the 27-day oscillations of the various parameters, then $m \geq 2$ solar revolutions (if m is measured with respect to the corresponding parameters of W) and $m \geq 1$ solar revolutions (if m is measured with respect to the 27-day variation of the corona radiation $\lambda = 5303$ Å). By comparing the diagrams of the corona radiation with the cosmic-ray diagrams, the best correlation is obtained if the diagram (E+W), i.e., that most closely corresponding to the integral characteristic of the corona radiation, and the diagram of N are taken as a basis. The main conclusion is that each method gives $m \neq 0$ ($m \geq 1$). It should be mentioned that in /8, 9, 10/* the lag times were determined over a period of 3−4 days (less than one solar revolution). In our opinion $m \geq 1$ solar revolutions.

The period of the IGY was investigated quite thoroughly. The main objective of our investigation was to examine the little investigated period of the rise

* In /8, 9, 10/ the 27-day variation of the cosmic radiation was compared mainly with the indices of the geomagnetic activity.

in the 20th cycle of the solar activity. The analysis shows that during this period, as during the IGY, there appears a distinct asymmetry (with a long lifetime τ) in the distribution of the active formations upon the sun and, consequently, in the 27-day oscillations of the cosmic radiation of long duration caused by them. Therefore, a comparison of the results of these two periods is of great interest. A detailed analysis of the data on the relations between the sun and the earth during the rise in the solar activity for the 20th cycle has not yet been performed. We shall discuss only some preliminary results. As was mentioned already before, in the first half of 1967 there appeared a fairly stable 27-day wave in the cosmic-radiation intensity (the possibility of such an investigation was noted by G.A. Bazilevskaya et al., private communication). We have studied the neutron data from various Soviet stations and the high-altitude Climax station (USA) for the period from November 1966 to September 1967 (Table 1). The use of the data obtained at Climax in the analysis of the 27-day cosmic-ray variations is very convenient, since this station has been operating regularly for a long time. Therefore, a comparison of the results for different periods of the solar activity can be readily effected.

TABLE 1. Neutron data of various stations

Station		Type of observation	Rigidity cutoff, GV	Period
Apatity	(USSR)	N_p	0.5	II
Yakutsk	(USSR)	N_p	1.38	II
Alma-Ata	(USSR)	N_p	6.6	II
Tbilisi	(USSR)	N_p, J_{pt}	6.9	II
Climax	(USA)	N_p	3.08	I, II
Dolgoprudnaya	(USSR)	C	2.2	II
Mirnyi	(USSR)	C	0.17	I

Remark: N_p – data on the neutron component corrected for the barometric effect; J_{pt} – data on the penetrating component corrected for the barometric and temperature effects; S – data on stratospheric intensity (at the altitude of the maximum in the cosmic radiation). Period I: July 1957 to September 1958; period II: November 1966 to September 1967.

The main method for finding the 27-day variations in the cosmic-radiation intensity was the method of combining Chree periods /11/. This method is very effective for the construction of similar diagrams of the asymmetry in the active formations upon the sun for periods with long lifetimes. In similar cases when choosing the "0" days for the Chree diagrams it is extremely effective to choose the "0" days according to the data on the planetary cosmic-radiation intensity. Since not all stations have been operating continuously, the selection of the "0" planetary cosmic-ray intensity using the data from all the stations is much more complicated. However, in many cases as a first approximation it suffices to use the "0" days determined from data of only several stations recording the cosmic-ray intensity, since in a fairly wide cosmic-ray energy range the "0" days determined from the data of several continuously recording stations having different cutoff thresholds almost coincide with the "0" days of the planetary cosmic-ray intensity. The "0" days were determined from

the data of the Apatity, Alma-Ata, Yakutsk and Climax stations. From these days (for brevity we shall call them planetary "0" days) (Table 2) the 27-day diagrams of the various parameters of the solar activity and the cosmic radiation were constructed by combining Chree periods. From the data of Table 2 27-day diagrams were constructed for those cosmic-radiation variables, which initially seemed insufficiently continuous /7, 12/. In Figures 2, 3, 4 and 5 are shown the corresponding 27-day Chree diagrams.

TABLE 2. Planetary "0" days according to data of three Soviet stations which record the neutron cosmic-ray component

Time	"0" days of the maxima N_p^{max}	"0" days of the minima N_p^{min}
February	21, 25, 26, 27, 28	7, 8, 9, 16, 17
March	23, 24, 25, 26, 27	7, 8, 9, 10, 11
April	1, 9, 10, 11, 16	3, 4, 5, 6, 30
May	18, 19, 20, 21, 22	9, 10, 26, 27, 28

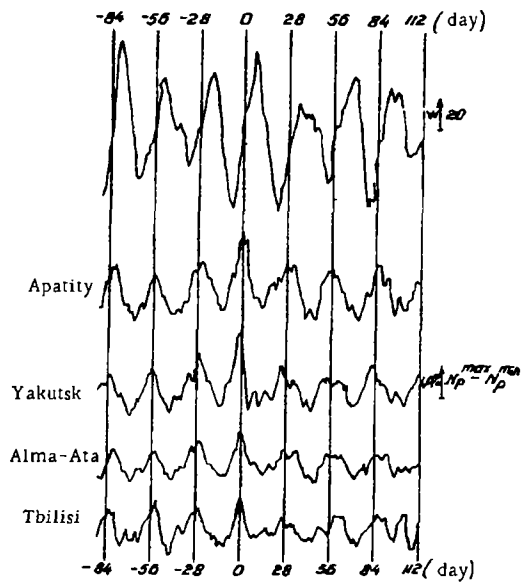

FIGURE 2. The resulting curves (period II) obtained as differences of the curves calculated by combining periods according to the "0" days of the maxima N_p^{max} and minima N_p^{min} of the intensity of the neutron cosmic-radiation component based on the data of the Apatity, Yakutsk, Alma-Ata and Tbilisi stations and the planetary numbers of the sunspots W.

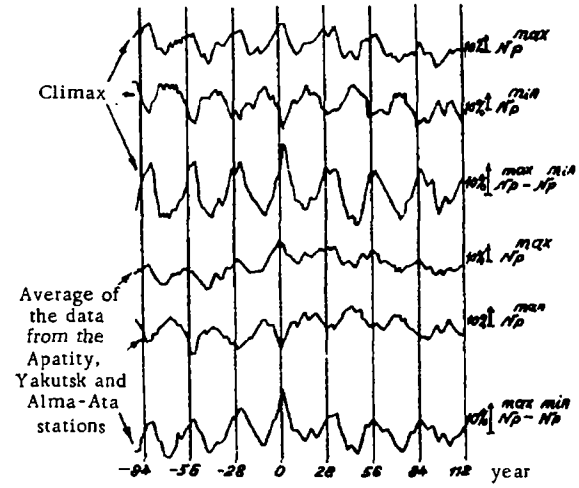

FIGURE 3. The resulting curves (period II) calculated by combining Chree periods according to the planetary "0" days of the maxima N_p^{max} and minima N_p^{min}, and also the curves of $N_p^{max}-N_p^{min}$, based on the data from the Apatity, Yakutsk and Alma-Ata stations (USSR) and separately for the data from the Climax station (USA).

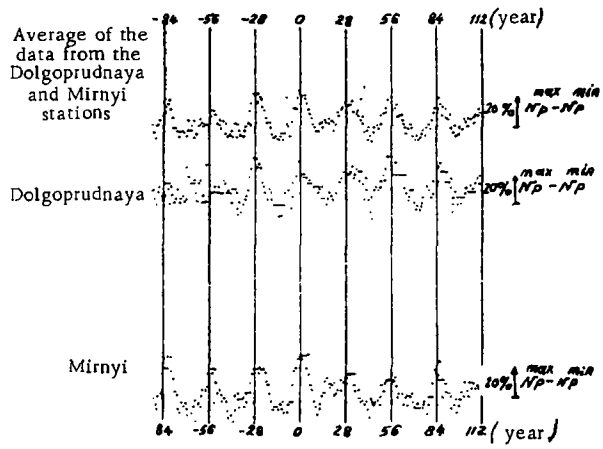
Average of the data from the Dolgoprudnaya and Mirnyi stations
Dolgoprudnaya
Mirnyi
-84 -56 -28 0 28 56 84 112 (year)
84 -56 -28 0 28 56 84 112 (year)

FIGURE 4. The resulting curves (period II) calculated by combining Chree periods according to the planetary "0" days of the maxima N_p^{max} and minima N_p^{min} of the intensity of the neutron component, and the corresponding difference curves $N_p^{max} - N_p^{min}$ based on stratospheric data on the cosmic radiation.

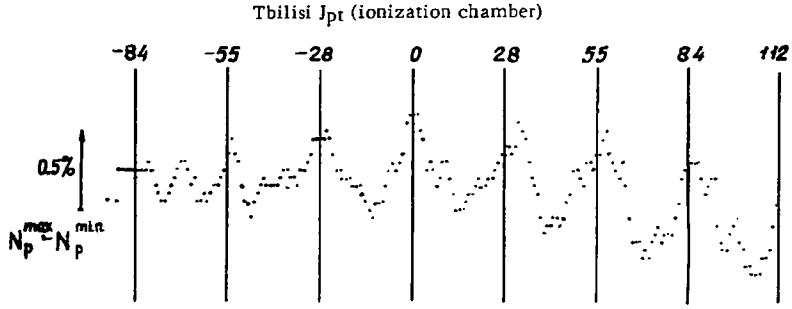

FIGURE 5. The 27-day variations of the penetrating component of the cosmic radiation J_{pt} (period II) derived from the difference of curves calculated by combining Chree periods according to planetary "0" days of N_p^{max} and N_p^{min} of the neutron-component intensity based on the data from the ionization chamber of the Tbilisi station and corrected for barometric and temperature effects.

From the above-described investigation the following conclusions can be made:

1. In the investigated period of a rise in the solar activity one can clearly detect 27-day variations both in the number of sunspots and in all components of the cosmic radiation that were analyzed.
2. The 27-day variations of the above parameters must be correlated with long-lived active formations on the sun.
3. From the latitude dependence of the amplitudes of 27-day variations of the neutron-component intensity, considering the 27-day diagrams of the stratospheric data, and also of the penetrating component of the cosmic radiation corrected for barometric and temperature effects, we can conclude that the spectrum of the 27-day variations of the cosmic radiation both for the period of the IGY (maximum of solar activity) and for the period of the rise in solar activity must be quite rigid.

Bibliography

1. Dorman, L.I. and L.Kh. Shatashvili.— In: Sbornik "Kosmicheskie luchi," "Nauka," No. 5:82, Moskva. 1963.
2. Dorman, L.I. and L.Kh. Shatashvili.— Geomagnetizm i aeronomiya, 3:979. 1963.
3. Brandt, J.C.— Astrophys. J., 147:201. 1967.
4. Alaniya, M.V., L.Kh. Shatashvili, and L.I. Dorman.— Canad. J. Phys., 46, S970. 1968.
5. Alaniya, M.V., O.G. Rogava, and L.Kh. Shatashvili.—Izvestiya AN SSSR, Seriya Fiz., 32, 1939. 1968.
6. Alaniya, M.V. and L.Kh. Shatashvili.— Synopses of Reports at the All-Union Conference on Physics of Cosmic Rays, Tashkent. 1968, Izd. FIAN, p.41. Moskva. 1968.
7. Alaniya, M.V. and L.Kh. Shatashvili.— Trudy V vsesoyuznoi ezhegodnoi zimnei shkoly po kosmofizike, Izd. Kol'skogo filiala AN SSSR, Apatity, p.294. 1968.

8. Kane, R.P.— Phys. Rev., 98:130. 1955.
9. Herden, T.S. and T. Thambyaphilai.— Phil. Mag., 46:1238. 1955.
10. Simpson, J.A.— Phys. Rev., 94:1017. 1954.
11. Chree, C.— Philos. J. trans., A213, 245. 1913; A212m, 76. 1913.
12. Shatashvili, L.Kh.— Trudy V Vsesoyuznoi ezhegodnoi zimnei shkoly po kosmofizike, Izd. Kol'skogo filiala AN SSSR, Apatity, p.281. 1968.

K.K. Fedchenko

MEASUREMENT OF THE COSMIC-RAY ANISOTROPY DURING A SOLAR CYCLE

Observations show that the amplitude and phase characteristics of the cosmic-ray anisotropy do not remain constant, but undergo both periodic as well as irregular variations. These variations in the anisotropy beyond the atmosphere and the geomagnetic field are completely determined by the anisotropy of the solar wind and depend both on its velocity and on the intensity and structure of the magnetic inhomogeneities. The aim of the present article is to study the variations in the cosmic-radiation anisotropy during a complete solar cycle.

The data used in this investigation came from the neutron-intensity data for the period 1958—1968 obtained at the two Soviet high-latitude stations Apatity and the Kheis Island, having narrow acceptance cones and enabling the observation of the fine structure of the diurnal variation.

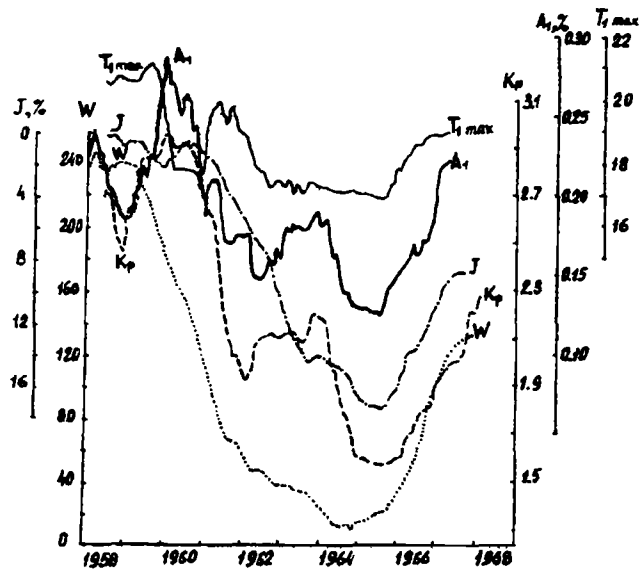

FIGURE 1. Changes in the amplitude and time of the maximum of the diurnal variation during a solar cycle:

A_1 — amplitude of the first harmonic; T_{1max} — time of the maximum; J — cosmic-ray intensity; W — Wolf's relative numbers; K_p — Bartels' planetary geomagnetic indices.

We shall first investigate the long-period changes in the diurnal cosmic-radiation variation during the solar cycle of 1958 – 1968. The data on the diurnal variation were averaged for each month of the above-mentioned period and were then analyzed by means of harmonic analysis, the phases being corrected for the deviations in the geomagnetic field /1/. The amplitude and phase characteristics of the diurnal variation thus obtained were smoothed by using a sliding average with a 12-month period. The annual means of the amplitude (A_1) and the phase (T_{1max}) of the first harmonic of the diurnal variation at the Kheis Island centered around the corresponding months are shown in Figure 1. Similar curves were also derived for the Apatity data, but are not shown in the figure in order to preserve clarity. In the same figure are also shown the smoothed annual means of the cosmic-ray intensity at Kheis Island (J), the solar activity (Wolf's relative numbers W) and the geomagnetic activity (Bartels' planetary geomagnetic indices K_p).

As can be seen from Figure 1, the changes in the amplitude of the diurnal variation during the complete solar cycle have a positive correlation with the changes in the solar and geomagnetic activity, and it seems that the correlation with the geomagnetic activity is stronger than with the solar activity, which indicates a less direct relation with the latter. There is a systematic shift in the phase of the diurnal variation toward earlier hours during the solar activity minimum. Similar results were also obtained by analyzing the data for the period 1933 – 1954 /2, 3/.

Thus the true anisotropy beyond the atmosphere and the geomagnetic field is a sensitive characteristic of the conditions in the interplanetary medium, and its variations with solar activity provide information on the corresponding changes in these conditions.

The 27-day modulation of the diurnal variation of the cosmic-ray intensity was investigated separately for the periods of maximum (1958) and minimum (1964) solar activity. The harmonic-analysis data of the diurnal variations of the neutron intensity for each day from the Apatity and Kheis Island stations were used for this purpose. The distribution of the first-harmonic amplitudes of the diurnal variation is shown in Figure 2 for 1958 and 1964 on the basis of data obtained on Kheis Island; the abscissa is the number of solar revolutions. Similar results were derived from the data gathered at Apatity station and, consequently, are not shown here.

It can be seen from Figure 2 that days having large amplitudes are grouped together, which indicates a tendency of a 27-day repetition of the diurnal variations; this tendency is more clearly marked for the period of the solar maximum (1958) than during the solar minimum (1964). The same correlation exists between the solar activity and the 27-day variation in the cosmic-ray intensity /4, 5/. The results obtained here indicate that there is a 27-day modulation of the cosmic-ray anisotropy both during the maximum and minimum of the solar activity and supports the assumption /6/ that this effect is related to the 27-day variation of the cosmic-ray intensity. This effect, when investigated in more detail, can yield valuable information on the azimuthal asymmetry of the solar wind and its dependence on solar activity.

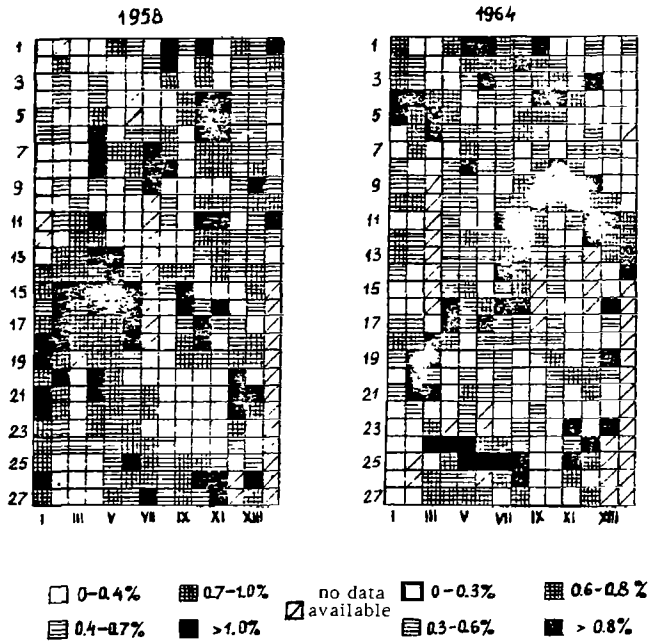

FIGURE 2. The 27-day modulation of the amplitude of the diurnal variation determined from data obtained on Kheis Island for 1958 and 1964.

In Figure 3 are shown the frequency distributions of the amplitudes of the first and second harmonics and phases of the diurnal variation of the cosmic-ray intensity determined from data obtained on Kheis Island for 1958 and 1964. Similar results were also obtained from the data of Apatity station and are therefore not shown here. It can be seen from Figure 3 that the most probable values of the amplitude of the first harmonic of the diurnal variation in 1958 and 1964 are 0.5 and 0.3%, respectively, and 0.3% for the second harmonic amplitude both during the minimum and maximum of the solar activity. The maximum of the anisotropy, corrected for atmospheric and geomagnetic effects, occurs at 18 − 20 hr local time, the maximum being shifted towards earlier times when going over from a high solar activity to a low one. This result agrees with the assumption of a diffusion mechanism causing the cosmic-ray anisotropy /7/.

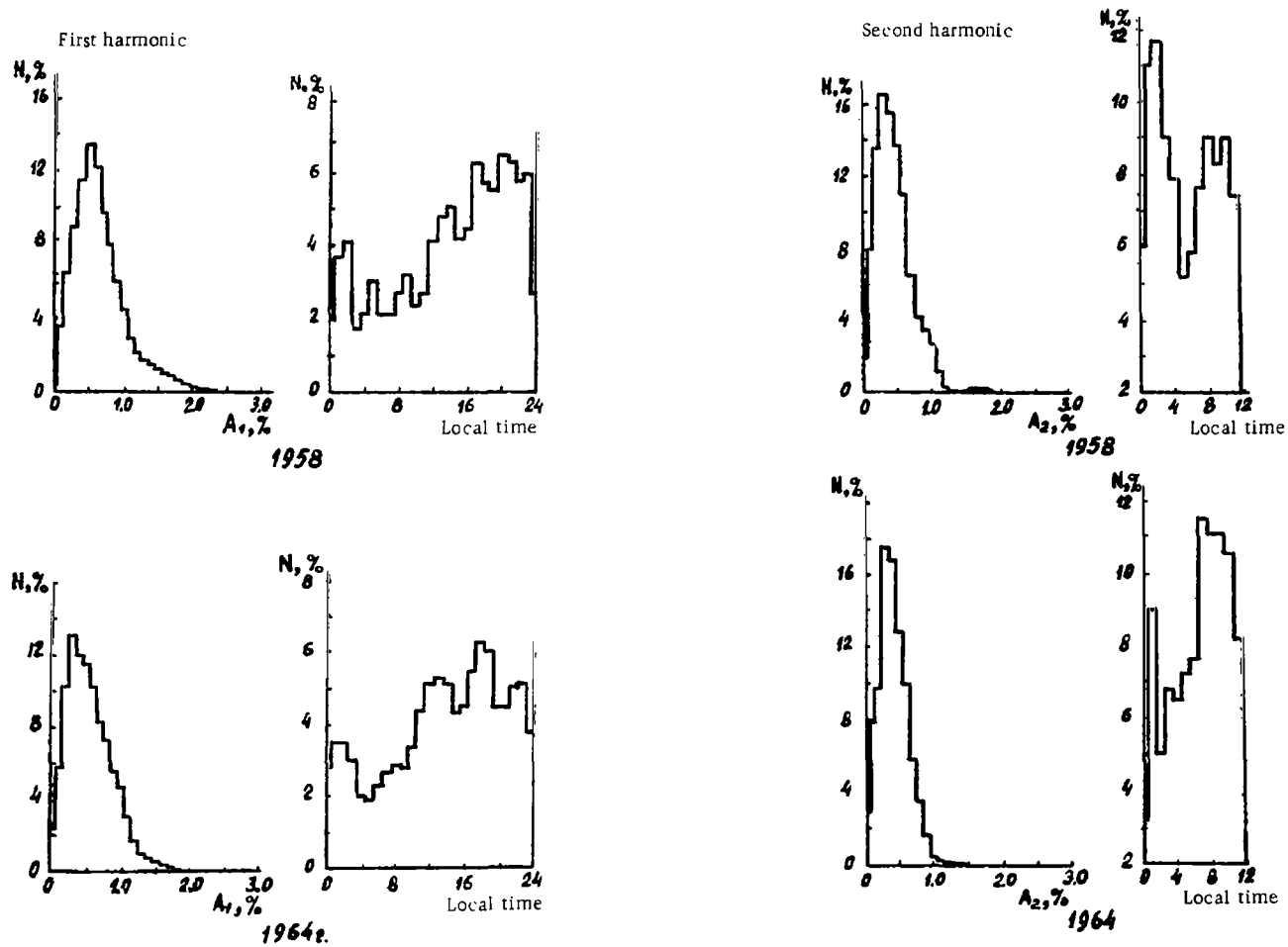

FIGURE 3. Frequency distribution of the amplitudes and phases of the diurnal (a) and semi-diurnal (b) variation based on data from Kheis Island for 1958 and 1964.

Bibliography

1. McCracken, K.I., U.R. Rao, B.C. Fowler, M.A. Shea, and D.F. Smart. Cosmic Ray Tables. — IQSY Instruction Manual No. 10. London. 1965.
2. Venkatesan, D. and A. Dattner. — Tellus, 11, 116. 1959.
3. Forbush, S.E. and D. Venkatesan. — J. Geophys. Res., 65, 2213. 1960.
4. Dorman, L.I. Variatsii kosmicheskikh luchei (Cosmic-Ray Variations). — Moskva, Gostekhizdat. 1957.
5. Dorman, L.I. Variatsii kosmicheskikh luchei i issledovanie kosmosa (Cosmic-Ray Variations and Space Research). — Moskva, Izdatel'stvo AN SSSR. 1964.
6. Dorman, L.I. — Izvestiya AN SSSR, Seriya Fiziki, 31(8):1333. 1967.
7. Krymskii, G.F. — Geomagnetizm i aeronomiya, 4(6):977. 1964.

Yu. I. Stozhkov

THE 11-YEAR INTENSITY MODULATION OF GALACTIC COSMIC RAYS AND THE HELIOGRAPHIC DISTRIBUTION OF SUNSPOTS

A detailed investigation of the influence of the 11-year solar activity cycle upon the cosmic radiation has shown that the cosmic-ray intensity is different at the same level of solar activity. This can be seen in Figure 1, where the variations in the relative cosmic-ray flux during May 1968 (the maximum cosmic-ray intensity at the end of the 19th and beginning of the 20th solar activity cycle) are given. It can be seen that the value of $\Delta N/N$ on the rising branches of the solar activity curves differs considerable from that on the falling branches.

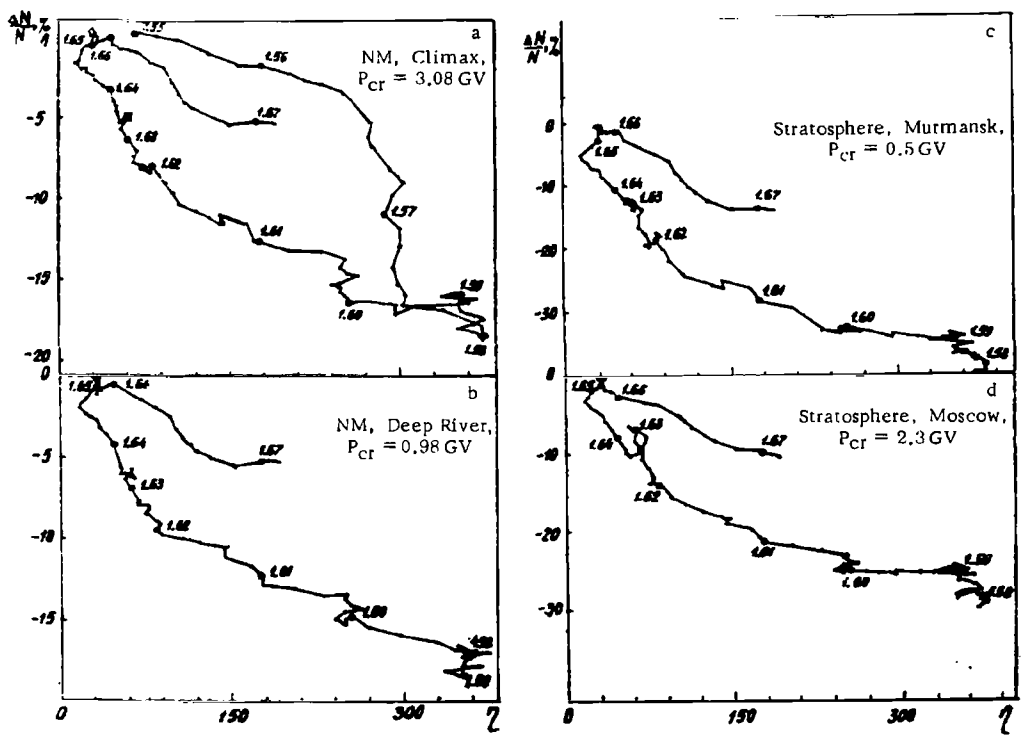

FIGURE 1. Cosmic-ray intensity $\Delta N/N$ as a function of the monthly average of the number of sunspot groups η:

a, b — neutron monitor data at Climax and Deep River; c, d — stratospheric data at Murmansk and Moscow; P_{cr} — magnetic rigidity.

If we consider the fact that the sunspots of each new cycle appear first at high latitude ($\zeta \sim 25°$) and then move gradually towards the sun's equator ($\zeta \sim 10°$) /1/, it can be assumed that the cosmic-ray intensity depends not only on the number of sunspot groups, but also on their average heliolatitude $\bar{\varphi}=\sum_{i=1}^{n}\varphi_i/\eta$, where ζ_i is the latitude of an individual group. The variation of the average heliolatitude of the sunspots during a solar cycle is shown in Figure 2. The values of η and $\bar{\zeta}$ were smoothed with a period of 6 months. It can be seen that the average heliolatitude $\bar{\zeta}$ is distinctly different during different parts of the solar cycle at the same level of the solar activity. For example, during the three periods: January, 1961 to April, 1964; January, 1965 to January, 1966 and January 1955 to January 1956, the value of $\bar{\zeta}$ was $\sim 10°$, $\sim 22°$ and $\sim 25°$, respectively.

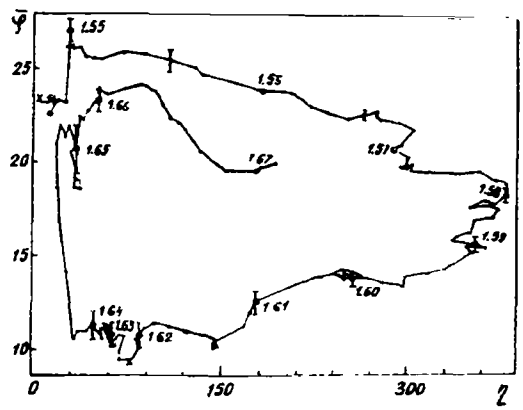

FIGURE 2. Average heliolatitude as a function of η.

From a comparison of Figures 1 and 2 it can be seen that for the same value of η the value of $|\Delta N/N|$ increases with a decrease in the average heliolatitude of the sunspots. For example, during 1967 and 1961, η was approximately 180, the ratio $(\frac{\Delta N}{N})_{61}/(\frac{\Delta N}{N})_{67} \cong 2$ and $\bar{\zeta}$ was $\sim 12°$ in 1961 and $\sim 20°$ in 1967. It thus follows that the modulation of galactic cosmic rays increases as the sunspots move closer to the equator. Since the increase in the number of sunspot groups η and the decrease in their average heliolatitude $\bar{\zeta}$ act in the same way upon the modulation of the cosmic radiation, i.e., they effect an increase in $|\Delta N/N|$, the similarity of the curves in Figures 1 and 2 is especially distinct along the rising branches of the solar activity cycle (1955 – 1957, 1966 – 1967). On the falling branch of the solar activity cycle the decrease of η and $\bar{\zeta}$ act in opposite directions, and, consequently, there is less similarity between the curves. The lack of a loop in Figure 1 for $\Delta N/N$ for $\eta \geq 300$, in spite of the existence of such a loop in ζ in Figure 2, is probably due to the influence of frequent Forbush effects during this period, which have distorted the cosmic-ray intensity modulation which is due to the general solar activity.

Thus, from the comparison of Figures 1 and 2 it can be assumed that the cosmic-ray intensity is a function of two solar activity parameters, i.e., $N = N(\eta, \bar{\zeta})$. (The possibility of such a dependence was suggested for the first time by Sarabai and Subramanian /2/, where this assumption was used to explain the amplitudes and phases of the diurnal variations during the solar activity cycle). The dependence on $\bar{\zeta}$ can be due to the small angular dimensions of the particle fluxes ejected from the active zones upon the sun. This assumption can be checked by using the oscillations of the Earth by $\pm 7°$ relative to the sun's equatorial plane during one year. The differences in the cosmic-ray intensity in the stratosphere when the Earth was above and below this plane can be seen from the data summarized in the table. The intensities are compared during periods when the number of sunspot groups and their average latitude in the northern hemisphere are equal, and much larger than in the southern hemisphere. It can be seen from the table that in the three cases given the effect is not significant, $\Delta N/N \leqslant +0.1\%/\text{deg}$. At the same time the variation of the heliolatitude gives $|\Delta N/N| \geqslant 1\%/\text{deg}$. Therefore, the dependence of the cosmic-ray intensity on the heliolatitude of the sunspots is not due to the narrowness of the particle fluxes, but probably due to the fact that sunspots at higher latitudes are less effective in modulating the cosmic radiation. Since the cosmic-ray modulation depends on the propagation speed of the magnetic inhomogeneities u and their density ρ in the interplanetary medium, the dependence of N on $\bar{\zeta}$ leads to a dependence of u and ρ on $\bar{\zeta}$.

Cosmic-ray intensities in the stratosphere

Observation date	Number of sunspot groups over the whole disk, η	Number of sunspot groups in the northern hemisphere, η_n	Average heliolatitude of the sunspot groups in the northern hemisphere. φ_n	Number of sunspot groups in the southern hemisphere, η_s	Average heliolatitude of the sunspot groups in the southern hemisphere. φ_s	Inclination of the Earth relative to the sun's equatorial plane, deg.	Intensity at the maximum, stratosphere, Murmansk, single counter, N_{max}	$\Delta N/N$, %/deg
Nov.1959	256	200	14.7	56	12.9	+2.5	2274 ± 12	0.00 ± 0.10
Mar.1960	236	160	13.3	76	14.5	−7	2275 ± 18	
Feb.1963	62	47	9.1	15	15.5	−6.5	2936 ± 27	-0.09 ± 0.11
Nov.1963	64	57	7.7	7	14.3	+4.5	2910 ± 23	
Feb.1967	218	150	18.3	68	21	−6.5	2794 ± 20	-0.10 ± 0.06
Aug.1967	223	140	18.9	83	24	+6.5	2766 ± 7	

Secondary variations of the cosmic radiation $\Delta N/N$ are related to the variations in the primary spectrum $\frac{\Delta D}{D}(p)$ incident upon the atmosphere in the following way /3/:

$$\frac{\Delta N}{N} = \int_{p_{cr}}^{\infty} \frac{\Delta \mathcal{D}}{\mathcal{D}}(p)\, W(p)\, dp,$$

where W(p) is the coefficient relating $\Delta D/D$ and $\Delta N/N$.

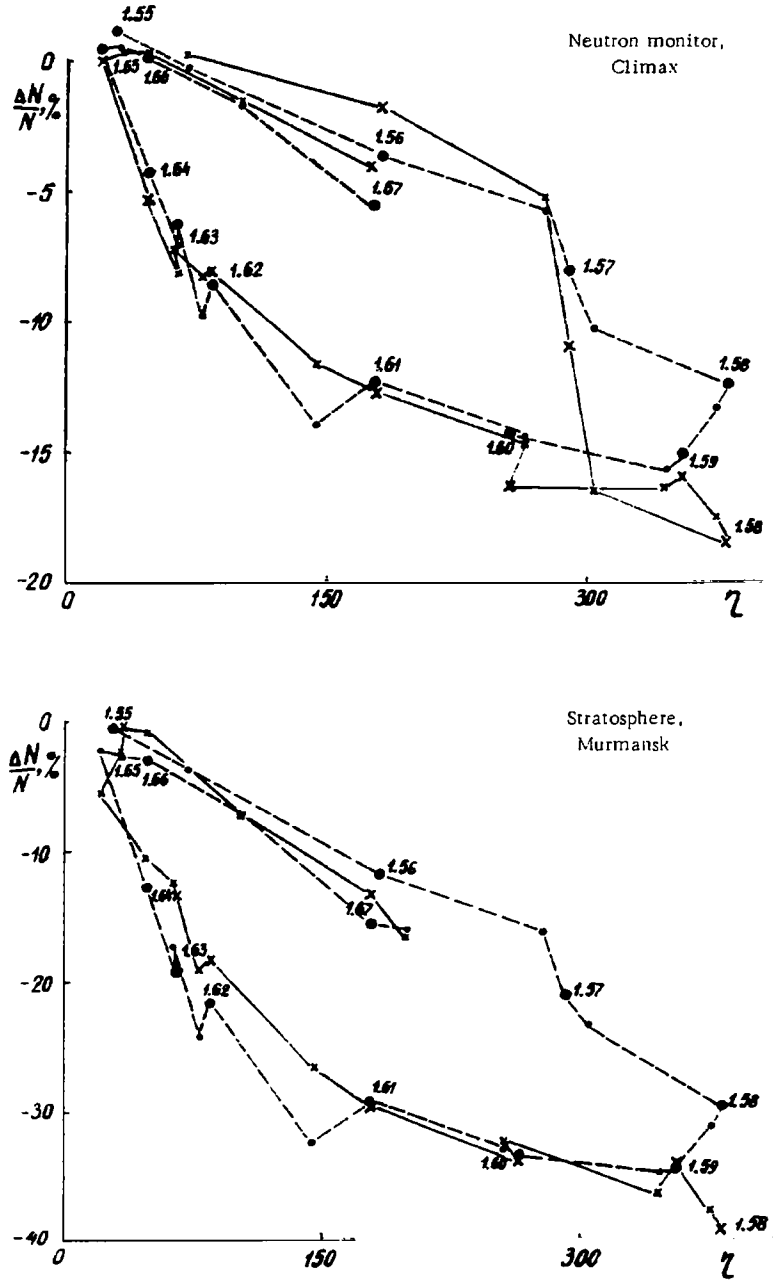

FIGURE 3. ΔN/N as a function of solar activity:

●— calculation, x — experiment.

Since the shape of the spectrum $\Delta D/D$ hardly varies during the solar cycle /4/ then, applying the mean-value theorem and using $\int_{P_{cr}}^{\infty} W(p)dp = 1$, we can write $\Delta N/N = \Delta D/D(\bar{p})$.

Thus, the observed secondary variations of the cosmic-ray intensity are directly related to the variation of the primary radiation. According to Parker's model of a spherically symmetric diffusion of cosmic rays, $\Delta N/N = \exp(-\psi) - 1$. The dependence of the modulation parameter ψ on the solar activity will be written as: $\psi = A \cdot \eta^{\alpha} \zeta^{-\beta}$. We shall separate the effects in the cosmic radiation caused by independent changes of η and ζ. It can be seen in Figure 2 that from March 1961 to October 1964 the number of sunspot groups changed from 150 to 40, while their heliolatitude remained almost constant ($\bar{\zeta} \cong 9 - 12°$). A similar situation occurred during 1955 – 1956, when r increased from 70 to 170, and $\bar{\zeta}$ remained almost constant ($23° - 26°$). These periods were used in order to derive the functional dependence of $\Delta N/N$ on η and $\bar{\zeta}$. Within experimental errors the values of α and β are the same for the cosmic-ray intensities measured in the stratosphere and those measured by a neutron monitor: $\alpha = 0.8$, $\beta = 1.5$. The constant A is equal to 0.3 for the stratosphere (Murmansk, single counter, $P_{cr} = 0.5$ GV) and 0.13 for the Climax neutron monitor data. The value $\alpha = 0.8$ agrees with the value determined in /5/. In Figure 3 are shown the experimental and computed values of $\Delta N/N$ as a function of η for the stratosphere (Murmansk) and for a neturon monitor (Climax). There exists satisfactory agreement between the calculations and experiment.

Taking into account the dependence of the cosmic-ray intensity on the number of sunspot groups and their average heliolatitude enables one to explain the nonunique relation between $\Delta N/N$ and the solar activity, the so-called phenomenon of hysteresis in the cosmic radiation. The dependence of the cosmic-ray intensity on the heliolatitude of the sunspots indicates that changes occur in the properties of the solar particle fluxes depending on their heliolatitude. Since the change in the number of sunspot groups and their average heliolatitude follow the same trend during the falling branches of different solar activity cycles /1/, one can expect that during the falling branch of the 20th solar activity cycle the dpendence of $\Delta N/N$ on η and ζ will be the same as during the 19th cycle.

The author would like to thank Dr. A. N. Charakhch'yan, and T. N. Charakhch'yan and G. A. Bazilevskaya for their useful advice and their interest in this study.

Bibliography

1. de Jager, C. Structure and Dynamics of the Solar Atmosphere. — In: Handbuch der Physik, S. Flügge, ed., 52, Springer Verlag, Berlin, Göttingen, Heidelberg. 1959.
2. Sarabai, V. and G. Subramanian. — Proc. Ninth Intern. Conf. on Cosmic Rays, p. 170, London. 1965.
3. Dorman, L. I. Variatsii kosmicheskikh luchei (Cosmic-Ray Variations). — Moskva, Gostekhizdat. 1957.
4. Stozhkov, Yu. I. and T. N. Charakhch'yan. — Geomagnetizm i aeronomiya, 8, 625. 1968.
5. Charakhch'yan, A. N. and T. N. Charakhch'yan. — Geomagnetizm i aeronomiya, 6, 486. 1966.

A. G. Zusmanovich, E. V. Kolomeets and Yu. A. Shakhova

THE MODULATION OF GALACTIC COSMIC RAYS

A large amount of data has been accumulated on the intensity of galactic cosmic rays during different periods of the solar activity cycle (sea-level data as well as data from measurements carried out in the upper atmosphere). The energy distribution of the particles has been measured quite well over a wide energy interval. In Figure 1 are shown the differential energy spectra of protons and α-particles for different periods of the solar activity /1/. In order to study the modulation effects upon the intensity of the cosmic radiation one has to know their relation with the solar activity.

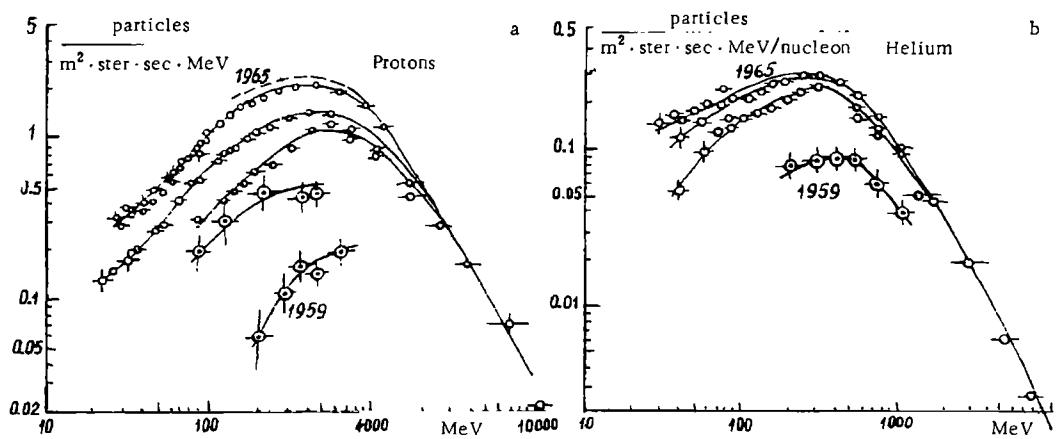

FIGURE 1. Differential energy spectra of protons and helium nuclei.

In Figure 2 are shown the variations in the cosmic-ray intensity (sea-level data), number of sunspots, radio emission from the sun and the radiation intensity of the corona (λ= 5303 Å) for the period 1964—1966 close to the minimum of the solar activity. The minimum in the number of sunspots occurred during August—September 1964, and the minimum in the corona radiation during March 1965. The intensity of the cosmic rays reached a maximum in April—May 1965. Thus, the cosmic-ray intensity lags behind the number of sunspots by about 10 months, and behind

the corona-radiation intensity by about 1 — 2 months. It was found /2 — 4/ that the experimental data are best described by the following modulation function $n(r) = n_0 \exp(-\frac{K}{R\beta})$, where K is the modulation depth, R is the particle's rigidity and β its velocity.

It has been shown /2, 4, 5/ that K = 0.3 — 0.6 for 1965 and that $\Delta K = 1$ for the period 1957 — 1965 /5/.

Using the proton differential spectrum for 1965 /6/, and the energy spectra of protons and helium nuclei /7/ for the period of the minimum in the cosmic-ray intensity according to sea-level data (April — May, 1965), we determined the values of K. In the first case /6/ K = 0.57, in the second case /7/ for protons below 2 GeV, K = 0.47, and for helium nuclei below 2 GeV, K = 0.22.

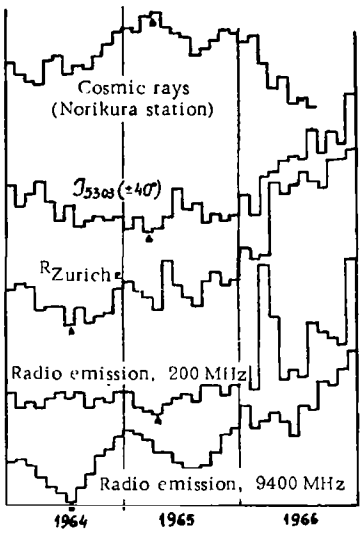

FIGURE 2. Variation in the cosmic-ray intensity and the solar activity during 1964 — 1966.

To calculate the relative change in K during the period 1959 — 1965 the data of Figure 1 and of /8 — 10/ were used. It was found that for the differential spectra of protons and helium nuclei $\Delta K = 1.9 \pm 0.1$. Lockwood and Webber /11/, using sea-level data, obtained $\Delta K \cong 2$ for the period 1958 — 1965. Consequently, from our results and those of other authors, K = 0.3 — 0.6 near the minimum of solar activity in 1965 and $\Delta K = 2$ from the maximum to the minimum of the last cycle of the solar activity. In /5, 12/ are given the values of the relative radial gradient δ of the cosmic-ray intensity in interplanetary space. Knowing K and δ, we can determine the size of the modulation region of the galactic cosmic rays. In /13, 14/ the energy losses of particles above 2 GeV were neglected while solving the diffusion equations of the galactic cosmic rays in the interplanetary medium. Thus, within the framework of the convective diffusion model there are three variants satisfying the experimental shape of the modulation function $\exp(-K/R\beta)$:

$$1.\quad n(r) = n_0 \exp\left[-\frac{u(r_s - r_1)}{\varkappa}\right],\quad u = const(r),\ \varkappa = const(r);$$

$$2.\quad n(r) = n_0 \exp\left[\frac{u_s r_s}{2\varkappa_s} E_i\left(-\frac{r^2}{6^2}\right)\right],\quad u = u_s \exp\left(-\frac{r^2}{6^2}\right),\ \varkappa = \frac{\varkappa_s}{r_s} r;$$

$$3.\quad n(r) = n_0 \exp\left\{\frac{u_s r_s}{2\varkappa}\sqrt{\frac{\varkappa}{\alpha}}\left[\Phi\left(\alpha\frac{r^2}{r_s^2}\right) - \Phi\left(\alpha\frac{r_1^2}{r_s^2}\right)\right]\right\},$$
$$u = u_s \exp\left(-\alpha\frac{r^2}{r_s^2}\right),\quad \varkappa = const(r).$$

In the second and third variants the velocity of the solar wind is given as the velocity of a strong shockwave. The value of r_2 is determined by δ and K

as follows:

$$1.\ \tau_2 - \tau_1 = \kappa/\delta,$$
$$2.\ E_i\left(-\frac{\tau_2^2}{\delta^2}\right) = +\frac{\kappa}{\delta\tau_s} e^{-\frac{\tau_s^2}{\delta^2}},$$
$$3.\ \Phi\left(\frac{\alpha\,\tau_2^2}{\tau_s^2}\right) = \Phi(\alpha) + \frac{\kappa\cdot x}{u_s\,\tau_s}.$$

The function $E_i(x)$ and $\Phi(z)$ are tabulated in /15/. From the experimental values of K and δ /5/ we get in all three variants $r_2 = 2-4$ AU.

Another method for determining the dimensions of the modulation region, besides calculating the modulation parameters, consists in determining the time lag between the cosmic-ray intensity and the solar activity level. However, in order to do this we must choose such an index of solar activity which enables the best characterization of the influence of the solar activity upon the modulation of the galactic cosmic rays in the interplanetary medium.

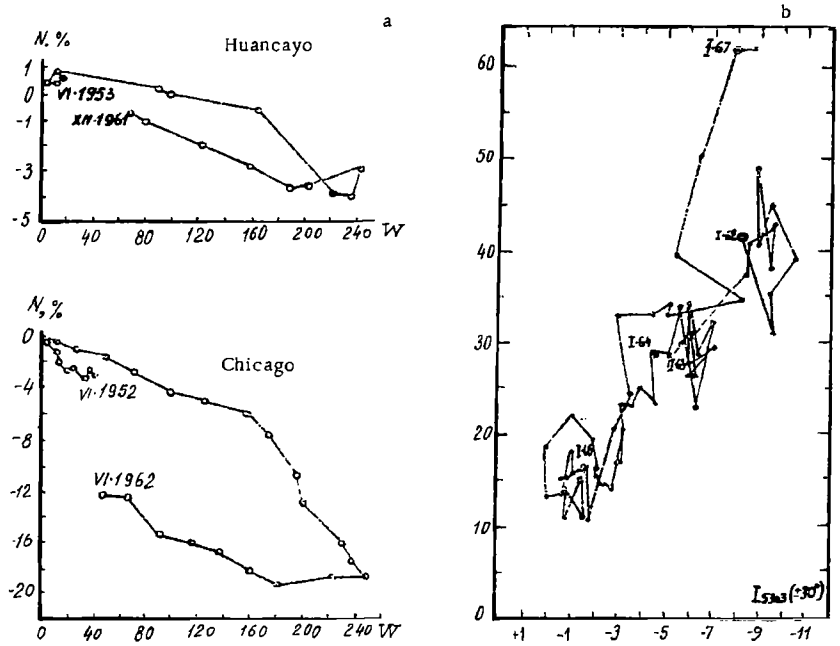

FIGURE 3. Hysteresis as a function of the index of solar activity:
a — number of sunspots; b — intensity of the corona line 5303 Å.

In Figure 3 are shown the hysteresis curves of the cosmic-ray intensity versus sunspot number /16/ and versus the intensity of the corona line 5303 Å in the band of heliolatitudes ± 30° /17/. It can be seen that in the second case the hysteresis is practically absent which agrees with the data of Figure 2. The correlation coefficients between the cosmic-ray intensity

and various indices of the solar activity are listed in the table. The best correlation is observed with corona radiation.

Correlation coefficients of annual means

Cosmic ray station	R, entire disk	I_{5303}, entire disk	I_{5303}, $\pm 40°$	Radio emission, MHz		
				200	2800	9400
Tule	0.95 ± 0.02	0.98 ± 0.01	0.99 ± 0.01	0.96 ± 0.02	0.94 ± 0.03	0.93 ± 0.03
Deep River	0.94 ± 0.02	0.98 ± 0.01	0.98 ± 0.01	0.97 ± 0.01	0.93 ± 0.03	0.94 ± 0.03
Norikura	0.93 ± 0.03	0.97 ± 0.01	0.96 ± 0.02	0.94 ± 0.03	0.92 ± 0.03	0.92 ± 0.03

In Figure 4 the time of the maximum of the solar radio emission is given as a function of the logarithm of the radio frequency. At frequencies of $\sim 10^4$ MHz the time of the maximum coincides with the maximum in the sunspot number, and at frequencies of $\sim 10^2$ MHz — with the maximum of the corona radiation. It can thus be concluded that the maximum at different levels of the solar atmosphere occurs at different times. This is probably related to the fact that the energy transfer from the photosphere to the corona for a quiet solar wind occurs slowly /18/. The largest correlation between the cosmic ray intensity and the corona radiation was observed in /5, 17, 19—21/. The lag is in this case 1—2 months. For such a delay time we obtain for the modulation function of type 1 for $u = (3-4)\cdot 10^7$ cm/sec: $r_2 = ut = 5-6$ AU for $\Delta t = 1$ month and $r_2 = 10-12$ AU for $\Delta t = 2$ months. For the modulation functions of types 2 and 3 we have

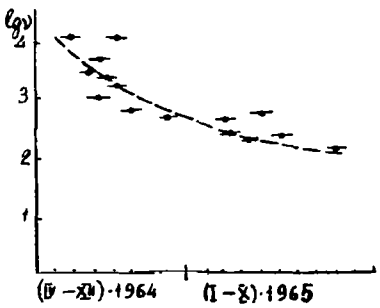

FIGURE 4. Time of the maximum of the solar radio emission as a function of the logarithm of the radio frequency.

$$\Delta t = \frac{1}{u_3}\int_{r_1}^{r_2} e^{\alpha \frac{r^2}{r_3^2}}\, dr$$

From the above expression for $\Delta t = 1-2$ months and $u = (3-4)\cdot 10^7$ cm/sec, $r_2 = 2-4$ AU. According to /5, 12/, $\Delta K = \frac{u(r_2-r_1)_{min}}{\varkappa}[\alpha(1+\frac{\Delta u}{u})\left(1 + \frac{\Delta(r_2-r_1)}{(r_2-r_1)_{min}}\right)-1]$, where u, $\varkappa$, $(r_2-r_1)_{min}$ are the values at the minimum of the solar activity. In /5/, using sea-level data and the results of /22/, $\Delta K = 1$; however, as was shown above, it is more probable that $\Delta K = 2$. Consequently, $(r_2-r_1)_{max} = 5-6$ AU, which agrees with the result obtained in /12/.

Bibliography

1. Webber, W.R.— The Proc. of Tenth Int. Conf. on Cosmic Rays, Calgary, Canada. 1967.
2. Silberberg, R.— Phys. Rev., 148, 1247. 1966.
3. Duggal, S.P., K. Pomerantz, and M.A. Nagashima.— Proc. Int. Conf. Cosmic Rays, 1, 161. 1965.
4. Durgaprasad, N.— J. Geophys. Res., 72, 965. 1967.
5. Zusmanovich, A.G. and E.V. Kolomeets.— Trudy V Vsesoyuznoi ezhegodnoi zimnei shkoly po kosmofizike, Izd. Kol'skogo filiala AN SSSR, Apatity, p. 311. 1968.
6. Freier, P.S. and C.J. Waddington.— J. Geophys. Res., 73, 4261. 1968.
7. Ormes, J.F. and W.R. Webber.— J. Geophys. Res., 73, 4231. 1968.
8. Fan, C.Y., G. Gloeckler, and J.A. Simpson.— Phys. Rev. Lett., 17, 329. 1966.
9. Balasubrahmanyan, V.K., E. Bolt, and R.A.R. Palmeira.— J. Geophys. Res., 72, 27. 1966.
10. Webber, W.R. and F.B. McDonald.— J. Geophys. Res., 69, 3097. 1964.
11. Lockwood, J.A. and W.R. Webber.— J. Geophys. Res., 72, 5977. 1967.
12. Zusmanovich, A.G., E.V. Kolomeets, R.A. Chumbanova, and Yu.A. Shakhova.— Geomagnetizm i aeronomiya (in print).
13. Dorman, L.I.— Kosmicheskie luchi, No. 8:305. 1967.
14. Zusmanovich, A.G., V.N. Ivanov, and E.V. Kolomeets.— Izvestiya AN SSSR, Seriya Fiziki, 32(11):1877. 1968.
15. Jahnke, E., F. Emde, and F. Lösch. Tables of Higher Functions.— B.G. Teubner, Stuttgart. 1960.
16. Dorman, I.V. and L.I. Dorman.— Kosmicheskie luchi, No. 7:15. 1965.
17. Simpson, J.A. and J.R. Wang.— Astrophys. J., 149, 73. 1967.
18. Solnechnyi Veter (Solar Wind).— Moskva, "Mir." 1968.
19. Hatton, C.G., P.S. Marsden, and A.C. Willets.— Canad. J. Phys., 46, 915. 1968.
20. Zusmanovich, A.G., E.V. Kolomeets, R.A. Chumbanova, and Yu.A. Shakhova.— Kosmicheskie luchi, No. 13 (in print).
21. Gnedyshev, M.N.— UFN, 90, 291. 1966; 1, 107. 1967.
22. Dorman, L.I., A.G. Zusmanovich, and E.V. Kolomeets.— Geomagnetizm i aeronomiya, 8:336. 1968.

V. P. Okhlopkov

THE 27-DAY VARIATIONS OF COSMIC RAYS AND SOLAR ACTIVITY DURING 1966—1967

Between November 1966 and May 1967 there was a clearly marked 27-day variation of cosmic rays, which could be traced to the variations in the sunspot number and the 10.7-cm radio emission. In order to correlate the cosmic-ray variations with the solar activity, the daily data (maximum cosmic-ray intensity measurements at the Mirnyi and Olen'ya stations, neutron measurements at Deep River and Climax, and geomagnetic activity) for the period of June 1, 1966 to December 31, 1967 were reduced by the method of sliding periodogram analysis. Each periodogram was plotted for 180 days, with sampling periods of 5 to 35 days at 20-day intervals. Over eight solar revolutions the periodograms clearly display the 27-day variation of cosmic rays.

The time dependence of the cosmic-ray and solar-activity variation amplitudes shows that the cosmic-ray variation lags 60 — 70 days behind the solar activity. For a solar-wind velocity of $4 \cdot 10^7$ cm/sec, this lag corresponds to a modulation region 14 — 16 AU in radius.

During the time interval under investigation the period of variation of the solar-activity indexes changed from 27 to 30 days. A similar change of period was also noted in the cosmic-ray intensity, but lagging 60 — 70 days behind the solar activity.

The Carrington distribution of the sunspot number and area exhibits a longitudinal asymmetry. From May 1967 the active longitude started moving eastward at a rate of 30 — 40° per month, and this could have produced the change in the variation period from 27 to 30 days.

The amplitude of the 27-day variations in the Wolf number during the investigated period is 45%, and in the longitudinal asymmetry it is 40%. Thus the observed variations must be due to the longitudinal sunspot asymmetry.

V. I. Shishov

GALACTIC COSMIC-RAY FLUCTUATIONS OF INTERPLANETARY ORIGIN

A theoretical consideration is given of the fluctuations of galactic cosmic rays, produced by the scattering of particles on interplanetary magnetic-field inhomogeneities when the latter are smaller than the Larmor radius of the particle. It has been shown that from the time distribution of the cosmic-ray fluctuations it is possible to determine the two-dimensional space structure of the magnetic-field inhomogeneities. It will be recalled that rocket measurements give only the one-dimensional structure of magnetic-field inhomogeneities. The cosmic-ray fluctuations originating in the interplanetary medium are best observed at stations whose asymptotic cone width is $< 6^\circ$, i.e., at high latitudes.

The size of the fluctuations is numerically evaluated on the basis of rocket measurements, assuming isotropy of the magnetic inhomogeneities. The rms-value of fluctuations with a period of $\lesssim 100$ min in the intensity of particles of energy $\approx 10^9$ eV is 0.2%. The rms-value of the fluctuations with a period of $\lesssim 10$ min is 0.06%.

M. V. Alaniya and O. G. Rogava

THE BAROMETRIC COEFFICIENT OF THE NEUTRON COSMIC-RAY COMPONENT WITH ALLOWANCE FOR PROTON AND MUON ABSORPTION

1. The variation of the barometric coefficient of the neutron cosmic-ray component is studied as a function of the total detected intensity and of the radioactive contamination of the counters, with allowance for the absorption of protons and muons producing neutrons in the detector.

2. The barometric coefficient of the neutron component is given as the sum

$$\bar{\beta} = (1 - \alpha_1^\circ - \alpha_2^\circ - \alpha_3^\circ - \alpha_4)\beta + \alpha_1^\circ\beta_1 + \alpha_2^\circ\beta_2 + \alpha_3^\circ\beta_3 + \alpha_4\beta_4,$$

where α_1° is the fraction of neutrons produced by secondary protons; α_2° is the fraction of neutrons produced by muon capture; α_3° is the fraction of neutrons produced by muons interacting with atmospheric nuclei, by shower nucleons, and pions; α_4 is the fraction of neutrons from radioactive contamination; $(1 - \alpha_1^\circ - \alpha_2^\circ - \alpha_3^\circ - \alpha_4)$ is the fraction of neutrons hitting the detector; β_1, β_2, β_3, β_4 and β are the respective barometric coefficients.

3. The values of the barometric-coefficient distortion $\Delta\beta = \bar{\beta} - \bar{\beta}_\Delta$ are calculated, where

$$\bar{\beta}_\Delta = \frac{1}{1+\Delta(h)}\left[1 + \Delta(h) - \alpha_1(h) - \alpha_2(h) - \alpha_3(h) - \alpha_4\right]\beta + \\ + \alpha_1(h)\beta_1 + \alpha_2(h)\beta_2 + \alpha_3(h)\beta_3 + \alpha_4\beta_4 ;$$

$$\alpha_1(h) = \alpha_1^\circ \exp[-\beta_1 h],\ \alpha_2(h) = \alpha_2^\circ \exp[-\beta_2 h],\ \alpha_3(h) = \alpha_3^\circ \exp[-\beta_3 h],$$

$$\alpha_4(h) = \alpha_4,\ \beta_4 = 0:$$

$$\Delta(h) = \alpha_1^\circ[\exp(-\beta_1 h) - 1] + \alpha_2^\circ[\exp(-\beta_2 h) - 1] + \alpha_3^\circ[\exp(-\beta_3 h) - 1] + (1 - \alpha_1^\circ - \alpha_2^\circ - \alpha_3^\circ - \alpha_4) \times [\exp(-\beta h) - 1]$$

and h is the deviation from the mean pressure h_0 at which the neutron-component intensity is taken as unity.

4. Using the experimental values of α_1°, α_2°, α_3° from Hughes et al.,* the distortion of the true barometric coefficient is shown to be 2—3%, when the total intensity varies within $\Delta(h) = \pm 0.1 - 0.2$ and the counter radioactivity $\alpha_4 = \pm 0.01 - 0.03$.

* Hughes, E.B., P. Fieldhouse, and P.L. Marsden.— J. Phys. Soc., Japan, 17, p.518. Suppl. A=II. 1962.

L. I. Dorman and A. V. Sergeev

ESTIMATE OF THE PARTIAL BAROMETRIC COEFFICIENT OF INTEGRAL MULTIPLICITY FOR THE NEUTRON COMPONENT OF SECONDARY COSMIC RAYS

L. I. Dorman /1/ introduced the concept of the partial barometric coefficient of integral multiplicity $m'(R,h)$ of secondary-particle production, defined by the equation $\beta'(R,h) = -\partial m'(R,h)/m'(R,h)\partial$. The theoretical calculation of the multiplicity function $m'(R,h)$ for the neutron component of secondary cosmic rays involves certain difficulties. We propose an alternative definition of $\beta'(R,h)$, given as a function of the intensity barometric coefficient $\beta'_{R_c}(h)$ and the coupling coefficient $W'_{R_c}(R,h)$, namely,

$$\beta'(R_c,h_\ell) = \beta'_{R_c}(h_\ell) - \frac{1}{W'_{R_c}(R_c,h_\ell)} \cdot \frac{\partial \beta'_{R_c}(h_\ell)}{\partial R_c}. \qquad (1)$$

For this purpose we first derived the empirical relationships (from the experimental data of /2, 3/ for the period of minimum solar activity):

$$\beta'_{R_c}(h_\ell) = -\frac{1}{a+bR_c} \ \%/\text{mb} \quad [\pm 0.01\ \%/\text{mb}], \qquad (2)$$

$$a = 1.216 + 14.75 \cdot 10^{-5} h_\ell$$

$$b = -0.832 \cdot 10^{-2} + 2.09 \cdot 10^{-5} h_\ell$$

$$0 \le R_c \le 15\ \text{GV}, \quad 680\ \text{mb} \le h_\ell \le 1000\ \text{mb};$$

$$W'_{15}(R_c,h_\ell) = A\, R_c^{-\gamma} - B\, e^{-\kappa R_c}, \qquad (3)$$

where R_c is the geomagnetic cutoff rigidity at the point of observation, GV.

Let us assume that, at $R_c \ge 15$ GV, $R_c \to R$.

Numerical values of A, r, B and k

Solar activity minimum	A	r	B	k	Approximation error, %/GV	Boundary conditions
Neutron component h_1 = 1000 mb	169.4	1.472	224.2	0.679	± 0.2	$R_c \ge 2.5$ GV
Neutron component h_2 = 680 mb	394.2	1.660	618.3	0.840	± 0.3	$R_c \ge 2.5$ GV

After substituting (2) and (3) into (1), we get

$$\beta^{i}(R, h_{\ell}) = -\frac{1}{\alpha+\beta R}\left\{1+\frac{\beta[A\cdot k\cdot R^{1-\gamma}-(\gamma-1)B\cdot e^{-\kappa R}]}{\kappa(\gamma-1)(\alpha+\beta R)(A\cdot R^{-\gamma}-B\cdot e^{-\kappa R})}\right\}. \qquad (4)$$

In the range $R_c - R \geq 10$ GV expression (4) reduces to

$$\beta^{i}(R, h_{\ell}) = -\frac{1}{\alpha+\beta R}\left\{1+\frac{\beta R}{(\gamma-1)(\alpha+\beta R)}\right\}. \qquad (5)$$

Expressions (4) and (5) thus provide the means of calculating $\beta^{i}(R, h_{\ell})$ for observation conditions under which the equations for $\beta^{i}_{R_c}(h_{\ell})$ and $W^{i}_{\geq 5}(R, h_{\ell})$ are valid. This makes it possible to allow accurately for the barometric correction in the observed cosmic-ray variations $[\delta J^{i}_{R_c}(h)/J^{i}_{R_c}(h)]_{obs}$ according to the observation conditions, the primary-variation spectrum $\delta\Omega/\Omega$, and its time changes for variations of different types.

The coefficients A, r, B, and k are specified in the table.

Bibliography

1. Dorman, L. I.— Geomagnetizm i aeronomiya, 6(6):1096. 1966.
2. Bashelet, F., P. Balata, E. Dyring, and N. Jucci.— Nuovo cimento, 35, 23. 1965.
3. Webber, W. R. and J. J. Quenby.— Phil. Mag., 4(41):654. 1959.

V. A. El'tekov and V. F. Nikitin

COMPARATIVE ANALYSIS OF DIFFERENT GEOMAGNETIC-FIELD MODELS

At the Scientific Research Institute of Nuclear Physics of Moscow State University a computer was used to calculate the vertical distribution of the earth's magnetic field within 3000 and 25,000 km, and 27 isoclinic maps were plotted for these heights. The calculations were made for the period of 1960.0 by means of 48 Gaussian constants. In order to simplify the calculations for the magnetic field at any point in space, instead of a Gaussian series use is normally made of various approximation models for the geomagnetic field strength B.

Comparison of the approximation models with Gaussian series shows that at low altitudes a Gaussian series with a fairly large number of terms is required. A dipole-quadrupole-octupole model yields good results for altitudes above 12,000 km. At altitudes above 15,000 km the values of B are satisfactorily calculated from a dipole-quadrupole model. The deviations of the field-strength values calculated from an excentric dipole are comparable to those in the dipole-quadrupole model. Calculations made with a central-dipole model throughout the altitude range up to 25,000 km yield inaccurate results.

S. A. Bel'skii

THE METEORIC VARIATION OF COSMIC RAYS NEAR THE NEW SOLAR-ACTIVITY PEAK IN 1967—1968

It is shown that a meteoric variation of cosmic rays occurred near the new solar-activity peak of 1967—1968. As during the previous solar-activity peak in 1957—1959, the effect manifests itself as a cosmic-ray increase against an overall background decrease. The pattern displayed conforms to the mechanism of meteoric cosmic-ray variation proposed earlier, according to which meteor streams contain regular magnetic fields, produced by the flux of charged micrometeors through the interplanetary plasma which act as traps (tunnels) for cosmic rays. Through these tunnels solar and galactic cosmic rays may cross the modulation cloud of magnetic inhomogeneities and penetrate into the orbital region of the earth with a density higher than in the surrounding space. Due to the interaction of the solar wind with the magnetic fields of the meteor streams the latter are stretched radially and driven far out by the solar wind, forming a kind of interplanetary magnetic-field generator. When the earth or a spacecraft traverses the meteoric magnetic fields, a roughly sectorial field structure should be observed. On earth, as a result of the particles caught in the meteoric magnetic trap, a cosmic-ray increase should occur with a background decrease due to the shielding of the earth by the regular magnetic field of the meteor stream, or only the decrease will be noted if there are no trapped particles. The data obtained on the meteoric variation of cosmic rays suggest that many cases of the Forbush effect and of increases at Forbush-effect minima are caused by meteoric variations due to individual meteor streams.

Section VI

METHODOLOGICAL PROBLEMS

Edited by V. A. Dergachev, I. N. Kapustin, and G. E. Kocharov

Yu. I. Serebrennikov

STATISTICAL ANALYSIS OF HYPOTHESES

Statistical analysis of hypotheses is an important branch of mathematical statistics, where the problem of interpreting the disagreement between experimental results and predictions or the disagreement between the results of "parallel" experiments is investigated. This interpretation can be formulated in terms of a set of hypotheses. One of these explains the discrepancy as the consequence of natural random fluctuations inherent in the results of the experiment. This hypothesis is called the null hypothesis and is designated by H_0. The other hypotheses, of physical or methodological nature, are combined in mathematical statistics into one hypothesis called the alternate hypothesis (designated by H_1). The aim of statistical analysis is to determine out of two possible hypotheses H_0 and H_1 the more probable one.

BASIC DEFINITIONS AND TERMINOLOGY

The main assumptions of the theory of probability and of mathematical statistics will be discussed briefly.

1. Random event. The central concept in the theory of probability is the concept of a random event. A random event A is an event which can either occur or not as a result of the realization of a set of conditions, in the presence of which the event A can occur. The realization of the set of conditions is called a trial. In one trial one cannot predict the occurrence or nonoccurrence of the event A.

2. The probability p(A) (or simply p) of the event A to happen in one trial. Let a trial be repeated N times and let m appear in N trials. To characterize the possibility of the event A occurring in one trial the frequency $W(A)=m/N$ is introduced. Performing many series of N trials each, a set of frequencies is obtained. Practice shows that this set of frequencies becomes more and more grouped around some positive number as N increases; this number is called the probability p(A) of an event A occurring. Obviously, $0 \leq p(A) \leq 1$.

3. The compound random event. The simultaneous occurrence in one trial of two nonidentical events A and B is called the product event and is designated by the symbol $A \cdot B$. For independent events $p(A \cdot B) = p(A) \cdot p(B)$. Events, which consist of one event out of A and B occurring (it is immaterial

which) or of both together, is called the sum of the events and is designated by the symbol $A+B$. In the general case $p(A+B)=p(A)+p(B)+p(A\cdot B)$.

4. Probability scheme. A situation consisting of a product of independent trials, in which the probability of some random event is constant, is called the Bernoulli scheme. If in the series of independent trials the probability of a random event is not conserved, the situation is called the Poisson scheme. If the probability of an event in some trial depends on the outcome of previous trials, the situation is called the Markov chain scheme.

5. Random variable. This can be discrete (designated by m) or continuous (designated by x). A discrete random variable is, as a rule, the result of counting the appearance of a random event while repeating the trials. A continuous random variable is the consequence of measurement errors or of the natural spread of some result due to the influence of many random factors.

6. The probability distribution of a random variable is its complete characterization. For a discrete random variable this is a discrete function $p(m)$ determining the probability of obtaining the numerical value m in one trial. For a continuous random variable this is the density distribution function $p(x)$, so that the product $p(x)dx$ determines the probability of the event having a numerical value in the interval from x to $x+dx$ in one trial. In the Bernoulli scheme the probability of m events occurring in N trials is given by the binomial distribution:

$$P(m,N)=\frac{N!}{m!(N-m)!}p^m(1-p)^{N-m}, \qquad (1)$$

where p is the probability of event A occuring in one trial. For $N\to\infty$ and $p\to 0$, i.e., when $pN\sim 1$, the asymptotic form of the binomial distribution corresponds to a Poisson distribution:

$$P(m)=\frac{\bar{m}^m}{m!}e^{-\bar{m}}, \qquad (2)$$

where $\bar{m}=Np$. A large class of continuous random variables are described by a Gaussian distribution (normal distribution):

$$p(x)=\frac{1}{\sqrt{2\pi\sigma^2}}e^{-\frac{(x-a)^2}{2\sigma^2}}. \qquad (3)$$

The normal distribution assumes a universal form, if instead of x the normalized deviation $z=\frac{x-a}{\sigma}$ is introduced:

$$p(z)=\frac{1}{\sqrt{2\pi}}e^{-\frac{z^2}{2}}. \qquad (4)$$

The probability of a random variable being the result of one measurement in some interval $m_1\le m\le m_2$ or $x_1\le x\le x_2$ is given by

$$P(m_1\le m\le m_2)=\sum_{m=m_1}^{m_2}p(m),\quad P(x_1\le x\le x_2)=\int_{x_1}^{x_2}p(x)dx. \qquad (5)$$

7. Numerical characteristics of a random variable (the parameters of its distribution). The expected value of a random variable (the center of the spread) is the mathematical expectation $M(m)=\bar{m}=\sum_{m} m\,P(m)$, $M(x)=\bar{x}=\int_{x} x\,p(x)dx$ (summation and integration over all possible values of the random variables). For a binomial distribution $\bar{m}=Np$, for a Poisson distribution $M(m)=\bar{m}$, for a normal distribution $\bar{x}=a$, $\bar{z}=0$. The parameter that characterizes the spread of a variable is the variance $D(m)=\sum_{m}(m-\bar{m})^2P(m)$, $D(x)=\int_{x}(x-\bar{x})^2p(x)dx$. For the binomial distribution $D(m)=Np(1-p)=Npq$, $(q=1-p)$, for the Poisson distribution $D(m)=\bar{m}$, and for the normal distribution $D(x)=\sigma^2$, $D(x)=1$. The standard deviation is defined as $\sigma(x)=+\sqrt{D(x)}$. The relative deviation is $\delta(x)=\sigma(x)/\bar{x}$. The median of a random variable x is defined by the equation $\int_{-\infty}^{\langle x\rangle}p(x)dx=\int_{\langle x\rangle}^{\infty}p(x)dx=1/2$.

8. The estimate of the numerical values of parameters characterizing a random variable from experimental results. The experiment consists of n independent measurements of the random variable x. If the experimental results are $x_1, x_2 \ldots x_i \ldots x_n$, the best unbiased estimates of $M(x)$ and $D(x)$ are the following quantities:

$$\left.\begin{aligned} \bar{x} \to \bar{x}_{ap} &= \frac{1}{n}\sum_{i=1}^{n} x_i, \\ D(x) \to S^2(x) &= \frac{1}{n-1}\sum_{i=1}^{n}(x_i-\bar{x}_{ap})^2, \\ D(\bar{x}_{ap}) \to S^2(\bar{x}_a) &= \frac{1}{n(n-1)}\cdot\sum_{i=1}^{n}(x_i-\bar{x}_a)^2 \end{aligned}\right\} \qquad (7)$$

GENERAL APPROACH TO THE STATISTICAL ANALYSIS OF HYPOTHESES

The basic idea of the statistical analysis of hypotheses can be formulated briefly in the following way. It is first assumed that the null hypothesis (H_0) is true. For the description of the random deviations of the experimental values from the expected ones a random variable ξ is introduced (this is the measure of the discrepancy between the experiment and the expected values, and can be discrete or continuous); its probability distribution $p_{H_0}(\xi)$ can be determined from the validity of H_0. From the experimental results the numerical value ξ_0 of the random variable ξ recorded in the experiment is determined. The value ξ_0 can be in contradiction with the function $p_{H_0}(\xi)$ and the null hypothesis has to be rejected as being false. If the value of ξ_0 does not contradict the function $p_{H_0}(\xi)$, then in the first approximation H_0 can be assumed to be true. The random variable ξ is often called the test of agreement. ξ_0 and $p_{H_0}(\xi)$ contradict each other if ξ_0 is too far away from the mathematical expectation $M(\xi)=\int_{\xi}\xi\cdot p_{H_0}(\xi)d\xi$ and falls into the region of ξ; the probability β of their occurrence from the point of view of hypothesis H_0 is so small, that the occurrence of ξ_0 in this region in one trial is practically negligible. If the probability β (called the confidence level) is given, then for the practical solution of the problem whether there is or is not a contradiction between ξ_0 and $p_{H_0}(\xi)$ the region of all possible values

values of ξ is divided in two: the statistically insignificant $\xi'_\beta \leq \xi \leq \xi''_\beta$ and the statistically significant $\xi \leq \xi'_\beta$ and $\xi \geq \xi''_\beta$. The boundary values ξ'_β and ξ''_β are determined according to the confidence level β specified from the following relation:

$$\int_{-\infty}^{\xi'_\beta} p_{H_0}(\xi)\,d\xi = \alpha\cdot\beta\,, \quad \int_{\xi''_\beta}^{\infty} p_{H_0}(\xi)\,d\xi = (1-\alpha)\,\beta, \tag{8}$$

where α is a parameter less than unity, $0 \leq \alpha \leq 1$. If ξ_0 turns out to be in the statistically significant region, it is assumed that there is a contradiction between ξ_0 and $p_{H_0}(\xi)$, and the null hypothesis is rejected.

From the abovesaid it is clear that if the hypothesis H_0 is true, then in a statistical analysis it can still happen that it will be rejected as being false. The probability of such a wrong conclusion, i.e., a so-called error of the first kind is obviously equal to the confidence level β. In the statistical analysis of hypotheses an error of the second kind occurs when the alternative hypothesis, which is true, is rejected. This occurs when the alternative hypothesis (H_1) is true, but the value of ξ_0 falls into the statistically insignificant region. The probability of making an error of the second kind should be kept as small as possible. This is achieved by a suitable choice of one or another variant of the random variable ξ and an optimum choice of the limits of the significant and insignificant regions of its values. For the investigation of the last possibility it will be assumed that the alternative hypothesis is true and that the random variable is determined by the probability distribution $p_{H_1}(\xi) \neq p_{H_0}(\xi)$. The distribution $p_{H_1}(\xi)$ is shifted with respect to $p_{H_0}(\xi)$ to the left or to the right; for concreteness the following case will be investigated (Figure 1). In this case the probability of making an error of the second kind is given by

$$\int_{-\infty}^{\xi''_\beta} p_{H_1}(\xi)\,d\xi = 1 - P(\xi''_\beta). \tag{9}$$

The quantity $P(\xi''_\beta)$ is called the power of the test ξ, $0 \leq P(\xi''_\beta) \leq 1$. As the power of the test increases, the probability of making an error of the second kind decreases.

An increase in the power of the test can be achieved by a suitable choice of the boundary values ξ'_β and ξ''_β which are determined by the choice of the parameter α in (8). The value of α is generally chosen as being equal to 0, 0.5 or 1. The value $\alpha = 0.5$ leads to the so-called two-sided variant of the test, if both values ξ'_β and ξ''_β are finite. It can be seen from Figure 1 and expression (9) that in the present example $\alpha = 0$ (one-sided, in this case right-handed, test) leads to an increase in the power of the test of making an error of the first kind at a constant value of the probability β.

Thus, the use of a one-sided test should be always attempted. If nothing is known about the distribution $p_{H_1}(\xi)$ relative to $p_{H_0}(\xi)$, it is recommended to determine the one-sided test by using the experimental values of ξ_0 and the median $\langle \xi \rangle_{H_0}$ for the distribution $p_{H_0}(\xi)$. If it turns out that $\xi_0 > \langle \xi \rangle_{H_0}$, a right-handed test should be used, and vice versa. In addition to the abovesaid it is known that the power of tests increases with the number of measurements n.

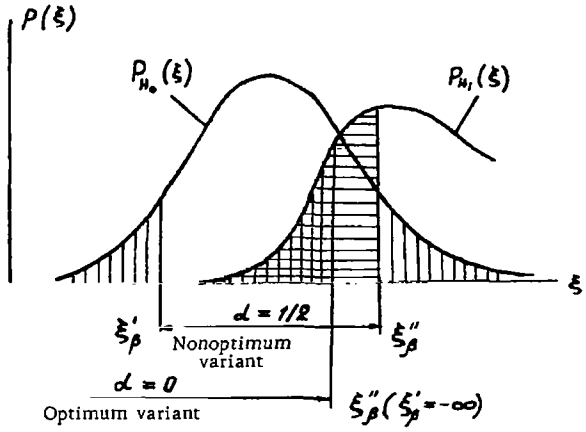

FIGURE 1. Two-sided and one-sided tests. The arrows indicate the boundaries of the statistically insignificant regions. The area below the curve $p_{H_1}(\xi)$ is shaded by horizontal lines. The cross-shaded area is numerically equal to the probability of an error of the second kind for a two-sided test. The area shaded by vertical lines is equal to the probability of errors of the first kind for a two-sided test.

The numerical value of the confidence level β is generally chosen in the interval $0.01 \leq \beta \leq 0.05$. From Figure 1 and (8—9) it follows that for a chosen test the power of the latter increases with β and vice versa, i.e., with an increase in the probability of admitting an error of the first kind the probability of making an error of the second kind decreases. Therefore, the numerical value of the confidence level β should be chosen according to physical considerations of tolerating an error of one or another kind.

NONPARAMETRIC TESTS

There exist tests which enable the analysis of measurements of a random variable x, i.e., tests which can possess any distribution. Such tests are called nonparametric. Two of these will be discussed here: the sign test (which lends itself to a complete analytical investigation) and the Wilkinson test.

The sign test. This test is used when one studies the qualitative influence of a controllable external factor γ upon some property of the object under investigation, for example, the physical or chemical properties of materials or the activity of living organisms, the influence of improvements upon the performance of some equipment, etc. The investigated property of the object is measured quantitatively and is thus described by some random variable x, which possesses a probability distribution $p(x)$. From the point of view of mathematical statistics the problem is reduced to determining the influence of the factor γ upon the function $p(x)$. For the experimental investigation of this problem N pairs of objects are taken and one object is subjected to the action of the factor γ. The experimental

results of the random variable x are tabulated as follows:

Pair number	x	x_γ	Sign of the difference, $x-x_\gamma$
1	x_1	x_{γ_1}	+
2	x_2	x_{γ_2}	+
3	x_3	x_{γ_3}	−
.	.	.	
.	.	.	
.	.	.	
i	x_i	x_{γ_i}	+
.	.	.	
.	.	.	
.	.	.	
N	x_N	x_{γ_N}	−

Assuming the validity of the null hypothesis, i.e., assuming

$$p(x) = p(x_\gamma), \tag{10}$$

the test ξ is chosen as the number of sign differences of $x - x_\gamma$ which is smaller. Let us assume for concreteness that the number of (+) signs is smaller, and let us denote this number by $m(+)$ ($\xi = m(+)$). If (10) is valid, the probability of obtaining a (+) sign p_+ or a (−) sign p_- are equal to one another $p_+ = p_- = 1/2$, since $p_+ + p_- = 1$ (the probability of an exact equality between x_i and x_{γ_i} vanishes if x is a continuous variable). Then the probability that in N independent pairs, i.e., in N independent experiments, a (+) sign will appear $m(+)$ times is described by a binomial distribution. Thus the "null" distribution $P_{H_0}[m(+)]$ is given by

$$P_{H_0}[m(+)] = \frac{N!}{m(+)![N-m(+)]!}\left(\frac{1}{2}\right)^N. \tag{11}$$

Using in this case a left-handed test and choosing a confidence level β, the limit value $m'_\beta(+)$ can be determined from

$$\sum_{m(+)=0}^{m'_\beta(+)} P_{H_0}[m(+)] = \beta. \tag{12}$$

The solutions of an equation of the type (12) are tabulated and the values of $m'_\beta(+)$ (or of $m'_\beta(-)$) for known N and β can be found (Table 1). If it turns out that the number of (+) signs observed in the course of an experiment is $m_0(+) < m'_\beta(+)$, the null hypothesis is rejected, and the influence of the factor γ upon the investigated property of the object is established. If $m_0(+) > m'_\beta(+)$, then in general two assumptions can be made: either the null hypothesis is true, or the alternative hypothesis is true after all, but the influence of the factor γ upon the quantity x is small and the difference between $P_{H_1}[m(+)]$ and $P_{H_0}[m(+)]$ is masked by the random fluctuations.

TABLE 1. The limit values of $m_{\beta}^{\pm}$ for the sign test (left-handed test)

N	Confidence level β				N	Confidence level β			
	0.01	0.05	0.10	0.25		0.01	0.05	0.10	0.25
1					46	13	15	16	18
2					47	14	16	17	19
3				0	48	14	16	17	19
4				0	49	15	17	18	19
5			0	0	50	15	17	18	20
6		0	0	1	51	15	18	19	20
7		0	0	1	52	16	18	19	21
8	0	0	1	1	53	16	18	20	21
9	0	1	1	2	54	17	19	20	22
10	0	1	1	2	55	17	19	20	22
11	0	1	2	3	56	17	20	21	23
12	1	2	2	3	57	18	20	21	23
13	1	2	3	3	58	18	21	22	24
14	1	2	3	4	59	19	21	22	24
15	2	3	3	4	60	19	21	23	25
16	2	3	4	5	61	20	22	23	25
17	2	4	4	5	62	20	22	24	25
18	3	4	5	6	63	20	23	24	26
19	3	4	5	6	64	21	23	24	26
20	3	5	5	6	65	21	24	25	27
21	4	5	6	7	66	22	24	25	27
22	4	5	6	7	67	22	25	26	28
23	4	6	7	8	68	22	25	26	28
24	5	6	7	8	69	23	25	27	29
25	5	7	7	9	70	23	26	27	29
26	6	7	8	9	71	24	26	28	30
27	6	7	8	10	72	24	27	28	30
28	6	8	9	10	73	25	27	28	31
29	7	8	9	10	74	25	28	29	31
30	7	9	10	11	75	25	28	29	32
31	7	9	10	11	76	26	28	30	32
32	8	9	10	12	77	26	29	30	32
33	8	10	11	12	78	27	29	31	33
34	9	10	11	13	79	27	30	31	33
35	9	11	12	13	80	28	30	32	34
36	9	11	12	14	81	28	31	32	34
37	10	12	13	14	82	28	31	33	35
38	10	12	13	14	83	29	32	33	35
39	11	12	13	15	84	29	32	33	36
40	11	13	14	15	85	30	32	34	36
41	11	13	14	16	86	30	33	34	37
42	12	14	15	16	87	31	33	35	37
43	12	14	15	17	88	31	34	35	38
44	13	15	16	17	89	31	34	36	38
45	13	15	16	18	90	32	35	36	39

Here arises the problem of the sensitivity of the sign test, and also of other tests. The influence of the factor γ may finally lead to a small change

$\Delta\left(-\frac{1}{2} \leq \Delta \leq +\frac{1}{2}\right)$ in the probability of a (+) sign appearing in each pair of objects. The definite observation of the case $|\Delta| > 0$ will occur when the probability of making an error of the second kind is small, i.e., the power of the sign test is sufficiently high. For $|\Delta| > 0$ the alternative distribution $P_{H_1}[m(+)]$ has the form

$$P_{H_1}[m(+)] = \frac{N!}{m(+)![N - m(+)]!} \cdot \left(\frac{1}{2} + \Delta\right)^{m(+)} \cdot \left(\frac{1}{2} - \Delta\right)^{N - m(+)}, \qquad (13)$$

and the power of the sign test (left-handed) is in this case given by

$$P[m'_\beta(+)] = \sum_{m(+)=0}^{m'_\beta(+)} P_{H_1}[m(+)]. \qquad (14)$$

If the numerical value of Δ is known or given a priori, the reliability with which the existence of Δ should be detected, i.e., the test's power, and the probability β of errors of the first kind are given, then (12) and (14) determine the conditions under which the sign test will have the desired sensitivity. These conditions are the number N of object pairs required and the limit value $m'_\beta(+)$. The solution of (12) and (14) shows that with all other conditions remaining the same the requirement of increasing the power of the test leads to a requirement of increasing the number of object pairs, and vice versa, an increase in the number of pairs N leads to an increase in the power of the test. Qualitatively this result can be understood from Figure 1. From the abovesaid it is clear that the power of the test increases as the overlap of the distributions P_{H_0} and P_{H_1} decreases. An increase in N leads to this effect, since the difference of the mathematical expectations of these two distributions increases with N: $\bar{m}_{H_1}(+) - \bar{m}_{H_0}(+) = N\left(\frac{1}{2} + \Delta\right) - N\frac{1}{2} = N\cdot\Delta$, and the relative deviation $\delta = \frac{\sqrt{N p_+ q_+}}{\bar{m}(+)}$ of the two distributions decreases: $\delta_{H_0} = \frac{\sqrt{N\frac{1}{2}\cdot\frac{1}{2}}}{N\frac{1}{2}} = \frac{1}{\sqrt{N}}$, $\delta_{H_1} = \sqrt{N\left(\frac{1}{2}+\Delta\right)\left(\frac{1}{2}-\Delta\right)}/N\left(\frac{1}{2}+\Delta\right) = \frac{1}{\sqrt{N}}\sqrt{\frac{1}{2}-\Delta}/\sqrt{\frac{1}{2}+\Delta}$. As an illustration of the solution of the system of equations (12) and (14) below are tabulated the number N of pairs necessary to detect for a given β a value of Δ with a confidence of 0.95:

Δ	$\beta = 0.01$	$\beta = 0.05$	$\beta = 0.1$
-0.05	1777	1297	1080
-0.1	442	327	267
-0.2	106	79	67
-0.3	44	35	28
-0.4	24	17	13
-0.45	15	12	11

In conclusion it should be noted that if the measurements of the random variable x contain pairs $x_i = x_{pi}$, these are either excluded from the analysis or the problem of choosing a (+) or (−) sign is decided by a toss of a coin.

Wilkinson test. A random variable x is studied experimentally; its probability distribution p(x) is unknown. The Wilkinson test (also the Smirnov and λ^2-test) is used when it is necessary to find whether the probability p(x) is constant with respect to the moment of repeated (or parallel) measurements of x. Let the first series of measurements contain n_1 measurements and the second one n_2. For convenience the measurements of the first series are denoted by $x: x_1, x_2, \ldots, x_{n_1}$, and the results of the second by $y: y_1, y_2, \ldots, y_{n_2}$. Both series are combined and x and y are ordered according to their numerical values. A so-called variational sequence is obtained: xyyxyxxy... (the indices are omitted). An inversion is any case in which y appears before x in the variational sequence. In the above sequence the number of inversions is determined as follows: the first x does not contribute an inversion, the second x contributes two inversions, since in front of it are two values of y, the third x contributes three, etc. The sum of inversions of the variational sequence (in the above example there are 8) is denoted by u. This is a random variable and is used as a test ($\xi \rightarrow u$). Van der Waerden /1/ showed that assuming the validity of the hypothesis H_0 for given n_1, n_2 and β the value of u_β separating the statistically significant from the nonsignificant regions of u can be determined by combinatorial methods. The mathematical expectation $\bar{u}$ and the dispersion $\sigma^2(u)$ of the distribution $P_{H_0}(u)$ can be calculated by combinatorial methods and are equal to:

$$\bar{u} = \frac{1}{2} n_1 n_2 ; \quad \sigma^2(u) = \frac{1}{12} n_1 n_2 (n_1 + n_2 + 1). \tag{15}$$

The computations necessary for the determination of u_β, specially for $n_1 \gg 1$, $n_2 \gg 1$, are, however, quite tedious. Investigations of the random variable u have shown that for $n_1 > 3$, $n_1 + n_2 > 20$ the distribution P_{H_0} is quite close to a normal distribution, so that without making an appreciable error it can be assumed to be normal with parameters given by (15).

The further uses of the Wilkinson test are similar to those described earlier. As in the case of the sign test, the power of the Wilkinson test increases with an increase in n_1 and n_2; the exact determination of the power of this test is difficult, since the distribution $P_{H_1}(u)$ is generally unknown. For x = y their position in the sequence is determined by a toss of a coin. In Table 2 are given exact values of u_β for a given β in the case of small values of n_1 and n_2. In Table 2, in contrast to other tables, the probability (expressed in percent) of the random variable u being smaller than or equal to the value in the table is given. However, by interchanging x and y a right-handed test can be converted into a left-handed one.

TABLE 2. Table of the limiting values u'_β for the Wilkinson test (left-handed test)

u	Sample sizes n_1 and n_2													
	2; 5	2; 6	2; 7	2; 8	2; 9	2; 10	3; 3	3; 4	3; 5	3; 6	3; 7	3; 8	3; 9	3; 10
0	4.76	3.57	2.78	2.22	1.82	1.52	5.00	2.86	1.79	1.19	0.83	0.61	0.45	0.35
1				4.44	3.64	3.03			3.57	2.38	1.67	1.21	0.91	0.70
2										4.76	3.33	2.42	1.82	1.40
3												4.24	3.18	2.45
4													5.00	3.85

TABLE 2 (cont'd)

u	Объемы выборок n_1 и n_2													
	4; 4	4; 5	4; 6	4; 7	4; 8	4; 9	4;10	5; 5	5; 6	5; 7	5; 8	5; 9	5; 10	6; 6
0	1.43	0.79	0.48	0.30	0.20	0.14	0.10	0.40	0.22	0.13	0.08	0.05	0.03	0.11
1	2.86	1.59	0.95	0.61	0.40	0.28	0.20	0.79	0.43	0.25	0.16	0.10	0.07	0.22
2		3.17	1.90	1.21	0.81	0.56	0.40	1.59	0.87	0.51	0.31	0.20	0.13	0.43
3			3.33	2.12	1.41	0.98	0.70	2.78	1.52	0.88	0.54	0.35	0.23	0.76
4				3.64	2.42	1.68	1.20	4.76	2.60	1.52	0.93	0.60	0.40	1.30
5					3.64	2.52	1.80		4.11	2.40	1.48	0.95	0.63	2.06
6						3.78	2.70			3.66	2.25	1.45	0.97	3.25
7							3.80				3.26	2.10	1.40	4.65
8											4.66	3.00	2.00	
9												4.15	2.76	
10													3.76	
11													4.96	

u	Sample sizes n_1 and n_2													
	6; 7	6; 8	6; 9	6; 10	7; 7	7; 8	7; 9	7;10	8; 8	8; 9	8; 10	9; 9	9;10	10; 10
0	0.06	0.03	0.02	0.01	0.03	0.02	0.01	0.01	0.01	0.00				
1	0.12	0.07	0.04	0.02	0.06	0.03	0.02	0.01	0.02	0.01	0.00	0.00		
2	0.23	0.13	0.08	0.05	0.12	0.06	0.03	0.02	0.03	0.02	0.01	0.01	0.00	
3	0.41	0.23	0.14	0.09	0.20	0.11	0.06	0.04	0.05	0.03	0.02	0.01	0.01	0.00
4	0.70	0.40	0.24	0.15	0.35	0.19	0.10	0.06	0.09	0.05	0.03	0.02	0.01	0.01
5	1.11	0.63	0.38	0.24	0.55	0.30	0.17	0.10	0.15	0.08	0.04	0.04	0.02	0.01
6	1.75	1.00	0.60	0.37	0.87	0.47	0.26	0.15	0.23	0.12	0.07	0.06	0.03	0.02
7	2.56	1.47	0.88	0.55	1.31	0.70	0.39	0.23	0.35	0.19	0.10	0.09	0.05	0.02
8	3.67	2.13	1.28	0.80	1.89	1.03	0.58	0.34	0.52	0.28	0.15	0.14	0.07	0.04
9		2.96	1.80	1.12	2.65	1.45	0.82	0.48	0.74	0.39	0.22	0.20	0.10	0.05
10		4.06	2.48	1.56	3.64	2.00	1.15	0.68	1.03	0.56	0.31	0.28	0.15	0.08
11			3.32	2.10	4.87	2.70	1.56	0.93	1.41	0.76	0.43	0.39	0.21	0.10
12			4.40	2.80		3.61	2.09	1.25	1.90	1.03	0.58	0.53	0.28	0.14
13				3.63		4.69	2.74	1.65	2.49	1.37	0.78	0.71	0.38	0.19
14				4.67			3.56	2.15	3.25	1.80	1.03	0.94	0.51	0.26
15							4.54	2.77	4.15	2.32	1.33	1.22	0.66	0.34
16								3.51		2.96	1.71	1.57	0.86	0.45
17								4.39		3.72	2.17	2.00	1.10	0.57
18										4.64	2.73	2.52	1.40	0.73
19											3.38	3.13	1.75	0.93
20											4.16	3.85	2.17	1.16
21												4.70	2.67	1.44
22													3.26	1.77
23													3.94	2.16
24													4.74	2.62
25														3.15
26														3.76
27														4.46

TESTS FOR THE ANALYSIS OF NORMALLY DISTRIBUTED RANDOM VARIABLES

1. Random choice of the experimental point. The simplest case occurring in an experiment will be discussed. Let some experimental dependence F(t) be plotted on the basis of N independently obtained experimental points. For any fixed value $t = t_i$ the function $(F(t_i)$ due to experimental reasons will be a random variable, whose fluctuations are normally distributed with a standard deviation $S(t_i)$ determined from the experimental results.

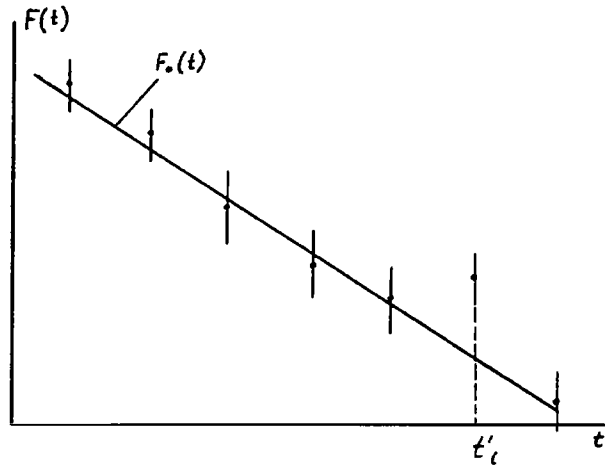

FIGURE 2. An appreciable deviation of one experimental point from the smooth dependence $F_0(t)$.

In the course of the experiment it is found that the experimental points are satisfactorily described by some expected function $F_0(t)$; however, one point $F(t'_i)$ deviates appreciably from $F_0(t'_i)$ (Figure 2), so that

$$\frac{F(t'_i)-F_0(t'_i)}{S(t'_i)} = Z_0 . \tag{16}$$

For the interpretation of this result it is necessary, as before, to establish the presence or absence of a contradiction between the result (16) and the null hypothesis. In order to do this the probability of one of the N experimental points having a normalized deviation $|z| = \frac{|F(t_i)-F_0(t_i)|}{S(t_i)} \geq z_0$ has to be computed. If it turns out that $P(|z| \geq z_0) < \beta$ (where β is the confidence level), this means that z_0 is in a statistically significant region which contradicts the null hypothesis, and the latter is rejected. If it is found that $P(|z| \geq z_0) > \beta$, then z_0 is in a statistically nonsignificant region and the null hypothesis is assumed to be valid. The probability that for some fixed value of t_i the normalized deviation z_i will satisfy the condition $|z_i| \geq z_0$ can be readily calculated:

$$P(|z_i| \geq z_0) = 2\int_{z_0}^{\infty} p(z_i)\,dz_i = 1 - 2\int_{0}^{z_0} p(z_i)\,dz_i = 1 - 2\Phi(z_0) = P_0, \tag{17}$$

where $\Phi(z_0) = \frac{1}{\sqrt{2\pi}}\int_0^{z_0} e^{-\frac{z^2}{2}}dz$ is the probability integral. In view of the fact that $p(z_i)$ is normal the probability of $|z_i| \geq z_0$ is the same for all experimental points. Therefore the event $|z_i| \geq z_0$ can occur for any of the N independent measurements with the same probability P_0, and the case at hand is identical to that of Bernoulli. The probability that one point out of N experimental points should satisfy the inequality $|z_i| \geq z_0$ can be calculated

from the binomial distribution:

$$P(N,1) = \frac{N!}{(N-1)!} P_0 (1-P_0)^{N-1} = N P_0 (1-P_0)^{N-1} \qquad (18)$$

As an example, let us take the case $N = 10$, $z_0 = 3$. According to (17) $P_0 = 0.0027$, i.e., $P(10, 1) = 0.026$. This value is of the order of β and the null hypothesis cannot be rejected. From (18) for a given value of β the boundary value $|z_\beta|$ satisfying $|z_i| > |z_\beta|$ for the fluctuation of one experimental point out of N can be calculated from $P(N, 1) = \beta$. Below are given the values of $|z_\beta|$ for different numbers N of experimental points and for $\beta = 0.02$: $N = 20, 40, 100, 1000$; $|z_\beta| = 3.3,\ 3.5,\ 3.7,\ 4.2$.

Thus, for an appreciable number of experimental points ($N > 10$) whose position can be described by a smooth function $F_0(t)$, the deviation of one of the points by 3σ from $F_0(t)$ in one measurement is not a statistically significant result. If there is a suspicion that the deviation of one point out of N experimental points by $z_0\sigma$ from the curve $F_0(t)$ is due to some effect, the reliable determination of the latter is possible only in a repeated, independent experiment.

2. χ^2-test. a. Let a random variable x, which obeys a normal distribution with a mean $\bar{x} = a$ and a standard deviation σ, be measured n times. The experimental results are $x_1, x_2, \ldots, x_i \ldots x_n$. In order to characterize the total spread of the experimental values x_i around the mean a quantity χ^2 is introduced, which corresponds to the sum over all measurements of the square of the normalized deviations $z_i = (x_i - a)/\sigma$:

$$\chi^2 = \sum_{i=1}^{n} \left(\frac{x_i - a}{\sigma}\right)^2 = \sum_{i=1}^{n} (z_i)^2. \qquad (19)$$

Sometimes not all n measurements of the random variable x are used in the analysis, but only those which satisfy some definite conditions, for example, $\sum_{i=1}^{n} x_i = c$ or $F(x_1, x_2, \ldots, x_n) = 0$, etc. The number of such conditions (relations) is denoted by s. Then the random variable is characterized by $k = n - s$, which is called the number of degrees of freedom. The number of degrees of freedom k is a parameter determining the probability distribution $p(\chi^2)$ of the random variable χ^2 /2/:

$$p(\chi^2) = \frac{1}{2^{\frac{k}{2}} \Gamma\left(\frac{k}{2}\right)} (\chi^2)^{\frac{k}{2}-1} e^{-\frac{1}{2}\chi^2}, \quad 0 \leq \chi^2 \leq \infty, \qquad (20)$$

where Γ is the gamma function. The numerical characteristics of $p(\chi^2)$ are also determined by the number of degrees of freedom $M(\chi^2) = k$, $D(\chi^2) = 2k$, and $M_0(\chi^2) = k - 2$ (M_0 is the most probable value). The curve $p(\chi^2)$ for several values of k is shown in Figure 3. The random deviations of the experimental results from the expected results can sometimes also be described by the χ^2-test when it is used as a test of agreement ($\xi \rightarrow \chi^2$).

b. Comparison between an empirical and a theoretical probability distribution. The experimentally observed probability distribution of some random quantity x (after n independent measurements) is represented by a histogram (Figure 4), where $m_i(x)$ is the number of cases in which the variable x was found to be in the i-th interval of width Δx, $1 \leq i \leq l$. The

histogram is compared with the theoretical prediction, whose ordinates are $m_i^\circ(x) = n\int_{x_i}^{x_i+\Delta x} p_\circ(x)dx$, where $p_\circ(x)$ is the theoretical probability distribution of x, and $x, \sum_{i=1}^{\ell} m_i(x) = \sum_{i=1}^{\ell} m_i^\circ(x)$. In Figure 4 the theoretical distribution is indicated by a dashed line. The deviation of the experimental distribution from the theoretical one in Figure 4 can be tested by a χ^2-test. Let us take one interval in the histogram in Figure 4. The experimentally observed value $m_i(x)$ in this interval is a specific value of the random variable m_i'.

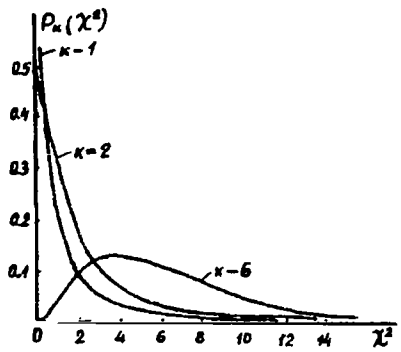

FIGURE 3. Probability density $p(\chi^2)$ for k (number of degrees of freedom) = 1, 2 and 6.

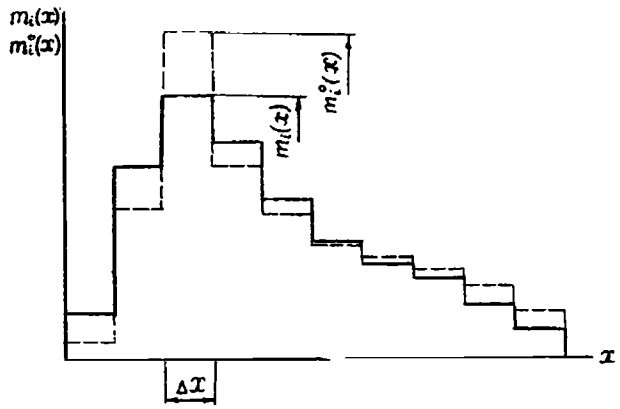

FIGURE 4. Experimental (solid line) and the theoretical (dashed line) histograms.

Let us determine the probability distribution of m_i'. All measurements of the random variable x are performed under identical conditions, so that its true distribution is constant during the measurements. Therefore, the probability p_i of observing in one measurement the random variable x in the i-th interval is $p_i = \int_{x_i}^{x_i+\Delta} p(x)dx = \text{const}$. Since the N measurements are independent, the fluctuations of m_i' are described by a binomial distribution:

$$P(N, m_i') = C_N^{m_i'} p_i^{m_i'}(1-p_i)^{N-m_i'} = \frac{N!}{m_i'!(N-m_i')!}\left(\frac{\bar{m}_i'}{N}\right)^{m_i'}\left(1-\frac{\bar{m}_i'}{N}\right)^{N-m_i'}, \qquad (21)$$

where $\bar{m}_i' = Np_i$ is the mathematical expectation of m_i'. For a small interval width Δx, where $p_i \ll 1$, and a sufficiently high number of statistical values N, when everywhere $m_i' \gg 1$, the distribution (21) has the asymptotic form:

$$P(m_i') = \frac{1}{\sqrt{2\pi\bar{m}_i'}} e^{-\frac{(m_i'-\bar{m}_i')^2}{2\bar{m}_i'}}, \qquad (22)$$

whose dispersion is $\sigma^2(m_i') = \bar{m}_i'$. It thus follows that when the above conditions are satisfied, in each of the ℓ intervals of the histogram the ordinates $m_i'(x)$ obey a normal distribution, but with different parameters.

If, however, the normalized deviations $z_i' = (m_i' - \bar{m}_i')/\sigma(m_i') = (m_i' - \bar{m}_i')/\sqrt{\bar{m}_i'}$ are used, all of them obey the same normal distribution with the parameters $\bar{z}_i' = 0$, $\sigma(z_i') = 1$:

$$P(z_i') = \frac{1}{\sqrt{2\pi}} e^{-\frac{1}{2}(z_i')^2}. \tag{23}$$

Consequently, the sum over all the ℓ intervals $\sum_{i=1}^{\ell}(z_i)^2$ (z_i are here the experimental results) is the value χ^2 (see (19)). In other words, the random deviations of the measured ordinates $\bar{m}_i(x)$ of the histogram from their mathematical expectations $m_i'(x)$ in all ℓ intervals of the histogram can be described by a single random variable:

$$\chi^2 = \sum_{i=1}^{\ell} z_i^2. \tag{24}$$

Returning to the interpretation of the discrepancy between theory and experiment, described graphically in Figure 4, the validity of the null hypothesis will be assumed as before. Since a correct theory should predict the mathematical expectations of all m_i, it will be assumed that $\bar{m}_i' = m_i^*$. The value $\chi^2 = \sum_{i=1}^{\ell} z_i^2$ (24) describes the random fluctuations of all m_i around m_i^* with the normalization $\sum_{i=1}^{\ell} m_i = \sum_{i=1}^{\ell} m_i^*$, $s = 1$ (one constraint), and this χ^2 has $k = \ell - 1$ degrees of freedom. As a test of the agreement between theory and experiment in Figure 4 is taken the χ^2 with $k = \ell - 1$ degrees of freedom, so that $p_\kappa(\chi^2)$ is determined.

In practical applications of the χ^2-test, the value χ^2 is calculated from the experimental data

$$\chi_e^2 = \sum_{i=1}^{\ell} z_i^2 = \sum_{i=1}^{\ell} \left(\frac{m_i - m_i^*}{\sqrt{m_i^*}}\right)^2 \tag{25}$$

and a confidence level is chosen. A right-handed test is used in the case that the theory provides a poor description of the experimental data, and the boundary value $(\chi^2)_\beta''$ is calculated from the equation

$$\beta = \int_{(\chi^2)_\beta''}^{\infty} p_\kappa(\chi^2)\, d\chi^2, \quad \kappa = \ell - 1. \tag{26}$$

The left-handed test is used in cases that the agreement between theory and experiment seems to be too good and their exists a suspicion of tampering with the data. In this case $(\chi^2)_\beta'$ is calculated from the equation

$$\beta = \int_{0}^{(\chi^2)_\beta'} p_\kappa(\chi^2)\, d\chi^2, \quad \kappa = \ell - 1. \tag{27}$$

As before, if χ_e^2 is statistically significant, the theory is rejected (or a possibility of biases in the data is investigated), and if χ_e^2 is statistically insignificant, it is assumed that the theory is valid. There always exists the danger that there is a discrepancy between theory and experiment which is masked by random fluctuations. It should be remembered that if the experiment is compared with two (or more) theories, and if in both

cases the values of the χ^2_* are statistically insignificant, their values cannot be used for the selection of the more "correct" theory.

The χ^2-test can be criticized on several grounds: the choice of the histogram intervals is quite arbitrary, and there is a loss of sometimes vital experimental information by the grouping of the experimental results into intervals. In addition, the probability distribution of the number of counts in each interval is, strictly speaking, not normal (it is assumed that the deviations from a normal distribution are negligible for $m_i(x) \geq 5-10$, with smaller values of m_i it is recommended to combine neighboring intervals of the histogram). All these factors reduce the power of the χ^2-test, and it is therefore recommended for χ^2_*-values which are statistically insignificant to test the result by using other tests. The necessity for additional checks can be established in a simple way. In each interval of the histogram in Figure 4 the sign of the difference between experimental and theoretical values of the ordinate is determined. If the sequence of the signs does not display any appreciable order, this constitutes additional proof that the deviations between theory and experiment are negligible. If the sign distribution shows an apparent order, the results of the χ^2-test should be regarded with suspicion.

c. The comparison of an experimentally estimated dispersion $s^2(x)$ with a known theoretical dispersion σ^2. A random variable x with a normal distribution having a dispersion σ^2 is studied. From n measurements $x_1, x_2, \ldots, x_n$ the experimental estimate of the dispersion $s^2(x)$ is computed, and it turns out that $s^2(x) \neq \sigma^2$. The choice between the null and alternative hypotheses in order to explain the result can be achieved by using the χ^2-test. It is known /2/ that if the null hypothesis is valid, the random quantity $(n-1)\cdot\frac{s^2(x)}{\sigma^2(x)}$ has a χ^2-distribution with $k = n-1$ degrees of freedom, i.e.,

$$(n-1)\frac{s^2(x)}{\sigma^2(x)} = \chi^2, \quad \kappa = n-1, \tag{28}$$

and consequently $p_{H_0} = p_\kappa(\chi^2)$ is determined. The further analysis is similar to the procedure discussed above.

d. The χ^2-test as a test of the homogeneity of two experimental distributions. The random variable x, whose probability distribution is unknown, was measured n_1 times, and from the measurements a histogram, similar to that in Figure 4, was plotted with ℓ intervals; m_{1i} are the ordinates and $\sum_{i=1}^{\ell} m_{1i} = n_1$. A repeated (or parallel) experiment was performed with n_2 measurements and once again a histogram was plotted, where m_{2i} are the ordinates and $\sum_{i=1}^{\ell} m_{2i} = n_2$. Can it be assumed that both histograms come from the same probability distribution p(x) (H_0 hypothesis) or not (H_1 hypothesis)? This problem can be analyzed using the χ^2-test. A random quantity can be constructed /2/ which under the assumption of the validity of the null hypothesis describes the deviation of one histogram from the other. It has a χ^2-distribution with $k = \ell - 1$ degrees of freedom. This quantity has the form

$$\chi^2 = n_1 \cdot n_2 \cdot \sum_{i=1}^{\ell} \frac{1}{m_{1i} + m_{2i}} \left(\frac{m_{1i}}{n_1} - \frac{m_{2i}}{n_2} \right)^2. \tag{29}$$

TABLE 3. Boundary values $(\chi^2_{\beta})''$ for the χ^2-test (right-handed variant)

K	β			K	β		
	0.05	0.01	0.001		0.05	0.01	0.001
1	3.84	6.63	10.8	26	38.9	45.6	54.1
2	5.99	9.21	13.8	27	40.1	47.0	55.5
3	7.81	11.3	16.3	28	41.3	48.3	56.9
4	9.49	13.3	18.5	29	42.6	49.6	58.3
5	11.1	15.1	20.5	30	43.8	50.9	59.7
6	12.6	16.8	22.5	31	45.0	52.2	61.1
7	14.1	18.5	24.3	32	46.2	53.5	62.5
8	15.5	20.1	26.1	33	47.4	54.8	63.9
9	16.9	21.7	27.9	34	48.6	56.1	65.2
10	18.3	23.2	29.6	35	49.8	57.3	66.6
11	19.7	24.7	31.3	36	51.0	58.6	68.0
12	21.0	26.2	32.9	37	52.2	59.9	69.3
13	22.4	27.7	34.5	38	53.4	61.2	70.7
14	23.7	29.1	36.1	39	54.6	62.4	72.1
15	25.0	30.6	37.7	40	55.8	63.7	73.4
16	26.3	32.0	39.3	41	56.9	65.0	74.7
17	27.6	33.4	40.8	42	58.1	66.2	76.1
18	28.9	34.8	42.3	43	59.3	67.5	77.4
19	30.1	36.2	43.8	44	60.5	68.7	78.7
20	31.4	37.6	45.3	45	61.7	70.0	80.1
21	32.7	38.9	46.8	46	62.8	71.2	81.4
22	33.9	40.3	48.3	47	64.0	72.4	82.7
23	35.2	41.6	49.7	48	65.2	73.7	84.0
24	36.4	43.0	51.2	49	66.3	74.9	85.4
25	37.7	44.3	52.6	50	67.5	76.2	86.7

K	β			K	β		
	0.05	0.01	0.001		0.05	0.01	0.001
51	68.7	77.4	88.0	76	97.4	107.6	119.9
52	69.8	78.6	89.3	77	98.5	108.8	121.1
53	71.0	79.8	90.6	78	99.6	110.0	122.3
54	72.2	81.1	91.9	79	100.7	111.1	123.6
55	73.3	82.3	93.2	80	101.9	112.3	124.8
56	74.5	83.5	94.5	81	103.0	113.5	126.1
57	75.6	84.7	95.8	82	104.1	114.7	127.3
58	76.8	86.0	97.0	83	105.3	115.9	128.6
59	77.9	87.2	98.3	84	106.4	117.1	129.8
60	79.1	88.4	99.6	85	107.5	118.2	131.0
61	80.2	89.6	100.9	86	108.6	119.4	132.3
62	81.4	90.8	102.2	87	109.8	120.6	133.5
63	82.5	92.0	103.4	88	110.9	121.8	134.7
64	83.7	93.2	104.7	89	112.0	122.9	136.0
65	84.8	94.4	106.0	90	113.1	124.1	137.2
66	86.0	95.6	107.3	91	114.3	125.3	138.4
67	87.1	96.8	108.5	92	115.4	126.5	139.7
68	88.3	98.0	109.8	93	116.5	127.6	140.9
69	89.4	99.2	111.1	94	117.6	128.8	142.1
70	90.5	100.4	112.3	95	118.8	130.0	143.3
71	91.7	101.6	113.6	96	119.9	131.1	144.6
72	92.8	102.8	114.8	97	121.0	132.3	145.8
73	93.9	104.0	116.1	98	122.1	133.5	147.0
74	95.1	105.2	117.3	99	123.2	134.6	148.2
75	96.2	106.4	118.6	100	124.3	135.8	149.4

Thus $p_{n_0}(\chi^2)$ is determined, and calculating χ_0^2 from (29) and choosing a confidence level β, it can be determined whether the deviation between the two histograms is significant or not. In Table 3 the values of χ_β^2 are listed for a right-handed test for different values of k and β.

3. ω^2-test. The critical remarks made concerning the χ^2-test, when it is used in the analysis of the agreement between theoretical and experimental histograms, motivates us to verify the result $(\chi_0^2 < (\chi^2)_\beta'')$ by other methods. For this purpose the ω^2-test is used, whose mathematical logic does not raise any critique and the experimental results do not lose their individuality. The use of this test is, however, slightly more complicated than in the case of the χ^2-test. A random variable x is studied experimentally with the purpose of checking an assumed distribution p(x), whose analytical form is known. As a result of the experiment n numerical values of x are obtained. These values are ordered according to their numerical values, and a variational sequence is obtained $x_1 < x_2 < \ldots < x_n$. From these data an experimental integral distribution $W_n(x)$ is obtained. $W_n(x_k)$ is the frequency of the occurence of events $x < x_k$ found from the variational sequence:

$$\left.\begin{aligned} &W_n(x < x_1) = 0 \\ &W_n(x_k \le x \le x_{k+1}) = \frac{k}{n}, \quad 1 \le k \le n-1 \\ &W_n(x \ge x_n) = 1 \end{aligned}\right\}, \tag{30}$$

The distribution $W_n(x)$ (a step function increasing from 0 to 1 with an increase in x_k) is compared with the theoretical integral distribution P(x):

$$P(x) = \int_{-\infty}^{x} p(x)\,dx, \tag{31}$$

and some disagreement is observed. Assuming the validity of the null hypothesis H_0, this disagreement can be described by the random variable ω^2:

$$\omega^2 = \int_{-\infty}^{+\infty} [W_n(x) - P(x)]^2 \cdot p(x) \cdot dx. \tag{32}$$

After the range of integration in (32) is divided into n+1 intervals in accordance with the length of the steps of $W_n(x)$, then using (30), expression (32) can be written as

$$\omega^2 = \int_{-\infty}^{x_1} [0 - P(x)]^2 p(x)\,dx + \sum_{k=1}^{n-1} \int_{x_k}^{x_{k+1}} \left[\frac{k}{n} - P(x)\right]^2 p(x)\,dx + \int_{x_n}^{\infty} [1 - P(x)]^2 p(x)\,dx,$$

which, after some rearranging can be written in a form convenient for practical applications:

$$\omega^2 = \frac{1}{12 \cdot n^2} + \frac{1}{n} \sum_{k=1}^{n} \left[P(x_k) - \frac{2k-1}{2n}\right]^2, \tag{33}$$

where $P(x_k) = \int_{-\infty}^{x_k} p(x)\,dx$.

The exact distribution $p_{H_0}(\omega^2)$ of the random variable ω^2 is quite complicated and is given in the original articles only. It was established, however, that if the number of measurements $n > 40$, the distribution of the product $n \cdot \omega^2$ is close to some asymptotic form from which the boundary values $(n \cdot \omega^2)''_\beta$ (right-handed test) can be calculated for different values of the confidence level β:

β	0.1	0.05	0.03	0.02	0.01
$(n\omega^2)''_\beta$	0.3473	0.4614	0.5489	0.6198	0.7435 .

In practical applications of the ω^2-test the value of $(n \cdot \omega^2)$ is calculated according to (33) from the values x_κ of the variational sequence and compared with the above table.

4. The Student test. a. Random variable t. In order to estimate the random deviation of the statistical estimate of the mathematical expectation $\bar{x}_a$ from the true mathematical expectation $\bar{x}$ of a random variable x which obeys a normal distribution with an unknown dispersion, Student introduced the random variable t:

$$t = \frac{\bar{x}_{ap} - \bar{x}}{\frac{S(x)}{\sqrt{n}}}, \tag{34}$$

where n is the number of measurements of x and S(a) is the statistical estimate of the standard deviation. The density distribution p(t) was derived by Student and has the shape:

$$p(t) = \frac{1}{\sqrt{\pi k}} \frac{\Gamma\left(\frac{k+1}{2}\right)}{\Gamma\left(\frac{k}{2}\right)} \cdot \left(1 + \frac{t^2}{k}\right)^{-\frac{k+1}{2}}, \quad -\infty < t < \infty, \tag{35}$$

where $k = n - 1$ is the number of degrees of freedom of t and Γ is the gamma function. The distribution p(t) is bell-shaped, and for $n > 30$ it practically coincides with the normal distribution with a mean of zero and a standard deviation of unity. For smaller values of n, p(t) becomes flatter. In some practical situations the random variable t can be used as a goodness of fit test.

b. The comparison of an experimentally determined mathematical expectation with theoretical predictions. For the estimate of the statistical significance of the detected deviation $\bar{x}_a \neq \bar{x}$ ($\bar{x}$ is the theoretical prediction) the random variable t should be used. From (34) is calculated the experimental value of the Student criterion t_e, and for a given value of confidence level β the boundary value t_β is calculated from (35). Thus, for a right-handed test t_β is found from the following equation:

$$\beta = \int_{t_\beta}^{\infty} p_\kappa(t) \cdot dt. \tag{36}$$

The values of t_β for given values of k and β can be found in Table 4, where the absolute values of t_β for a two-sided test, $\alpha = 1/2$ in (8), and $|t'_\beta| = |t''_\beta| = |t_\beta|$ due to the symmetry of p(t) around zero are given. The values of $|t_\beta|$ in the table were derived from the equation:

$$\frac{\beta}{2} = \int_{t_\beta}^{\infty} p_\kappa(t)\, dt. \tag{37}$$

Therefore, when finding the boundary value of t''_β (or of t'_β) for a given value of β in a one-sided test, a confidence level equal to 2β should be used in Table 4. The above test can be used, when $\bar{x}$ is well known, in the search of systematic errors.

TABLE 4. The boundary values $|t_\beta|$ for the Student test (two-sided variant)

K	β 0.3	0.2	0.1	0.05	0.02	0.01
1	1.963	3.078	6.314	12.706	31.821	63.657
2	1.386	1.886	2.920	4.303	6.965	9.925
3	1.250	1.638	2.353	3.182	4.541	5.841
4	1.190	1.533	2.132	2.776	3.747	4.604
5	1.156	1.476	2.015	2.571	3.365	4.032
6	1.134	1.440	1.943	2.447	3.143	3.707
7	1.119	1.415	1.895	2.365	2.998	3.499
8	1.108	1.397	1.860	2.306	2.896	3.355
9	1.100	1.383	1.833	2.262	2.821	3.250
10	1.093	1.372	1.812	2.228	2.764	3.169
11	1.088	1.363	1.796	2.201	2.718	3.106
12	1.083	1.356	1.782	2.179	2.681	3.055
13	1.079	1.350	1.771	2.160	2.650	3.012
14	1.076	1.345	1.761	2.145	2.624	2.977
15	1.074	1.341	1.753	2.131	2.602	2.947
16	1.071	1.337	1.746	2.120	2.583	2.921
17	1.069	1.333	1.740	2.110	2.567	2.898
18	1.067	1.330	1.734	2.101	2.552	2.878
19	1.066	1.328	1.729	2.093	2.539	2.861
20	1.064	1.325	1.725	2.086	2.528	2.845
21	1.063	1.323	1.721	2.080	2.518	2.831
22	1.061	1.321	1.717	2.074	2.508	2.819
23	1.060	1.319	1.714	2.069	2.500	2.807
24	1.059	1.318	1.711	2.064	2.492	2.707
25	1.058	1.316	1.708	2.060	2.485	2.787
26	1.058	1.315	1.706	2.056	2.479	2.779
27	1.057	1.314	1.703	2.052	2.473	2.771
28	1.056	1.313	1.701	2.048	2.467	2.763
29	1.055	1.311	1.699	2.045	2.462	2.756
30	1.055	1.310	1.697	2.042	2.457	2.750
∞	1.03643	1.28155	1.64485	1.95996	2.32634	2.57582

c. The comparison of two experimental estimates of a mathematical expectation. Given that a random variable x, which is normally distributed with unknown $\bar{x}$ and $\sigma^2(x)$, is being studied. From n_1 measurements $x_{11} x_{12} \dots x_{1i} \dots x_{1n_1}$ the result $\bar{x}_{1a} = \frac{1}{n_1}\sum_{i=1}^{n_1} x_{1i}$ is obtained, and from n_2 repeated (or parallel) measurements the result $\bar{x}_{2a} = \frac{1}{n_2}\sum_{i=1}^{n_2} x_{2i}$. It turns out that $\bar{x}_{1a} \neq \bar{x}_{2a}$. In the analysis of such a case a Student test can be used.

TABLE 5. The boundary values F'_{β} of the Fisher test (right-handed variant). Confidence and denominator in $F = \frac{S_1^2}{S_2^2}$

K_2	K_1 for I	2	3	4	5	6	7	8	9	I0	II	I2	I3	I4	I5
I	I6I	200	2I6	225	230	234	237	239	24I	242	243	244	245	245	246
2	I8.5	I9.0	I9.2	I9.2	I9.3	I9.3	I9.4	I9.4	I9.4	I9.4	I9.4	I9.4	I9.4	I9.4	I9.4
3	I0.I	9.55	9.28	9.I2	9.0I	8.94	8.89	8.85	8.8I	8.79	8.76	8.74	8.73	8.7I	8.70
4	7.7I	6.94	6.59	6.39	6.26	6.I6	6.09	6.04	6.00	5.96	5.94	5.9I	5.89	5.87	5.86
5	6.6I	5.79	5.4I	5.I9	5.05	4.95	4.88	4.82	4.77	4.74	4.70	4.68	4.66	4.64	4.62
6	5.99	5.I4	4.76	4.53	4.39	4.28	4.2I	4.I5	4.I0	4.06	4.03	4.00	3.98	3.96	3.94
7	5.59	4.74	4.35	4.I2	3.97	3.87	3.79	3.73	3.68	3.64	3.60	3.57	3.55	3.53	3.5I
8	5.32	4.46	4.07	3.84	3.69	3.58	3.50	3.44	3.39	3.35	3.3I	3.28	3.26	3.24	3.22
9	5.I2	4.26	3.86	3.63	3.48	3.37	3.29	3.23	3.I8	3.I4	3.I0	3.07	3.05	3.03	3.0I
I0	4.96	4.I0	3.7I	3.48	3.33	3.22	3.I4	3.07	3.02	2.98	2.94	2.9I	2.89	2.86	2.85
II	4.84	3.98	3.59	3.36	3.20	3.09	3.0I	2.95	2.90	2.85	2.82	2.79	2.76	2.74	2.72
I2	4.75	3.89	3.49	3.26	3.II	3.00	2.9I	2.85	2.80	2.75	2.72	2.69	2.66	2.64	2.62
I3	4.67	3.8I	3.4I	3.I8	3.03	2.92	2.83	2.77	2.7I	2.67	2.63	2.60	2.58	2.55	2.53
I4	4.60	3.74	3.34	3.II	2.96	2.85	2.76	2.70	2.65	2.60	2.57	2.53	2.5I	2.48	2.46
I5	4.54	3.68	3.29	3.06	2.90	2.79	2.7I	2.64	2.59	2.54	2.5I	2.48	2.45	2.42	2.40
I6	4.49	3.63	3.24	3.0I	2.85	2.74	2.66	2.59	2.54	2.49	2.46	2.42	2.40	2.37	2.35
I7	4.45	3.59	3.20	2.96	2.8I	2.70	2.6I	2.55	2.49	2.45	2.4I	2.38	2.35	2.33	2.3I
I8	4.4I	3.55	3.I6	2.93	2.77	2.66	2.58	2.5I	2.46	2.4I	2.37	2.34	2.3I	2.29	2.27
I9	4.38	3.52	3.I3	2.90	2.74	2.63	2.54	2.48	2.42	2.38	2.34	2.3I	2.28	2.26	2.23
20	4.35	3.49	3.I0	2.87	2.7I	2.60	2.5I	2.45	2.39	2.35	2.3I	2.28	2.25	2.22	2.20
2I	4.32	3.47	3.07	2.84	2.68	2.57	2.49	2.42	2.37	2.32	2.28	2.25	2.22	2.20	2.I8
22	4.30	3.44	3.05	2.82	2.66	2.55	2.46	2.40	2.34	2.30	2.26	2.23	2.20	2.I7	2.I5
23	4.28	3.42	3.03	2.80	2.64	2.53	2.44	2.37	2.32	2.27	2.23	2.20	2.I8	2.I5	2.I3
24	4.26	3.40	3.0I	2.78	2.62	2.5I	2.42	2.36	2.30	2.25	2.2I	2.I8	2.I5	2.I3	2.II
25	4.24	3.39	2.99	2.76	2.60	2.49	2.40	2.34	2.28	2.24	2.20	2.I6	2.I4	2.II	2.09
26	4.23	3.37	2.98	2.74	2.59	2.47	2.39	2.32	2.27	2.22	2.I8	2.I5	2.I2	2.09	2.07
27	4.2I	3.35	2.96	2.73	2.57	2.46	2.37	2.3I	2.25	2.20	2.I7	2.I3	2.I0	2.08	2.06
28	4.20	3.34	2.95	2.7I	2.56	2.45	2.36	2.29	2.24	2.I9	2.I5	2.I2	2.09	2.06	2.04
29	4.I8	3.33	2.93	2.70	2.55	2.43	2.35	2.28	2.22	2.I8	2.I4	2.I0	2.08	2.05	2.03
30	4.I7	3.32	2.92	2.69	2.53	2.42	2.33	2.27	2.2I	2.I6	2.I3	2.09	2.06	2.04	2.0I
32	4.I5	3.29	2.90	2.67	2.5I	2.40	2.3I	2.24	2.I9	2.I4	2.I0	2.07	2.04	2.0I	I.99
34	4.I3	3.28	2.88	2.65	2.49	2.38	2.29	2.23	2.I7	2.I2	2.08	2.05	2.02	I.99	I.97
36	4.II	3.26	2.87	2.63	2.48	2.36	2.28	2.2I	2.I5	2.II	2.07	2.03	2.00	I.98	I.95
38	4.I0	3.24	2.85	2.62	2.46	2.35	2.26	2.I9	2.I4	2.09	2.05	2.02	I.99	I.96	I.94
40	4.08	3.23	2.84	2.6I	2.45	2.34	2.25	2.I8	2.I2	2.08	2.04	2.00	I.97	I.95	I.92
42	4.07	3.22	2.83	2.59	2.44	2.32	2.24	2.I7	2.II	2.06	2.03	I.99	I.96	I.93	I.9I
44	4.06	3.2I	2.82	2.58	2.43	2.3I	2.23	2.I6	2.I0	2.05	2.0I	I.98	I.95	I.92	I.90
46	4.05	3.20	2.8I	2.57	2.42	2.30	2.22	2.I5	2.09	2.04	2.00	I.97	I.94	I.9I	I.89
48	4.04	3.I9	2.80	2.57	2.4I	2.29	2.2I	2.I4	2.08	2.03	I.99	I.96	I.93	I.90	I.88
50	4.03	3.I8	2.79	2.56	2.40	2.29	2.20	2.I3	2.07	2.03	I.99	I.95	I.92	I.89	I.87
60	4.00	3.I5	2.76	2.53	2.37	2.25	2.I7	2.I0	2.04	I.99	I.95	I.92	I.89	I.86	I.84
70	3.98	3.I3	2.74	2.50	2.35	2.23	2.I4	2.07	2.02	I.97	I.93	I.89	I.86	I.84	I.8I
80	3.96	3.II	2.72	2.49	2.33	2.2I	2.I3	2.06	2.00	I.95	I.9I	I.88	I.84	I.82	I.79
90	3.95	3.I0	2.7I	2.47	2.32	2.20	2.II	2.04	I.99	I.94	I.90	I.86	I.83	I.80	I.78
I00	3.94	3.09	2.70	2.46	2.3I	2.I9	2.I0	2.03	I.97	I.93	I.89	I.85	I.82	I.79	I.77
I25	3.92	3.07	2.68	2.44	2.29	2.I7	2.08	2.0I	I.96	I.9I	I.87	I.83	I.80	I.77	I.75
I50	3.90	3.06	2.66	2.43	2.27	2.I6	2.07	2.00	I.94	I.89	I.85	I.82	I.79	I.76	I.73
200	3.89	3.04	2.65	2.42	2.26	2.I4	2.06	I.98	I.93	I.88	I.84	I.80	I.77	I.74	I.72
300	3.87	3.03	2.63	2.40	2.24	2.I3	2.04	I.97	I.9I	I.86	I.82	I.78	I.75	I.72	I.70
500	3.86	3.0I	2.62	2.39	2.23	2.I2	2.03	I.96	I.90	I.85	I.8I	I.77	I.74	I.7I	I.69
I000	3.85	3.00	2.6I	2.38	2.22	2.II	2.02	I.95	I.89	I.84	I.80	I.76	I.73	I.70	I.68

levels $\beta = 0.05$ and 0.01. k_1 and k_2 are number of degrees of freedom of the numerator and

$\beta = 0.05$

16	17	18	19	20	22	24	26	28	30	40	50	60	80	100
246	247	247	248	248	249	249	249	250	250	251	252	252	252	253
19.4	19.4	19.4	19.4	19.4	19.5	19.5	19.5	19.5	19.5	19.5	19.5	19.5	19.5	19.5
8.69	8.68	8.67	8.67	8.66	8.65	8.64	8.63	8.62	8.62	8.59	8.58	8.57	8.56	8.55
5.84	5.83	5.82	5.81	5.80	5.79	5.77	5.76	5.75	5.75	5.72	5.70	5.69	5.67	5.66
4.60	4.59	4.58	4.57	4.56	4.54	4.53	4.52	4.50	4.50	4.46	4.44	4.43	4.41	4.41
3.92	3.91	3.90	3.88	3.87	3.86	3.84	3.83	3.82	3.81	3.77	3.75	3.74	3.72	3.71
3.49	3.48	3.47	3.46	3.44	3.43	3.41	3.40	3.39	3.38	3.34	3.32	3.30	3.29	3.27
3.20	3.19	3.17	3.16	3.15	3.13	3.12	3.10	3.09	3.08	3.04	3.02	3.01	2.99	2.97
2.99	2.97	2.96	2.95	2.94	2.92	2.90	2.89	2.87	2.86	2.83	2.80	2.79	2.77	2.76
2.83	2.81	2.80	2.78	2.77	2.75	2.74	2.72	2.71	2.70	2.66	2.64	2.62	2.60	2.59
2.70	2.69	2.67	2.66	2.65	2.63	2.61	2.59	2.58	2.57	2.53	2.51	2.49	2.47	2.46
2.60	2.58	2.57	2.56	2.54	2.52	2.51	2.49	2.48	2.47	2.43	2.40	2.38	2.36	2.35
2.51	2.50	2.48	2.47	2.46	2.44	2.42	2.41	2.39	2.38	2.34	2.31	2.30	2.27	2.26
2.44	2.43	2.41	2.40	2.39	2.37	2.35	2.33	2.32	2.31	2.27	2.24	2.22	2.20	2.19
2.38	2.37	2.35	2.34	2.33	2.31	2.29	2.27	2.26	2.25	2.20	2.18	2.16	2.14	2.12
2.33	2.32	2.30	2.29	2.28	2.25	2.24	2.22	2.21	2.19	2.15	2.12	2.11	2.08	2.07
2.29	2.27	2.26	2.24	2.23	2.21	2.19	2.17	2.16	2.15	2.10	2.08	2.06	2.03	2.02
2.25	2.23	2.22	2.20	2.19	2.17	2.15	2.13	2.12	2.11	2.06	2.04	2.02	1.99	1.98
2.21	2.20	2.18	2.17	2.16	2.13	2.11	2.10	2.08	2.07	2.03	2.00	1.98	1.96	1.94
2.18	2.17	2.15	2.14	2.12	2.10	2.08	2.07	2.05	2.04	1.99	1.97	1.95	1.92	1.91
2.16	2.14	2.12	2.11	2.10	2.07	2.05	2.04	2.02	2.01	1.96	1.94	1.92	1.86	1.88
2.13	2.11	2.10	2.08	2.07	2.05	2.03	2.01	2.00	1.98	1.94	1.91	1.89	1.86	1.85
2.11	2.09	2.07	2.06	2.05	2.02	2.00	1.99	1.97	1.96	1.91	1.88	1.86	1.84	1.82
2.09	2.07	2.05	2.04	2.03	2.00	1.98	1.97	1.95	1.94	1.89	1.86	1.84	1.82	1.80
2.07	2.05	2.04	2.02	2.01	1.98	1.96	1.95	1.93	1.92	1.87	1.84	1.82	1.80	1.78
2.05	2.03	2.02	2.00	1.99	1.97	1.95	1.93	1.91	1.90	1.85	1.82	1.80	1.78	1.76
2.04	2.02	2.00	1.99	1.97	1.95	1.93	1.91	1.90	1.88	1.84	1.81	1.79	1.76	1.74
2.02	2.00	1.99	1.97	1.96	1.93	1.91	1.90	1.88	1.87	1.82	1.79	1.77	1.74	1.73
2.01	1.99	1.97	1.96	1.94	1.92	1.90	1.88	1.87	1.85	1.81	1.77	1.75	1.73	1.71
1.99	1.98	1.96	1.95	1.93	1.91	1.89	1.87	1.85	1.84	1.79	1.76	1.74	1.71	1.70
1.97	1.95	1.94	1.92	1.91	1.88	1.86	1.85	1.83	1.82	1.77	1.74	1.71	1.69	1.67
1.95	1.93	1.92	1.90	1.89	1.86	1.84	1.82	1.80	1.80	1.75	1.71	1.69	1.66	1.65
1.93	1.92	1.90	1.88	1.87	1.85	1.82	1.81	1.79	1.78	1.73	1.69	1.67	1.64	1.62
1.92	1.90	1.88	1.87	1.85	1.83	1.81	1.79	1.77	1.76	1.71	1.68	1.65	1.62	1.61
1.90	1.89	1.87	1.85	1.84	1.81	1.79	1.77	1.76	1.74	1.69	1.66	1.64	1.61	1.59
1.89	1.87	1.86	1.84	1.83	1.80	1.78	1.76	1.74	1.73	1.68	1.65	1.62	1.59	1.57
1.88	1.86	1.84	1.83	1.81	1.79	1.77	1.75	1.73	1.72	1.67	1.63	1.61	1.58	1.56
1.87	1.85	1.83	1.82	1.80	1.78	1.76	1.74	1.72	1.71	1.65	1.62	1.60	1.57	1.55
1.86	1.84	1.82	1.81	1.79	1.77	1.75	1.73	1.71	1.70	1.64	1.61	1.59	1.56	1.54
1.85	1.83	1.81	1.80	1.78	1.76	1.74	1.72	1.70	1.69	1.63	1.60	1.58	1.54	1.52
1.82	1.80	1.78	1.76	1.75	1.72	1.70	1.68	1.66	1.65	1.59	1.56	1.53	1.50	1.48
1.79	1.77	1.75	1.74	1.72	1.70	1.67	1.65	1.64	1.62	1.57	1.53	1.50	1.47	1.45
1.77	1.75	1.73	1.72	1.70	1.68	1.65	1.63	1.62	1.60	1.54	1.51	1.48	1.45	1.43
1.76	1.74	1.72	1.70	1.69	1.66	1.64	1.62	1.60	1.59	1.53	1.49	1.46	1.43	1.41
1.75	1.73	1.71	1.69	1.68	1.65	1.63	1.61	1.59	1.57	1.52	1.48	1.45	1.41	1.39
1.72	1.70	1.69	1.67	1.65	1.63	1.60	1.58	1.57	1.55	1.49	1.45	1.42	1.39	1.36
1.71	1.69	1.67	1.66	1.64	1.61	1.59	1.57	1.55	1.53	1.48	1.44	1.41	1.37	1.34
1.69	1.67	1.66	1.64	1.62	1.60	1.57	1.55	1.53	1.52	1.46	1.41	1.39	1.35	1.32
1.68	1.66	1.64	1.62	1.61	1.58	1.55	1.53	1.51	1.50	1.43	1.39	1.36	1.32	1.30
1.66	1.64	1.62	1.61	1.59	1.56	1.54	1.52	1.50	1.48	1.42	1.38	1.34	1.30	1.28
1.65	1.63	1.61	1.60	1.58	1.55	1.53	1.51	1.49	1.47	1.41	1.36	1.33	1.29	1.26

TABLE 5 (cont'd)

N_2	N_1 for I	2	3	4	5	6	7	8	9	I0	II	I2	I3	I4	I5
2	98.5	99.0	99.2	99.2	99.3	99.3	99.4	99.4	99.4	99.4	99.4	99.4	99.4	99.4	99.4
3	34.I	30.8	29.5	28.7	28.2	27.9	27.7	27.5	27.3	27.2	27.I	27.I	27.0	26.9	26.9
4	2I.2	I8.0	I6.7	I6.0	I5.5	I5.2	I5.0	I4.8	I4.7	I4.5	I4.4	I4.4	I4.3	I4.2	I4.2
5	I6.3	I3.3	I2.I	II.4	II.0	I0.7	I0.5	I0.3	I0.2	I0.I	9.96	9.89	9.82	9.77	9.72
6	I3.7	I0.9	9.78	9.I5	8.75	8.47	8.26	8.I0	7.98	7.87	7.79	7.72	7.66	7.60	7.56
7	I2.2	9.55	8.45	7.85	7.46	7.I9	6.99	6.84	6.72	6.62	6.54	6.47	6.4I	6.36	6.3I
8	II.3	8.65	7.59	7.0I	6.63	6.37	6.I8	6.03	5.9I	5.8I	5.73	5.67	5.6I	5.56	5.52
9	I0.6	8.02	6.99	6.42	6.06	5.80	5.6I	5.47	5.35	5.26	5.I8	5.II	5.05	5.00	4.96
I0	I0.0	7.56	6.55	5.99	5.64	5.39	5.20	5.06	4.94	4.85	4.77	4.7I	4.65	4.60	4.56
II	9.65	7.2I	6.22	5.67	5.32	5.07	4.89	4.74	4.63	4.54	4.46	4.40	4.34	4.29	4.25
I2	9.33	6.93	5.95	5.4I	5.06	4.82	4.64	4.50	4.39	4.30	4.22	4.I6	4.I0	4.05	4.0I
I3	9.07	6.70	5.74	5.2I	4.86	4.62	4.44	4.30	4.I9	4.I0	4.02	3.96	3.9I	3.86	3.82
I4	8.86	6.5I	5.56	5.04	4.69	4.46	4.28	4.I4	4.03	3.94	3.86	3.80	3.75	3.70	3.66
I5	8.68	6.36	5.42	4.89	4.56	4.32	4.I4	4.00	3.89	3.80	3.73	3.67	3.6I	3.56	3.52
I6	8.53	6.23	5.29	4.77	4.44	4.20	4.03	3.89	3.78	3.69	4.62	3.55	3.50	3.45	3.4I
I7	8.40	6.II	5.I8	4.67	4.34	4.I0	3.93	3.79	3.68	3.59	3.52	3.46	3.40	3.35	3.3I
I8	8.29	6.0I	5.09	4.58	4.25	4.0I	3.84	3.7I	3.60	3.5I	3.43	3.37	3.32	3.27	3.23
I9	8.I8	5.93	5.0I	4.50	4.I7	3.94	3.77	3.63	3.52	3.43	3.36	3.30	3.24	3.I9	3.I5
20	8.I0	5.85	4.94	4.43	4.I0	3.87	3.70	3.56	3.46	3.37	3.29	3.23	3.I8	3.I3	3.09
2I	8.02	5.78	4.87	4.37	4.04	3.8I	3.64	3.5I	3.40	3.3I	3.24	3.I7	3.I2	3.07	3.03
22	7.95	5.72	4.82	4.3I	3.99	3.76	3.59	3.45	3.35	3.26	3.I8	3.I2	3.07	3.02	2.98
23	7.88	5.66	4.76	4.26	3.94	3.7I	3.54	3.4I	3.30	3.2I	3.I4	3.07	3.02	2.97	2.93
24	7.82	5.6I	4.72	4.22	3.90	3.67	3.50	3.36	3.26	3.I7	3.09	3.03	2.98	2.93	2.89
25	7.77	5.57	4.68	4.I8	3.86	3.63	3.46	3.32	3.22	3.I3	3.06	2.99	2.94	2.89	2.85
26	7.72	5.53	4.64	4.I4	3.82	3.59	3.42	3.29	3.I8	3.09	3.02	2.96	2.90	2.86	2.82
27	7.68	5.49	4.60	4.II	3.78	3.56	3.39	3.26	3.I5	3.06	2.99	2.93	2.87	2.82	2.78
28	7.64	5.45	4.57	4.07	3.75	3.53	3.36	3.23	3.I2	3.03	2.96	2.90	2.84	2.79	2.75
29	7.60	5.42	4.54	4.04	3.73	3.50	3.33	3.20	3.09	3.00	2.93	2.87	2.8I	2.77	2.73
30	7.56	5.39	4.5I	4.02	3.70	3.47	3.30	3.I7	3.07	2.98	2.9I	2.84	2.79	2.74	2.70
32	7.50	5.34	4.46	3.97	3.65	3.43	3.26	3.I3	3.02	2.93	2.86	2.80	2.74	2.70	2.66
34	7.44	5.29	4.42	3.93	3.6I	3.39	3.22	3.09	2.98	2.89	2.82	2.76	2.70	2.66	2.62
36	7.40	5.25	4.38	3.89	3.57	3.35	3.I8	3.05	2.95	2.86	2.79	2.72	2.67	2.62	2.58
38	7.35	5.2I	4.34	3.86	3.54	3.32	3.I5	3.02	2.92	2.83	2.75	2.69	2.64	2.59	2.55
40	7.3I	5.I8	4.3I	3.83	3.5I	3.29	3.I2	2.99	2.89	2.80	2.73	2.66	2.6I	2.56	2.52
42	7.28	5.I5	4.29	3.80	2.49	3.27	3.I0	2.97	2.86	2.78	2.70	2.64	2.59	2.54	2.50
44	7.25	5.I2	4.26	3.78	3.47	3.24	3.08	2.95	2.84	2.75	2.68	2.62	2.56	2.52	2.47
46	7.22	5.I0	4.24	3.76	3.44	3.22	3.06	2.93	2.82	2.73	2.66	2.60	2.54	2.50	2.45
48	7.I9	5.08	4.22	3.74	3.43	3.20	3.04	2.9I	2.80	2.72	2.64	2.58	2.53	2.48	2.44
50	7.I7	5.06	4.20	3.72	3.4I	3.I9	3.02	2.89	2.79	2.70	2.63	2.56	2.5I	2.46	2.42
55	7.I2	5.0I	4.I6	3.68	3.37	3.I5	2.98	2.85	2.75	2.66	2.59	2.53	2.47	2.42	2.38
60	7.08	4.98	4.I3	3.65	3.34	3.I2	2.95	2.82	2.72	2.63	2.56	2.50	2.44	2.39	2.35
70	7.0I	4.92	4.08	3.60	3.29	3.07	2.9I	2.78	2.67	2.59	2.5I	2.45	2.40	2.35	2.3I
80	6.96	4.88	4.04	3.56	3.26	3.04	2.87	2.74	2.64	2.55	2.48	2.42	2.36	2.3I	2.27
90	6.93	4.85	4.0I	3.54	3.23	3.0I	2.84	2.72	2.6I	2.52	2.45	2.39	2.33	2.29	2.24
I00	6.90	4.82	3.98	3.5I	3.2I	2.99	2.82	2.69	2.59	2.50	2.43	2.37	2.3I	2.26	2.22
I25	6.84	4.78	3.94	3.47	3.I7	2.95	2.79	2.66	2.55	2.47	2.39	2.33	2.28	2.23	2.I9
I50	6.8I	4.75	3.92	3.45	3.I4	2.92	2.76	2.63	2.53	2.44	2.37	2.3I	2.25	2.20	2.I6
200	6.76	4.7I	3.88	3.4I	3.II	2.89	2.73	2.60	2.50	2.4I	2.34	2.27	2.22	2.I7	2.I3
300	6.72	4.68	3.85	3.38	3.08	2.86	2.70	2.57	2.47	2.38	2.3I	2.24	2.I9	2.I4	2.I0
500	6.69	4.65	3.82	3.36	3.05	2.84	2.68	2.55	2.44	2.36	2.28	2.22	2.I7	2.I2	2.07
I000	6.66	4.63	3.80	3.34	3.04	2.82	2.66	2.53	2.43	2.34	2.27	2.20	2.I5	2.I0	2.06

$\alpha = 0.01$

16	17	18	19	20	22	24	26	28	30	40	50	60	80	100
99.4	99.4	99.4	99.4	99.4	99.5	99.5	99.5	99.5	99.5	99.5	99.5	99.5	99.5	99.5
26.8	26.8	26.8	26.7	26.7	26.6	26.6	26.6	26.5	26.5	26.4	26.4	26.3	26.3	26.2
14.2	14.1	14.1	14.0	14.0	14.0	13.9	13.9	13.9	13.8	13.7	13.7	13.7	13.6	13.6
9.68	9.64	9.61	9.58	9.55	9.51	9.47	9.43	9.40	9.38	9.29	9.24	9.20	9.16	9.13
7.52	7.48	7.45	7.42	7.40	7.35	7.31	7.28	7.25	7.23	7.14	7.09	7.06	7.01	6.99
6.27	6.24	6.21	6.18	6.16	6.11	6.07	6.04	6.02	5.99	5.91	5.86	5.82	5.78	5.75
5.48	5.44	5.41	5.38	5.36	5.32	5.28	5.25	5.22	5.20	5.12	5.07	5.03	4.99	4.96
4.92	4.89	4.86	4.83	4.81	4.77	4.73	4.70	4.67	4.65	4.57	4.52	4.48	4.44	4.42
4.52	4.49	4.46	4.43	4.41	4.36	4.33	4.30	4.27	4.25	4.17	4.12	4.08	4.04	4.01
4.21	4.18	4.15	4.12	4.10	4.06	4.02	3.99	3.96	3.94	3.86	3.81	3.78	3.73	3.71
3.97	3.94	3.91	3.88	3.86	3.82	3.78	3.75	3.72	3.70	3.62	3.57	3.54	3.49	2.47
3.78	3.75	3.72	3.69	3.66	3.62	3.59	3.56	2.53	3.51	3.43	3.38	3.34	3.30	3.27
3.62	3.59	3.56	3.53	3.51	3.46	3.43	3.40	3.37	3.35	3.27	3.22	3.18	3.14	3.11
3.49	3.45	3.42	3.40	3.37	3.33	3.29	3.26	3.24	3.21	3.13	3.08	3.05	3.00	2.98
3.37	3.34	3.31	3.28	3.26	3.22	3.18	3.15	3.12	3.10	3.02	2.97	2.93	2.89	2.86
3.27	3.24	3.21	3.18	3.16	3.12	3.08	3.05	3.03	3.00	2.92	2.87	2.83	2.79	2.76
3.19	3.16	3.13	3.10	3.08	3.03	3.00	2.97	2.94	2.92	2.84	2.78	2.75	2.70	2.68
3.12	3.08	3.05	3.03	3.00	2.96	2.92	2.89	2.87	2.84	2.76	2.71	2.67	2.63	2.60
3.05	3.02	2.99	2.96	2.94	2.90	2.86	2.83	2.80	2.78	2.69	2.64	2.61	2.56	2.54
2.99	2.96	2.93	2.90	2.88	2.84	2.80	2.77	2.74	2.72	2.64	2.58	2.55	2.50	2.48
2.94	2.91	2.88	2.85	2.83	2.78	2.75	2.72	2.69	2.67	2.58	2.53	2.50	2.45	2.42
2.89	2.86	2.83	2.80	2.78	2.74	2.70	2.67	2.64	2.62	2.54	2.48	2.45	2.40	2.37
2.85	2.82	2.79	2.76	2.74	2.70	2.66	2.63	2.60	2.58	2.49	2.44	2.40	2.36	2.33
2.81	2.78	2.75	2.72	2.70	2.66	2.62	2.59	2.56	2.54	2.45	2.40	2.36	2.32	2.29
2.78	2.74	2.72	2.69	2.66	2.62	2.58	2.55	2.53	2.50	2.42	2.36	2.33	2.28	2.25
2.75	2.71	2.68	2.66	2.63	2.59	2.55	2.52	2.49	2.47	2.38	2.33	2.29	2.25	2.22
2.72	2.68	2.65	2.63	2.60	2.56	2.52	2.49	2.46	2.44	2.35	2.30	2.26	2.22	2.19
2.69	2.66	2.63	2.60	2.57	2.53	2.49	2.46	2.44	2.41	2.33	2.27	2.23	2.19	2.16
2.66	2.63	2.60	2.57	2.55	2.51	2.47	2.44	2.41	2.39	2.30	2.25	2.21	2.16	2.13
2.62	2.58	2.55	2.53	2.50	2.46	2.42	2.39	2.36	2.34	2.25	2.20	2.16	2.11	2.08
2.58	2.55	2.51	2.49	2.46	2.42	2.38	2.35	2.32	2.30	2.21	2.16	2.12	2.07	2.04
2.54	2.51	2.48	2.45	2.43	2.38	2.35	2.32	2.29	2.26	2.17	2.12	2.08	2.03	2.00
2.51	2.48	2.45	2.42	2.40	2.35	2.32	2.28	2.26	2.23	2.14	2.09	2.05	2.00	1.97
2.48	2.45	2.42	2.39	2.37	2.33	2.29	2.26	2.23	2.20	2.11	2.06	2.02	1.97	1.94
2.46	2.43	2.40	2.37	2.34	2.30	2.26	2.23	2.20	2.18	2.09	2.03	1.99	1.94	1.91
2.44	2.40	2.37	2.35	2.32	2.28	2.24	2.21	2.18	2.15	2.06	2.01	1.97	1.92	1.89
2.42	2.38	2.35	2.33	2.30	2.26	2.22	2.19	2.16	2.13	2.04	1.99	1.95	1.90	1.86
2.40	2.37	2.33	2.31	2.28	2.24	2.20	2.17	2.14	2.12	2.02	1.97	1.93	1.88	1.84
2.38	2.35	2.32	2.29	2.27	2.22	2.18	2.15	2.12	2.10	2.01	1.95	1.91	1.86	1.82
2.34	2.31	2.28	2.25	2.23	2.18	2.15	2.11	2.08	2.06	1.97	1.91	1.87	1.81	1.78
2.31	2.28	2.25	2.22	2.20	2.15	2.12	2.08	2.05	2.03	1.94	1.88	1.84	1.78	1.75
2.27	2.23	2.20	2.18	2.15	2.11	2.07	2.03	2.01	1.98	1.89	1.83	1.78	1.73	1.70
2.23	2.20	2.17	2.14	2.12	2.07	2.03	2.00	1.97	1.94	1.85	1.79	1.75	1.69	1.66
2.21	2.17	2.14	2.11	2.09	2.04	2.00	1.97	1.94	1.92	1.82	1.76	1.72	1.66	1.62
2.19	2.15	2.12	2.09	2.07	2.02	1.98	1.94	1.92	1.89	1.80	1.73	1.69	1.63	1.60
2.15	2.11	2.08	2.05	2.03	1.98	1.94	1.91	1.88	1.85	1.76	1.69	1.65	1.59	1.55
2.12	2.09	2.06	2.03	2.00	1.96	1.92	1.88	1.85	1.83	1.73	1.66	1.62	1.56	1.52
2.09	2.06	2.02	2.00	1.97	1.93	1.89	1.85	1.82	1.79	1.69	1.63	1.58	1.52	1.48
2.06	2.03	1.99	1.97	1.94	1.89	1.85	1.82	1.79	1.76	1.66	1.59	1.55	1.48	1.44
2.04	2.00	1.97	1.94	1.92	1.87	1.83	1.79	1.76	1.74	1.63	1.56	1.52	1.45	1.41
2.02	1.98	1.95	1.92	1.90	1.85	1.81	1.77	1.74	1.72	1.61	1.54	1.50	1.43	1.38

Assuming the validity of the null hypothesis H_0, another random variable t can be constructed from the two random variables $\bar{x}_{1a}$ and $\bar{x}_{2a}$ /2/:

$$t = \sqrt{\frac{n_1 \cdot n_2 (n_1 + n_2 - 2)}{n_1 + n_2}} \cdot \frac{\bar{x}_{1a_0} - \bar{x}_{2ap}}{\sqrt{(n_1 - 1) S_1^2(x) + (n_2 - 1) S_2^2(x)}}, \qquad (38)$$

where $S^2(x) = \frac{1}{n-1} \sum_{i=1}^{n} (x_i - \bar{x}_a)^2$, which obeys a Student distribution (35) with $k = n_1 + n_2 - 2$ degrees of freedom. Choosing a confidence level β, t_β is calculated from (36). Comparing t_β with t_o, which was calculated from the experimental results according to (38), enables us to choose the more likely hypothesis between H_0 and H_1 (in this case H_1 describes the situation that in the two series of measurements random variables with different mathematical expectations were studied).

5. The Fisher test is used for the comparison of the results of two experiments intended to estimate the dispersion of a normally distributed random variable x. In the first experiment n_1 measurements were performed and the statistical estimate of the dispersion was obtained $S_1^2(x) = \frac{1}{n_1 - 1} \sum_{i=1}^{n_1} (x_{1i} - \bar{x}_{1a})^2$, in the second experiment based upon n_2 measurements the estimate $S_2^2(x) = \frac{1}{n_2 - 1} \sum_{i=1}^{n_2} (x_{2i} - \bar{x}_{2a})^2$ was obtained. The disagreement $S_1^2(x) \neq S_2^2(x)$ has to be interpreted.

In the case that there are only random fluctuations in the experimental data, Fisher derived the exact distribution of the random variable $F = S_1^2 / S_2^2$. The distribution p(F) is a function of two parameters $k_1 = n_1 - 1$ and $k_2 = n_2 - 1$, and has the following shape:

$$p(F) = \frac{\Gamma\left(\frac{k}{2}\right)}{\Gamma\left(\frac{k_1}{2}\right) \cdot \Gamma\left(\frac{k_2}{2}\right)} \cdot (k_1)^{\frac{k_1}{2}} \cdot (k_2)^{\frac{k_2}{2}} \cdot \frac{F^{\frac{k_1}{2} - 1}}{(k_2 + k_1 \cdot F)^{\frac{k}{2}}}, \quad 0 \leq F < \infty, \qquad (39)$$

where $k = k_1 + k_2$ and Γ is the gamma function. The form of the function p(F) is similar to $p(\chi^2)$ for $k > 2$. F is generally calculated as the ratio of the larger to the smaller values of the dispersion ($F_o > 1$). Therefore, a right-handed test is used and F_β'' is determined from

$$\beta = \int_{F_\beta''}^{\infty} p_{k_1 k_2}(F)\, dF, \qquad (40)$$

where β is the confidence level.

In Table 5 are given the values of F_β'' for various values of k_1 and k_2 and for two values of the confidence level β : 0.01 and 0.05.

Bibliography

1. Waerden, B. L. van der. Mathematische Statistik. Berlin, Springer. 1957.
2. Smirnov, N. V. and I. V. Dunin-Barkovskii. Kurs teorii veroyatnosti i matematicheskoi statistiki dlya tekhnicheskikh prilozhenii (Course on the Theory of Probability and Mathematical Statistics for Technical Supplements). — Moskva, Izdatel'stvo, Nauka. 1965.

O. B. Vasil'ev

ANALYSIS OF HIDDEN PERIODICITIES AND THE POSSIBILITY OF STATISTICAL PREDICTION

The analysis of hidden periodicities of a process is impossible without the exact knowledge of the properties of the function being analyzed, since, depending on the character of the process, a specific method of spectrum computation should be used. Below different function classes are analyzed according to their spectral types, a short review of the existing methods of obtaining spectrum estimates is given and one of the methods of determining the possibility of statistical prediction is described along with an estimate of the stability of the derived periods and their amplitudes. As an illustration the Zurich series of Wolf numbers (1749 — 1966) /1/ is used.

FUNCTIONS AND THEIR SPECTRA

The shape of the function's spectrum (satisfying the Dirichlet conditions) will depend first of all on whether the function is periodic, almost periodic, nonperiodic or random, and, secondly, on whether it is defined in a finite or infinite interval of its argument, at all points or only at separate ones. A survey of the spectrum determination of these function types according to the terminology of /2/ is presented in the table.

Periodic processes have a discrete harmonic spectrum. Also almost periodic functions have a discrete spectrum (except for the case where they are defined for all points in a finite interval); this likewise applies to functions which are defined at discrete points of a finite interval. In all other cases the functions have a continuous spectrum.

The discrete spectrum is always presented as an amplitude spectrum of the periodic components. The continuous spectrum of nonperiodic processes is presented in the form of a spectral density. For random stationary ergodic processes only the energy spectrum is nonrandom, i.e., it can be both discrete or continuous. For almost periodic functions both the amplitude and the energy spectra can be computed.

In all cases that the function is defined at discrete points of the interval the spectrum is bounded by the Nyquist frequency. The definition of the function in a finite interval leads for all functions, with the exception of periodic functions, to a smoothing of the spectrum with spectral weights of a unit rectangular pulse, whose length is equal to the interval in which the function is defined. The discrete spectrum of functions defined at separate points of a finite interval (except for periodic functions) is

Survey of the determination of function spectra

Function types	Region and form of definition: at all points of the interval $(-\infty, +\infty)$	at all points of the interval $(0, T)$	at equally spaced points of the interval $(-\infty, +\infty)$	at equally spaced points of the interval $(0, T)$
I Periodic functions $F(t)=F(t+nP)$ [2-8]	$F(t)=\sum_{k=0}^{\infty} C_k e^{2\pi k \frac{t}{P} i} = \sum_{k=0}^{\infty} C_k \sin(2\pi k \frac{t}{P}+\varphi_k) =$ $=\sum_{k=0}^{\infty}(a_k \sin 2\pi k \frac{t}{P} + b_k \cos 2\pi k \frac{t}{P}).$ $(0,P): C_k = \frac{1}{P}\int_{-P/2}^{+P/2} F(t) e^{-2\pi k \frac{t}{P} i} dt,$ $a_k = \frac{2}{P}\int_{-P/2}^{+P/2} F(t)\sin 2\pi k \frac{t}{P} dt,\ b_k = \frac{2}{P}\int_{-P/2}^{+P/2} F(t)\cos 2\pi k \frac{t}{P} dt,$ $C_k = \sqrt{a_k^2 + b_k^2},\ t_g \varphi_k = \frac{b_k}{a_k}$	$\tau < T < P: F(t) = \sum_{k=0}^{\infty} C_k e^{2\pi k \frac{t}{P} i} =$ $=\sum_{k=0}^{\infty}(a_k \sin 2\pi k \frac{t}{P} + b_k \cos 2\pi k \frac{t}{P}).$ a_k, b_k determined from the system of equations $F(t_\ell) = \sum_{k=0}^{k/2}(a_k \sin 2\pi k \frac{t_\ell}{P} + b_k \cos 2\pi k \frac{t_\ell}{P}),$ where $\ell = 1,2,\dots L,\ k \ll L$, arbitrary k	$F(t_\ell) = \sum_{k=0}^{k/2} C_k e^{2\pi k \frac{t_\ell}{P} i} =$ $=\sum_{k=0}^{\infty}(a_k \sin 2\pi k \frac{t_\ell}{P} + b_k \cos 2\pi k \frac{t_\ell}{P})$ $(0,P): C_k = \frac{1}{P}\sum_{\ell=0}^{L} F(t_\ell) e^{-2\pi \frac{t_\ell}{P} i} \Delta t,$ $a_k = \frac{2}{P}\sum_{\ell=0}^{L} F(t_\ell)\sin 2\pi k \frac{t_\ell}{P} \Delta t,\ b_k = \frac{2}{P}\sum_{\ell=0}^{L} F(t_\ell)\cos 2\pi k \frac{t_\ell}{P} \Delta t,$ $\omega_k \le \omega_c = \frac{\pi}{\Delta t} = \frac{\pi k}{P}.$	$\tau < T < P: F(t_\ell) = \sum_{k=0}^{k/2} C_k e^{2\pi k \frac{t_\ell}{P} i} =$ $=\sum_{k=0}^{k/2}(a_k \sin 2\pi k \frac{t_\ell}{P} + b_k \cos 2\pi k \frac{t_\ell}{P}).$ a_k, b_k determined from the system of equations $F(t_\ell) = \sum_{k=0}^{k/2}(a_k \sin 2\pi k \frac{t_\ell}{P} + b_k \cos 2\pi k \frac{t_\ell}{P}),$ where $\ell = 1,2,\dots L,\ k = L,\ \omega_k < \omega' = \frac{\pi L}{P} < \omega_c.$ k - arbitrary
II Nonperiodic functions $f(t)$ [2,5]	$f(t) = \frac{1}{2\pi}\int_{-\infty}^{+\infty} S(\omega) e^{i\omega t} d\omega,$ $S(\omega) = \int_{-\infty}^{+\infty} f(t) e^{-i\omega t} dt,$ $S(\omega) = \pi \frac{dc}{d\omega}.$	$f_T(t) = f(t)\zeta(t),$ $\zeta(t) = \begin{cases} 1 & \text{for } 0 \le t \le T, \\ 0 & \text{for } t<0,\ t>T. \end{cases}$ $S_T(\omega) = \frac{1}{2\pi}\int_{-\infty}^{+\infty} S(\omega-\nu)\sigma(\nu) d\nu,$ $\sigma(\nu)\int_0^T \zeta(t) e^{i\nu t} dt = T \frac{\sin\nu\frac{T}{2}}{\nu\frac{T}{2}}$	$f(t_\ell) = \frac{1}{2\pi}\int_0^{\omega_c} S(\omega) e^{i\omega t_\ell} d\omega,$ $S(\omega) = \sum_{\ell=-\infty}^{+\infty} f(t_\ell) e^{-i\omega t_\ell} \Delta t,$ $\omega \le \omega_c = \frac{\pi}{\Delta t}.$	$f(t_\ell) = \sum_{k=0}^{k/2} C_k e^{i\omega_k t_\ell} =$ $=\sum_{k=0}^{k/2} C_k \sin(\omega_k t_\ell + \varphi_k).$ $C_k = \frac{1}{T}\sum_{\ell=1}^{L} f(t_\ell) e^{-i\omega_k t_\ell} \Delta t,$ $k = L;\ \omega_k \le \omega_c = \frac{\pi k}{T},$ ω_k - arbitrary
III Random functions (stationary, ergodic) $\zeta(t)$ [2-9, 12]	$B(t) = \zeta(t)\zeta(\tau-t),$ $B(t) = \frac{1}{2}\int_{-\infty}^{+\infty} G(\omega) e^{i\omega t} d\omega = \int_{-\infty}^{+\infty} G(\omega)\cos\omega t\, d\omega$ $G(\omega) = \frac{1}{\pi}\int_{-\infty}^{+\infty} B(t) e^{-i\omega t} dt = \frac{2}{\pi}\int_{-\infty}^{\infty} B(t)\cos\omega t\, dt,$ $G(\omega) = \frac{1}{\pi}\lim_{T\to\infty}\frac{1}{T}\lvert S_T(\omega)\rvert^2.$	$B_T(t) = B(t)\zeta_\tau(t),$ $\zeta_\tau(t) = \begin{cases} 1 & \text{for } 0 \le t \le T, \\ 0 & \text{for } t<0,\ t>T. \end{cases}$ $G_T(\omega) = \int_{-\infty}^{+\infty} G(\omega-\nu)\sigma(\nu) d\nu,$ $\sigma(\nu) = T\frac{\sin\nu\frac{T}{2}}{\nu\frac{T}{2}}.$	$B(t_\ell) = \zeta_\ell(t)\zeta_\ell(t-\ell-\Delta t),$ $B(t_\ell) = \int_0^{\omega_c} G(\omega)\cos\omega t_\ell d\omega.$ $G(\omega) = \frac{2}{2\pi}\sum_{\ell=-\infty}^{+\infty} B(t_\ell)\cos\omega t_\ell \Delta t_\ell$ $\omega \le \omega_c = \frac{\pi}{\Delta t}.$	$B(t_\ell) = \zeta_\ell(t)\zeta_\ell(t-\ell-\Delta t),$ $B(t_\ell) \approx \rho(t_\ell),$ $\rho(t_\ell) = \sum_{k=1}^{k/2} \lvert C_k\rvert^2 \cos\omega_k t_\ell.$ $G(\omega_k) = \frac{2}{\pi}\sum_{\ell=0}^{k-1} B(t_\ell)\cos\omega_k t_\ell \Delta t,$ $\lvert C_k\rvert^2 = \frac{1}{T}\sum_{\ell=0}^{k-1}\rho(t_\ell)\cos\omega_k t_\ell \Delta t,$ $\omega_k \le \frac{\pi k}{T},\ \omega_k$ - arbitrary
IV Almost periodic functions $\lvert\varphi(t+\rho)-\varphi(t)\rvert < \varepsilon$ [13-14]	$\varphi(t) = \sum_{k=0}^{\infty} C_k e^{i\omega_k t}$ $B(t) M\{\varphi(\tau-t)\} = \sum_{k=1}^{\infty}\lvert C_k\rvert^2 e^{i\omega_k t},$ $C_k = M\{\varphi(t) e^{-i\omega_k t}\},$ $\lvert C_k\rvert^2 = M\{B(t) e^{-i\omega_k t}\},$ $\sum_{k=1}^{\infty}\lvert C_k\rvert^2 = M\{\lvert\varphi(t)\rvert^2\}.$	$\varphi_T(t) = \varphi(t)\zeta_\tau(t),$ $B_T(t) = B(t)\zeta_\tau(t).$ $S_T(\omega) = \sum_{k=1}^{\infty} C_k(\nu_k)\sigma(\omega-\nu_k),$ $G_T(\omega) = \sum_{k=1}^{\infty}\lvert C_k(\nu_k)\rvert^2\sigma(\omega-\nu_k).$	$\varphi(t_\ell) = \sum_{k=0}^{\infty} C_k e^{i\omega_k t_\ell}$ $B(t_\ell) = \sum_{k=1}^{\infty}\lvert C_k\rvert^2 e^{i\omega_k t_\ell} = \sum_{k=1}^{\infty}\lvert C_k\rvert^2 \cos\omega_k t_\ell,$ $C_k = M\{\varphi(t_\ell) e^{-i\omega_k t_\ell}\},$ $\lvert C_k\rvert^2 = M\{B(t_\ell) e^{-i\omega_k t_\ell}\} = M\{(t_\ell)\cos\omega_k t_\ell\},$ $\omega_k \le \omega_c = \frac{\pi}{\Delta t}$	$\varphi(t_\ell) = \sum_{k=0}^{k/2} C_k e^{i\omega_k t_\ell} = \sum_{k=0}^{k/2} C_k \sin(\omega_k t_\ell + \varphi_k),$ $B(t_\ell) = \sum_{k=1}^{k/2}\lvert C_k\rvert^2 e^{i\omega_k t_\ell} = \sum_{k=1}^{k/2}\lvert C_k\rvert^2 \cos\omega_k t_\ell \rho(t_\ell),$ $C_k = \frac{1}{T}\sum_{\ell=0}^{n}\varphi(t_\ell) e^{-i\omega_k t_\ell} \Delta t,$ $\lvert C_k\rvert^2 = \frac{1}{T}\sum_{\ell=1}^{n}\rho(t_\ell)\cos\omega_k t_\ell \Delta t,$ $\omega_k \le \omega_c = \frac{\pi k}{T},\ \omega_k$ - произвольны

approximately inscribed in the continuous spectra of these functions defined at all points of the same intervals.

In functions with a bounded spectrum there can occur an exchange of frequencies larger than the Nyquist frequency ω_c by lower ones. In order to avoid this the interval over which the function is defined should be chosen so that $\Delta t \leq \pi/\omega_c$, or the oscillations with frequencies larger than ω_c should be suppressed.

A function defined at k points of a finite interval can in the general case be represented exactly by a set of N arbitrary periodic components, where $N = k/2$. In this case functions of different types seem to have identical spectra. However, this is not so — periodic functions contain harmonic components only; for almost periodic functions the main part of the energy of the process is in general contained in N' harmonics, and $N' \ll k/2$ (this condition is similar to the significance of reducing the remaining dispersion of a series according to Fisher while successively removing N' periodic components).

Experimentalists encounter only rarely processes which can be described by one of the above function types. Real processes consist generally of a superposition of a almost periodic function $\varphi(t)$ and a random function $\xi(t)$; other combinations occur very seldom. A spectrum of a real process will naturally be a sum of the spectra of its components. In order to compute the spectrum of a process a method should be applied which is suitable for all function types involved in the process being investigated.

METHODS OF ANALYZING HIDDEN PERIODICITIES

In order to avoid the distortion of the spectral estimates the process being investigated is subjected to a preliminary treatment: suppression of oscillations with $\omega > \omega_c$, smoothing of the spectrum, etc. The smoothing is performed by a moving-average operator, Whittaker operator, approximation by a polynomial, etc. For any arbitrary method coefficients of smoothing and smoothness can be introduced. For a moving-average operator the smoothing coefficient is defined as $\sigma = \frac{\epsilon_0 - \epsilon}{\epsilon_0 - \epsilon_s}$, $0 \leq \sigma \leq 1$ and the smoothness coefficient as $\gamma = \frac{\epsilon_s}{\epsilon}$, $0 \leq \gamma \leq 1$, where ϵ is the relative root-mean-square difference between two neighboring points in the smoothed series, ϵ_0 — in the original series, ϵ_s — for a sinusoid with a period equal to the dominant period of the process. Averaging the Zurich series of Wolf numbers ($\gamma_0 = 0.1$) with a period of 12 months, we obtain $\sigma = 0.95$ and $\gamma = 0.7$.

It is generally assumed that the precision of determining the frequencies of the periodic components is of the order of $1/2T$, where T is the interval length. This is true, however, for random processes only. In the general case /1/: $\Delta\omega_\kappa \approx \frac{1}{\pi T} \cdot \frac{\sigma_0}{C_\kappa}$, where c_κ is the amplitude of the periodic component being removed and σ_0 is the remaining dispersion of the series after removing all "realistic" periodic components.

Harmonic and quasiharmonic spectral analysis. The harmonic spectral analysis can be applied only to processes which are purely periodic. In

the case of arbitrary nonperiodic processes it can be used only in interpolation problems, since in this case we artificially impose upon the process being investigated a periodicity condition within the interval of its definition. To a nonperiodic process one can apply formally only a quasiharmonic analysis with a frequency step of $\Delta\omega < 1/2T$. Since the process is defined in a finite interval only, the different lines of the periodic components (if they are present in the process under investigation) are broadened. The line shape in a quasiharmonic analysis coincides with the spectrum of the sinusoid

$$f(t) = \sin \Omega t, \quad 0 \leq t \leq T: \quad S_T = \frac{\Omega}{\Omega^2 - \omega^2}\left[1 - e^{-i\omega t}\left(\cos \Omega t + i \frac{\omega}{\Omega} \sin \Omega t\right)\right].$$

This spectrum has many peaks. When smoothing this spectrum during the calculations, different time windows can be used; their influence upon the spectrum will be discussed below. The spectrum of the Zurich series of Wolf numbers obtained by the quasiharmonic analysis is shown in Figure 1a.

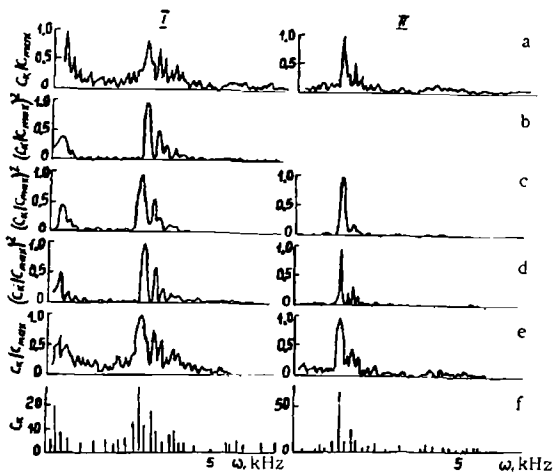

FIGURE 1. Frequency spectra of the Zurich series of Wolf numbers:

I — regular series; II — alternating-sign series, where a minus sign is placed in front of all the Wolf numbers in every odd cycle. 1a — quasiharmonic spectral analysis; 1b — correlational spectral analysis with a rectangular window; 1c — Tukey's time window; 1d — exponential weight function; 1e—modified method of Buys-Ballot; 1f —successive coordinate-frequency removal method.

Correlational spectral analysis. In the correlational spectral analysis a quasiharmonic analysis of the correlation function B(t) is performed (by using one cosine Fourier transform due to the parity of B(t)). As a result we obtain the energy spectrum or the spectrum of the squares of the

amplitudes of the periodic components of the process under investigation /15/ and the nonrandom energy spectrum of a random stationary ergodic process. The line shape of $|C_\kappa|^2$ is similar to the line shape in a simple quasiharmonic analysis and different time windows are also used for its smoothing in the computational process.

If in the general case $G(\omega) = \frac{1}{\pi}\sum^{\infty} B(t_i)\cos\omega t_i$, then by using a time window $\lambda(t_i)$, we obtain $G^*(\omega) = \frac{1}{\pi}\sum_{i=1}^{n-1} B_n(t_i)\lambda(t_i)\cos\omega t_i$. In doing so $\delta = \int_{-\infty}^{\infty}[G(\omega) - G^*(\omega)]^2 d\omega$ will be minimal if $\lambda(t) = B(t)/M\{B_N^2(t)\}$, i.e., the optimum shape of the time window depends on the properties of the process under investigation /16/.

Many shapes of time windows are used: rectangular window B(t), cut-off or truncated estimates, estimates of Bartlett, Hemming, Chebyshev, Hahn, Tukey, etc. The choice of the time window depends on the properties of the series being investigated. The currently most widely used window is that of Tukey /17–19/. The line shape is in this case $G(\kappa) = \frac{1}{2}\delta_\kappa C_{\kappa_0}^2[\Phi(\kappa_0-\kappa) + \Phi(\kappa_0+\kappa)]$, where $\Phi(n) = \sin\pi n/2\pi n(1-\frac{n}{N})$, $\delta_\kappa = \begin{cases} 1/2 & \text{for } \kappa = 0,\ \kappa = N \\ 1 & \text{for } 0 < \kappa < N \end{cases}$, $\kappa = 2T/P$, $C_{\kappa_0}P$ — the amplitude and period of the given spectral line. The line shape has only one peak.

When calculating B(t) for a function defined over a finite interval, its precision decreases with an increase in t, and at the interval limits values B(t) > 1 do not have any meaning. The elimination of B(t) > 1 can be achieved by introducing instead of B(t) an autocorrelation function $\rho(t)$, which is calculated according to the formula for the correlation coefficient. The correction of the behavior of $\rho(t)$ can be achieved approximately by an exponential weight function $E_{N^*}(t_n) = 1$, for $0 \le n \le N^*$; $E_{N^*}(t_n) = e^{-\alpha(n-N^*)}$ for $N^* \le n \le N$, /1/, where α and N^* are determined from the analysis of $B_N(t)$ of the series under investigation.

The spectra of the Zurich series of Wolf numbers obtained by the method of correlational spectral analysis are shown in Figures 1b, c, d.

Operator spectral analysis (periodogram analysis). This group contains methods used to obtain spectral estimates without the application of Fourier transforms. As an example in Figure 1e is shown the spectrum of the Zurich series of Wolf numbers, obtained by the following method: $C_\kappa(\omega) = \sigma\{C_{t_i\omega}[P_{t_i}(W)]\}$ (the terminology is according to /1/).

Estimates of the fine structure of the line spectrum of a process. The estimate of the amplitude of the different periodic components present in the process can be effected more precisely by subtracting the line shape from the spectrum obtained (successive frequency removal of periodic components) /1/, or by exclusion of these components by the method of least squares (successive coordinate removal) /20/, or by the combination of these two methods. The example of the discrete spectrum of the Zurich series of Wolf numbers obtained by the last method is shown in Figure 1f.

In calculating the spectra it is necessary to estimate the intervals of significance of the amplitudes C_κ for chosen confidence levels. It seems that in the analysis of real physical processes this can be achieved best by using the Student distribution, as in the calculation of the coefficients of a multiple regression. With $\omega_c = \pi/\Delta t$ the number of degrees of freedom is $f = N - 2 \approx N$, where N is the number of points in the series. When increasing the period P of the periodic components being removed, also the

density of observations per unit of phase will be increased $P/2\Delta t$ times, i.e., a part of our observations will be duplicated (in the dispersion of the data we are interested in the dispersion of averages only). Thus, the effective number of degrees of freedom for an arbitrary P is $f_{eff} \approx \approx N \cdot 2\Delta t/P = 2T/P$, i.e., the precision of amplitude determination increases as the number of periods in the double interval length increases.

Finally, the power of a single component of a random process has a χ^2-distribution, so that as a measure of the nonrandomness of a periodic component we should take $p_n = 1 - \frac{1}{\sigma^2} e^{-\frac{S_n}{\sigma^2}}$, where S_n is the power of the n-th periodic component, σ^2 is the average power of one component of a random process, $\sigma^2 = B(0)/N$.

POSSIBILITIES OF STATISTICAL PREDICTION

Under statistical prediction in contradistinction to physical and cross-correlational prediction we understand a prediction based only on the available information about a process in an interval of its argument preceding the period of prediction. One way of effecting a statistical prediction can be the use of a method based on the computation of the frequency spectrum of the process and its presentation in the form of a sum of the periodic components obtained.

If the process can be described better as more periodic components are taken (it is exact if the number of the periodic components is N = k/2, where k is the number of points in the series), this is not so in case of prediction. Reducing the error to zero, we attribute a periodic character to all random errors present in the series being analyzed, and therefore we shall also predict them. This is meaningless and will only render the prediction poorer. To obtain the most accurate prediction only those components should be used which really characterize (are physically real) the given process and are stable along the argument intervals being analyzed. The estimate of the significance and stability of the periodic components can be achieved by different methods, one of these being trial prediction. Trial prediction enables us to estimate the possibilities of statistical prediction.

Given a set of periodic components of a process which are obtained from its frequency spectrum during the period of observation (T_1, T_2), which ends before the last moment of observation T, the partial sums can be formed: $W_{cal,N}(t) = \sum_{i=0}^{N} c_i \sin(\omega_i t + \varphi_i), c_{i+1} < c_i, c_N = 1, 2, 3 \ldots$, we can thus predict our series for the period (T_1, T_2), and with the observation results compute the root-mean-square error of the prediction $\sigma(N)$. It turns out that by increasing N the prediction becomes first poorer, later some periodic components improve it while some render it poorer, and finally, for very large N the prediction becomes generally poorer. Each addition of a new periodic component contributes: $\Delta\sigma_{N,i} = \sigma(N-1) - \sigma(N) \approx \Delta\sigma_i$. If we now compute $W_{cal,N}(t)$ so that $\Delta\sigma_{i+1} < \Delta\sigma_i$, we shall obtain a curve with one minimum. For different (T_1, T_2) these curves will naturally be different. For each process an optimum time interval (T_1, T_2) can be found which gives a minimum value of σ_{min}.

Thus the position of σ_{min} enables us to estimate which periodic components obtained are real and stable, and the value of σ_{min} can be used to estimate the possibilities of statistical prediction.

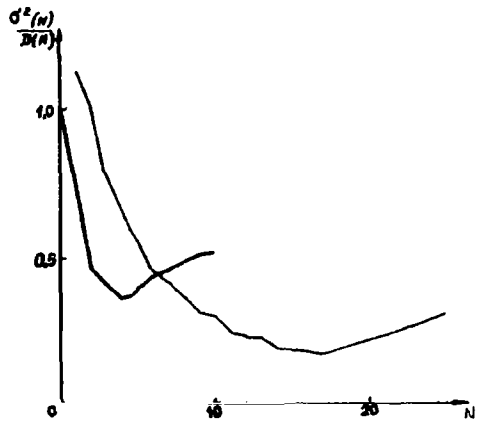

FIGURE 2. Prediction curves for the Zurich series of Wolf numbers for (T_2, T) equal to 12 years and (T_1, T_2) equal to 54 and 206 years.

In Figure 2 are shown two prediction curves for the Zurich series of Wolf numbers with (T_1, T_2) equal to 54 and 206 years and (T_2, T) equal to 12 years. Since the trial prediction is not optimum in this case, the predicted Wolf numbers for the future will not be given here.

Bibliography

1. Vasil'ev, O.B. and K.A. Kandaurova.— Byull. "Solnechnye Dannye," No. 12:85. 1968.
2. Kharkevich, A.A. Spektry i analiz (Spectra and Analysis).— Moskva, Fizmatgiz. 1957.
3. Hardy, G.H. and W.W. Rogosinski. Fourier Series.— University Press, Cambridge. 1950.
4. Lanczos, C. Applied Analysis.— Prentice Hall, Englewood Cliffs, N.J. 1956.
5. Zel'dovich, Ya.B. and A.D. Myshkis. Elementy prikladnoi matematiki (Elements of Applied Mathematics).— Moskva, Izdatel'stvo Nauka. 1967.
6. Levin, B.R. Teoreticheskie osnovy statisticheskoi radiotekhniki, Kn. 2 (Theoretical Foundations of Statistical Radiotechnique, Book 2).— Moskva, "Sovetskoe Radio." 1968.
7. Serebrennikov, M.G. Garmonicheskii analiz (Harmonic Analysis).— Moskva -Leningrad, Gostekhizdat. 1948.

8. Krylov, V.I. and L.G. Kruglikova. Spravochnaya kniga po chislennomu garmonicheskomu analizu (Handbook of Numerical Harmonic Analysis).— Minsk, "Nauka i Tekhnika." 1968.
9. Sveshnikov, A.A. Prikladnye metody teorii sluchainykh funktsii (Applied Methods in the Theory of Random Functions).— Moskva, Izdatel'stvo Nauka. 1968.
10. Romanenko, A.F. and G.A. Sergeev. Voprosy prikladnogo analiza sluchainykh protsessov (Problems of Applied Analysis of Random Processes).— Moskva, "Sovetskoe Radio." 1968.
11. Pugachev, V.S. Vvedenie v teoriyu veroyatnostei (Introduction to Probability Theory).— Moskva, Izdatel'stvo Nauka. 1968.
12. Pustyl'nik, E.I. Statisticheskie metody analiza i obrabotki nablyudenii (Statistic Analysis Methods and Evaluation of Observations).— Moskva, Izdatel'stvo Nauka. 1968.
13. Bohr, H. Fastperiodische Funktionen.— Berlin, J. Springer. 1932.
14. Guter, R.S., L.D. Kudryavtsev, and B.N. Levitan. Elementy teorii funktsii (Elements of the Theory of Functions).— Moskva, Fizmatgiz. 1963.
15. Serebrennikov, M.G. and A.A. Pervozvanskii. Vyyavlenie skrytykh periodichnostei (Revealing Hidden Periodicities).— Moskva, Izdatel'stvo Nauka. 1965.
16. Ismatkhodzhaev, S.K.— Izvestiya AN Uzbekskoi SSR, Seriya Tekhnicheskikh Nauk, 3, 5. 1963.
17. Tukey, J.W. The Sampling Theory of Power Spectrum Estimates.— Symp. on Application of Autocorrelation Analysis to Physical Problems, Wood Hole, Mass. 1949.
18. Blackman, R.B. and J.W. Tukey.— The Bell System Tech. J., 34, 1. 1958.
19. Munk, W.H., F.E. Snodgrass, and M.J. Tucker.— Bull. Scripps Inst. Oceanology, Univ. California, 7, 47. 1959.
20. Anderson, C.N.— Terr. Mag. Atm. El., No. 2:44. 1939.

K. A. Kandaurova

A FAST FOURIER TRANSFORM

At present continuous periodic functions are widely subjected to analytical investigation. These computations require enormous amounts of computer time. For large amounts of data (from hundreds to thousands of points) the calculations take up sometimes tens of hours. In 1965 Cooley and Tukey /1/ developed a computer algorithm, which was named the fast Fourier transform. This algorithm reduces the computational time by a factor of 100 relative to the direct method, but unfortunately it can be applied only in cases consisting of 2^N points, where N is an integer. Therefore, we have attempted to construct a fast Fourier transform for any number of points.

The Fourier integral is calculated by the Monte Carlo method. The convergence rate of the regular Monte Carlo method is relatively low (of the order of $1/\sqrt{N}$). In order to increase the precision of the calculation without increasing N an importance sampling method was used (more random points are chosen in the more important regions of the integration interval).

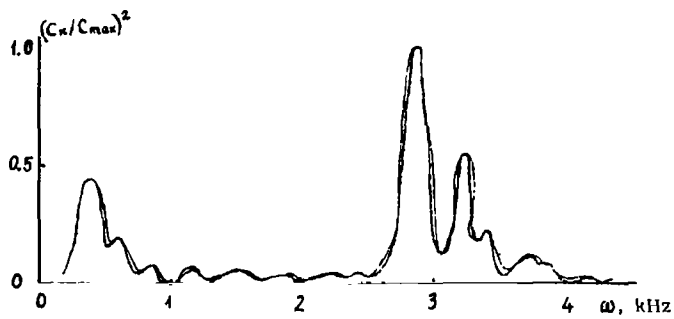

Spectrum calculated by a regular method (thick line) and by the Monte Carlo method (thin line).

In order to introduce a time window this method was used together with Tukey's weight function. The total number of points taken in the interval in which the autocorrelation function is defined was 400. The random numbers were introduced into the computer in groups of $512_{10} = 1000_8$, and

in the calculation of each point of the spectrum they were taken consecutively, so that the origins of their selection were pseudorandom. The spectrum values obtained were smoothed out by using a moving-average operator over 5 points. The performance of the algorithm was tested using the Zurich series of Wolf numbers (2600 points). The computation time for one point was reduced by more than a factor of 10 as compared to the previous method. The deviations of the results obtained (see figure) from those calculated by the regular method were 2 — 3% /2/.

The possibilities of reducing the computation time by means of the algorithm were not fully utilized. It is suggested to group the points in intervals of the argument of the cosine and to calculate the values of the autocorrelation function selectively, which will reduce the computation time appreciably. The grouping according to cosines and the selective computation of the autocorrelation function can be used without the Monte Carlo method in computing the spectra of series with less than 1000 points.

Bibliography

1. Cooley, I.W. and J.W. Tukey.— Math. Comput., 19, 297. 1965.
2. Vasil'ev, O.B. and K.A. Kandaurova.— Byull. "Solnechnye Dannye," No. 12:47. 1968.

Ya. L. Blokh and I. N. Kapustin

A PERFORMANCE CRITERION FOR A NEUTRON SUPERMONITOR

For an unbiased estimate of the performance of neutron supermonitors and to effect comparisons between them quantitative performance criteria are necessary. It is obvious that these criteria should not depend on the average recorded intensity or on the amplitudes of the recorded variations.

It is suggested to use as such a criterion the signal-to-noise ratio of the instrument being investigated to the signal-to-noise ratio of an ideal setup /1/. The ideal instrument has the same area and geometry as the real one. The primary information recorded by such an instrument is transmitted without distortions. The performance criterion will be denoted by ψ_τ. According to the above definition

$$\psi_\tau = \frac{\Delta n}{S_n} \cdot \frac{\sigma_N}{\Delta N}, \qquad (1)$$

where Δn is the amplitude of the variation at the output of the instrument, $\Delta n = n_1 - n_2$; ΔN is the amplitude of the variation at the output of an ideal instrument, $\Delta N = N_1 - N_2$; S_n is the root-mean-square deviation of the data from the real instrument; σ_N is the root-mean-square deviation of hypothetical data from the ideal instrument. Assuming that data from the ideal instrument obey a Poisson distribution, we have

$$\sigma_N = \sqrt{N}. \qquad (2)$$

In order that (1) can be used in practical cases, the unknown N will be replaced by n — the average counting rate of the real instrument. From /1, 2, 3/

$$N = \frac{n}{\kappa(1-n\tau)}, \qquad (3)$$

where k is the multiplication factor of the supermonitor and T is the dead time of the radio channel. Since $\Delta N = N_1 - N_2$, and assuming that the variations of k are small compared to the relative variation $\Delta N/N$, we obtain

$$\Delta N = \frac{n_1}{\kappa(1-n_1\tau)} - \frac{n_2}{\kappa(1-n_2\tau)} = \frac{\Delta n}{\kappa(1-n_1\tau)(1-n_2\tau)}.$$

Considering the fact that the amplitude of the variations being studied is small, we obtain

$$\Delta N = \frac{\Delta n}{(1-\bar{n}T)^2 K}. \tag{4}$$

Substituting (3) and (4) into (1), we have

$$\psi_z = \frac{\sqrt{n \cdot K}}{S_n}(1-nT)^{3/2}. \tag{5}$$

When using this expression, it should be remembered that at most cosmic ray stations (CRS) the dead time in each supermonitor channel is independent for any pair of counters, while due to the production of stars between counter pairs there is a remaining multiplication factor k = 1.1 /1/.

Allowing for the fact that generally the data were obtained during some time interval t and after a scaling of z, expression (5) should be rewritten as

$$\psi_z = \frac{\sqrt{N \cdot K \cdot z}}{S_N}\left(1 - \frac{N z \cdot T}{3t}\right)^{3/2}, \tag{6}$$

where N is the number of pulses recorded during the time interval t after a scaling of z. Considering the fluctuations in N while estimating S_N, the final expression for the performance is given by

$$\psi_z = \sqrt{K \cdot z} \cdot \frac{\sum_{i=1}^{m} \sqrt{N_i}\cdot\left(1 - \frac{z N_i \cdot T}{3t}\right)^{3/2}}{m \cdot S_N}, \tag{7}$$

where m is the number of values of N_i used. The estimate of S_N can be computed according to the data of /4/.

The performance factor ψ_z reflects not only the quality of operation of the instrument, but also the correctness of the dead time T chosen. For any real instrument ψ_z will be always less than unity, since the presence of the multiplication factor k and of the dead time T will always lead to a distortion of the recorded data and consequently to a poorer signal-to-noise ratio.

In /1/ an empirical expression was derived which relates the multiplication factor and k the dead time T with the expected dispersion of the data:

$$\frac{n^3}{N^3} = \frac{\sigma_n^2}{\sigma_N^2}, \tag{8}$$

where σ_n^2 is the expected dispersion of the data at the output of the instrument. Substituting the value of N from (3) and σ_n^2, which is equal to N, into (8), we obtain

$$\sigma_n = K(1-nT)\sqrt{n}. \tag{9}$$

Replacing S_n in (5) by the theoretically expected value σ_n, we obtain the maximum possible value of the performance factor for a given instrument for definite values of T and k:

$$\psi_0 = \sqrt{\frac{1-nT}{K}}. \tag{10}$$

The last expression was derived in /1/ by a slightly different method.

Bibliography

1. Kapustin, I.N. and M.Yu. Medvedev.— Kosmicheskie Luchi, No.11. 1969 (in print).
2. Kapustin, I.N.— Geomagnetizm i aeronomiya, No.1:165. 1967.
3. Gnedenko, B.V.— ZhETF, No.1:101. 1941.
4. Blokh, Ya.L. and I.A. Pimenov.— Geomagnetizm i aeronomiya, No.1:53. 1969.

I. N. Kapustin

MATHEMATICAL CORRECTION OF DATA FROM MULTIPLICITY RECORDERS

The intensities of the neutron cosmic-ray component obtained as the output from a multiplicity recorder $n_1, n_2, \ldots n_i \ldots n_j$ with $\sum_{i=1}^{j} n_i = n_*$ are appreciably distorted due to coincidences leading to the distortion of the variations being studied /1/. In /2/ a model of a multiplicity recorder was proposed which automatically corrects the above-described distortions. At present many cosmic-ray stations are operated whose data are not corrected automatically. The correction of these data should be performed by some mathematical procedure.

In setting up the equations for the correction of the data it is assumed that the primary particle fluxes responsible for the various multiplicities are independent and have a Poisson distribution in time. The total flux of all multiplicities is distributed according to the same law. In setting up the equations the distortions due to the dead time of the radio channel and the incomplete sampling of stars owing to the finite sampling time are neglected. Thus, the corrected intensities $N_1, N_2 \ldots N_i \ldots N_j$, with $\sum_{i=1}^{j} N_i = N_*$, represent the primary flux distorted by the above two effects. Since the distortions due to the dead time of the radio channel and the finite time of star sampling are constants for every instrument, these can be neglected when studying the variations of the different multiplicities.

The general form of the equations for correcting the data, allowing for the effect of coincidences, is

$$n_i = N_i \cdot \alpha_i + n_{is}, \qquad (1)$$

where α_i is the coefficient of decrease in the intensity of i-fold stars due to their production of stars of different multiplicities; n_{is} is the intensity of coincidences of stars of different multiplicity giving false stars of multiplicity i; $N_i \cdot \alpha_i$ is the rate of true i-fold stars (per unit time), so that

$$\alpha_i = P_{N_* T} \cdot P_{0N_*}, \qquad (2)$$

where $P_{N_* T}$ is the probability that the produced star of multiplicity i will not fall into the sampling time initiated by any previous star, and that its first detected neutron will initiate the sampling time T; P_{0N_*} is the probability

that no star of any multiplicity or a part of it will fall within the sampling time initiated by a star of multiplicity i. The rate of initiating the sampling time is n_o. The total time the channel is occupied by sampling times T is $n_o T$, so that

$$P_{N_o T} = 1 - n_o T. \tag{3}$$

The last expression was introduced for the first time in /3/, and was subsequently derived more rigorously in /4/. Starting from Poisson's law

$$P_{0N_o} = \frac{(N_o T)^0}{0!} \cdot e^{-N_o T} = e^{-N_o T}, \tag{4}$$

whence

$$\alpha_i = \alpha = (1 - n_o T) \cdot e^{-N_o T} \tag{5}$$

The term n_{is} consists of a combination of coincidences of stars with different multiplicities producing false stars with a multiplicity of i. For convenience all coincidence combinations will be divided into three groups — a, b, c. The rate of such coincidences will be respectively denoted by $n_{i\alpha r}$, $n_{i\beta r}$, $n_{i\gamma r}$, where i is the multiplicity due to the coincidences, r is the number of stars produced in a coincidence, r = 2 is the number of stars produced in double coincidences, r = 3 the number in triple coincidences, etc.
Thus,

$$n_{is} = \sum_{r=2}^{max} n_{i\alpha r} + \sum_{r=2}^{max} n_{i\beta r} + \sum_{r=2}^{max} n_{i\gamma r}. \tag{6}$$

Type a. To this type belong all complete double, triple, etc., coincidences (Figure 1a). The sampling time is initiated by the first neutron detected from a star of multiplicity x. The stars of multiplicities y, z... fall within the sampling time, so that the total number of neutrons detected during the sampling time T, is equal to x + y + z + ... = i. Each single coincidence of type a will be denoted as $n_{x+y=i}$ for r = 2, or $n_{x+y+z=i}$ for r = 3, etc. The number of double coincidences of type a is given by

$$n_{x+y=i} = n'_x \cdot P_{1N_y} \cdot P_{0\bar{N}_y} \cdot P'_{0N_y}, \tag{7}$$

where n'_x is the number of cases in which the sampling time T is initiated by stars of multiplicity x; P_{1N_y} is the probability of one complete star of multiplicity y occurring during this sampling time; $P_{0\bar{N}_y}$ is the probability that no star of any multiplicity different from y, or a part of it, will fall into the sampling time T; P'_{0N_y} is the probability that no star of multiplicity y will fall partially within the sampling time T.

Starting from Poisson's law, we have

$$P_{1N_y} = N_y (T - M_y) \cdot e^{-N_y (T - M_y)}, \tag{8}$$

$$P_{0\bar{N}_y} = e^{-(N_o - N_y) T}, \tag{9}$$

$$P'_{0N_y} = e^{-N_y M_y}, \tag{10}$$

where M_y is the mathematical expectation of the time interval between the detection of the first and last neutron from a y-fold star. Therefore, $n_{x+y=i} = n_x \cdot N_y (T - M_y) \cdot e^{-N_0 T}$.

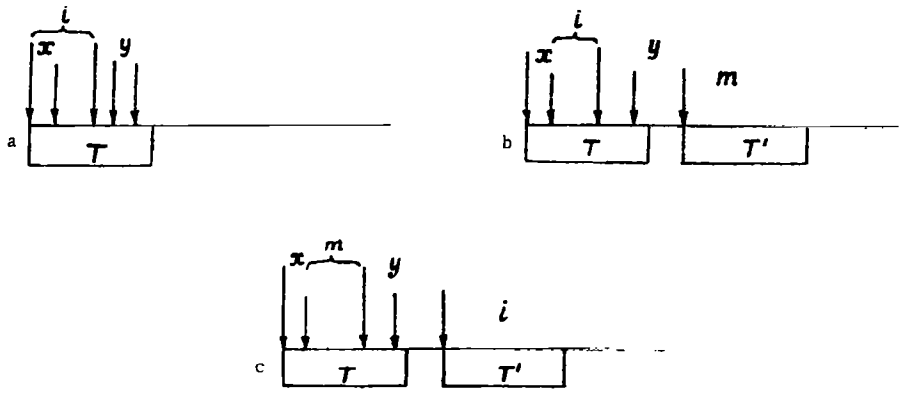

FIGURE 1. Types of coincidence of stars of different multiplicity producing an i-fold star.

Similarly to (2),

$$n_x = N_x \cdot P_{N_0 T}. \tag{11}$$

Remembering that $P_{N_0 T}$ is equal to (3), we get

$$n_{x+y=i} = N_x N_y (T - M_y)(1 - n_0 T) \cdot e^{-N_0 T} \tag{12}$$

The multiplicities x and y are arbitrary, their sum is i. The term $n_{i\alpha z}$ consists of a sum of terms containing all combinations of x and y giving a sum i. Triple coincidences of type a have two forms: $n_{x+y+y=i}$ and $n_{x+y+z=i}$.

$n_{x+y+y=i} = n'_x \cdot P_{2N_y} \cdot P_{0\bar{N}_y} \cdot P'_{0N_y}$, where $P_{2N_y} = \frac{N_y^2 (T - M_y)^2}{2} e^{-N_y (T - M_y)}$ is the probability of two y-fold stars within the time T. Using (9), (10) and (11), we have

$$\begin{aligned} n_{x+y+y=i} &= \frac{N_x N_y^2 (T - M_y)^2}{2} \cdot (1 - n_0 T)\, e^{-N_0 T}, \\ n_{x+y+z=i} &= n'_x \cdot P_{1N_y} \cdot P_{1N_z} \cdot P_{0\overline{N_y N_z}} \cdot P'_{0N_y} \cdot P'_{0N_z}, \end{aligned} \tag{13}$$

where $P_{0\overline{N_y N_z}}$ is the probability that no star or part of it with a multiplicity different from y or z will occur within the sampling time T,

$$P_{0\overline{N_y N_z}} = e^{-(N_0 - N_y - N_z) \cdot T}. \tag{14}$$

Taking into account (8), (9) and (11), we obtain

$$n_{x+y+z=i} = N_x N_y N_z (T - M_y)(T - M_z)(1 - n_0 T) \cdot e^{-N_0 T} \tag{15}$$

The multiplicities x, y and z are arbitrary, as long as their sum is i. The term n_{ic3} consists of the sum of all terms containing the possible combinations x, y and z. Similarly, the expressions for four-, five-fold, etc., coincidences can be calculated.

Type b. (Figure 1b). This type of coincidence contains the incomplete two-, three-fold, etc., coincidences producing false stars of multiplicity i during the sampling time T. Each single case of such a coincidence will be written as $n_{x+y=i+m}$ for r = 2, $n_{x+y+z=i+m}$ for r = 3, where the y-fold star falls completely within the sampling time T, and the z-fold star only partially; $n_{x+y\beta+z\gamma=i+m}$ for r = 3, where β neutrons of a y-fold star and γ neutrons of a z-fold star were detected during the time T. The number of double coincidences of type b is given by

$$n_{x+y=i+m} = n'_x \cdot P'_{iN_y}(\tau) \cdot P_{o\bar{N}_y} \cdot P_{oN_y}(\bar{\tau}),$$

where $P'_{iN_y}(\tau)$ is the probability that only i-x neutrons from a y-fold star are detected during the sampling time T; $P_{o\bar{N}_y}$ is the probability that no star or part of it with a multiplicity different from y will be recorded during the time T (9); $P_{oN_y}(\bar{\tau})$ is the probability that no other number of neutrons from a y-fold star will be recorded during the time T.

$$P'_{iN_y}(\tau) = N_y \tau \cdot e^{-N_y \tau}, \tag{16}$$

$$P_{oN_y}(\bar{\tau}) = e^{-N_y(T-\tau)} \tag{17}$$

From (3) and (11) we obtain

$$n_{x+y=i+m} = N_x N_y \cdot \tau (1 - n_o T)\ e^{-N_o T}, \tag{18}$$

where τ is the mathematical expectation of the time interval between the recording of the corresponding neutrons from a star.

The total number of terms of double coincidences of type b is $n_i b_2$ and is equal to the number of combinations x from 1 to j and y from 2 to j, giving a sum of i with a remainder m. The numbers of three-, four-fold, etc., coincidences of type b can be found in a similar way.

Type c (Figure 1c). Coincidences similar to type b coincidences; however, the i-fold star is not formed during the time T, but during the sampling time T', and the multiplicity of the star that initiated the sampling time has no effect upon the i-fold star. The number of double coincidences n_{ic2} is given by

$$n_{ic2} = \sum_{y=i+1}^{j} n_o P'_{iN_y}(\tau) \cdot P_{o\bar{N}_y} \cdot P_{oN_y}(\bar{\tau}).$$

Taking into account (9), (16) and (17), we have

$$n_{ic2} = n_o \tau \cdot e^{-N_o T} \sum_{y=i+1}^{j} N_y . \tag{19}$$

The number of three-, four-fold, etc., coincidences can be found in a similar way.

Substituting into the initial equation (1) the value of o and all values $n_{i,s}$ for different values of i, we get a set of j equations with j unknowns $N_1, N_2, \ldots,$ $\ldots, N_j$, which in principal can be solved. The large number of terms which make up each of the terms $n_{i,s}$ leads to appreciable technical difficulties in solving the set of equations (1). Below an approximate method for solving this set of equations is suggested. The method consists in the successive determination of the N_i's starting with the lowest multiplicity i = 1. It turns out that the terms contributing the most to the value of $n_{i,s}$ (type a coincidences) can be determined with maximum precision. Terms contributing only little can be determined only approximately (here the resulting error is estimated). Terms giving only very small contributions can be neglected, estimating also the error involved in doing so.

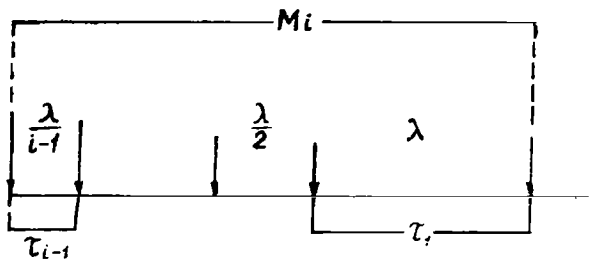

FIGURE 2. Mathematical expectation of the time distribution of the neutrons recorded in an i-fold star.

Before we attempt to find the values $N_1, N_2, \ldots, N_j$ we shall determine the mathematical expectation M_i of the time interval between the recording of the first and last neutrons of an i-fold star and the mathematical expectation τ_ℓ (ℓ is the interval number, starting with the last interval) of the interval between recorded neutrons (Figure 2). We shall need these quantities in the future. In order to simplify the calculations of M_i and τ_ℓ it will be assumed that there are not two neutron diffusion regions in the supermonitor /5/, but only one with a constant diffusion time λ. Since the outside diffusion regions are remote from the counters, the contribution from these regions to the total counting rate is small and the error made will be less than 10%, which will be taken into account in estimating the total error. It will be assumed that in the inner diffusion region there are i neutrons, all of which are eventually recorded, forming an i-fold star. Considering the diffusion laws, the probability density distribution of the appearance of the first prong of an i-fold star is equal to

$$p_{1,i} = \frac{i}{\lambda} \exp\left(-\frac{it}{\lambda}\right). \tag{20}$$

The mathematical expectation of the recording time of the first prong from an i-fold star is correspondingly given by

$$M_{1,i} = \int_0^\infty \frac{it}{\lambda} \exp\left(-\frac{it}{\lambda}\right) dt = \frac{\lambda}{i}. \tag{21}$$

After the recording of the first neutron of an i-fold star there remain in the diffusion region $i-1$ neutrons. The mathematical expectation of the time interval between the detection of the first and second neutron will be $\lambda/i-1$, etc. The mathematical expectation of the time interval between the detection of the last two neutrons will be $\lambda/i-(i-1)$. In view of the fact that the numbering of the intervals between the recorded neutrons is started from the final interval, the mathematical expectation of the first interval between the prongs of the star will be λ, of the second one $\lambda/2$, etc., i.e.,

$$\tau_\ell = \lambda/\ell . \tag{22}$$

From the above expression it is easy to determine the mathematical expectation of the detection time of the whole i-fold star:

$$M_i = \sum_{\ell=1}^{i-1} \frac{\lambda}{\ell} . \tag{23}$$

For a one-pronged star expression (23) is meaningless, since $M_1 = 0$.

Determination of N_1. From (1) we have $n_1 = N_1\alpha + n_{1s}$. Since the expression for n_{1s} for $i = 1$ has only one term, namely n_{1c2}, we obtain

$$N_1 = \frac{n_1 - n_{1c2}}{\alpha} . \tag{24}$$

From (19), and taking (22) into account, we have

$$n_{1c\ell} = n_0\lambda \cdot e^{-N_0 T} \sum_{i=\ell}^{j} N_i . \tag{25}$$

In expressions (24) and (25) there are unknown terms N_0 and $\sum_{i=2}^{j} N_i$. For $N_0 \approx 25\ \text{sec}^{-1}$ and $T = 1.5 \cdot 10^{-3}$ sec, $n_{1c2}/N_1 \approx 0.4\%$. Replacing $\sum_{i=2}^{j} N_i$ by $\sum_{i=2}^{j} n_i$, an error of $+5\%$ in the determination of n_{1c2} is made (see the expression for N_2) and about -0.02% in the value of N_1. Replacing $e^{-N_0 T}$ by $(1-n_0 T)$, an error of $+0.04\%$ relative to $e^{-N_0 T}$ is made and about -0.04% in the value of N_1. Making allowance for these findings and (5), we obtain

$$N_1 = \frac{n_1}{(1-n_0 T)^2} - \frac{n_0\lambda \sum_{i=2}^{j} n_i}{1-n_0 T} . \tag{26}$$

The values of $N_2, N_3, \ldots, N_j$ can be determined in a similar way:

$$N_2 = \frac{n_2}{(1-n_0 T)^2} - N_1^2 T - N_1 \sum_{i=2}^{j} \frac{\lambda}{i-1} n_i - \frac{n_0\lambda \sum_{i=2}^{j} n_i}{2(1-n_0 T)} , \tag{27}$$

$$N_3 = \frac{n_3}{(1-n_0 T)^2} - N_1 N_2 (2T-\lambda) - N_2^2\lambda - \frac{N_1^3 T^2}{2} - N_1 \sum_{i=3}^{j} \frac{\lambda}{i-2} n_i - N_2 \sum_{i=3}^{j} \frac{\lambda}{i-1} n_i - \frac{n_0\lambda \sum_{i=3}^{j} n_i}{3(1-n_0 T)} , \tag{28}$$

$$\begin{aligned} N_4 = {} & \frac{n_4}{(1-n_0 T)^2} - N_1 N_3 \left(2T - \tfrac{3}{2}\lambda\right) - N_2^2 (T-\lambda) - 2 N_2 N_3 \lambda - \frac{N_3^2\lambda}{2} - N_1^2 N_2 \left(\tfrac{3}{2}T^2 - T\lambda\right) - \\ & - N_1 \sum_{i=4}^{j} \frac{\lambda}{i-3} n_i - N_2 \sum_{i=4}^{j} \frac{\lambda}{i-2} n_i - N_3 \sum_{i=4}^{j} \frac{\lambda}{i-1} n_i - \frac{n_0\lambda \sum_{i=4}^{j} n_i}{4(1-n_0 T)} , \end{aligned} \tag{29}$$

$$N_5 = \frac{n_5}{(1-n_0T)^5} - N_1N_4\left(2T-\frac{11}{6}\lambda\right) - N_2N_3\left(2T-\frac{5}{2}\lambda\right) - 2N_2N_4\lambda - N_3N_4\lambda - N_3^2\lambda - \frac{N_4^2\lambda}{3} -$$
$$- \frac{3}{2}N_1^2N_3(T^2-T\lambda) - \frac{1}{2}N_1N_2^2(3T^2-4T\lambda+\lambda^2) - N_1\sum_{i=5}^{j}\frac{\lambda}{i-4}n_i - N_2\sum_{i=5}^{j}\frac{\lambda}{i-3}n_i - \quad (30)$$
$$- N_3\sum_{i=5}^{j}\frac{\lambda}{i-2}n_i - N_4\sum_{i=5}^{j}\frac{\lambda}{i-1}n_i - \frac{n_0\lambda\sum_{i=5}^{j}n_i}{5(1-n_0T)},$$

$$N_6 = \frac{n_6}{(1-n_0T)^6} - N_1N_5\left(2T-\frac{25}{12}\lambda\right) - N_2N_4\left(2T-\frac{17}{6}\lambda\right) - N_3^2\left(T-\frac{3}{2}\lambda\right) - 2N_2N_5\lambda - 2N_3N_4\lambda -$$
$$- N_3N_5\lambda - N_4^2\frac{\lambda}{2} - \frac{2}{3}N_4N_5\lambda - \frac{N_5^2\lambda}{4} - N_1N_2N_3(3T^2-5T\lambda+\tfrac{3}{2}\lambda^2) - N_1^2N_4\left(\frac{3}{2}T^2-\frac{11}{6}T\lambda\right) - \quad (31)$$
$$- N_1\sum_{i=6}^{j}\frac{\lambda}{i-5}n_i - N_2\sum_{i=6}^{j}\frac{\lambda}{i-4}n_i - N_3\sum_{i=6}^{j}\frac{\lambda}{i-3}n_i - N_4\sum_{i=6}^{j}\frac{\lambda}{i-2}n_i - N_5\sum_{i=6}^{j}\frac{\lambda}{i-1}n_i - \frac{n_0\lambda\sum_{i=6}^{j}n_i}{6(1-n_0T)}.$$

In setting up expressions (26 — 31) all two-fold and three-fold coincidences of type a, and all two-fold coincidences of types b and c were taken into account. In the expressions for type c coincidences all values of N_i were replaced by n_i. In the expressions for type b coincidences the values of N_i were replaced by n_i only in those cases where i was equal to or larger than the multiplicity N being determined in that case. Approximate estimates of the errors made by replacing N_i by n_i are summarized in the table. The approximate estimates of the contributions of n_{i5} to N_i and of the errors due to the approximate determination of λ are also tabulated. The values given are different for different values of n_0.

Estimates of the errors in equations (26—31)

Multiplicity	Contribution $n_{i5}: n_0, \%$	Error due to replacing N_i by n_i $n_i \cdot n_0^2, \%$	Error due to the approximation in $\lambda \cdot n_0, \%$
1	$1.3 \cdot 10^{-2}$	$-5 \cdot 10^{-5}$	$+1.3 \cdot 10^{-3}$
2	−0.4	-10^{-4}	$+3 \cdot 10^{-3}$
3	−0.7	$-1.8 \cdot 10^{-4}$	$-2 \cdot 10^{-3}$
4	−1.0	$-3 \cdot 10^{-4}$	$-7 \cdot 10^{-3}$
5	−1.3	$-4 \cdot 10^{-4}$	$-2 \cdot 10^{-2}$
6	−1.9	$-5 \cdot 10^{-4}$	$-3 \cdot 10^{-2}$

Bibliography

1. Kapustin, I.N. and V.A. Radkevich.— Present collection, Part 2, p. 141.
2. Kapustin, I.N.— Geomagnetizm i aeronomiya (in print).
3. Veksler, V., A. Bibergal', and M. Ivanov.— ZhETF, No. 3:490. 1935.
4. Gnedenko, B.V.— ZhETF, No. 1:101. 1941.
5. Hatton, C.J. and E.V. Tomlinson.— Nuovo cimento, B-53, No. 1: 63. 1968.

I. N. Kapustin and V. A. Radkevich

ON THE COINCIDENCE EFFECT IN THE RECORDING OF THE NEUTRON COMPONENT OF COSMIC RAYS

In /1—2/ is indicated an increase of the barometric coefficient with an increase in the multiplicity of the "stars" of the neutron component of the cosmic rays. An investigation of a multiplicity recorder model on a computer by Monte Carlo methods and the calculations performed show that for a proportional increase in the rate of all stars there appears owing to the longer collection time of stars a so-called coincidence effect, which manifests itself in the coincidence of stars of different multiplicity and in the distortion of the information at the output of the multiplicity recorder. This effect leads to an apparent shift of the recorded neutron spectrum towards higher energies when the cosmic-ray intensity increases, and vice versa. In Figure 1 are shown the ratios J_{out}/J_{in} (out-to-in intensities) for stars of different multiplicity (1, 2, 3, . . ., 6) at different mean total intensities. The curves were computed analytically using formulas for random coincidences and as a check by Monte Carlo methods on a computer (the points for the multiplicities 1, 2 and 3 and a total intensity $J_o = 100\ sec^{-1}$ are shown in Figure 1). The initial intensity distribution of stars of different multiplicity was taken from /3/ and was corrected for a dead time $t = 10\ \mu sec$ and a finite star collection time $T = 1$ msec.

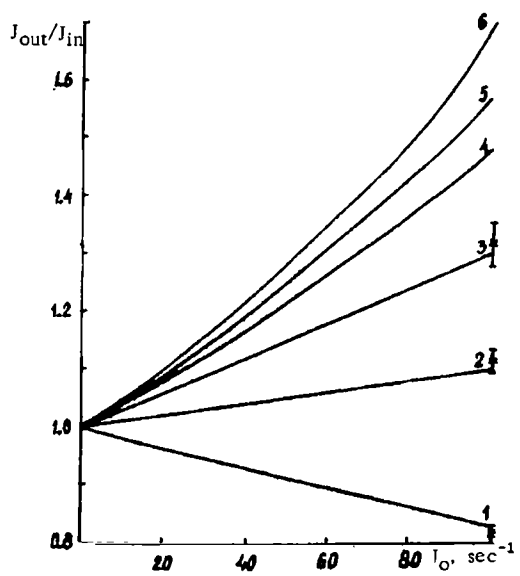

FIGURE 1. Distortion of the output data in recording multiplicities due to the coincidence effect as a function of the total intensity J_o.

It can be seen from Figure 1 that neglecting the coincidence effect in evaluating the data leads to a distortion of the variation of stars of different intensities, and in particular to an apparent increase in the barometric coefficient with star multiplicity. The expected increase in the barometric coefficient for an increase in the star multiplicity was calculated for a neutron supermonitor for average rates of 10, 20 and 30 sec^{-1}. The results are shown in Figure 2, where β_i/β_1 is the ratio of the barometric

coefficient of i-fold stars to the barometric coefficient of one-fold stars. In the same figure are also shown experimental data taken from /2/ on the increase of the barometric coefficient. It can be seen that an appreciable fraction of the increase in the barometric coefficient can be explained by the coincidence effect.

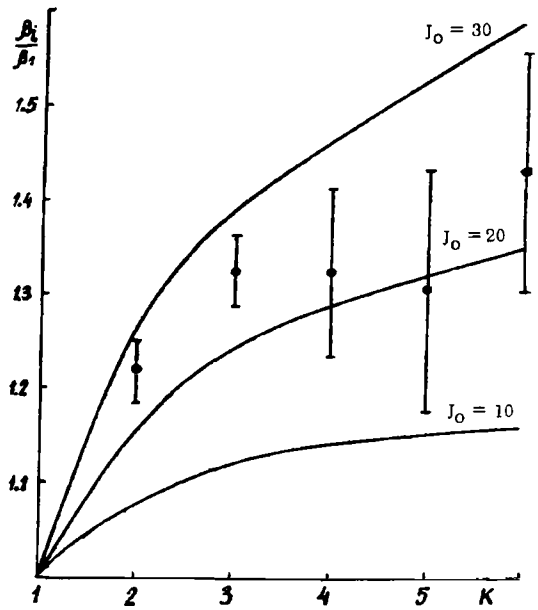

FIGURE 2. Expected apparent increase in the barometric coefficient due to the coincidence effect for stars of different multiplicity.

It is clear from the abovesaid that for the correct interpretation of data on multiplicities while investigating their variations it is necessary to correct for the coincidence effect.

It should be noted that when changing the geometry of the monitor, its basic parameters (dead time and collection time), and also the geomagnetic latitude, the intensity distributions of stars of different multiplicity also change, and the curves shown in Figure 1 are not universal curves for all supermonitors.

In /4/ a method is applied which automatically excludes the coincidence effect, and it seems that these corrections are not needed.

Bibliography

1. Dyring, E. and B. Sporre.— Arkiv för Geofysik, 5(67):71. 1967.

2. Kodama, M. and Y. Ishida.— Report on Ionosphere and Space Research in Japan, 21(1—2):55. 1967.
3. Hatton, C.I. and Carmichael. Experimental Investigation of the NM-64 Neutron Monitor, preprint.— Chalk River Nuc. Labor. Atomic Energy of Canada Limited. 1964.
4. Nobles, R.A., R.A. Albev, F.B. Hughes, I.I. Newkirk, and M. Walt.— J. Geophys. Res., 72, 3815. 1967.

V. S. Smirnov and V. G. Ustinovich

COMPUTER PROCESSING OF SCR DATA

The aim of the present paper is to propose a block diagram of the daily processing of SCR data. All calculations were performed assuming that the data are distributed according to Poisson's law.

The data were processed according to the following scheme:

1. The first block selects the data of the i-th component and performs the control of the data input.

2. The second block provides information on the stability of the monitor. The calculations were performed according to the following formula:

$$Q_i = \frac{\Sigma[(J_i' - J_i'') - (\bar{J}' - \bar{J}'')]^2}{\Sigma (J_i' + J_i'')} = 1,$$

where J_i' and J_i'' are data not corrected for losses due to pressure and counting; $\bar{J}'$ and $\bar{J}''$ are diurnal means. In the case of normal operation of all instruments all values of Q_i should be close to unity. The deviations from this value have a normal distribution.

3. The third block excludes all deviations greater than 3σ and checks the zero level of the monitor by a method, whereby the ratios

$$\kappa' < \frac{J_i'}{J_i''} < n', \quad \kappa'' < \frac{J_i''}{J_i'''} < n'', \quad \kappa''' < \frac{J_i'''}{J_i'} < n'''$$

are determined. If a deviation occurs, two inequalities are not satisfied. The limits are improved during the process of correcting the deviations. The zero level of the instrument is checked by comparing the ratios obtained with the reference ratios.

4. The fourth block corrects the data for the barometric effect according to:

$$J_0 = J_t \exp(-\beta \delta h),$$

where β is the barometric coefficient.

5. The fifth block determines the daily perturbation:

$$R_i = \frac{\Sigma[(J_i' + J_i'') - (\bar{J}' + \bar{J}'')]^2}{\Sigma (J_i' + J_i'')} \geq 1,$$

where J_i', J_i'' are data corrected for the meteoric effect; $\bar{J}'$, $\bar{J}''$ are diurnal means for a quiet day. For an unperturbed day the values of R_i are close to unity, for a perturbed day $R_i > 1$. The boundary is determined on one side only.

6. The sixth block performs a harmonic analysis based on 24 points (Taylor's method). The amplitude and phase of the first and second harmonics are determined.

7. The seventh block performs the printing of all the data; Q_i is the stability criterion; R_i is the perturbation criterion; $\bar{J}', \bar{J}'', \bar{J}''', \bar{J}^{iv}$ are intensities for each section, not corrected for pressure (for the calculation of the barometric coefficient); $\bar{P}$ is the mean diurnal pressure, ΣJ^i is the sum over three (four) sections, corrected for the meteoric effect; r_1, r_2, ζ_1, ζ_2 are respectively amplitudes and phases of the first and second harmonics.

The monthly processing of the data consists in correcting the meson component for the temperature effect and in the printing of a standard table.

I. A. Kuz'min

INSTRUMENTATION FOR THE MEASUREMENT OF X-RAY BREMSSTRAHLUNG IN THE STRATOSPHERE IN THE ZONE OF POLAR AURORAE

The characteristics of electron injections in the zone of polar aurorae are investigated by both direct methods by using rockets and satellites, as well as by indirect methods (polar aurorae, riometers, variations of the magnetic field and X-ray radiation due to the bremsstrahlung of the electrons at the upper boundary of the atmosphere).

The drawbacks of the observations performed with rockets and satellites are related to their high velocities, so that only integral information on the energy spectrum of the radiation is obtained without the possibility of separating time and spatial effects. Ground-level observations do not enable the precise determination of the energy characteristics of the injections. Measurements of X-ray bremsstrahlung in the stratosphere by balloons, on the other hand, yield a more precise energy spectrum and the space and time characteristics of the injected electrons. Three measurement methods with balloons are currently in use:

1. Peak flights — flights whereby rubber balloons are employed. The balloon rises until the rubber envelope bursts, after which a rapid descent follows. The flight duration is 1.5 — 3 hours.

2. Drifting flights — here balloons consisting of polyethylene envelopes with a volume of up to 100,000 m^3 are used. Flight duration is 30 — 40 hours, flight altitude is 30 — 40 km.

3. Flights of long-lived drifting balloons. For such flights global jet streams at high latitudes can be utilized. The realization of such a project is possible with the cooperation of several countries over whose territories the route of the balloon crosses. The flight duration is up to several months /1/.

A large collection of detectors is used in balloon flight for investigating the radiation characteristics: 1) gas-discharge Geiger counter with a detection efficiency of 96 — 98% for the charged component and about 1% for photons; 2) ionization chamber, which detects the total ionizing component; 3) Geiger counter telescope separating the charged component from the X-ray radiation; 4) scintillation counter with a crystal detector and having a detection efficiency of close to 100% for X-rays.

In the initial period of investigations of the injected electrons many detectors were used in balloon flights so that the X-rays could be clearly separated from the cosmic-ray background. Examples are the Anderson balloon /2/, the standard SPARMO balloon /3/, and the Polar Geophysical Institute's RKL-10 /4/. In these sondes the typical combination is a Geiger counter telescope with a four-channel isotropic scintillation spectrometer.

As a result of many observations it was established that the electron injections have a very complex time and space distribution /5/. For the investigation of specific properties of these injections special sondes are sent up by balloons.

For the investigation of the time characteristics with a resolution of milli-seconds large-area (up to 20 cm^2) scintillation detectors are used and the transmission of the data back to ground is performed by a logarithmic counting rate to voltage converter /6/. The dimensions of the injection regions and the directions of the incoming particles are measured by means of directional scintillation counters. This is achieved by using various collimators. The first instrument of this type had two directional counters which measured the ratio of the horizontal and vertical fluxes /7/. The injection region dimensions and their motion were measured in several experiments /8, 9, 10/, in which directional counters with narrow acceptance angles were used; the field of view could be narrowed down to 2 km in diameter at the altitude where the electrons are stopped /9/. A combination of several counters can be used to estimate the motion of the injection regions by observing the intensity variation at the output of each detector. Experiments for the detailed investigation of the energy spectrum in the 15 — 100 keV range by using a 128-channel scintillation spectrometer are being planned /10/.

The telemetry systems used to transmit the information are generally based upon the frequency separation of channels. Most often AM-FM and FM-FM modulation methods are used. Recently, digital telemetry is being employed for information transmission. An important role in the development of telemetry systems is played by the development of elements controlling the proper operation of the telemetry system.

Bibliography

1. Pfotzer, G. — In: "High Latitude Particles and the Ionosphere," p. 167, London, Logus Press. 1965.
2. Enemark, D. Design Manual for Transistor Circuits, edited by J. M. Carroll. — New York, McGraw-Hill, p. 262. 1961.
3. Saeger, K. H., L. Rossberg, and G. Spitz. — SPARMO Bulletin, 3, No. 1. 1968.
4. Kuz'min, I. A. Radiozond RKL-10, tekhnicheskoe opisanie (Radiosonde RKL-10, Technical Description). — Fondy PGI. 1967.
5. Lazutin, L. L. — Present collection, Part 1.
6. Anderson, K. A. A Review of Balloon Measurements of X-Rays in the Auroral Zone. — University of California, UCB-64/4. 1964.
7. Gosling, J. T. — J. Geophys. Res., 71, 835. 1966.
8. Parks, G. K. — J. Geophys. Res., 72, 215. 1967.
9. Parks, G. K., D. W. Milton, and K. A. Anderson. — J. Geophys. Res., 72, 4587. 1967.
10. Cotin, F. and M. Maral. — SPARMO Bulletin, 2, No. 3—4. 1967.

L. A. Shapovalova and V. I. Tergoev

DEVICE FOR OBTAINING COSMIC-RAY INTENSITIES AT FIVE-MINUTE INTERVALS

When all information channels are connected in the 42-channel automatic SCR recording system, there remain 16 channels which can be utilized to obtain 5-minute values of the neutron cosmic-ray component intensities and 15-minute values of the atmospheric pressure, without changing the normal data collection interval of 1 hour. This can be effected in the following way. The information from three sections of the supermonitor is summed up by the SU-1 amplifier, counted by the DBYa cells of the BS/ EUM block and enters into 12 free channels of the SCR register sequentially every 5 minutes, while the pressure information is fed into four channels, also sequentially, every 15 minutes.

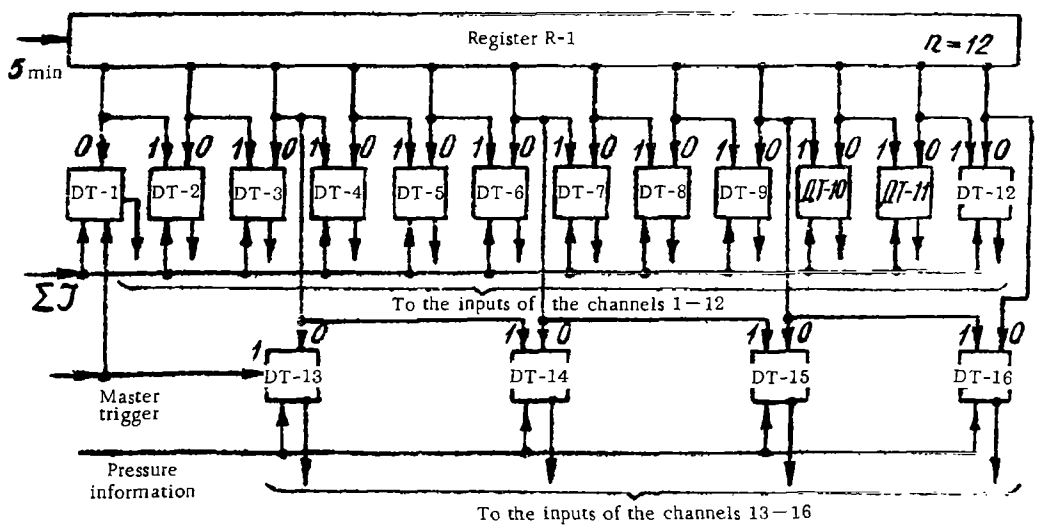

Functional block diagram

The switching of the information is performed by a series of functional nodes, connected into one block. The functional diagram of the block is shown in the figure. The information from the supermonitor is presented parallelly to the dynamical triggers DT-1 and DT-12, and the pressure to DT-13 and DT-16. The triggers operate at the rate of the incoming information and transfer it to the inputs of the corresponding register channels. The switching on and off of the triggers is effected by an instruction from a shift register R-1 with a division coefficient of 12, controlled by pulses from the P-6-15 register of the control element of the recorder.

For the construction of the present circuit about 100 FTM units, two pulse amplifiers and a 12.6-V filter are required (according to diagrams given in the description of the recorder).

M. A. Kovalenko and L. A. Shapovalova

PERFORMANCE DATA OF THE IRKUTSK SCR STATION

The SCR station consists of a neutron supermonitor (three sections), an azimuthal telescope (four telescopes with cubical geometry), a 42-channel automatic recording system and an auxilliary recording arrangement. The Irkutsk station began operation in January, 1967. Data on the neutron intensity are being transferred to MTsD from April, 1968, and data on the muon component from October, 1968. It should be stressed that a running-in period of three months was allowed for.

The mean value of the supermonitor intensity is 506,000 counts/hr, and of the azimuthal telescope — 246,000 counts/hr. As a criterion of the reliability of the data on the neutron component we chose the ratios of the counting rates of the separate sections of the monitor:

$$\frac{J_A(P_i)}{J_B(P_i)} = \frac{J_A(\bar{P})\, e^{-\beta \Delta P}}{J_B(\bar{P})\, e^{-\beta \Delta P}} = const \pm \Delta C.$$

In the figure are shown the ratios of two sections of the supermonitor for the period May, 1968, to January, 1969. From these data it can be concluded that the instrumental error of the supermonitor during that period did not exceed ± 0.35%.

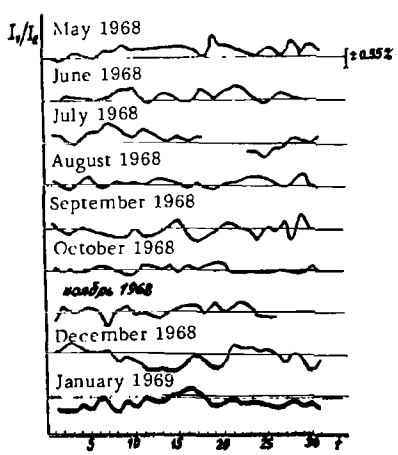

The ratio of the counting rates of two sections of the supermonitor.

The reliability of the data obtained by the azimuthal telescope was determined by comparing them with a standard telescope. These comparisons indicate that the instrumental error of the azimuthal telescope is ± 0.2%.

In order to demonstrate the performance of the SCR station below are given the breakdown periods from May, 1968 to February, 1969, which caused a complete loss of information: overloading of the mains — 78 hours (0.72%), power failure — 188 hours (1.73%), telegraphic equipment failure — 13 hours (0.12%), recorder failure — 46 hours (0.42%). During this period there were failures of individual components: 1 transistor, 3 tunnel diodes and

1 capacitor. In the operation of the electronic circuits of the super-monitor there was one failure attributable to the manufacturer, one due to an instability of the high voltage and one due to a failure of the dead-time univibrator. There were no electronic failures in the azimuthal telescope during the period from October, 1968 to January, 1969.

A. S. Inchin, A. Manshalina, Yu. I. Okulov and I. A. Pimenov

ONE POSSIBILITY OF APPROXIMATING THE LATITUDE DEPENDENCE CURVE

The increase in the precision of calculating the coupling coefficients depends directly upon the precision of approximating the latitude dependence curve /1/. In this case the approximation of the experimental data is generally performed by assuming a priori an analytical dependence between the variables being investigated and a consequent determination of the unknowns in this relation by the method of least squares. Here we shall discuss the possibility of approximating the latitude dependence curve by Lagrange interpolation polynomials /2/. The main feature of this approach is that for the analytical description of the experimental points obtained there is no need to choose a definite functional dependence.

There is a set of experimental points $y_i = f(x_i)$ $(i = 0, 1, 2, 3 \ldots n)$. The form of the function is unknown. The polynomial $Q_m(x)$ and the function $f(x_i)$ will be assumed to be close, if they coincide over the given set of points, i.e., if

$$Q_m(x_i) = f(x_i) \cdot \tag{1}$$

There exists a unique polynomial of degree not higher than n, which has at the points $x_0, x_1, \ldots, x_n$ the given values /2/. The coefficients λ_i of the polynomial $Q_m(x)$ can be determined from the following set of equations:

$$\left.\begin{array}{l} \lambda_0 + \lambda_1 x_0 + \lambda_2 x_0^2 + \ldots \lambda_n x_0^n = y_0 \\ \lambda_0 + \lambda_1 x_1 + \lambda_2 x_1^2 + \ldots \lambda_n x_1^n = y_1 \\ \vdots \qquad\qquad\qquad\qquad \vdots \\ \lambda_0 + \lambda_1 x_n + \lambda_2 x_n^2 + \ldots \lambda_n x_n^n = y_n \end{array}\right\}. \tag{2}$$

The determinant of the system (2) is Vandermonde's determinant:

$$\begin{vmatrix} 1 & x_0 & x_0^2 & \ldots & x_0^n \\ 1 & x_1 & x_1^2 & \ldots & x_1^n \\ & \vdots & & & \vdots \\ 1 & x_n & x_n^2 & & x_n^n \end{vmatrix} = \prod_{0 \le p < q \le n} (x_q - x_p) \neq 0 \ , \tag{3}$$

and consequently, the system (2) has a unique solution. However, the range of the possible values of the argument can be fairly large and the approximation by one polynomial can be unsatisfactory. Therefore it is better to approximate the function by several polynomials at different intervals of the function $y_i = f(x_i)$.

Later the problem will arise of approximating several polynomials by one polynomial. The best results in determining the parameters of this polynomial are presumably achieved when the following condition is satisfied:

$$S=\sum_{(\varkappa)}^{\ell}\int_{a_\varkappa}^{b_\varkappa}\left[Q_m^*(x_i)-Q_m^{(\varkappa)}(x_i)\right]^2 dx = min, \tag{4}$$

where, according to (1), $Q_m(x_i) = f^{(\varkappa)}(x_i)$; $Q_m^*(x_i) = f^*(x_i)$, $Q_m^*(x_i)$ — the "connecting" polynomial, $Q_m^{(\varkappa)}(x_i)$ — polynomials approximating definite parts of the curve. Expression (4) will have a minimum, if

$$\frac{\partial S}{\partial \lambda_i} = 0 . \tag{5}$$

The condition expressed in (5) leads to the following system of equations:

$$\left.\begin{aligned}
&\lambda_1\sum_{\varkappa=1}^{\ell}\int_{a_\varkappa}^{b_\varkappa}\varphi_1(x)\varphi_1(x)dx+\lambda_2\sum_{\varkappa=1}^{\ell}\int_{a_\varkappa}^{b_\varkappa}\varphi_2(x)\varphi_1(x)dx+\cdots+\lambda_m\sum_{\varkappa=1}^{\ell}\int_{a_\varkappa}^{b_\varkappa}\varphi_m(x)\varphi_1(x)dx=\sum_{\varkappa=1}^{\ell}\int_{a_\varkappa}^{b_\varkappa}f^{(\varkappa)}(x)\varphi_1(x)dx\\
&\lambda_1\sum_{\varkappa=1}^{\ell}\int_{a_\varkappa}^{b_\varkappa}\varphi_1(x)\varphi_2(x)dx+\lambda_2\sum_{\varkappa=1}^{\ell}\int_{a_\varkappa}^{b_\varkappa}\varphi_2(x)\varphi_2(x)dx+\cdots+\lambda_m\sum_{\varkappa=1}^{\ell}\int_{a_\varkappa}^{b_\varkappa}\varphi_m(x)\varphi_2(x)dx=\sum_{\varkappa=1}^{\ell}\int_{a_\varkappa}^{b_\varkappa}f^{(\varkappa)}(x)\varphi_2(x)dx\\
&\qquad\vdots\qquad\qquad\qquad\qquad\vdots\qquad\qquad\qquad\qquad\vdots\\
&\lambda_1\sum_{\varkappa=1}^{\ell}\int_{a_\varkappa}^{b_\varkappa}\varphi_1(x)\varphi_m(x)dx+\lambda_2\sum_{\varkappa=1}^{\ell}\int_{a_\varkappa}^{b_\varkappa}\varphi_2(x)\varphi_m(x)dx+\cdots+\lambda_m\sum_{\varkappa=1}^{\ell}\int_{a_\varkappa}^{b_\varkappa}\varphi_m(x)\varphi_m(x)dx=\sum_{\varkappa=1}^{\ell}\int_{a_\varkappa}^{b_\varkappa}f^{(\varkappa)}(x)\varphi_m(x)dx
\end{aligned}\right\}, \tag{6}$$

where $\varphi_1(x)$, $\varphi_2(x), \ldots \varphi_m(x)$ is a system of linearly independent functions generating the "connecting" polynomial $Q_m^*(x)$. Thus the problem of determining the coefficients $\lambda_1, \lambda_2, \ldots \lambda_m$ of the polynomial $Q_m^*(x)$ is reduced to the problem of solving the system of equations (6), whose determinant differs from zero, and consequently, the system (6) has a unique solution.

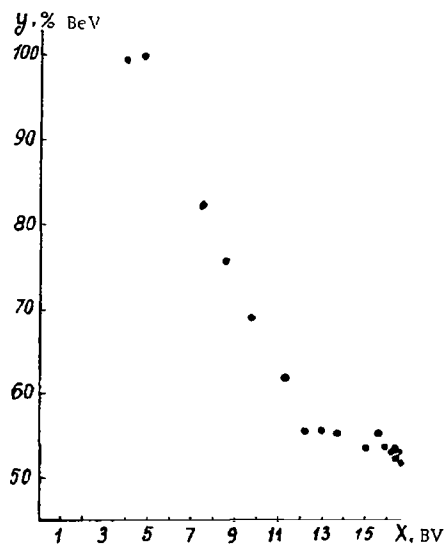

FIGURE 1. Intensity of the neutron component as a function of the rigidity.

In order to test the expediency of this method, the data from the latitude expedition in 1962 — 1963 of the schooner "Zarya" were analyzed: the experimental dependence of the intensity of the neutron cosmic-ray component (%/BeV) upon the rigidity BV. In Figure 1 are shown the points for $y_i = f(x_i)$.

The approximation was performed in the argument range from 4.1 to 16.5. The approximation was performed in two stages. In the first stage were found the polynomial parameters approximating the characteristic parts of the curve: the regions of the "knee," inflection points and local minima. The calculation was performed in three slightly differing ways. Then, the parameters of the polynomial $Q_m^*(x)$ were calculated according to (4)—(6)

for each variant of the calculation. The values of y^* (%/BeV) correspond to the values of the polynomial $Q^*_m(x)$ at the points of the experimental curve. In Figure 2 are shown the connecting polynomials $Q^*_m(x)$ for each variant of the calculation and the experimental points. The calculations were performed on the BESM-3M computer. The whole cycle of calculations for the three variants took about 40 minutes of computer time.

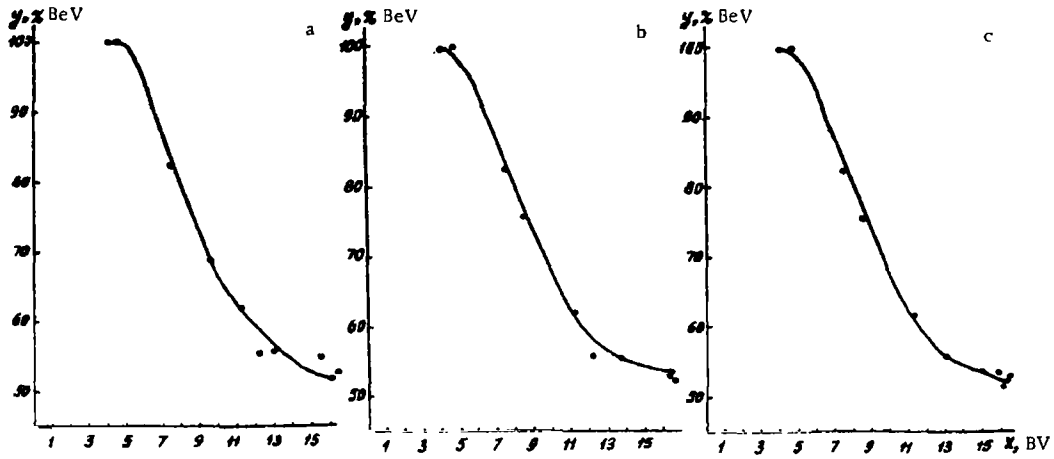

FIGURE 2. Graphs of the connecting polynomials:

a — variant A; b — variant B; c — variant C.

Variant A

X, BV	4.1	4.8	7.5	9.7	11.3	12.2	13	15.6	16.2	16.5
y_{exp}, %/BeV	99.8	100	82.4	68.9	61.9	55.6	55.8	55.3	51.9	52.8
Polynomials $Q_m^{(k)}(x)$	$Q_m^{(1)}(x) = -1.98x^2 + 17.9x +$			$Q_m^{(2)}(x) = 1.61x^3 - 54.5x^2 +$				$Q_m^{(3)}(x) = 5.92x^2 - 194x +$		
	$+ 59.6$			$+ 606x - 2157$				$+1641$		
Polynomial $Q_m^*(x)$	$Q_m^*(x) = 0.0022x^5 - 0.12x^4 + 2.67x^3 - 27.4x^2 + 126.3x - 108$									
	99.8	100	83.1	68.1	61.5	58.9	56.9	52.4	52.8	52.8

Variant B

X, BV	4.1	4.8	7.5	8.5	11.3	13	15	15.9	16.2	16.4	16.5
y_{exp}, %/BeV	99.8	100	82.4	75.5	61.8	55.8	53.6	53.6	51.9	52.5	52.8
Polynomials $Q_m^{(k)}(x)$	$Q_m^{(1)}(x) = 0.42x^3 - 9.01x^2 +$				$Q_m^{(2)}(x) = 0.67x^2 - 19.9x +$			$Q_m^{(3)}(x) = -84.4x^3 + 4112x^2 -$			
	$+54.9x - 3.55$				$+201$			$-66760x + 361284$			
Polynomial $Q_m^*(x)$	$Q_m^*(x) = -0.0089x^4 + 0.40x^3 - 6.1x^2 + 32.7x + 44.4$										
y^*, %/BeV	99.8	98.7	83.7	76.6	60.8	55.9	53.5	52.6	52.1	51.8	51.7

Variant C

X, BV	4.1	4.8	7.5	8.5	11.3	12.2	13.7	15.6	16.4	16.5	16.6
y_{exp}, %/BeV	99.8	100	82.4	75.5	61.9	55.6	55.3	55.3	52.5	52.8	51.8
Polynomials $Q_m^{(k)}(x)$	$Q_m^{(1)}(x) = 0.42x^3 - 9.01x^2 +$				$Q_m^{(2)}(x) = -0.64x^3 +$				$Q_m^{(3)}(x) = 3x + 3.29$		
	$+ 54.9x - 3.55$				$+26.8x^2 - 370x + 1750$						
Polynomial $Q_m^*(x)$	$Q_m^*(x) = -0.0089x^4 + 0.40x^3 - 6.23x^2 + 32.9x + 44$										
y^*, %/BeV	99.8	98.7	83.7	76.6	60.9	57.9	55.1	53.7	52.7	52.6	52.2

It seems that the analysis of the whole latitude dependence curve by the method discussed above will lead to negative results, since even if the difficulty of smoothly connecting the polynomial obtained in the region $x > 17$ BV with the function $y = x^{-\alpha}$ is overcome, the expression obtained as result can turn out to be too complicated. However, the proposed method can be quite useful when describing only part of the latitude dependence curve, since in principal the precision in this case is higher than in the method of least squares. This could probably be useful in those cases in which the experimental data points are not uniform.

The authors would like to express their gratitude to L. I. Dorman and G. F. Krymskii for their helpful advice and discussion of the results.

Bibliography

1. Dorman, L. I. Variatsii kosmicheskikh luchei (Cosmic Ray Variations). — Moskva, Gostekhteoretizdat. 1957.
2. Goncharov, V. L. Teoriya priblizheniya i interpolirovaniya funktsii (The Theory of Function Approximation and Interpolation). — Moskva, Gostekhizdat. 1954.

E. A. Damaskinskii

SPARK CHAMBERS

The considerable advances in the study of the properties of elementary particles during the last eight years are connected with the use of spark chambers. If we divide the different devices used for the detection of particles into two groups, namely, counters (scintillation counters, Cherenkov counters, etc.) and track instruments (nuclear emulsions, bubble chambers, etc.), the spark chamber occupies an intermediate position between these two groups of detectors. In Table 1 the main characteristics of track instruments are compared. It can be seen that the precision of trajectory determination of a particle by a spark chamber is comparable with the spatial resolution of other track chambers, and the time resolution is close to the corresponding characteristics of counters. A spark chamber can operate in a mode similar to that of a bubble chamber, so that all particles traversing its volume are recorded. But in contrast to bubble chambers the operation of a spark chamber can be controlled by a system of counters. The spark chamber is the only track chamber the data from which can be received without photographing the tracks (filmless methods). An additional advantage is its simplicity and relative low construction cost.

TABLE 1. Comparison of the characteristics of track instruments

Track instrument	Sensitive time, sec	Recovery time, sec	Spatial resolution, cm	Possibility of control
Nuclear emulsion	—	—	10^{-4}	No
Cloud chamber	$4 \cdot 10^{-3}$	30	10^{-1}	Yes
Diffusion chamber	—	5	10^{-1}	Yes
Bubble chamber	10^{-3}	1	10^{-2}	No
Spark chamber	$5 \cdot 10^{-7}$	10^{-2}	10^{-1}	Yes

The combination of the above properties has determined the wide use of spark chambers, primarily at charged-particle accelerators. The use of spark chambers for the detection of cosmic rays has begun only recently. The many possibilities of applying spark chambers in cosmic-ray studies will be discussed below.

There exist several chamber types differing in their mechanism of operation. The characteristics of the various chambers depend upon the operating conditions (filling, pressure p, gap width d and parameters of the

high voltage pulse). Below are given typical values for the operating parameters of chambers which can be at present easily achieved in practice.

Principle of operation of the spark chamber. Under the name spark chambers is understood that class of instruments, in which a gas discharge is localized along the trajectory of a charged particle (the completion of the discharge by a spark breakdown is not compulsory). A schematic diagram of a controlled spark chamber is shown in Figure 1.

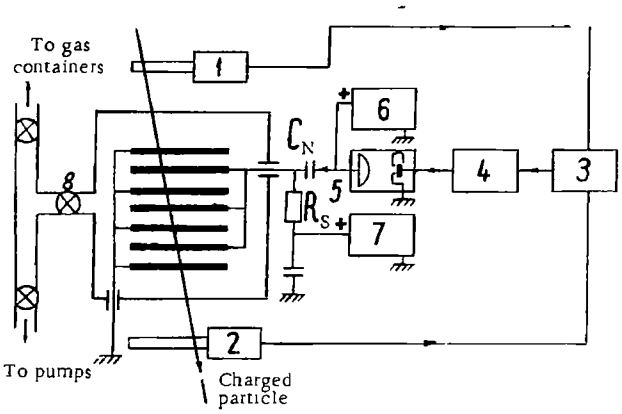

FIGURE 1. Schematic diagram of a controlled spark chamber:

1, 2 — scintillation counters; 3 — selection device; 4 — trigger pulse shaper; 5 — switching element of the high-voltage generator (spark gap or thyratron); 6 — high-voltage source; 7 — clearing field supply; 8 — vacuum valve.

The spark chamber generally consists of a parallel-plate capacitor filled with an inert gas. A cosmic ray traverses counters 1 and 2 connected to circuit 3, which enables the selection of the desired events. The signal from 3 is fed to the trigger pulse shaper 4 which controls the discharge device 5. The latter causes a high-voltage pulse with an amplitude of about 10 kV to appear on the chamber electrodes.

The electrons produced in the chamber gas by the charged particle passing through it develop a cascade under the action of the electric field near the trajectory of the particle, and at a sufficiently high field intensity the cascade causes a spark discharge in the gas. The discharge produced near the track is recorded on a film or by some filmless method (Figure 2).

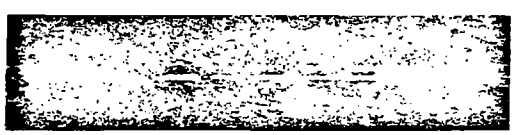

FIGURE 2. Particle track in a five-gap spark chamber.

The precision with which the discharge follows the particle track depends upon the angle φ between the direction of particle motion and that of the electric field. For small values of φ the typical rms deviation from the particle trajectory is 0.2 mm. We are often interested in the angle between the particle trajectory and some fixed direction in space (e.g., the scattering angle of the particle by a target). The precision of determining this angle depends obviously upon the track length in the chamber and for a 10-cm long track it is about 10^{-3} rad.

Efficiency. The efficiency E of a spark gap is the ratio of the number of particles detected (presence of a spark near the particle trajectory) to the total number of particles which traversed this gap. Most chambers have an efficiency close to 100%. For different gases this efficiency is achieved for different values of the high-voltage pulse U. In Figure 3 is shown the dependence of the efficiency upon the high-voltage pulse U for inert gases /1/. In polyatomic gases $E \approx 100\%$ is achieved at appreciably higher values of U.

What is the efficiency of detecting several particles simultaneously traversing a spark gap? Wide-gap chambers have a high efficiency for detecting several particles. It was shown that for a 10-cm gap the efficiency is the same for 1 to 50 particles /2/. For the detection of several particles it is best to fill the chamber with neon. The detection efficiency of several particles in chambers filled with polyatomic gases is close to zero.

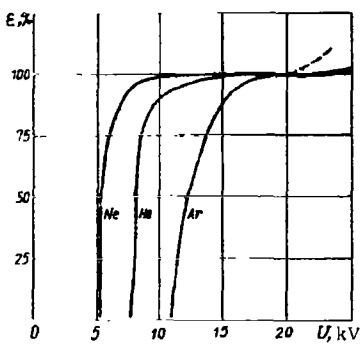

FIGURE 3. Spark chamber characteristics for different inert gases.

The time characteristics of spark chambers are determined by two parameters: memory time and recovery time. The memory time τ_m of a chamber is that time during which the electrons produced by the particle and capable of forming a discharge are preserved in the chamber. For different types of chambers τ_m varies between fractions and tens of microseconds. Thus, for $\tau_m = 1\,\mu$sec the chamber is capable of selecting an event of interest in a flux of 10^6 particles/sec passing through the sensitive volume of the chamber.

The recovery time determines the possible rate of the chamber operation. The recovery time Γ_r is that interval of time after the firing of the chamber after which the chamber can once again detect a particle with the spark formed near the trajectory of the new particle. The recovery time T_r is of the order $0.5 - 100\,\mu$sec for different types of chambers. Thus, the chamber can be operated 10 to 2000 times per second. Generally, under experimental conditions the rate is determined not by the chamber, but by the auxiliary equipment (e.g., film transport of the camera, high-voltage rectifier power, etc.).

Design and operation of spark chambers. The technique of spark-gap construction has been brought at present to such a level that the spark chamber can be operated immediately after assembly. Spark chambers can have different geometries: plane-parallel or cylindrical, single-gap or multi-gap. The electrodes are made of metal (iron, lead, aluminum, etc.)

or of conducting transparent glass. In different experiments electrodes from several microns to several centimeters thickness were used. Filmless spark chambers with wire electrodes are being widely used.

The requirements of pumping and filling the chamber are quite simple: the chamber is pumped down to vacuum and generally filled with an inert gas (most often Ne, He or a mixture of these two gases) at a pressure $p \sim 1$ atm. The description of various spark chamber designs can be found in /1, 3/.

Spark chambers with a gap of the order of 1 cm are fed by high-voltage generators with a thyratron or spark gap. The triggering of a spark chamber by a spark gap is faster than by a device using a thyratron. A spark-gap system is easier to build, is capable of switching higher currents, is cheap and is used successfully with spark chambers having a high capacitance. The spark gap can be triggered by a circuit with one secondary emission tube. For experiments performed with balloons or satellites a low-power supply system with a spark gap controlled by a low-amplitude pulse was developed /4/.

For spark chambers with gaps larger than 10 cm high-voltage pulse generators of the Marx type are used. The problems of high-voltage supply for spark chambers have been discussed in detail in /1, 5/.

Methods of obtaining information. Photography of the tracks in the spark chamber is one of the main methods of obtaining information. Generally, two mutually perpendicular projections of the spark gap are photographed. This enables the unique determination of the coordinates of one spark. In cases where there are several sparks in a gap their identification can be facilitated by the different brightness and shape of the various spark images. The spark brightness is adequate for its recording by a standard film with a sensitivity of 60 – 250 units GOST at an aperture of 8 to 16.

In the literature /1, 3/ are described different systems for photographing the tracks of charged particles. The optical distortions due to the camera can be estimated or measured experimentally, and corresponding corrections can be introduced /6/. The measurements of the spark coordinates is performed manually or with the aid of special automatic machines /7/. It should be mentioned here that the evaluation of spark chamber pictures is simpler than for bubble chamber pictures, since the spark coordinates can be measured with a lower precision and the picture is less cluttered up by background events.

In order to improve the precision the statistics have to be increased. The number of pictures increases up to $\sim 10^6$. From this number events satisfying certain criteria have to be selected (kinematics of the process being studied, geometry of the experiment, etc.). The manual evaluation of spark chamber pictures is very laborious. Automatic measuring machines can measure the spark coordinates in one frame in 1 – 3 seconds, i.e., 10^6 frames can be processed in 1 – 3 months. A computer with a speed of 10^6 operations per second can reconstruct the track in space in ~ 30 milliseconds and process all the information in about 3 hours. Therefore, the main delay in obtaining the final results is due to the measurements of the spark coordinates on film. The solution is to forego photographing the tracks and use some filmless method of data extraction.

In recent years several methods of filmless data extraction from spark chambers have been developed /8/. The common principal of all

filmless methods is the following. Pick-up devices sensitive to the effects accompanying a gas discharge (pressure increase, electric field, etc.) are used. The electric signals from these sensors can be uniquely related to the position of the sparks. These signals can be either recorded for later processing by a computer (off-line operation) to be fed directly to a computer and processed during the experiment (on-line operation).

So far only one particle has been detected in spark chambers with a filmless recording of data. In principle, the tracks of several particles simultaneously traversing the chamber could be recorded, but this complicates matters appreciably.

In the study of elementary particle interactions wire spark chambers with magnetostrictive lines /9/ or ferrite cores /11/ were used, as well as spark chambers with television cameras /11/ and acoustic detectors /12/. We shall discuss briefly each of the above methods, and then compare their technical possibilities.

Wire chambers possess a short recovery time (i.e., they can be used in high-flux particle beams) and contain a small amount of material along the particle path. The electrodes of such counters are made of wires ~ 0.1 mm in diameter stretched parallel to one another at intervals of ~ 1 mm. One end of the wire is connected to a common bus bar, the other end is electrically insulated. The control of the chamber is achieved by conventional means.

When the data is obtained via a magnetostrictive line, an insulated strip of a magnetostrictive material is placed on the wire electrode (Figure 4). Around that wire along which the discharge current flows a magnetic field is produced. At the point where the wire crosses the magnetostrictive line there occurs a local magnetization of the line causing a change in volume (magnetostrictive effect). The elastic deformation propagates along the line in both directions and can be recorded by the inverse magnetostrictive effect (change of the magnetization due to the formation) in ferromagnetic coils placed at the ends of the line.

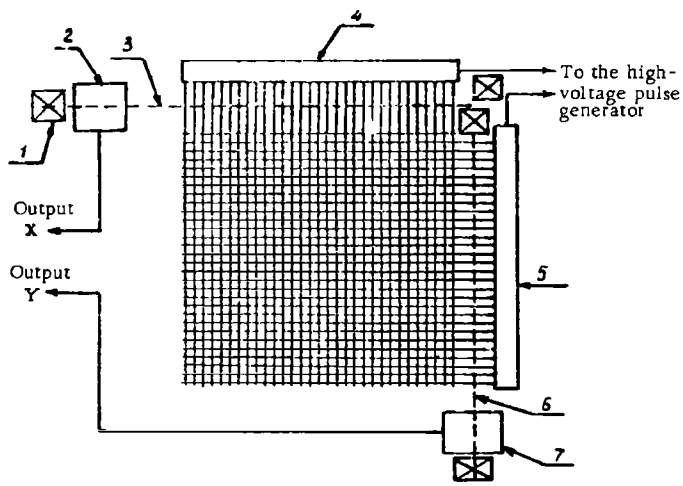

FIGURE 4. Wire chamber with a magnetostrictive line readout:

1 — damping device; 2 — pick-up coil of the x-plane; 3 — magnetostrictive strip of the x-plane; 4 — high-voltage bus bar; 5 — ground bus bar; 6 — magnetostrictive strip of the y-plane; 7 — pick-up coil of the y-plane.

Knowing the propagation velocity of the ultrasonic wave in the strip material and the time from the spark generation to the time of the pulse appearing in the coil one coordinate of the spark can be determined. The other coordinate is obtained in a similar way by an electrode placed at 90° with respect to the first one. The time interval is measured in the following way. The signal from the coincidence circuit starts a high frequency pulse generator connected to a scaler. The pulse from the coil stops this generator. Knowing the frequency of the generator and the number of pulses counted, the time of the ultrasonic wave propagation can be readily determined. The precision with which the spark coordinate is determined depends upon the precision of the charge localization near the track and upon the precision of measuring the time interval. The spatial resolution of the coordinates from several sparks depends upon the width of the magnetostrictive pulse. The data readout time depends upon the chamber dimensions and the propagation velocity of the ultrasonic wave in the magnetostrictive material (this velocity is $\approx 5\ \text{mm}/\mu\text{sec}$).

The data is read out by magnetic cores by passing each wire through a magnetic core with a rectangular hysteresis loop and grounding it (Figure 5). When the high-voltage pulse is applied to the wires, the discharge occurs between those wires which are close to the particle trajectory. The current flowing along the wire changes the magnetization in the corresponding ferrite core. The pulse from the output winding gives the core number, i.e., the spark coordinate.

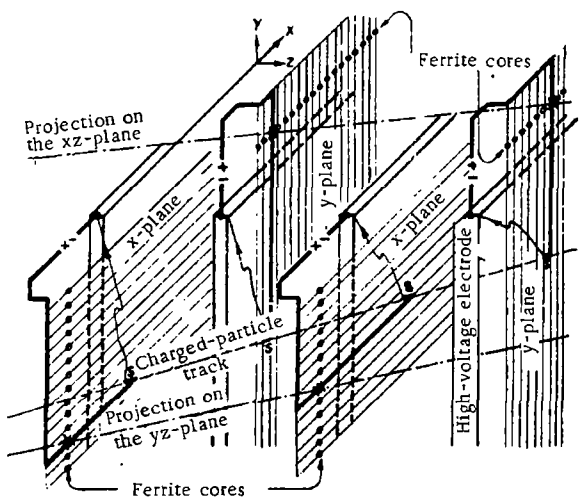

FIGURE 5. Wire spark chamber with a ferrite-core readout:

S — spark; ○, ☼ — ferrite cores in the states "0" and "1," respectively; ± — high-voltage pulse (+ is grounded). The currents flowing in the chamber are designated by a thick line.

During the readout the ferrite cores are interrogated sequentially by a pulse which returns all cores to their initial state. The readout time

depends upon the method of interrogating the cores. In order to reduce the readout time a whole group of cores can be interrogated simultaneously. The precision of the coordinate determination and the spatial resolution are determined generally by the inter-wire distance.

Television data readout. As in the case of regular photography, the image of the spark chamber is focused by means of mirrors and lenses upon the screen of a vidicon. The sensitive element of a vidicon consists of a photoconducting layer upon a transparent conducting surface (Figure 6). This layer is charged to an uniform negative potential by a scanning electron beam. When a spark is formed the areas upon which the image of the spark fell are discharged. The output signal is obtained when the electron beam recharges these areas and a current flows through a load resistor. The load resistance is the input resistance of the image intensifier.

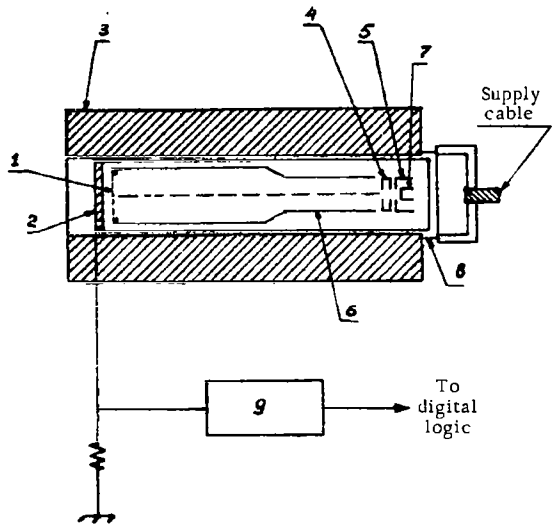

FIGURE 6. Vidicon diagram:

1 — grid no. 4; 2 — screen; 3 — focusing and deflecting coils; 4 — grid no. 2; 5 — grid no. 1; 6 — grid no. 3; 7 — cathode; 8 — metal nipple; 9 — image intensifier.

The spark coordinates are determined in the following way. Upon reaching the spot discharged by the spark the scanning beam connects a pulse generator to a scaler and switches it off when reaching the end of a line. Knowing the beam velocity and the scanning time, the position of the spark relative to the vidicon edge can be determined. The precision of the spark coordinate and the spatial resolution depend upon several factors: the resolution of the vidicon, chamber dimensions, sweep linearity and stability, brightness of the light signal, etc. The resolution of industrial vidicons is 500 lines, the dimensions of the sensitive area is $9 \times 12.7\ mm^2$. The readout time consists of the scanning time and the time required to erase the old image. The scanning time of one line is of the order of

several tens of microseconds. The time to erase the image is 2 — 3 times longer.

In acoustical spark chambers the position of the spark is determined by the time t it takes the sound to travel the distance r from the spark to a sound receiver. For a constant sound velocity $v_0 = \text{const}$, $r = v_0 t$. However, the pressure wave produced by the spark is a shockwave and its velocity $v = v_0 + \Delta v$ depends upon r and the energy W of the spark. The presence of the shockwave causes the sonic signal to arrive from a known distance r earlier by Δt than predicted from the relation $t = r/v_0$. It can be assumed that the sonic signal was emitted at a distance Δr from the spark center, i.e., the spark has a dimension Δr. For the i-th sonic receiver $r = v_0 t_i + \Delta r$. The microphone is placed at such a distance from the spark that the assumption of a constant sound velocity introduces only small errors in the measurements of spark coordinates.

For the determination of the position of the spark four microphones are placed in each spark gap of the spark chamber. This enables us to calculate v_0, Δr and the coordinates x and y. As sound receivers piezoelectric or electrostatic (capacitance) microphones are used. The method of measuring the time t was already described in the discussion of wire chambers with a magnetostrictive readout. The factors determining the spatial resolution and the readout time are the same for acoustic spark chambers as for magnetostrictive spark chambers. It should be kept in mind that the sound velocity in an acoustic chamber is lower by one order of magnitude and for neon $\approx 0.5\,\text{mm}/\mu\text{sec}$.

Comparison of different methods of data readout. It is difficult to determine the criteria for the use of any particular method. It seems that the main factor in choosing a method for data recording is its reliability. The recording of complex multipronged events is generally done by photography with a subsequent visual processing of the film. Filmless systems for the detection of several particles are quite complicated and expensive and are mainly used for the detection of single particles. In experiments at accelerators wire chambers with a gap of the order of 1 cm are most often used. The acoustic method is superior to other filmless methods in the precision of the determination of the spark position. This becomes very important when measuring particle momenta by means of chambers placed in a magnetic field. The television method is the most convenient for obtaining the information from wide-gap (≥ 10 cm) chambers and streamer chambers.

It is the author's opinion that for balloon and satellite experiments the most promising are the television and acoustic methods. The advantage of the first method is that commercial television systems can be used, while the second method uses a simple logic for event selection in the case of single particles and requires a relatively low-frequency radio channel (~ 1 MHz). In Table 2 the various methods for obtaining the information from spark chambers are compared. The mean (not ultimate) spark chamber parameters are given in this table.

Measurement of particle momenta and energies. Spark chambers placed in a magnetic field were used to measure particle momenta. The precision of momentum determination at $p = 1$ GeV/c with narrow-gap chambers is 0.5 — 1.0% (taking into account the instabilities of the magnetic field). Alikhanyan et al. /13/ were the first to discover that the discharge in wide-gap chambers in a magnetic field is bent. Bayukov et al. /14/

TABLE 2. Comparison of different spark chambers and data recording methods (data taken from /7, 8, 9–12, 16/)

Method		Signal amplitude, mV	Signal-to-noise ratio	Precision of coordinate determination for one spark (standard deviation), mm	One-dimensional resolution of two sparks, mm	Data readout time	Chamber dead time, msec	Possibility of operation in a magnetic field
Wire chamber	Ferrite cores	–	>10	0.3–0.5	≥1*	≥1–100 μsec	≈0.2	No
	Magneto-strictive readout	0.01–0.1 mV/turn of the pick-up coil	–	0.3–0.5	≥3*	≥100* μsec	~10	≥20 kgauss
Acoustic chamber		1–50	≈10	0.2	≥2	≥1 μsec	~10	Yes
Vidicon readout		1–3**	≈10	0.5	≥1*	≥60–100** μsec/spark gap	~10	≤50 gauss
Photography of tracks		–	–	0.2	≥1	film transport 0.3 sec/frame, measurement of spark coordinates in one picture 1–3 sec	~10	Yes

* The data are estimates for a $50 \times 50 \times 1\ cm^3$ chamber. A wire spacing of 1 mm was assumed for the wire chambers.

** For a LI-408 vidicon and an energy of 0.02 joule fed into the spark.

measured the energy of protons on the basis of their range in a spark chamber. One of the main efforts in developing the spark chamber technique is directed at present towards the possibility of particle identification.

The best results in measuring the primary ionization were obtained with streamer chambers. In /15/ was shown the possibility of measuring the relativistic rise of the primary ionization with an error of 2%. The streamer chamber, in which the discharge is localized near the particle trajectory irrespective of the angle between the direction of motion of the particle and the electric field, is an instrument with many possible future uses in particle experiments. The properties of the streamer chamber are described in detail in /1/.

In wide-gap chambers a dependence of the discharge brightness upon the ionization power of the particle was found /1/. There exist many possibilities for particle identification by means of narrow-gap spark chambers /14/. Development in this field is continuing and gas-discharge devices with new interesting properties will probably be suggested in the future.

The specific features of spark chambers in cosmic-ray investigations should be stressed. Spark chambers possess a large light yield and a relatively low weight. In experiments performed with balloons or satellites there exists the possibility of a direct transmission of data on the events being studied. Some examples of spark chamber applications will be mentioned below.

High-energy electrons, positrons, and photons produce a shower in a lead-plate spark chamber, a fact which clearly separates these particles from other relativistic particles. If at the same time the detection efficiency for several particles in the same gap is high, the photon or electron energy can be determined from the number of sparks at a given depth. Spark chambers for the detection of photons in outer space are described in /17/.

Spark chambers together with a magnetic field were used to measure particle momenta of the primary cosmic radiation /18/. The estimates for the maximum measurable momentum are $10^{11}-10^{12}$ eV/c. A spark chamber is probably the most suitable detector for cosmic-ray neutrinos. Many other applications of spark chambers can be indicated: in ionization calorimeters for energy measurements of particles with energies ≥ 100 GeV, in muon spectrometers, etc.

Bibliography

1. Daion, M.I., B.A. Dolgoshein, V.I. Efremenko, G.A. Leksin, and V.A. Lyubimov. Iskrovaya kamera (The Spark Chamber).— Moskva, Atomizdat. 1967.
2. Bolotov, V.N. and M.I. Devishev.— ZhETF, 46, 1990. 1964.
3. Spark Chamber Symposium.— Rev. Scient. Instrum., 32, 480. 1961; Proc. 1962 Conf. on Instrum. High Energy Physics.— Nucl. Instrum. and Methods, p. 20. 1963.

4. Gorodinskii, G.M., E.A. Damaskinskii, A.S. Denisov, M.P. Konstantinova, E.M. Kruglov, S.P. Kruglov, and N.P. Mokrovskii.— PTE, No.2:69. 1967.
5. Vorob'ev, G.A. and G.A. Mesyats. Tekhnika formirovaniya vysokovol'tnykh nanosekundnykh impul'sov (Generation of High-Voltage Nanosecond Pulses).— Leningrad. Atomizdat. 1963;
Lavoie, L., S. Parker, C. Rey, and D.M. Schwartz.— Rev. Scient. Instrum., 35, 1567. 1964;
Schrank, C., G. Henry, Q.A. Kerns and R. Swanson.— Rev. Scient. Instrum., 35, 1326. 1964.
6. Borkovskii, M.Ya., E.A. Damaskinskii, and S.P. Kruglov.— Preprint FTI—014, Leningrad. 1967;
Bystritskii, I., F. Legar, M. Maly, O. Sgon, and Z. Yanout.— PTE, No.5:55. 1966.
7. Legar, F., M. Maly, O. Sgon.— PTE, No.5:78. 1966;
Goldschmidt-Clermont, Yu.— Preprint OIYaI E-1806, Dubna. 1964;
Wenzel, W.A.— Ann. Rev. Nucl. Sci., 14, 205. 1964.
8. Proc. Inf. Meet. on Filmless Spark Chamber Techniques and Associated Computer Use.— Preprint CERN 64-30, June 1964.
9. Fisher, J.— Proceedings of the International Conference on Electromagnetic Interactions at Low and Intermediate Energies, Dubna, February 1968. Moskva. Izdatel'stvo AN SSSR, 4, 179. 1967;
Gavrilov, A.S., I.A. Golutvin, Yu.V. Zanevskii, S.S. Kirillov, B.A. Kulakov, L.G. Makarov, and E.N. Tsyganov.— PTE, No.6:69. 1966.
10. Ehrmann, C.H.— IEEE, NS-13, 503. 1966;
Golutvin, I.A., Yu.V. Zanevskii, B.A. Kulakov, and E.N. Tsyganov.— PTE, No.5:66. 1966.
11. Perez-Mendez, V.— IEEE, NS-12, 13. 1965.
12. Ögelman, H.B., J.P. Delvaille, and K.I. Greisen.— Phys. Rev. Lett., 17, 491. 1966.
Lillethum, E., B. Maglic, G. Manning, C.A. Stahlbrandt, et al.— Nuovo cimento suppl., 2, 310. 1964.
13. Alikhanyan, A.I., T.L. Asatiani, and E.M. Matevosyan.— ZhETF, 44, 773. 1963.
14. Bayukov, Yu.D., L.S. Vorob'ev, G.A. Leksin, V.L. Stolin, V.B. Fedorov, and V.D. Khovanskii.— PTE, No.1:77. 1966.
15. Davidenko, V.A., B.A. Dolgoshein, V.K. Semenov, and S.V. Somov.— ZhETF, 55, 426. 1968.
16. Gorodinskii, G.M., E.A. Damaskinskii, M.P. Konstantinova, E.M. Kruglov, N.P. Morkovskii, and A.M. Romanov.— PTE, No.2:64. 1967;
Kantserov, V.A., Yu.P. Kulyabichev, B.S. Rozov, and B.I. Tereshchenko.— PTE, No.1:53. 1968;
Bekrenev, V.S., S.P. Kruglov, D.L. Nikolaev, and A.I. Shcheglovskii.— Preprint FTI-160, Leningrad. 1968.
17. IEEE, NS-13, No.1. 1966.
Dean, A.I.— Nucl. Instrum. Meth., 65, 293. 1968.
Helmken, H.F. and G.G. Fazio.— IEEE, NS-13, 486. 1966.
18. Daion, M.I. and V.Kh. Volynskii.— ZhETF, Vol.37:906. 1959.
De Shong, I.A., R.H. Hildebrand, and P. Meyer.— Phys. Rev. Lett., 12, 3. 1964.

L. V. Bakonov, K. N. Ermakov, V. D. Lebedev,
A. V. Monakhov, V. I. Rozum and M. V. Stabnakov

HEAVY-LIQUID BUBBLE CHAMBER FOR INVESTIGATIONS IN COSMIC-RAY PHYSICS

Track chamber detectors, nuclear emulsions and cloud chambers, are in use for a long time already in cosmic-ray experiments. The advantage of these methods of particle detection is especially great when the problem consists of identifying an unknown particle. The first picture of a positron track was obtained in a cloud chamber. In a similar way mesons were discovered in the cosmic radiation.

The main advantage of the nuclear emulsion is its high density (10^{22} nuclei/cm^3), or, in other words, the probability of a nuclear interaction is high. However, nuclear emulsions are not suited for the study of space-time variations of the cosmic rays. The cloud chamber /1/ can, on the other hand, yield space-time characteristics of the detected radiation. But even at high pressures the density does not exceed 10^{19} nuclei/cm^3. The low density renders the conditions for event identification appreciably worse.

The bubble chamber, in which tracks of charged particles are formed in the form of chains of vapor bubbles in a superheated liquid, is an instrument which combines the advantages of the nuclear emulsion and the cloud chamber. The density of the liquid in the bubble chamber varies from $3 \cdot 10^{22}$ nucleons/cm^3 (liquid hydrogen) to $\sim 10^{24}$ nucleons/cm^3 (xenon). In bubble chambers a large variety of liquids can be used. In principle, almost any liquid with suitable thermodynamic properties can be used, i.e., there exists the possibility of choosing the nuclear composition of the chamber liquid for different experiments. For example, it can be used as a photon detector with a high detection efficiency. The bubble chamber possesses no "memory" and is therefore independent of the amount of radiation incident upon the chamber in one cycle; this radiation has no effect upon the next cycle of the chamber. In other words, there is no danger of overexposing the chamber in one or more cycles. The events recorded upon film are fixed in time by the chamber cycle, while the rate of the chamber expansion can be determined according to the problem being studied. The existing methods of processing bubble chamber pictures enable us to carry out analyses of angular distributions with an error of not more than 1°. The bubble chamber detects all charged particles: protons, electrons, α-particles. A freon (CF_3Br) filled chamber detects in addition to charged particles also photons with a high efficiency. The solid angle for a suitable bubble chamber design can be made large enough, which is very important

for cosmic rays, which have an isotropic spatial distribution. By means of a bubble chamber the energy, mass and direction of motion of a particle can be determined. All these features make the bubble chamber an extremely convenient instrument for the study of the space-time variations of the cosmic rays. There are at present no basic difficulties in mounting a bubble chamber in satellites in the upper layers of the atmosphere. The information on the weight of equipment in satellites leads us to hope that large bubble chambers could be mounted in satellites.

PARTICLE IDENTIFICATION IN A BUBBLE CHAMBER

The tracks of charged particles incident upon the chamber while the latter is sensitive are recorded photographically. The chamber volume is photographed by two or more cameras. The stereo pairs obtained in this way are then measured on special measuring machines with the aim of a subsequent reconstruction of the track coordinates in space, since the coordinates comprise the main portion of the data on the particle.

For the kinematical analysis of events the angles between the tracks have to be measured. The particle range is determined by the length of the track in the chamber. The range is the main method of identifying particles which are produced and stopped in the chamber. The range determines the particle energy. The product of the particle momentum and its relative velocity $p\beta$ is determined by measuring the multiple scattering, i.e., by measuring the track direction at many points, since the tracks are not straight, especially in a heavy liquid. The measurement of scattering is the main method of particle identification in heavy-liquid (high density, high atomic number) chambers operating without a magnetic field. The methods used for measuring the particle scattering from the track picture were developed for nuclear emulsions. Knowing the particle range and the multiple scattering in the chamber the mass of the particle can be determined.

The final processing of the results obtained, i.e., yielding the characteristics of the particles detected by the chamber, is performed by means of special computer programs /2/.

From the above discussion it follows that a heavy-liquid bubble chamber operating without a magnetic field, i.e., in conditions typical for a self-contained mode of operation, enables one to derive practically all the information on the charged particles recorded in the chamber. In addition, a chamber of even moderate dimensions filled with freon can serve as photon detector with a high detection efficiency. In addition to determining the composition of the radiation, the chamber automatically gives also its space-time characteristics.

SELF-CONTAINED BUBBLE CHAMBER MODEL

In FTI im. A. F. Ioffe AN USSR a heavy-liquid chamber was constructed for the performance of special dosimetric experiments on the FTI synchrocyclotron. The same chamber with certain design modifications of

the auxiliary parts could have been used on balloons for studies in the upper atmosphere.

In the design of this chamber allowance was made for the fact that the chamber has to detect protons and photons over quite a large energy interval. The liquid chosen for operating the chamber was bromine freon F13-V1. The thermodynamic properties of this type of freon render it convenient for a self-contained chamber. The energy range being detected is determined by the chamber dimensions and the liquid composition. It is obvious that an increase in the chamber dimensions leads to an appreciable increase of the weight. A chamber of small dimensions, however, has appreciably poorer detection possibilities.

The geometrical factor of the chamber is 500 $cm^2 \cdot$ sterad. The detection threshold is 50 MeV for protons, 200 MeV for α-particles and 6 MeV for photons. Charged particles are recorded in the chamber with 100% efficiency, while the detection probability of photons is at least 70%.

A chamber which can be mounted in a balloon is described schematically in Figure 1. A hermetically sealed envelope (7) containing the chamber (4) is enclosed in a heat shield (6). The chamber is placed so that the up-down direction should be shielded by the auxiliary components of the chamber. The main components of the chamber are described below.

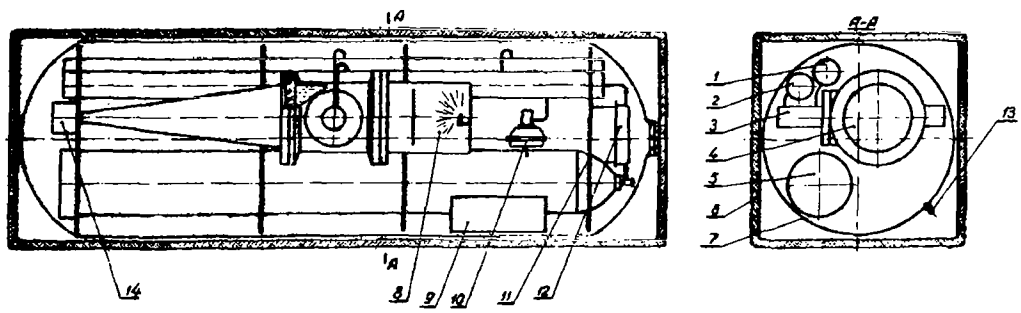

FIGURE 1. Proposed design for a bubble chamber to be mounted in balloons:

1 — high-pressure receiver; 2 — low-pressure receiver; 3 — electromagnetic valve; 4 — bubble chamber; 5 — container V = 40 l, p = 150 atm; 6 — heat shield; 7 — hermetically sealed vessel; 8 — chamber light source; 9 — control circuits and supply unit; 10 — pressure stabilizer; 11 — rigid fin; 12 — pressure control unit; 13 — safety valve; 14 — stereoscopic camera system.

The chamber body (Figure 2) is a thin-walled stainless steel cylinder of 200 mm inner diameter with three ribs for better rigidity. The wall thickness is 2 mm, the volume 5.3 liters. The chamber is closed at both ends by two plane glass windows 70 mm thick. The chamber is illuminated and photographed via these windows. In a side wall of the chamber there is an opening covered by an elastic diaphragm (2) controlling the expansion (Figure 3).

Expansion system (Figure 3). In order that a charged particle traversing the chamber liquid should form a track, the liquid has to be superheated to a definite degree. This is achieved by a special electromagnetic valve (1) which reduces the pressure on the diaphragm (2) from P_h to P_l /3/. The

excess gas is transferred to the container (3), where it is kept at the pressure P_1 by means of the pressure stabilizer (4). The operating parameters of the chamber are thus kept fixed, which is very important for prolonged operation of the chamber.

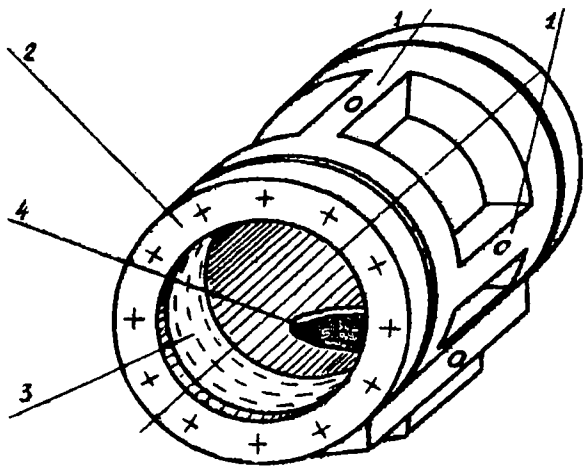

FIGURE 2. Body of a heavy-liquid bubble chamber:

1 — chamber body; 2 — flange; 3 — glass window; 4 — diaphragm.

After reducing the pressure, the electromagnetic valve returns to its original position, again delivering gas at a pressure P_h from container (5) to the diaphragm. The container (5) is connected to the gas source (7) (V = 40 liter, P = 150 atm) via a standard reduction valve.

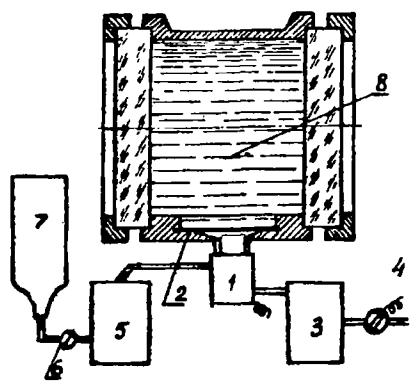

FIGURE 3. Expansion system of a bubble chamber.

During one expansion cycle 5 liters of gas under normal conditions are removed from under the diaphragm. The gas leaks in the above-described system are estimated to be 2 liter/min. From the above data on the gas consumption the amount of gas in a standard 40-liter cylinder (P = 150 atm) is sufficient for a continuous operation of the above-described bubble chamber for 10 hours at a rate of one expansion per minute.

Illumination system. The chamber light source is of a very simple design. Its principle of operation is shown in Figure 4. It illuminates the whole track length. The light source is a IFK-120 flash tube. The energy consumption during one chamber cycle is 40 joule.

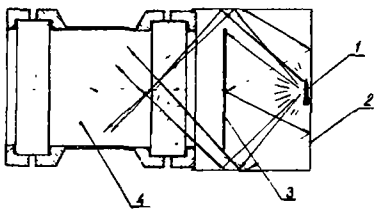

FIGURE 4. Illumination system:

1 — flash tube; 2 — reflecting envelope; 3 — screen; 4 — illuminated volume.

Photography. The spatial coordinates of the tracks are determined from stereophotographs of the chamber volume. In the chamber being described the photography was performed by two "Jupiter-8" lenses ($F = 52.5$ mm, $2\beta = 45°$). The distance between the lenses — the base — was 120 mm. The average demagnification was 8. A 35-mm perforated film of type KN-4S was used. The film transport was common to both cameras. To facilitate the scanning of the film each frame had its number imprinted on the film.

Control system. The bubble chamber is controlled electronically, the control unit performing the following tasks: 1) varying the pressure in the chamber by means of an electromagnetic valve; 2) switching on the flash tube; 3) film transport by switching on and off an electric motor, imprinting the frame number on the film.

The time interval between two subsequent chamber expansions can be varied over a wide range. The estimated weight of the whole system, including the auxiliary equipment, is about 300 kg, the capacity is 600 stereopairs.

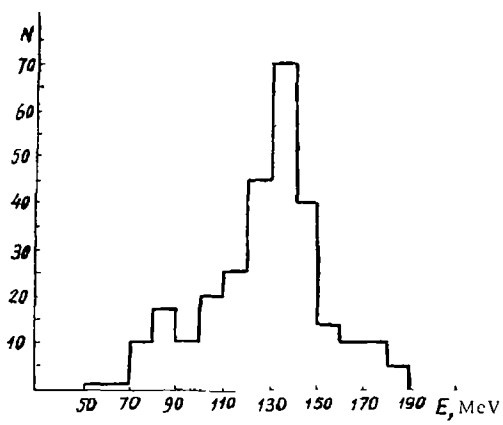

FIGURE 5. The proton energy spectrum observed in the chamber.

A chamber filled with freon 13-V1 was successfully tested in a proton beam of the synchrocyclotron of the Joint Institute for Nuclear Research. Several thousands of pictures were taken. The proton beam incident upon the chamber possessed a wide energy spectrum ($E_{p\,max} = 150$ MeV). The spectrum obtained after processing the pictures is shown in Figure 5. From this figure it follows that protons with energies from 50 to 140 MeV are detected in the chamber with an efficiency close to 100%. The final evaluation of the results obtained indicates the possibilities of using the heavy-liquid bubble chamber without a magnetic field in physics experiments. From the details given above it seems feasible to use this chamber in balloon flights in the upper layers of the atmosphere.

The problem of using standard films for photographing the chamber while cosmic rays are incident upon the chamber was investigated. The allowable integral proton flux ($E_p = 660$ MeV) causing a film blackening of $D = 0.35$. was determined experimentally. The allowable flux turned out to be $6 \cdot 10^8$ protons/cm^2. One can get rid of the influence of less energetic protons by suitable shielding, since the volume of the film magazines is not large, and the shielding does not cause any appreciable increase in weight. There are no fundamental difficulties in supplying the various elements of the chamber with power. The expansion method used does allow the operation of the chamber for long periods of time due to the appreciable gas consumption. The use of other, nonpneumatic expansion methods, for chamber expansion do not seem probable at present. There remains only one way, namely the design of a pneumatic expansion system with a lower gas consumption. A method which looks promising is based on utilizing the elastic properties of the operating liquid /4/. Calculations indicate that such a pneumatic expansion system could reduce the gas consumption by a factor close to 5, which will increase appreciably the data that could be obtained by a bubble chamber under the same conditions. In this way the chamber could operate for much longer periods of time, and there is the possibility of mounting the bubble chamber in a satellite and performing detailed studies of particle fluxes in outer space.

The chamber described is the first attempt at designing such an instrument for cosmic-ray investigations. The use of a bubble chamber enables the determination of the angular distribution of ionizing particles, their spectrum over a fairly wide energy range, the composition of the ionizing radiation and its space-time characteristics.

The authors would like to thank G. E. Kocharov, A. M. Romanov, E. I. Chuikin and V. A. Romanov for their participation in the discussions on a self-contained bubble chamber.

Bibliography

1. Das Gupta, N. and S. Gosh. Kamera Vil'sona i ee primenenie v fizike (Cloud Chamber and its Use in Physics). — Moskva, Gostekhizdat. 1947.
2. Bukat, G. M., N. M. Vershilova, K. N. Ermakov, E. A. Kotikov, and T. Ya. Yurevich. Programma geometricheskoi rekonstruktsii dlya EVM "Minsk-22" (Geometrical Reconstruction Program for the "Minsk-22" Computer). — Preprint FTI, No. 175. 1969.

3. Aleksandrov, Yu.A., G.S. Voronov, V.M. Gorbunov, N.B. Delone, and Yu.I. Nechaev. Puzyr'kovye kamery (Bubble Chambers).— Moskva, Gosatomizdat. 1963.
4. Dykes, M.S. and G. Bachy.— International Colloquium on Bubble Chambers, Heidelberg. 1967.

V. S. Chukin

MATERIALS FOR THE OPTICAL SYSTEMS OF CHERENKOV AND SCINTILLATION COUNTERS

The amplitude resolution of scintillation and Cherenkov counters is limited by the spread of the input signal. The spread is due to the statistical nature of a whole series of processes occurring in the detector — lightguide — photomultiplier system. These processes can be divided into the following three groups: 1) the generation of photons in the detector by the radiation being detected; 2) the propagation of the photons in the optical system of the counter; 3) the signal generation in the photomultiplier. Below are given some results of experimental investigations performed with the aim of searching for and developing new materials to improve the light yield and the light collection in the detector — lightguide — photomultiplier system, and thereby improve the measuring properties of Cherenkov and scintillation counters. Taking into account the appreciable difference between the spectrum of the Cherenkov radiation (Figure, curve 13) and of the radiation produced in a scintillator (curve 1), photomultipliers and materials with suitable spectral characteristics should be used in Cherenkov counters (curve 12).

Since the Cherenkov radiation intensity increases rapidly with a decrease in wavelength, one of the main possibilities of increasing the light yield from a Cherenkov counter is to use a radiator with a sufficiently high refractive index (if it is not limited by the energy threshold of the particles being detected) and a good transmission in the short-wave region. In many cases Plexiglas (n = 1.5) can be used. Commercial Plexiglas in general does not possess a good transmission in the short-wave region.

The investigations performed on the light transmission of various polymers /1/ based on high-purity methylmetacrylate made it possible to determine the composition of Plexiglas having a high transmission in the short-wave region (curve 7). Such a type of Plexiglas can be recommended as a radiator and lightguide in Cherenkov counters. It is interesting to note that plastic scintillators based on especially pure methylmetacrylate /2/ have a higher transmission $\alpha = 0.010\,cm^{-1}$) than polystyrene-base plastics ($\alpha = 0.035\,cm^{-1}$); (curves 4 and 3). Curve 2 in the figure is the transmission spectrum of a 10-mm thick monocrystal of TlCl. This material can be effectively utilized as a radiator in total absorption Cherenkov counters ($x_0 = 0.94\,cm$, $\rho = 7.0\,g/cm^3$, n = 2.2).

In order to reduce light losses in the optical system of the counter due to reflections at the interfaces of different parts, the material used for effecting the optical contact should have a high transmission coefficient in the wavelength region of the radiation being detected and also a suitable refractive index. The best results are achieved when its refractive index

lies between the refractive indices of the materials being brought into contact. In many cases it is advisable to use materials having bonding properties /3/. In the figure are shown the transmission spectra of several bonding materials based on various compounds and used in experimental setups used for investigating primary cosmic radiation /4/. The optical and mechanical properties of these bonding compounds possess several advantages over the often used Canadian balsam (curve 5).

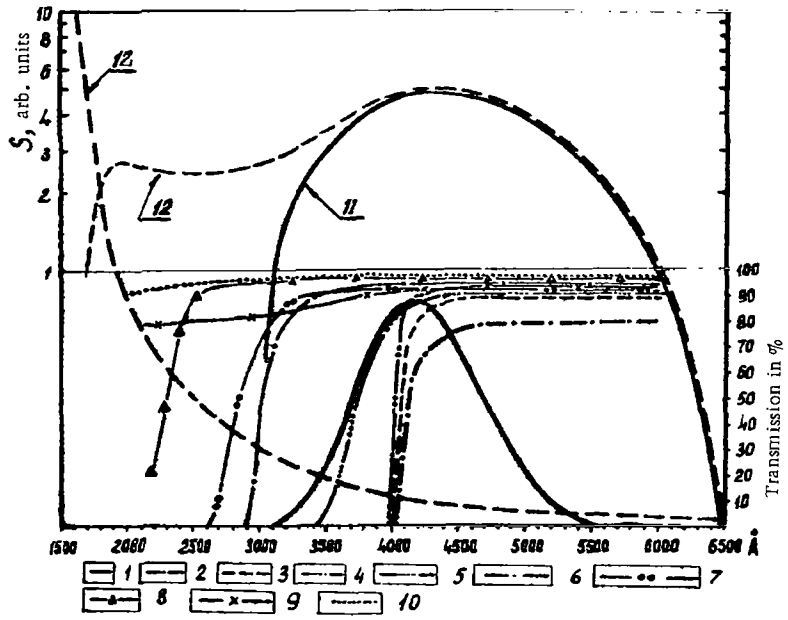

FIGURE. Some spectral-optical characteristics:

1 — emission spectrum of NaI(Tl). Transmission spectra; 2 — TlCl monocrystal (10 mm); 3 — polystyrene-base plastic scintillator (10 mm); 4 — polymethylmeta-crylate-base plastic scintillator (10 mm); 5 — Canadian balsam (40 μ thick); 6 — epoxy optical glue (40μ thick); 7 — Plexiglas with improved transmission; 8 — glue on a monomeric cyanacrylate (30μ thick); 9 — KV-3 silicon grease (50μ thick); 10 — Silicon fluid FS-75 (30μ thick); 11 — spectra characteristic of FEU-52; 12 — spectral characteristic of FEU-39A; 13 — Cherenkov radiation spectrum.

Bibliography

1. Rubtsov, M. A., M. I. Frolova, and V. S. Chukin. Organicheskoe steklo dlya detektorov cherenkovskikh schetchikov (Plexiglas for Detectors in Cherenkov Counters). — PTE (in print).
2. Gunder, O. A. Doklad na V Vsesoyuznoi konferentsii po sintezu, proizvodstvu i ispol'zovaniyu stsintillyatorov (Fifth All-Union Conference on the Synthesis, Production and Utilization of Scintillators). — Khar'kov, June 1969 (in print).
3. Chukin, V. S. — Preprint FIAN SSSR, No. 96. 1967.
4. Chukin, V. S. — Author's Summary of Candidate's Thesis, Izd. FIAN SSSR. 1968.

G. M. Gorodinskii and E. M. Kruglov

ON THE POSSIBILITY OF DETERMINING THE DIRECTION AND POLARIZATION OF A PHOTON BY TWO CONSECUTIVE COMPTON SCATTERINGS IN THE DETECTOR MATERIAL

Below a method is described for determining the direction of a photon based upon the detection of two consecutive Compton scatterings. This method can be utilized in the construction of detectors for the search and investigation of localized astrophysical gamma-ray sources in the energy range from 1 to 50 MeV. The detector should be made of scintillator fibers. The efficiency of such a chamber of dimensions $150 \times 150 \times 150\ mm^3$ increases from 3 to 40%, when the energy of the incident photons decreases from 50 to 5 MeV. The geometry factor of such a detector is $200\ cm^2 \cdot$ sterad. The angular resolution $\Delta\psi$ in the azimuth is given by the expression

$$\Delta\psi = \left(\frac{\rho \varkappa d \beta_0^2}{20}\right)^{\frac{1}{3}} \frac{\sin\theta}{\sin\xi},$$

and the resolution $\Delta\theta$ in the zenith is computed from the relation $\cos\theta = 1 - \frac{T}{k'(T+k')}$ and is determined by the energy resolution of the instrument, where ρ is the density of the scintillator material, g/cm^2; $\varkappa$ is a coefficient of the order of unity; d is the diameter of the scintillator fiber, mm; β_0^2 is the mean square multiple scattering angle in a 1-cm thick scintillator, $(\text{radian})^2$; θ is the angle between the primary and the scattered photons; ξ is the angle between the scattered photon and the electron; k' and Γ are the energies of the scattered photon and the electron, respectively.

Below are given the smaller of the errors $\Delta\theta$ and $\Delta\psi$ which are obtained for $\rho = 1.05\ g/cm^2$ (polystyrene), $d \approx 0.5$ mm as a function of the primary photon energy k and the ratio of energies k'/k.

k	k'/k = 0.9	k'/k = 0.7	k'/k = 0.5	k'/k = 0.3	k'/k = 0.1
50	20'	30'	40'	1° 40'	1° 50'
25	25'	40'	1° 15'	2°	3°
10	—	2°	4° 30'	5°	5° 30'
5	—	—	5° 30'	8° 20'	8° 40'

In comparison with other detectors the scintillation chamber can have in the same energy interval an angular resolution better by one order of magnitude and a geometry factor larger by two to three orders of magnitude.

In the energy range below 10 MeV it is better to use a hodoscope or wire spark chambers together with multiwire proportional counters for the detection of successive Compton scatterings. The angular resolution, efficiency and geometry factor of such detectors is comparable with the corresponding parameters of the scintillation chamber.

Detectors based upon the detection of two successive Compton scatterings are sensitive to the linear polarization of the primary photons, and the asymmetry coefficient R increases with a decrease in the primary photon energy and reaches 12% for primary photons of ~ 5 MeV. The ability to detect polarization is an important advantage of the proposed method, since the instruments used in gamma astronomy are not sensitive to polarization.

Bibliography

1. Butslov, M.M., V.I. Komarov, O.V. Savchenko, and L.I. Soroko.— PTE, No.3:84. 1965.
2. Akimov, Yu.K., M.M. Butslov, O.V. Savchenko, and L.I. Soroko.— Atomnaya Energiya, 12(5):413. 1962.
3. Savchenko, O.V.— PTE, No.4:142. 1959.
4. Reynolds, G.T. and P.E. Condon.— Rev. Scient. Instr., 28, 1098. 1957.

V. V. Petrov

FIVE-CHANNEL ANALYZER FOR LOW-LEVEL SIGNALS

The analyzer described below has been operating for several years in a low-background system measuring very small amounts of radioactive gases /1/. Since the measurement times generally vary from several days to months, the requirements on the stability and reliability of the system are very stringent. Since the detailed knowledge of the pulse-height spectrum is not required in this case, it is possible to use an analyzer with a small number of channels.

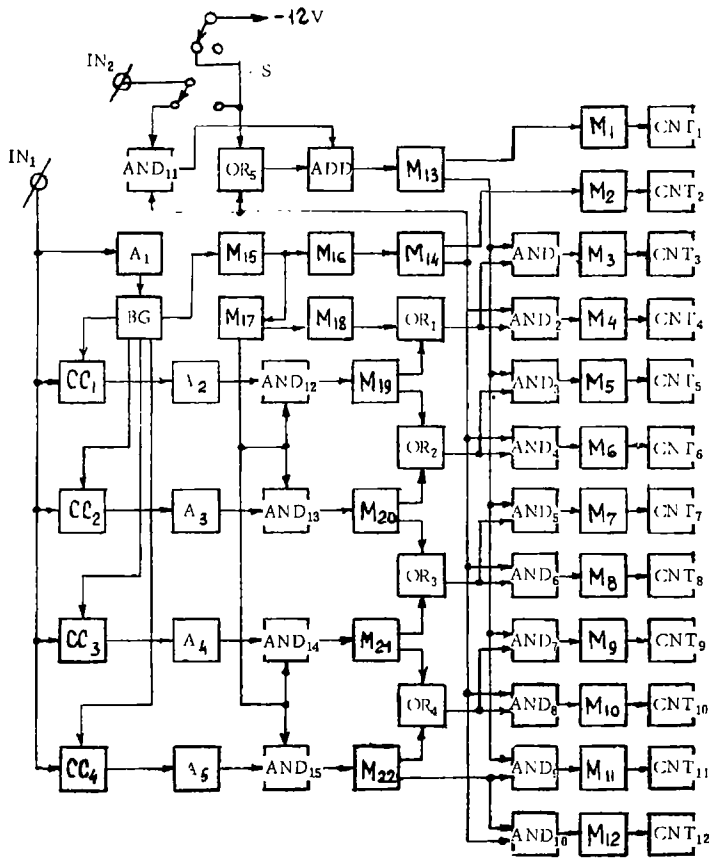

FIGURE 1. Block diagram of the pulse-height analyzer.

A characteristic feature of this pulse-height analyzer is the fact that the pulse-height analysis is performed without preliminary amplification. This makes it possible to forego the amplifier — one of the unstable elements of the measuring system. The block diagram of the pulse-height analyzer is given in Figure 1.

The negative pulses are fed to the analyzer input IN_1, to which are connected four comparison cascades CC and the amplifier A_1. The first threshold of the analyzer is determined by the amplification factor of the amplifier A_1. The amplified pulses trigger a blocking generator BG. The pulses shaped by the blocking generator with a durtion of 10 μsec are limited by a D818V Zener diode having a temperature instability of 0.01%/1°C and are fed to a voltage divider, which determines the necessary thresholds, and from there to the corresponding comparison cascades. These cascades are based on differential amplifiers (Figure 2).* The comparison cascades $CC_1 - CC_4$, together with the error signal amplifiers $A_2 - A_4$ and the output coincidence circuits $AND_{12} - AND_{15}$ form four discriminators. The discriminators are the main elements of the analyzer which determine its precision of operation. The operation features will be discussed in detail.

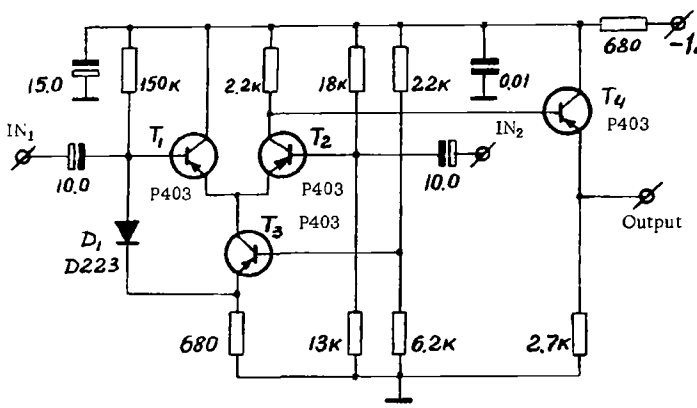

FIGURE 2. Differential amplifier.

It is well known /2/ that the output pulse from a differential amplifier operating in a pulse mode can be written as

$$U_{out} = \kappa_d (U_{in} - U_b) + \kappa_s (U_{in} + U_b) = \kappa_d \left[(U_{in} - U_b) + \frac{U_{in} + U_b}{N} \right], \qquad (1)$$

where U_{in} is the pulse height of the input pulse at IN_1; U_b is the bias voltage at IN_2; k_d is the amplification factor of the difference signal; k_s is the transmission coefficient of the resulting pulse; N is the ratio between the amplification factor of a symmetrical input signal at IN_1 and IN_2 and the amplification factor of two equal input signals.

* The diode D_1 in the comparison circuit is a means of protection against overloads, which can occur when connecting the analyzer to a device matching the pulse source with the analyzer input.

This ratio is often called the suppression coefficient of the total signal. The condition for the operation of the comparison cascade can be written as $U_{out} = U'_{th}$, where U_{th} is the threshold sensitivity of the circuit following the differential amplifier. Using this condition, the relative error of the discriminator is given by

$$\delta_{in} = \frac{U_{th}}{U_b}\delta_{th} + \frac{2}{N}\delta_N + \delta_b , \qquad (2)$$

where δ_{in} is the instability (relative error) of the discriminator transformed to the input; $U_{th} = U'_{th}/k_d$ is the threshold sensitivity of the discriminator (sensitivity at $U_b = 0$); U_b is the bias voltage (discriminator threshold); $\delta_{th} = \delta_d + \delta_{ts}$ is the relative error in U_{th}; δ_r is the relative error in the amplification factor of the difference pulse in the differential amplifier; δ_{ts} is the relative error in U'_{th}; δ_N is the relative error of N; δ_b is the relative error in the bias voltage.

From expression (2) it follows that in order to achieve the smallest possible value of δ_{in} it is necessary to reduce U_{th} and increase N. The minimum value of U_{th} is determined by the internal noise of the differential amplifier. N can be increased by using the highest possible values of the emitter resistance in the differential amplifier /2/. In the above circuit the differential resistance of the collector transition of the T_3 transistor serves as the emitter resistance. Measurements have shown that for the circuit shown in Figure 2, N = 8000, $\delta_N = 0.8\%/°C$, $k_r = 27$, $\delta_r = 0.1\%/°C$ in the temperature interval from −20 to +60°C. The specifications of the transistors used in the circuit were $\alpha = 0.97$ and $I_{co} \leq 1\,\mu A$ at 20°C. Measurements with two comparison circuits yielded almost identical results. Thus the error of the comparison circuit was $\frac{2}{N}\delta_N = 0.0002\%/°C$. This quantity was also measured directly, and the result was confirmed.*

One peculiarity of the discriminator should be mentioned. Due to the difference in the leading edges of the pulses being investigated and the bias pulse, and also due to the different arrival times of these pulses at the input of the comparison circuit there appears a voltage overshoot leading the error signal. When this pulse passes through the differentiating circuits of the amplifier, this overshoot causes a change in the pulse height of the error signal. The spread in the delays of the signal and bias pulses, and also the instabilities in the differentiating elements can lead to a drift of the discriminator threshold equivalent to a drift in the bias voltage. In the general case this error can be written as

$$\delta_v = c\,\frac{\tau_3}{\tau_{dif}}\,\delta_c , \qquad (3)$$

where τ_3 is the duration of the overshoot; τ_{dif} is the differentiation constant of the error signal amplifier; c is a coefficient depending upon the ratio of the leading edges of the signal and error pulses and the integration constant τ_i of the error signal amplifier (c is always less than unity); δ_c is the error in the error pulse height shift.

From (3) it follows that δ_v can be decreased by choosing τ_{dif} as large as possible. The error signal amplifier should be constructed from nonoverloading circuits so that during the time τ_3 there will be no recharging of the

* The time instability of the comparison could not be observed during 6 hours of continuous operation, and therefore only an upper limit of 0.0015% could be established.

capacitances between the cascades. It should be mentioned that the increase in τ_{dif} hardly increases the noise at the input of the differential amplifier; however, when choosing τ_{dif}, the spectral power distribution of the noise in the device matching the signal source with the analyzer input should be taken into account /3/. In the analyzer under discussion the differentiation constants of the error signal amplifiers $A_2 - A_5$ were chosen to be 40μsec. With this value the noise at the input of the comparison cascades with $\tau_i = 1.5\mu$sec was $40 - 50\mu$V (at the 3σ level). From here U_{th} was chosen as 100μV. The range of the analyzer thresholds was $0.1 - 100$ mV at the input, $\delta_{th} = 2\%/°C$. The noise at the input of the amplifier A_1 was 20μV (at the 3σ level) for $\tau_i = 1.5\mu$sec, $\tau_{dif} = 30\mu$sec.

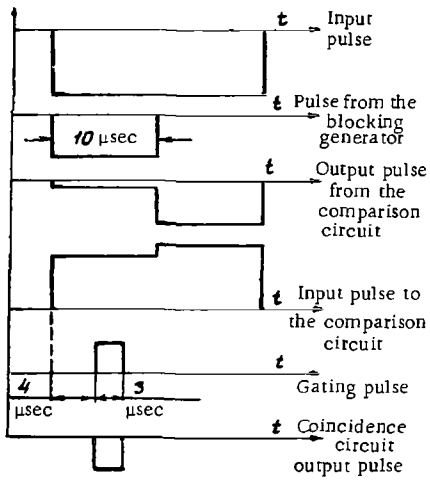

FIGURE 3. Voltage diagram in the discriminator.

The operation of the discriminators of the analyzer is explained in the voltage diagram in Figure 3. The output of multivibrator M_{17} serves as a gating pulse which has a duration of 3μsec. The gating pulses are delayed by the multivibrator M_{15} for 4μsec with respect to the leading edge of the input pulse. This delay eliminates the influence of the error signal overshoots caused by the base-collector capacitances of transistors T_1 and T_2 (see Figure 2). During this time the oscillations produced by the self-induction of the wire potentiometers in the bias voltage block are attenuated. The output pulses from the coincidence circuits $AND_{12} - AND_{15}$ trigger the multivibrators $M_{19} - M_{22}$, the output pulses of which have a duration of 20μsec. The separation of the pulses among the channels is performed in the usual way /4/ by the anticoincidence circuits $OR_1 - OR_4$. The memory of the analyzer consists of electromechanical counters $CNT_1 - CNT_{12}$, type SB-1M. The counters are operated by pulses from the multivibrators $M_1 - M_{12}$. The memory is divided into two parts. The even-numbered counters record all input pulses. The odd-numbered counters operate in coincidence or anticoincidence (depending on the position of the

switch S) of the input pulses with some external pulses (e.g., from an active shielding system). The counters are controlled by the coincidence circuits $AND_1 - AND_{12}$. The pulses from the gating multivibrator M_{14} (duration 8 μsec) are delayed with respect to the leading edge of the input pulse by 8 μsec by the multivibrator M_{16}. This delay makes it possible to operate the analyzer in coincidence or anticoincidence with external pulses which do not coincide with the detector pulses times. These modes of analyzer operation are achieved by the circuits AND_{11} and OR_5, which trigger the multivibrator M_{13} (duration of output pulse 8 μsec) via the adder ADD. The total number of pulses recorded by the five channels of the analyzer should coincide with the numbers recorded by CNT_1 and CNT_2. This serves as a check on the reliability of the electronics.

When operating with a low-background system, pulses from the proportional counter are rare events, so that no effort was made to render the analyzer fast. The present analyzer can operate with mean rates of 10 pulses/sec. It is designed to operate with input pulses having a duration of at least 10 μsec and a risetime less than 2 μsec. All components except those in Figure 2 are standard and therefore are not described here. The analyzer is supplied by a regulated power source of +2 and −12V. The reliability of this instrument is borne out by three years of trouble-free operation in a low-background system. The threshold drifts do not exceed $0.5\%/U_{in} + 20\mu V$ for a month, when operating in the temperature range from 10 to 30°C.

The author would like to thank G. E. Kocharov as well as V. O. Naidenov and Yu. N. Starbynov for their valuable cooperation in solving several problems which occurred during the development of the present analyzer. The author would also like to thank O. M. Voropaev for his help in the construction of the instrument.

Bibliography

1. Kocharov, G. E. and V. O. Naidenov. — Preprint FTI AN SSSR, No. 133. 1968.
2. Landy, R., D. Davis, and A. Albrecht. Spravochnik radio-inzhenera. — Gosenergoizdat. Moskva-Leningrad. [Russian translation. 1961].
3. Gillespie, A. B. Signal, Noise and Resolution in Nuclear Counter Amplifiers. London, Pergamon Press. 1953.
4. Gorn, L. S., I. S. Krashennikov, and B. I. Khazanov. Elektronika v spektrometrii yadernykh izluchenii (Electronics for Nuclear Radiation Spectroscopy). — Moskva, Gosatomizdat. 1963.

V. S. Eletskii

A METHOD FOR DETERMINING THE PARAMETERS OF TUNNEL-DIODE PULSE-HEIGHT DISCRIMINATORS

In recent years tunnel diodes are being used more often in pulse-height discriminators. However, until now there is no simple analytical method for the design of the spectrometric channel, nor a precise engineering calculation of tunnel-diode discriminators.

The spectrometric channel consists of a detector, preamplifier, amplifier and one or several tunnel-diode pulse-height discriminators.

The sensitivity of the lower-limit discriminator determines the gain of the amplifier and the error in the trigger threshold:

$$\Delta = \frac{\Delta I_s}{I_s} \cdot 100\%, \qquad (1)$$

where I_s is the minimum required pulse height to trigger the tunnel diode; ΔI_s is the necessary change in I_s caused by changing the discriminator trigger level due to an unstable operation of the circuit.

A precise computation of ΔI_s which is due to variation in the supply voltages, temperature drifts of the peak current and its degradation cannot be effected on the basis of a linear tunnel-diode characteristic. Therefore, in order to clarify the simple relation between the current and voltage, measurements of the initial, rising part of the characteristics of the tunnel diodes AI101A, AI101B, AI101V, AI101D and AI101I were performed. These measurements have shown that: 1) for all these tunnel diodes the initial parts of the characteristic are identical; 2) this part of the characteristic can be very well described by a part of a sinusoid from 0 to 90°; 3) the sinusoidal dependence is not influenced by temperature.

The relation between the current and the voltage along the initial, rising part of the tunnel-diode characteristic, as deduced from the measurements, is given by (2)

$$I_* = I_1 \sin \frac{\pi v_0}{2 v_1}, \qquad (2)$$

where v_0 is the displacement voltage; v_1 is the peak voltage of the characteristic.

The variation of the parameters I_* and I_s related to the unstable operation of the circuit can be easily determined from the above sinusoidal relation.

When the supply voltage varies by $\pm \Delta v$, the value of I'_* can be determined precisely:

$$I'_* = I_1 \sin \frac{\pi (v_0 \pm \Delta v)}{2 v_1}. \qquad (3)$$

The temperature drift and the degradation of the peak current can be easily allowed for by using the following relations:

$$I''_{\bullet} = I'_{1} \sin \frac{\pi v_{\bullet}}{2 v_{1}} , \tag{4}$$

$$I''_{s} = I'_{1} - I'_{1} \sin \frac{\pi v_{\bullet}}{2 v_{\bullet}} . \tag{5}$$

V. V. Yur'ev, A. M. Romanov and E. V. Myakinin

A "PHOSWICH" FAST-NEUTRON SCINTILLATION DETECTOR

In the measurements of the fluxes and spectra of fast (1 — 10 MeV) neutrons in the upper atmosphere and beyond it scintillation counters of the "phoswich" type are used. The compound scintillator in these detectors is made of materials with different characteristics (fluorescence times, etc.) and is viewed by one photomultiplier. We have compared different scintillators containing stilbene or an organic liquid in a thin (6 mm) plastic scintillator. Liquid scintillators based on α-methylnaphthalene, pseudocumol and phenylcyclohexane were manufactured at the Research Institute of Single Crystals. The comparisons were performed with the same electronic circuits and the same FEU-53 photomultiplier.

For the separation of neutrons from photons the difference in the ratios of the fast and slow components of the light pulses for proton and electron recoils was used. This is achieved in the "n — γ" channel by a circuit which compares the pulses from the anode and the last dynode. Charged particles which pass through the plastic into the inner scintillator produce a pulse exceeding the upper threshold of the differential discriminator in the chain of the eleventh dynode of the photomultiplier. The discriminator thresholds were set according to the ratio of the light yields from protons and electrons in stilbene and liquid scintillators. Sources of Cs^{137}, Co^{60}, Po-Be and Pu-Be were used for calibration. The pulses from the differential analyzer (after delay) together with the pulses from the "n — γ" channel are fed to a coincidence circuit (in the counting mode) or to a linear transmitter (in the spectroscopic mode).

In measurements with "phoswich" scintillators with an inner scintillator of 30 mm thickness the efficiency achieved was 8 — 10% for E = 4.5 MeV and 5.5 — 6.5% for E = 14 MeV with the discrimination coefficient for Co^{60} photons of $(2-4)\cdot 10^{-5}$.

The conclusion was that as an inner scintillator a liquid is preferable to an organic crystal. The dimensions of the former are not limited, a fact that is important in measurements of weak fluxes, especially with an increase of the upper limit of neutron energies. Among the liquid scintillators phenylcyclohexane is the best choice, since no glass container is required. L. E. Grudskaya from the Research Institute of Single Crystals participated in the measurements.

S. V. Golenetskii, V. N. Il'inskii, R. L. Aptekar',
Yu. A. Gur'yan, E. P. Mazets, V. N. Panov and
T. V. Kharitonova

MULTICHANNEL GAMMA SPECTROMETER FOR COSMIC-RAY INVESTIGATIONS

A multichannel spectrometer for investigating photons in the energy range from 0.3 to 2.5 MeV and intended to be used in satellites is described. The spectrometer separates the photons from the charged-particle background, controls this background, records detailed photon spectra and also records frequently the photon intensities under conditions of rapidly varying the counting rates along the orbit.

The spectrometer is composed of a scintillation detector of the "fosvich" type, a 64-channel pulse-height analyzer, a two-channel differential analyzer, a charged-particle accumulator and other devices for the logical processing of the information on board and its transmission into the telemetric channels. This spectrometer was mounted in the "Cosmos-135" and "Cosmos-163" satellites.*

The separation of the scintillator pulses from photons and charged particles was performed by a circuit with a resonant loop and a tunnel diode. The photomultiplier was fed by an economical high-voltage converter with multiple multiplication of the voltage and temperature compensation. The differential analyzer was used to investigate the intensity distribution of the gamma radiation in the energy intervals from 0.4 to 0.6 and from 0.6 to 2.5 MeV. In the multichannel analyzer the memory is of the dynamical type utilizing an ultrasonic delay line. The storage of the pulse-height information before its transfer to the memory in a digital form, and also the generation of the channel pulses by dividing a series of gating pulses ensure a stable operation of the analyzer over a wide temperature range. The capacity of the analyzer channels was 2^{11}, the nonlinearity of the scale did not exceed 1%, the average dead time was 2.8 μsec and did not depend upon the spectrum shape.

The stability of the spectrometer was checked during flight by continuously observing the 0.511-MeV line in the spectrum.

* Konstantinov, B.P., and R.L. Aptekar', et al., Present collection, Part 1.

R. S. Zavel'skii

ABSOLUTE AGE DETERMINATION BY THE RADIOACTIVE CARBON METHOD

1. PRINCIPLES OF THE METHOD

Radioactive carbon is produced on earth by cosmic-ray neutrons interacting with nitrogen in the atmosphere. A living organism is in a state of continuous exchange with the surroundings. Therefore, the specific activity of carbon in the organism has to be equal to the specific activity of carbon in the ambient medium. A radioactive material decays exponentially. Therefore, the specific activity in a sample at time t will equal

$$\mathcal{J}_t = \mathcal{J}_0 e^{-\lambda t}. \qquad (1)$$

From this expression the absolute age of the sample can be determined from its time of death to the time of the measurement:

$$t = \frac{1}{\lambda} \ln \frac{\mathcal{J}_0}{\mathcal{J}_t}, \qquad (2)$$

where J_0 is the initial specific activity of the carbon sample; J_t is the specific activity of the carbon sample at time t and $\lambda = 1.2446 \cdot 10^{-4}$ (yr^{-1}) is the decay constant of C^{14}.

It turned out that within measurement errors the determination of the absolute age does not depend upon the geomagnetic latitude of the sample origins or upon their altitudes above sea level, which points to a fairly rapid averaging due to the mixing of the atmosphere. In addition it was found that when the slight difference between the initial specific activities of above-ground and sea organisms is considered, the results of radioactive carbon dating are independent of the sample type. Finally, when comparing ages as determined by carbon dating with absolute ages known from historic facts or tree rings, the results agree well within experimental errors. On the basis of these results Libby /1/ concluded the validity of the assumptions put forward by him /2/ and which form the basis of the radiocarbon dating method:

1. The intensity of the cosmic radiation near the earth, the intensity of the neutron flux and, accordingly, the specific activity of carbon in the atmosphere have been constant for at least over the last several tens of thousands of years.

2. The specific activity of carbon in a living organism of a given type is equal and constant, and is thus a "universal" constant of living matter.

3. After the death of the organism the specific activity of carbon in it decays exponentially. Therefore, this method provides the possibility of determining the absolute age of organic samples.

2. MEASUREMENT TECHNIQUE

In the first stages of development of the carbon dating method mesh-walled counters operating as Geiger counters were used. Later gas-filled proportional counters were employed successfully. The further improvement in the measuring systems which increased the reproducibility of the results was achieved by using liquid scintillators with photomultipliers. At present, gas-filled counters are used in carbon dating systems, when the amount of the initial material is limited; when there are no limitations, scintillators are used.

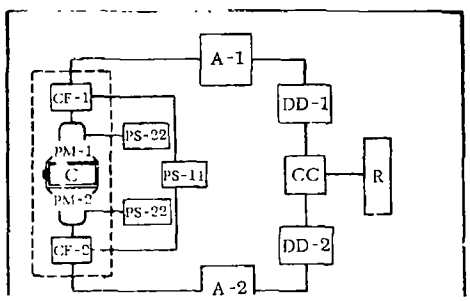

FIGURE 1. Carbon dating system with two photomultipliers in coincidence:

C — cuvette with the working solution; PM-1, PM-2 — photomultipliers; CF-1, CF-2 — cathode followers; PS-11, PS-22 — power supplies; A-1, A-2 — amplifiers; DD-1, DD-2 — differential discriminators; CC — coincidence circuit; R — recorder.

A typical carbon dating system is shown in Figure 1. The cuvette, photomultipliers and cathode followers are placed inside a metal container and serve as the detector of the system. In order to reduce the background the detector is placed inside a massive shielding of lead and mercury. The differential discriminators eliminate low-level noise signals and those pulses produced by the cosmic radiation which are bigger than the pulses corresponding to the maximum energy of the C^{14} β-spectrum. Owing to its time selection of pulses the coincidence circuit reduces the background once again. Finally, a favorable ratio of counts from the sample to the background is achieved. Thus, for example, in the carbon dating system of the USSR Academy of Sciences /3/ with a 24-ml cuvette the counting from a standard sample is 120 min^{-1} while the background is 6 min^{-1}. Consequently, the maximum age that can be determined by such a system is 50,000 years. Further improvement of the scintillation carbon dating system came not only after the improvement of the counting parameters, but also after the measurement possibilities were increased. We have developed a two-channel carbon dating system /4/, in which the counting is performed simultaneously in two regions of the energy spectrum: the working region and a control region (Figure 2). The working region corresponds to the energy spectrum of radioactive carbon, and the control region lies above the maximum energy of C^{14} β-decay. Such a setup enables us to determine whether there are other radioactive materials in the sample, and also to control the background while the sample is being measured /5/.

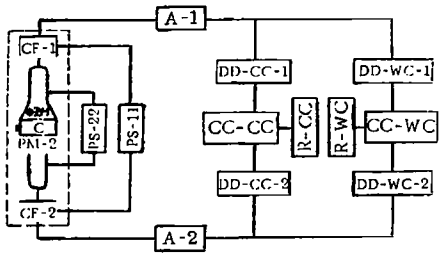

FIGURE 2. Block diagram of a two-channel carbon dating system:

C — cuvette with working solution; PM-1, PM-2 — photomultipliers; CF-1, CF-2 — cathode followers; PS-11, PS-22 — power supplies; A-1, A-2 — amplifiers; DD-CC-1, DD-CC-2 — control-channel discriminators; DD-WC-1, DD-WC-2 — working channel discriminators; CC-CC — control-channel coincidence circuit; CC-WC — working-channel coincidence circuit; R-CC, R-WC — control- and working-channel recorders.

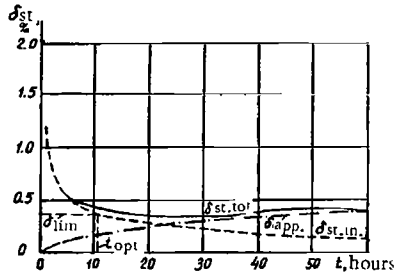

FIGURE 3. The "intrinsic" ($\delta_{st.in.}$), instrumental (δ_{app}) and total ($\delta_{st.tot}$) relative errors of determining the activity of a standard sample as a function of the measurement time.

Let us consider the problem of improving the measurement accuracy. In carbon dating measurements it is generally assumed that the experimental quantities obtained in repeated measurements of a given sample obey Poisson statistics. Since in such measurements the number of radioactive nuclei is sufficiently large, their half-life by far exceeds the duration of a series of measurements, the counting yields only positive integral values, and events belonging to nonoverlapping time intervals are statistically independent. Consequently, there can be no objections to using the Poisson distribution /6/. As far as the experimental values of such a quantity are concerned, they will be described by a Poisson distribution only if the instrumental distortions can be neglected.

When increasing the measurement time, the relative Poisson error of the result decreases inversely proportional to the square root of the measurement time. However, the instrumental distortions are continuously accumulated and increased. Therefore, when increasing the measurement time, a point is reached where the systematic errors are of the same order of magnitude as the statistical errors. If the measurement time is increased still further, the systematic errors become larger than the statistical errors (Figure 3). In such a case the more general binomial distribution can be used, which for a large enough number of measurements approaches the normal distribution /7/. Appropriate calculations can determine the instability coefficient of the apparatus, which is the relative instrumental error accumulated during a standard period of time, for example, one hour. From this value the measuring time during which the systematic errors are still negligible can be determined, and also the corresponding measurement error. The first quantity is the optimal measurement time (t_{opt}), while the

second is the limiting precision of the system (δ_{lim}) (Figure 3). It can be easily seen that measuring after the optimal time does not improve the precision at first, and later makes it even worse. In order to decrease the relative error below the limiting precision several series of measurements are carried out each for a duration t_{opt} and after each set of measurements a recalibration of the system is performed. In a series of l measurements of equal duration the relative error is $\sqrt{l}$ times smaller than the limiting error. Thus, the determination of the instability coefficient of a carbon dating system enables us to determine its suitability for a given problem, to choose the necessary number of measurements and their duration and, finally, to obtain the smallest possible error /8/.

3. IMPROVEMENTS IN THE METHOD

During the further development of the carbon dating method it turned out that the basic assumptions made by Libby are satisfied only approximately and have to be rendered more precise. The specific activity of carbon in the atmosphere and other reservoirs has varied slightly in the past. This is explained by a large number of reasons.

The production of C^{14} on earth is mainly due to nuclear reactions of neutrons with nitrogen nuclei in the earth's atmosphere. The neutrons in the atmosphere are secondary particles produced by primary cosmic radiation. The cosmic-radiation intensity incident upon the earth, and consequently, the specific carbon activity, vary with the solar activity / 9, 10, 11/. The variation in the specific activity due to this effect is 1 — 2% (Figure 4, curve 1), which corresponds to an error of 80 — 160 in the age determined by carbon dating. This error is obvious if the variation of the initial specific carbon activity is not allowed for.

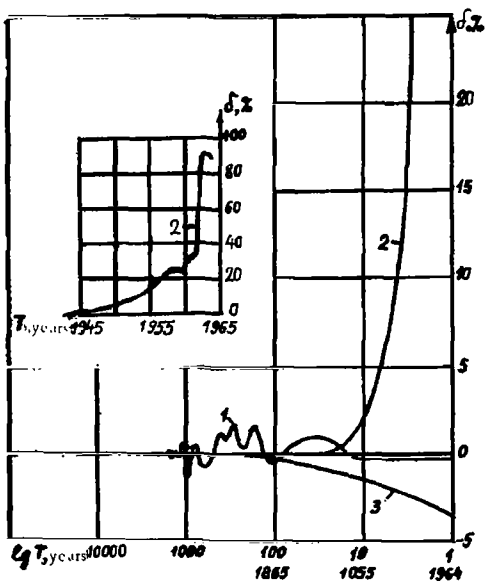

FIGURE 4. Relative variation of the specific carbon activity in the past:

1 — periodic variation in the concentration of C^{14} related to the solar activity; 2 — variations due to the effects of nuclear tests; 3 — variations due to the so-called industrial effect.

An additional source of radioactive carbon in the earth's biosphere lies in the test blasts of nuclear and especially thermonuclear weapons. The contamination of the atmosphere by radioactive carbon from nuclear tests has a global character. The magnitude of this effect reached 90% of the average specific carbon activity during the period prior to the blasts /12/. However, at present, due to the test ban in the atmosphere the nuclear effect tends to decrease.

Since nuclear tests started only 25 years ago, they have no effect upon the age determination of older samples (Figure 4, curve 2).

Another cause for the variations in the concentration of radioactive carbon in the biosphere is due to the dilution of the natural carbon isotope mixture by stable isotopes. This dilution is caused by the industrial discharge of carbon dioxide into the atmosphere, and also by the volcanic activity of the earth. This phenomenon has a global character. However, close to big cities and in zones of active volcanoes local effects are also observed /13/. The magnitude of the industrial effect (or, as it is often called, the Suess effect) and its time dependence are known (Figure 4, curve 3). Since its influence started only about 130 years ago, this effect plays no role in the carbon dating of samples older than this age.

The fractionation of carbon isotopes occurs when the carbon goes over from one carbon-containing reservoir into another, and the relative amounts of the various isotopes change. The fractionation is caused by the interface between two media having different permeabilities for light and heavy isotopes /14/. The fractionation coefficient can reach several percent /15/, which can cause an error of several hundreds of years in the age as determined by carbon dating. The study of the fractionation of the different carbon isotopes has shown that the change in the ratio C^{14}/C^{12} is higher by about a factor of two than the change in the ratio C^{13}/C^{12}. By measuring independently the relative concentration of the stable isotopes C^{13}/C^{12} (e.g., by a mass spectrometer), the change in the relative concentration of C^{14}/C^{12} in a given sample can be determined and the appropriate correction for the age can be made.

4. LIMITS OF THE METHOD

The lower limit of the carbon dating method is the zero age. The upper age limit of the carbon dating method has been raised several times during the last 10 — 15 years and at present in most carbon dating laboratories constitutes 40,000 — 50,000 years. However, in several cases the absolute age of samples was determined to be 60,000 — 70,000 years. The maximum age that can be determined by a given system with sufficiently high accuracy and reliability depends upon its parameters and is the experimental upper age limit of that system. However, there exists a fundamental upper age limit of the carbon dating method which can be determined from the following considerations /16/. When measuring the absolute age of samples of organic origin by the carbon dating method, only the decay of that radioactive carbon that entered the organism from the surrounding medium is considered. However, due to neutron interactions with nitrogen and carbon nuclei in the given organism there is production of a small amount of "inherent" radioactive carbon. This radioactive carbon is produced inside the organism both during its life as well as after its death. After the death of the organism the amount of radioactive carbon of external origin continuously decreases, while the amount of radioactive carbon produced in the organism continuously increases (Figure 5).

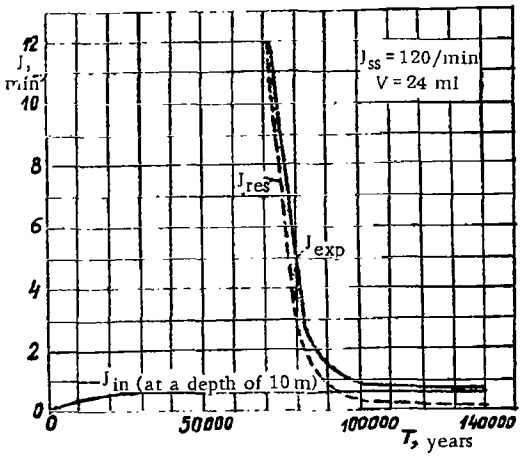

FIGURE 5. Carbon activity in a sample as a function of time:

J_{res} — residual activity; J_{in} — "inherent" activity; J_{exp} — experimentally measured activity; J_{ss} — standard sample activity.

Samples whose absolute age is 30,000 — 50,000 years are generally found at a depth of 10 — 15 m. The neutron flux at a depth of 10 m is determined mainly by the neutron emission of minerals. The neutron emission of minerals varies, depending upon their composition, over a fairly wide range:

$$(0.14 - 1.44) \cdot 10^{-3}\ n \cdot cm^{-2} \cdot sec^{-1}\ /17, 18/.$$

When the residual specific activity of the carbon which the organism received from the outside reaches the same order of magnitude as the specific activity of the carbon produced inside the organism, the precision of the age determination drops appreciably. When the residual specific activity of carbon becomes smaller than the internally produced activity, the sample's age becomes indefinite. This limit can vary depending upon the chemical composition of the sample and its neutron activity. On the average it is 90,000 — 100,000 years /16/.

CONCLUSIONS

The development of the carbon dating method has lead to more precise assumptions upon which the method is based, to an improvement in the measuring techniques and to an establishment of a fundamental upper age limit.

As a result of the analysis of the various problems encountered and their successful solution the reliability of the carbon dating method has increased.

At present the carbon dating method is one of the basic methods of constructing age scales for investigations in archeology and quaternary geology. The carbon dating method makes possible the study of certain cosmic processes that occurred in the past. We can therefore expect in the coming years a further development in its range of applications.

Bibliography

1. Libby, W. F.—In: Izotopy v geologii, p. 318. Izd. inostr. lit. Moskva. [Russian translation. 1954.]
2. Libby, W. F.— Phys. Rev., 69, 671. 1946.
3. Zavel'skii, F. S. and V. A. Alekseev.— PTE, No. 2:73. 1966.
4. Zavel'skii, F. S.— Byull. komissii po opredeleniyu absolyutnogo vozrasta geologicheskikh formatsii, Issue 8:150. 1967.
5. Zavel'skii, F. S.— PTE, No. 1:230. 1969.
6. Gol'danskii, V. I., A. V. Kutsenko, and M. I. Podgoretskii. Statistika otschetov pri registratsii yadernykh chastits (Statistics of Counting Nuclear Particles).— Moskva, Fizmatgiz. 1950.
7. Smirnov, N. V., I. V. Dunin-Barkovskii. Kratkii kurs matematicheskoi statistiki dlya tekhnicheskikh prilozhenii (A Brief Course of Mathematical Statistics for Technical Applications).— Moskva, Fizmatgiz. 1959.
8. Zavel'skii, F. S.— PTE, No. 4:69. 1968.
9. Simpson, J. A.— J. Geophys. Res., 65, 1615. 1960.
10. De Vries, H. L.— Proc. Koningkl. Ned. Acad. Wetenschap., BGI, No. 2:1. 1958.
11. Stuiver, M.— J. Geophys. Res., 66, 273. 1961.
12. General Assembly Supplement, No. 14 (A/5814). 1964.
13. Sulerzhitskii, L. D. and V. S. Forova.— Doklady AN SSSR, 171(6):1421. 1966.
14. Crig, H.— Tellus, 9, 1. 1957.
15. Keeling, C. D.— Gecchim. Cosmochim. Acta, 24, 277. 1961.
16. Zavel'skii, F. S.— Doklady AN SSSR, Seriya Geologiya, 180(5):1189. 1968.
17. Shmonin, L. I., V. V. Cherdyntsev, L. L. Kashkarov, and V. F. Ostapenko.— Uchenye Zapiski Kazakhskogo GU, 30(5):25. 1957.
18. Khaldeev, O. D. and V. V. Cherdyntsev.— Trudy Kazakhskogo GU, Issue 2:29. 1960.

National Aeronautics and Space Administration
WASHINGTON, D. C. 20546

OFFICIAL BUSINESS

POSTAGE AND FEES PAID
NATIONAL AERONAUTICS AND
SPACE ADMINISTRATION

10U 001 55 51 3DS 71088 00903
AIR FORCE WEAPONS LABORATORY /WLOL/
KIRTLAND AFB, NEW MEXICO 87117

ATT E. LOU BOWMAN, CHIEF,TECH. LIBRARY

Printed in Jerusalem, Israel

TT 70-50080
NASA TT F-630